Dissolution of Fe(III)- and Mn(III,IV)- (hydr)oxides

by deferrioxamine B

Thesis by

Thomas Lloyd

In Partial Fulfillment of the Requirements

for the Degree of

Doctor of Philosophy

California Institute of Technology

Pasadena, California

1999

Acknowledgements

No thesis is the work of one. There are many ways of contributing: direct interaction, spiritual support, financial support, physical support. First thanks to the Mellon Foundation for supporting this research; further thanks is due to the Ciba-Geigy Corporation for supplying material fundamental to this study. Direct interaction requires the first heartfelt gratitude: Linda Scott for her unfailing commitment to the whole and for her smile; Fran Matzen for understanding lack of understanding of the ways of Keck and the outside world; Bruce Nairn for his patience and generosity; Rich Eastvedt and Hai Vu for their unfailing generosity. Dr. Peter Green and Dr. Nathan Dalleska provided insight and encouragement; while Steve Szczepankiewicz is a truly great person, sharing his time and knowledge unselfishly. Discussions with the Morgan-Hoffmann-Hering Group lead to inevitable insight. Wai Kwan provided excellent work in the face of adversary. The Caltech RA's, need more be said?

I would like to thank my teachers for their patience and enthusiasm.

Great thanks goes to my Thesis Committee: John Bercaw, Janet Hering, Michael Hoffmann, and James Morgan for their excellent criticisms and insight.

I must particularly thank James Morgan, my thesis advisor. I have found a true mentor in him, a fantastic rarity. He has acted as a friend, with vision far surpassing the walls of lab and classroom; as a teacher and advisor, there is no peer.

Gary Sposito deserves my deepest appreciation for allowing me to pursue my curiosity, supporting a musical life of science, and showing me the poetry of our work.

My family gets all the thanks that a family deserves: believing in me, encouraging me, celebrating with me, giving me money...

Finally, all my love and thanks go to Grace Zimmerman for her support, teaching, love, and energy unsurpassed.

Abstract

Microbially produced siderophores are thought to have evolved to increase the availability of iron in oxic aqueous systems. Historically, it has been assumed that siderophores interact with iron found in Fe(III)-(hydr)oxides, removing iron from the solid to form ferrated aqueous species of the siderophore available for uptake by the microorganism. However, this proposed interaction of siderophore with the solid phase has not been examined in detail.

The work presented in this thesis examines the interaction of a model trihydroxamic acid siderophore (deferrioxamine B) with synthetic Fe(III)-, Mn(III), Mn(IV)- (hydr)oxide particles. The experiments were designed to characterize the mineral dissolution process mediated by deferrioxamine B (DFA). DFA was found to dissolve all the solid particles used in the study. The Fe(III)- (hydr)oxides dissolved exclusively by a nonreductive mechanism. The dissolution is a surface-mediated process. Dissolution of manganite was found to be analogous to the Fe(III)-(hydr)oxide dissolution process, while the dissolution of pyrolusite was found to follow a complicated mechanism that involves reductive processes. The interactions between DFA and the solid surface are examined experimentally and theoretically.

Under the conditions in which (i) the concentration of DFA in solution remains essentially constant over the course of the reaction, i.e., the concentration of the ferrated form of DFA (FA) is much less than $[DFA]_{tot}$ over the whole time of the reaction, and (ii)

the concentration of available surface sites remains constant, the dissolution rate can be modeled as a pseudo-zeroth order reaction, where

$$R = k'.$$

Under the same conditions and where the concentration of adsorbed DFA is measured, the dissolution rate can be modeled as a pseudo-first order process, where

$$R = k \, [\equiv Fe - DFA],$$

where $[\equiv Fe - DFA]$ is defined as the concentration of adsorbed DFA. Conditions (i) and (ii) imply that a necessary condition for observation of a pseudo-zeroth order process is that $[\equiv Fe - DFA]$ remains constant over the course of the reaction. Where these conditions fail, the dissolution process becomes more complicated, and the experiments presented here do not address these cases in detail.

Index

Chapter 3 52

Interaction of DFA and FA with the Surface of a Synthetic Hematite

Dissolution of Synthetic Hematite with a Goethite Impurity

Chapter 8

Conclusion

Appendix

The Quantification of Nanomolar Concentrations of Fe(II) Using Electrospray Mass Spectrometry

Tables and Figures

Chapter 1

Cartoon of ligand mediated dissolution of a transition metal oxyhydroxide

(i.) Ligand travels from bulk solution to surface.

(ii.) Covalent bonds form between ligand and surface; other chemical activity may occur,

such as electron transfer or surface rearrangement.

(iii.) The bonds between the surface metal center that is bound to the ligand and the bulk

solid are broken and the metal-ligand complex desorbs

(a) pe-pH diagram of the Fe-CO_2-H_2O system with the metastable am-Fe(OH)$_3$(s)

    as the solid phase. $C_T = 10^{-3}$ M, Fe(II) and Fe(III) = 10^{-5} M, T = 25°C

    (Stumm and Morgan, 1996).

(b) pe-pH diagram of the Mn-CO_2-H_2O system with the following solid phases

    considered: Mn(OH)$_2$(s), MnCO$_3$(s), Mn$_3$O$_4$(s), γ-MnOOH(s), and MnO$_2$.

    $C_T = 10^{-3}$ M, Mn$_T = 10^{-5}$ M, T = 25°C (Stumm and Morgan,1996).

Two potential mechanisms for siderophore mediated Fe-transport. (a.) The Fe(III)-

siderophore complex binds to a cell surface receptor that reduces the Fe(III) to Fe(II),

reducing the affinity of the Fe to the siderophore, and allowing the Fe(II) to be actively

transported across the cell wall into the cell interior. (b.) In this scenario, the Fe(III)-

siderophore complex is transported as a whole into the cell via a specific transport system; an intracellular reductase reduces the Fe(III) to Fe(II), after which the Fe(II) is released into the cell.

Dissolved Fe released per unit hematite mass in the presence of oxalate, ascorbate, or siderophore from Pseudomonas sp 11C (100 mg hematite for oxalate and ascorbate, 21 mg hematite for siderophore) taken from Hersman et al., (1995).

Chapter 2

Peak assignments for the DFA FTIR spectrum

Thermodynamic constants for DFA and FA. Data taken at 20°C, I = 0.1 M $NaNO_3$. (From (Schwarzenbach and Schwarzenbach, 1963))

Energy distributions for various initial conditions for DFA in solution.

Energy distributions for various initial conditions for DFA at the surface of a model hematite.

Energy difference Δ = (isolated – surface)

(A) Experiment 2, unsolvated. This picture shows the energy-minimized structure of the unsolvated DFA in a vacuum.

(B) Experiment 6. This picture shows the energy-minimized structure of the solvated DFA in vacuum.

(A) Experiment 7. The figure depicts the energy-minimized structure of the docked unsolvated DFA onto the model hematite surface.

(B) Experiment 9. The figure depicts a stick model of the energy-minimized structure of the solvated linear DFA molecule.

Chapter 3

Equations governing the reaction of DFA with the hematite surface.

Charateristics of hematite

Adsorption Constants for FA on Hematite

Adsorption parameters for the Langmuir model of the adsorption of DFA onto hematite

PCS particle size distributions for $p_aH = 6$; [DFA] varies as indicated. Signal reported is

percent of total volume of particles. The line shows the cumulative distribution. Note

that the scale of the x-axis varies among the plots.

PCS particle size distributions for $p_aH = 7$; [DFA] varies as indicated. Signal reported is

percent of total volume of particles. The line shows the cumulative distribution. Note

that the scale of the x-axis varies among the plots.

PCS particle size distributions for $p_aH = 7.5$; [DFA] varies as indicated. Signal reported

is percent of total volume of particles. The line shows the cumulative distribution. Note

that the scale of the x-axis varies among the plots.

PCS particle size distributions for $p_aH = 8$; [DFA] varies as indicated. Signal reported is

percent of total volume of particles. The line shows the cumulative distribution. Note that

the scale of the x-axis varies among the plots.

PCS particle size distributions for $p_aH = 9$; [DFA] varies as indicated. Signal reported is

percent of total volume of particles. The line shows the cumulative distribution. Note that

the scale of the x-axis varies among the plots.

Chapter 4

First order rate constants for the dissolution of hematite in the presence of DFA. The units on the y-axes are reported on a per gram hematite (l.h. side) and on a per m^2 surface area (r.h. side), and differ by a factor of 23 m^2 (g hematite)$^{-1}$.

A comparison of observed zeroth-order dissolution rates to those determined by adsorption parameters.

p_aH 5 speciation. (a.) $[DFA]_0 = 10^{-3}$ m; (b.) $[DFA]_0 = 10^{-4}$ m; (c.) $[DFA]_0 = 10^{-5}$ m.

p_aH 6 speciation. (a.) $[DFA]_0 = 10^{-3}$ m; (b.) $[DFA]_0 = 10^{-4}$ m; (c.) $[DFA]_0 = 10^{-5}$ m.

p_aH 7 speciation. (a.) $[DFA]_0 = 10^{-3}$ m; (b.) $[DFA]_0 = 10^{-4}$ m; (c.) $[DFA]_0 = 10^{-5}$ m.

p_aH 8 speciation. (a.) $[DFA]_0 = 10^{-3}$ m; (b.) $[DFA]_0 = 10^{-4}$ m; (c.) $[DFA]_0 = 10^{-5}$ m.

paH 9 speciation. (a.) $[DFA]_0 = 10^{-3}$ m; (b.) $[DFA]_0 = 10^{-4}$ m; (c.) $[DFA]_0 = 10^{-5}$ m.

Potential at the hematite surface as a function of p_aH for I = 0.01, 0.1 and 1.0 m. Data are calculated from observed surface charge densities using Gouy-Chapmann theory.

Dissolution of hematite as a function of ionic strength and p_aH. [DFA] = 10^{-4} m.

Chapter 5

(b) SC hematite, post-dissolution.

(c) Goethite, synthetic.

(d) Expected hematite XRD lines.

(e) Expected goethite XRD lines.

(f) SC hematite, pre – post dissolution.

(g) sol gel hematite post dissolution.

(a.) SC hematite dissolution at pH = 4, [hematite] = 1.00 g kg^{-1}. [DFA]$_0$ varies from 0 to

10^{-3} m.

(b.) [DFA] in solution as a function of time.

(a.) SC hematite dissolution at pH = 5, [hematite] = 1.00 g kg^{-1}. [DFA]$_0$ varies 5 x 10^{-6}

to 10^{-3} m.

(b.) [DFA] in solution as a function of time.

(a.) SC hematite dissolution at pH = 6, [hematite] = 1.00 g kg^{-1}. [DFA]$_0$ varies from 0 to

10^{-3} m.

(b.) [DFA] in solution as a function of time.

(a.) SC hematite dissolution at pH = 7, [hematite] = 1.00 g kg^{-1}. [DFA]$_0$ varies from 10^{-6}

to 10^{-3} m.

(b.) [DFA] in solution as a function of time.

(a.) SC hematite dissolution at pH = 8, [hematite] = 1.00 g kg^{-1}. [DFA]$_0$ varies from 0

to 10^{-3} m.

(b.) [DFA] in solution as a function of time.

(a.) SC hematite dissolution at pH = 9, [hematite] = 1.00 g kg^{-1}. [DFA]$_0$ varies from 10^{-5}

to 10^{-3} m.

(b.) [DFA] in solution as a function of time.

Pseudo-zeroth order dissolution rates for SC hematite expressed as log R vs. pH, [DFA] =

10^{-5}, 10^{-4}, 10^{-3} m.

Dissolution of SC hematite with [hematite] varying by a factor of 10. [DFA] = 10^{-3} m.

The rates vary by a factor of 2.9.

Propeller-stirred, pH-stat dissolution reaction. T = 25°C[DFA]$_0$ = 10^{-3} m, pH varies,

[hematite] = 1.00 g kg^{-1}.

Additions of acid and base as a function of time; pH = 4.

(a.) Raw data.

(b.) Linear fit for early data and late data. R$_{early}$ = 6.59 x 10^{-7} mol$_{OH^-}$ kg^{-1} h^{-1}; R$_{late}$ = 3.31

x 10^{-8} mol$_{OH^-}$ kg^{-1} h^{-1}.

(b.) Spectra showing the formation of Mn(III) – DFA complex as MnO_4^- is added to a

Mn(II) – DFA solution.

UV-visible calibration curve of Mn(III) – DFA at 312 nm, showing an extinction

coefficient of 1.93886 x 10^3 m^{-1} cm^{-1}.

LCV absorbance at 592 nm as a function of dissolved $[MnO_2]$.

LCV data for two separate dissolution experiments. Solution was unbuffered, pH ~ 7.

Dissolution of manganite in the presence of DFA; $[DFA]_0$ = 1 x 10^{-3} m. System is

unbuffered, pH_0 = 7.

Dissolution of manganite. $[DFA]_0$ = 1 x 10^{-3} m; $[\gamma\text{-MnOOH}]$ = 1.00 g kg^{-1}. (a.)

Dissolution curves as a function of pH. (b.) Pseudo-zero[th] order rate constants as a

function of pH.

Manganite dissolution at pH = 7, varying $[DFA]_0$.

Dissolution of MnO_2 with DFA, pH = 7. (a.) Dissolution as a function of time; $[DFA]_0$ =

10^{-3} m. Graph shows $[Mn]_{tot}$ and $[Mn(III)DFA]$. (b.) UV – visible spectra of the

filtrate from the Aldrich MnO_2 dissolution as a function of time. Note the

appearance of the shoulder at 275 nm for late time.

MnO_2 dissolution (Aldrich) in the time region of $0.7\,h < t < 3.5\,h$. The rates match and

all the Mn formed can be accounted for by Mn(III)-DFA.

Spectra filtrates from the dissolution of MnO_2, T. Lloyd preparation, pH = 7. Note that

although focusing on 312 nm gives erratic data as a function of time, there exists a

peak at 312 nm.

Illumination experiment at pH = 8, O_2 present. (a.) All spectra from $t = 0$ to $t = 43,200$ s,

$\Delta t = 600$ s are pictured. Note that there is no discernible change in the spectra.

(b.) Time trace of 312 nm, also showing no significant change over the course of the

experiment.

Spectra of various preparations of Mn(III) – DFA, comparing the spectrum of the

solution after the addition of H_2O_2 in the presence of O_2

Exchange of Fe(III) for Mn(III) in the DFA complex. Addition of Fe(III) was at 31 s.

Chapter 7

A comparison of pseudo-zero[th] order rates of Fe(III)-(hydr)oxide dissolution with DFA;

$[DFA]_0 = 10^{-4}$ m for all data.

Appendix

Chapter 1

Introduction

Microorganisms play an important role in mineral weathering (Berthelin, 1988; Cornell and Schindler, 1987; Hersman et al., 1995; Kostka and Nealson, 1995; Page and Huyer, 1984; Roden and Zachara, 1996). Solid minerals provide a source of micronutrients and a solid substrate to support microbial colonization. Microorganisms are ubiquitous in aqueous environments, occupying niches in even the most extreme environments (Brock et al., 1994). Through metabolism, these organisms synthesize a myriad of compounds, all of which have the potential to affect the minerals that are exposed to them. The interactions can include adsorption onto the mineral surface and chemical reaction at the surface and have the potential to influence precipitation and dissolution of minerals.

The work presented herein examines the effect of a certain class of microbially produced compounds, siderophores, on the dissolution and precipitation of synthetic iron and manganese (hydr)oxides. The work addresses the following questions: (1) How do siderophores interact with the (hydr)oxide surface? (2) Do siderophores affect the rates of dissolution? (3) What are the mechanisms of siderophore mediated dissolution?

1.1 Metal (hydr)oxides

The hydrous oxide minerals are the stable end-products of weathering processes. As mineral parent material comes under the influence of physical and chemical weathering processes in an oxic environment, the dissolved products reprecipitate to form oxides and

hydroxides (Bolt and Bruggenwert, 1976). As the oxides of aluminum, silicon, iron, and manganese form from saturated solution, particles having equivalent radii of 10^{-9}–10^{-2} m are formed (Bolt and Bruggenwert, 1976; Schwertmann and Cornell, 1991). The fraction of material with radii less than 10^{-5} m dominatines, with the larger particles often being cemented aggregates of smaller crystals (Schwertmann and Taylor, 1977). This size distribution results in a large reactive surface area per mass of oxide. For example, consider a gram of mixed Fe(III)(hydr)oxide containing particles with an average density of 4.6 g cm^{-3} and an average spherical equivalent radius of 10^{-7} m. This gram of material contains approximately 10^{13} particles and has a combined total surface area of approximately 10 m^2.

Mineral surfaces mediate many of the abiotic chemical transformations that occur in natural waters, from relatively straightforward adsorption events to surface dependent chemical transformations. This role in natural water systems has implications in the availability of mineral and non-mineral nutrients, the fate of organic and inorganic pollutants, and the speciation of humic material and soluble aqueous compounds.

1.2 Mineral Weathering

Two processes dominate the chemical weathering of (hydr)oxide minerals: reductive and hydrolytic reactions. Both involve the adsorption of a dissolved ligand to the adsorbent surface, forming some sort of ligand-surface species. Small organic acids such as oxalate and citrate that are released as products of microbial respiration accelerate Fe(III)(hydr)oxide dissolution rates (Banwart et al., 1989; Cornell and Schindler, 1987; Maurice et al., 1995; Siffert and Sulzberger, 1991; Stumm and Wollast, 1990; Sulzberger
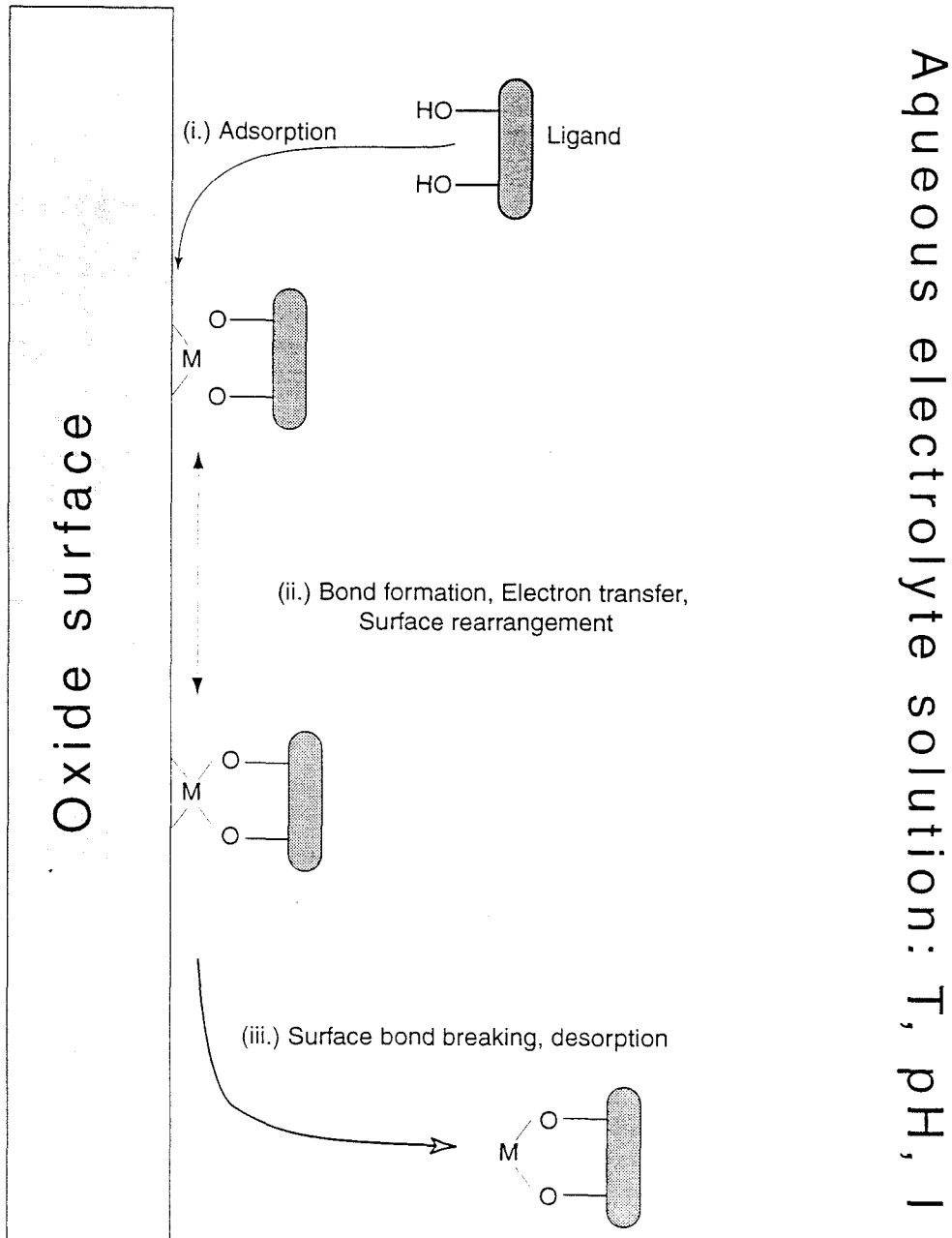
Figure 1
Cartoon of ligand mediated dissolution of a transition metal oxyhydroxide
(i.) Ligand travels from bulk solution to surface.
(ii.) Covalent bonds form between ligand and surface; other chemical activity may occur, such as electron transfer or surface rearrangement.
(iii.) The bonds between the surface metal center that is bound to the ligand and the bulk solid are broken and the metal-ligand complex desorbs.

et al., 1989; Zinder et al., 1986), while also influencing the morphology of oxide crystals that form in their presence (Cornell and Schwertmann, 1979; Cornell, 1985; Cornell and Giovanoli, 1985.) The mechanism of the dissolution depends on the ambient conditions. For example, oxalate can act reductively in the presence of near UV light, or hydrolytically in the absence of UV light (Stumm and Sulzberger, 1992). Figure 1 illustrates the proposed general mechanisms for ligand-mediated dissolution of Fe(III)(hydr)oxides, where the ligands are in general small organic acids.

1.3 Role of Biota in Weathering Processes

The influence of biota on the dissolution and precipitation of the metal oxides is of particular interest. Organisms directly or indirectly harness the energy of the sun, converting solar energy into chemical and mechanical energy. In this process, organic compounds are synthesized that are quite reactive with respect to the ambient chemical environment. For example, reduced species are formed that can react exergonically with the oxide minerals:

(1) α-FeOOH(s) + 2H$^+$ + 1/2H$_2$C$_2$O$_4$ = Fe^{2+}(aq) + CO$_2$(g) + 2H$_2$O
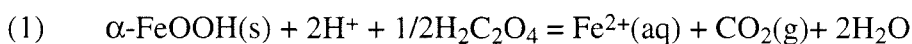
$\Delta G^\circ_f = -109.8$ kJ mol^{-1}

log K = 19.2

If the concentrations of the reacting species are as follows: [H$^+$] = 10^{-7} M, [H$_2$C$_2$O$_4$] = 10^{-4} M, [Fe^{2+}] = 10^{-12}M and P$_{CO_2}$ = 10$^{-3.5}$atm, then $\Delta G = -106.9$ kJ mol^{-1}. Thus, the presence of the organic ligand oxalic acid generates a strong thermodynamic driving

force for the dissolution of goethite. It is reasonable to suppose that such a reaction as (1) is mediated by a surface–complex intermediate, and that the rate at which these types of reactions occur depends significantly on the surface species involved (Stumm and Wollast, 1990).

The rate of uptake of oxygen by respiring organisms helps to define the oxygen profiles in natural waters, determining the redox gradients in natural water systems and thereby the stability of (hydr)oxides that are transported down the redox gradient to a more reducing environment.

Both iron and manganese are important microbial nutrients, often used as electron acceptors in respiration, or electron donors in anaerobic metabolism (Brock et al., 1994; Ehrenreich and Widdel, 1994; Emerson and Revsbech, 1994; Lee and Tebo, 1994; Lonergan et al., 1996; Moffett, 1994; Nealson and Saffarini, 1994; Robinson, 1993; Roden and Zachara, 1996). If O_2 is equilibrated at ambient atmospheric levels with an aqueous system, then the stable oxidation state of Fe is Fe(III). Fe(III) is very insoluble over a large pH range.

Examining the pϵ-pH diagram in figure 2(a), wherein the total concentration of Fe has been fixed at a representative level, it is seen that in the most relevant region for oxic surface waters, the meta-stable form of iron is am-Fe(OH)$_3$ (Stumm and Morgan, 1996). Figure 2(b) depicts the equivalent manganese system. A simple speciation calculation is shown in table 1, where it is clear that the sum of the concentrations of the soluble forms of Fe(III) are very low.

In many environments, concentrations of the major nutrients C, N, O, P, H, S, K, Mg, Ca and Na are sufficient to sustain dense microbial populations, while the microbially available Fe (Fe(III)(aq)) may be of limited supply. Even if one allows for a reservoir of Fe(III) that is complexed by some pool of organic ligands and is readily exchangeable, continual growth of the microbial population will soon exhaust this supply, leaving the population again limited for Fe(III)(aq). The only remaining source of iron and manganese is found in the solid phase. Therefore, increasing access to this phase becomes an important strategy for the competitiveness of a species.

Table 1

Speciation of Fe(III) in the presence of hematite at pH = 7

species	Fe^{3+}	$FeOH^{2+}$	$Fe(OH)^{2+}$	$Fe(OH)_3(aq)$	$Fe(OH)^{4-}$	Total free Fe(III)
log C	-21.70	-16.89	-13.37	-13.26	-15.30	-13.01

1.4 Siderophores

Many microorganisms are confronted with a chemical environment wherein there exists a limited supply of readily available soluble Fe(III) and a large reservoir of Fe(III) in the form of Fe(III)(hydr)oxides. A number of organisms have evolved mechanisms for the synthesis of an exogenously released ligand that has a huge affinity for Fe(III) (Albrecht-Gary et al., 1994; Albrecht-Gary et al., 1995; Demange et al., 1990a; Neilands, 1981; Neilands, 1982; Neilands, 1984; Rogers et al., 1987),

(a.)
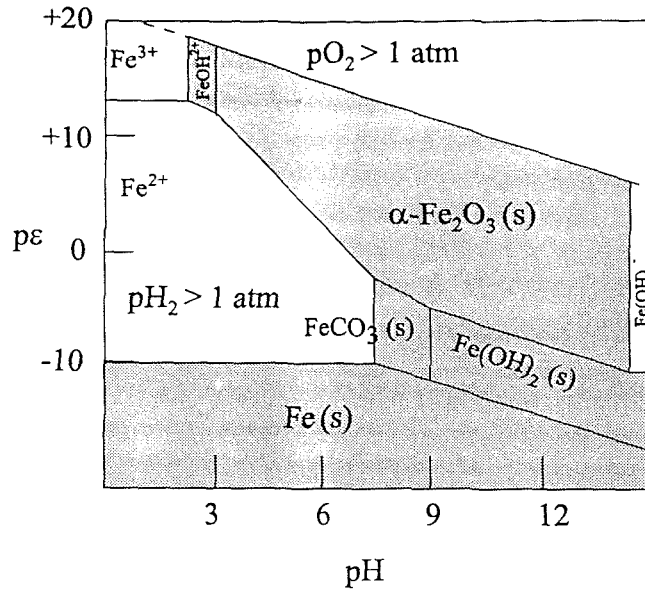
(b.)
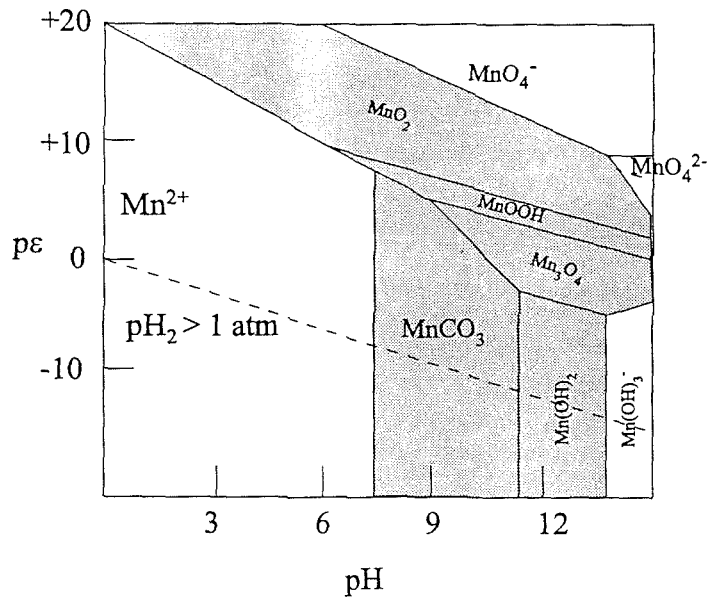
Figure 2

(a) pe-pH diagram of the Fe-CO_2-H_2O system with the metastable am-Fe(OH)$_3$(s) as the solid phase. $C_T = 10^{-3}$ M, Fe(II) and Fe(III) = 10^{-5} M, T = 25°C (Stumm and Morgan, 1996).

(b) pe-pH diagram of the Mn-CO_2-H_2O system with the following solid phases considered: Mn(OH)$_2$(s), MnCO$_3$(s), Mn$_3$O$_4$(s), γ-MnOOH(s), and MnO$_2$. $C_T = 10^{-3}$ M, Mn$_T = 10^{-5}$ M, T = 25°C (Stumm and Morgan,1996).

(Wendenbaum et al., 1983). These ligands have been termed siderophores (from the Greek, sideros, meaning iron), and may have stability constants as large as 10^{50} (Neilands, 1983) for the reaction:

$$Fe(III)(aq) + siderophore = Fe\text{-}siderophore \qquad \log K = 20 - 50 \qquad (1)$$
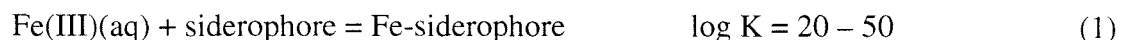
The stability of the Fe(III)–siderophore complex is sufficient to tip the energetic scales towards an increase in the soluble aqueous iron in heterogeneous systems.

However, it is not yet clear how siderophores interact with the major reservoir of iron, the solid Fe(III)(hydr)oxides. Siderophores have been found only in aerobes and facultative aerobes (Neilands, 1981). Limiting the availability of Fe(III)(aq) to the organisms induces the synthesis of siderophore by the organisms (Albrecht-Gary et al., 1995; Demange et al., 1990a; Hersman et al., 1995; Neilands, 1983; Neilands, 1984; Page, 1995). Since most of the Fe(III) in oxic environments is in the form of a solid (hydr)oxide, it is reasonable to assume that the organisms have evolved the siderophore synthesis pathways to increase the solubility of the Fe(III)(hydr)oxide, and to provide a stable form of Fe(III)(aq) that will be transported across the cell membrane.

Figure 3 depicts two proposed mechanisms for siderophore mediated uptake of Fe(III). Common to these mechanisms is the reduction of the Fe(III) bound to the siderophore to Fe(II). The change in Fe valence state causes a greatly reduced affinity of the Fe(II) to the siderophore, and is followed by removal of the Fe(II) from the Fe(II) – siderophore complex. The Fe(II) is then incorporated into the cell's metabolic pathways.

Some preliminary work (Hersman et al., 1995) has shown that it is reasonable to suggest that the mechanism by which siderophores influence the solubility of Fe(III)(hydr)oxides is mediated by surface–adsorbate interactions. In the work presented in this thesis the interaction of a model siderophore, deferrioxamine B, with representative Fe(III)- and Mn(III, IV)- (hydr)oxides will be examined.

(a.)   (b.)
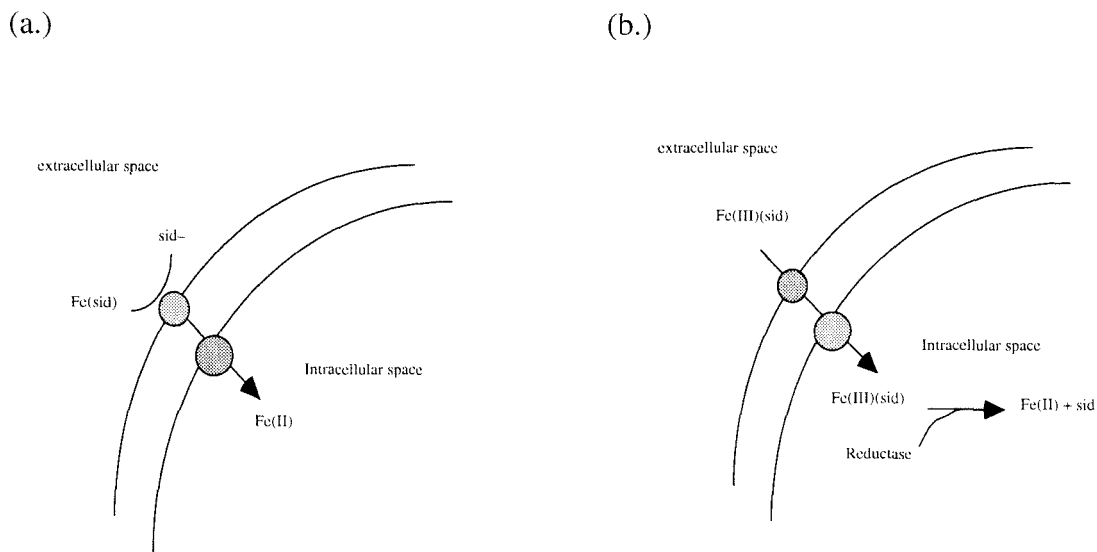
Figure 3

Two potential mechanisms for siderophore mediated Fe-transport. (a.) The Fe(III)-siderophore complex binds to a cell surface receptor that reduces the Fe(III) to Fe(II), reducing the affinity of the Fe to the siderophore, and allowing the Fe(II) to be actively transported across the cell wall into the cell interior. (b.) In this scenario, the Fe(III)-siderophore complex is transported as a whole into the cell via a specific transport system; an intracellular reductase reduces the Fe(III) to Fe(II), after which the Fe(II) is released into the cell.

1.5 The Dissolution and Precipitation of Iron(III)(hydr)oxides

In natural waters, various amorphous and crystalline oxides may form when the solubility

product of their components is exceeded:

$$nM^{j+} + \frac{nj}{2}H_2O \leftrightarrow M_nO_{(\frac{nj}{2})}(s) + njH^+ \qquad *K_{s0}^{-1} \qquad (2)$$
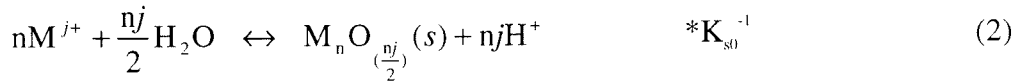
in the oxide case; or, in the case of the iron oxyhydroxides

$$Fe^{3+} + 2H_2O \leftrightarrow FeOOH(s) + 3H^+ \qquad (3)$$

where the solid phase can be in any of the allowable crystalline phases, and K_s is the

solubility constant. If the system of interest is open to fluxes of material in and out of the

system, then both the dissolution reaction and the precipitation reaction must be

considered. Furthermore, it may be the case that the first stable solid to form in such a

system will not be the thermodynamically stable phase, rather a meta-stable solid. For

example, goethite is found ubiquitously in soils (Schwertmann and Taylor, 1977), but is

thermodynamically unstable with respect to its transformation to hematite. However,

hematite forms via a ferrihydrite intermediate. Therefore, goethite must dissolve and

form a new phase prior to the formation of hematite (Schwertmann and Taylor, 1977).

This process of dissolution and reprecipitation represents a large energetic barrier that

must be overcome, and will govern the meta-stability of the solid phases within the

system. Thus, it is often the case that the system is in a pseudo-equilibrium state, moving

slowly towards a free energy minimum.

1.6 Dissolution

When considering the kinetics of precipitation and dissolution reactions in natural systems, the physical, chemical and biological processes that define the system must be included. The case of siderophore induced dissolution of Fe(III)-(hydr)oxides is particularly interesting because it is likely that the biological system of siderophore synthesis coevolved with earth's increasingly oxic environment: as the atmospheric concentration of O_2 increased, the availability of soluble iron decreased and an evolutionary advantage was gained through the ability to scavenge Fe(III) from solid phases. Some recent work has shown that siderophore is produced by a *Pseudomonas* species when the sole source of Fe in the growth medium is a synthetic colloidal hematite. The siderophore production in the hematite–containing medium is greater than that in a medium in which Fe is not added at all, and the only Fe source is that from trace impurities in the medium (Hersman, personal communication.) Other studies have shown that the solid iron oxide particles can act as terminal electron acceptors for iron reducing bacteria (DiChristina, 1994; Roden and Zachara, 1996). Manganese reducing bacteria are able to utilize Mn(IV) oxides as terminal electron acceptors as well (DiChristina, 1994; Nealson and Myers, 1992; Petrie, 1995), affecting their solubility. But, *further study is* needed to address the mechanisms by which Mn-oxides are solubilized in the presence of microorganisms.

Microscopy shows that there is a close association of the above-mentioned *Pseudomonas* species with the hematite particles (Hersman, personal communication.) It might be

expected that there exists some sort of positive feedback mechanism within this organism that induces the production and release of siderophore. This feedback may be simply a response to the increased iron uptake with increased siderophore release, or may be in concert with the effect of the organism's association with the particle. In either case, the organism acts to optimize its metabolic return on the energetic investment in siderophore synthesis to remain competitive within its niche. One recent study shows that the production of siderophore by *Azobacter vinelandii* is stimulated in an iron limited medium in the presence of solid manganese oxides (Page, 1995). This evidence supports a surface-active siderophore induced dissolution mechanism.

In the course of respiration, organisms excrete a myriad of oxidized carbon compounds, often taking the form of polycarboxylic acids, such as citric and oxalic acids. These acids have been shown to strongly influence the stability of Fe(III)(hydr)oxides by accelerating their dissolution above the basal level (Banwart et al., 1989; Pekhonen et al., 1993; Siffert and Sulzberger, 1991; Stumm et al., 1984; Sulzberger et al., 1989). In soils, compounds such as oxalate can attain concentrations on the order of 50 mmol $(kg\ soil)^{-1}$ (Fox and Comerford, 1992). While the concentration of siderophores is expected to vary widely (8–1800 mg/l, equivalent to approximately 0.01–1 mM siderophore (Hersman et al., 1995)), siderophore induced dissolution may have a disproportionate influence by virtue of greater dissolution rates or microconcentration of siderophore at the particle surface. Since siderophores are produced aerobically, they may in fact dominate the iron cycling in oxic horizons of soils and surface waters.

The significance of siderophores as a percentage of the overall flux of soluble iron in a particular system may vary greatly depending on the context. For example in an anoxic environment, it is not expected that siderophores will play any role at all, given that they are not produced anaerobically. In soil systems, wherein microbes are found to be closely associated with particle surfaces, it is expected that the close proximity of the organism to the surface of iron-containing minerals would optimize the potential for interaction of the siderophore with the mineral surface. If one thinks of the particular siderophore-utilizing microbe as a geochemical reactor, then the major role of the iron-siderophore system is as an enabler for the reactor. In natural systems where the soluble iron limits the growth of organisms, the increased availability of the iron afforded by the siderophore system will allow the population to mediate the whole host of reactions characteristic of microbial systems. The integrated effect of these reactions on the chemistry of the iron in the system may indeed be greater than the direct effect of the siderophore itself. Thus, it becomes important to understand the role of siderophores in the stability of Fe(III)(hydr)oxides.

1.7 Colloids

As soils and subsoils experience the dynamics of weathering, significant fractions of reactive surfaces are created in the form of colloids that may exist as a suspension or as coatings on mineral grains (Maurice et al., 1995). The importance of this material fraction arises not only from the increased surface to volume ratio, but from the ability of this fraction to be transported through groundwaters and soils. If the adsorbed phase is the dominant phase of a pollutant of interest, then understanding the stability of this phase

becomes of great importance. It is thought that colloidal particles may experience a greater average velocity through a pore system than the ambient fluid. This phenomenon has been observed (Mau, 1992) and can be explained by the velocity profile of the fluid in the pore space. If one assumes that the pore space can be modeled as a cylinder, then the velocity profile will be parabolic, reaching a maximum in the center of the cylinder, and a minimum at the walls. Since the colloidal particles have a finite size with respect to this macroscopic description, they experience a size exclusion effect whereby larger particles will be, on average, closer to the center of the cylinder and thus experience an increased average velocity than that integrated over the whole cylindrical cross section. If particles dissolve as a function of time (or, equivalently, distance) as they travel through the system, then one expects the average flux of particles, and adsorbed species, to decrease (assuming the number of particles is conserved and ignoring coagulation).

1.8 Scope of Work

Kinetic Studies

The first question addressed in this work is: How do siderophores affect the rate of Fe(III)(hydr)oxide dissolution?

Although siderophores vary from organism to organism, there are some commonalties. The complexing functionalities on the majority of currently characterized siderophores are catecholates

([catecholate structure]) and hydroxamates ([hydroxamate structure]) (Neilands, 1981). It is often the
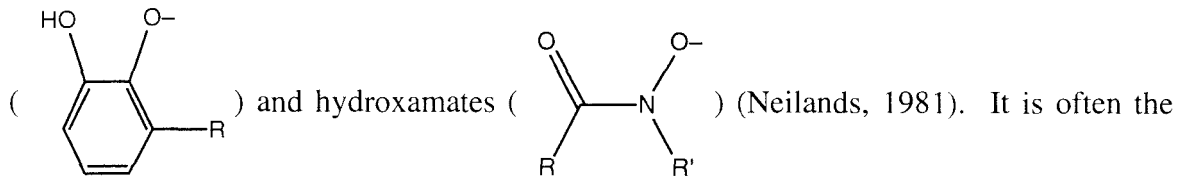
case that a siderophore will have three of either the catecholate or the hydroxamate

functionalities to complete the octahedral coordination sphere of the Fe – siderophore

complex. However, mixed siderophores have been observed, wherein there exists some

combination of n hydroxamates and 3-n catecholates (Demange et al., 1990b). These

functionalities tend to reside on a more or less modified polypeptide framework, forming

a macrocyclic complex with Fe(III). The compounds have molecular weights ranging

from about 500 to 2000 g mole^{-1}, and vary greatly in their backbone structure.

The first set of experiments presented in this thesis examines the effect of a trihydroxamic

acid siderophore, deferrioxamine B (DFA) on the rate of dissolution of synthetic α-Fe_2O_3

(hematite). Figure 4 shows the results from an experiment wherein a siderophore isolated

from a *Pseudomonas* species has been incubated in a closed reactor vessel with synthetic

hematite, illustrating a typical result at one set of experimental conditions (Hersman et

al., 1995).

For a given siderophore ligand, the master variables explored will be:

[DFA]

> Adsorption isotherms as a function of pH are generated. Dissolution rates are
>
> measured as a function of [DFA] in representative ranges of surface coverage.

pH

The dissolution experiments are performed over a range of 4 < pH < 9. Surface

coverage and the nature of the bonding at the surface will depend on the surface

and solution speciation, and, since DFA has pK_a's within the proposed pH range

of study, it is expected that there will be a strong pH dependence of the rate.
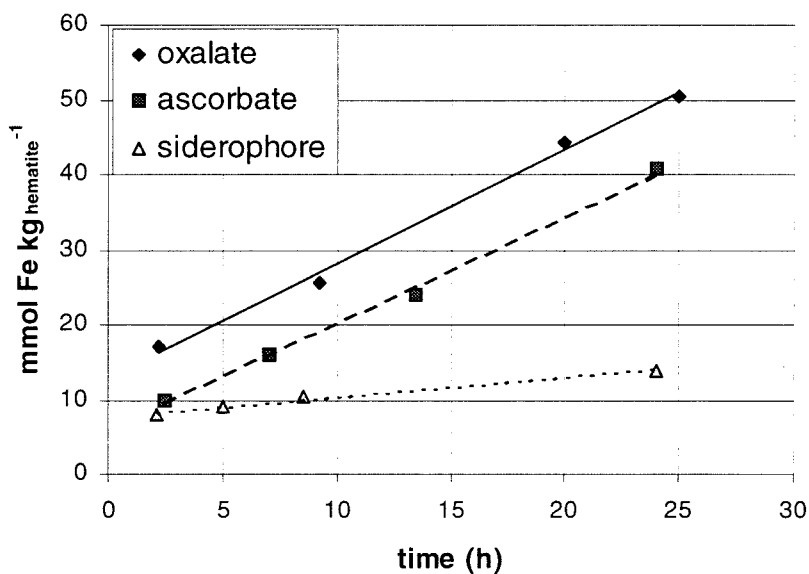
Figure 4

Dissolved Fe released per unit hematite mass in the presence of oxalate, ascorbate, or

siderophore from *Pseudomonas* sp 11C (100 mg hematite for oxalate and ascorbate, 21

mg hematite for siderophore) taken from Hersman et al., (1995).

Solid phase

Two separate preparations of hematite particles of differing morphologies are utilized in the dissolution experiments, one having a goethite impurity. The dissolution rates are compared. Synthetic preparations of goethite, lepidochrosite, manganite and pyrolusite are examined for their dissolution properties.

Ionic strength

A constant ionic strength is maintained for each experiment, fixed by addition of $NaClO_4$. For one preparation of hematite, the ionic strength is varied from 0.01 m to 1.0 m, and the rates of dissolution are compared.

Ambient conditions

Constant temperature is maintained for all experiments. For one hematite preparation the temperature is increased from 25°C to 35°C, and the effect on the dissolution rate is observed. All the experiments are performed in an inert atmosphere, under a positive pressure of N_2. The pH of a given experiment is maintained at a constant level and for one set of experiments the consumption or generation of protons is recorded in detail. Constant agitation is maintained that is sufficient to prevent mass transfer limitation on the dissolution rate.

Once the experiments are concluded, a rate law must be proposed that captures the physical and chemical behavior of the system. The rate law must be consistent with the proposed dissolution mechanism that accounts for the observed behavior of the system. In general, the rate law will be of the form (Lasaga, 1995):

$$R = k_0 A_{\min} e^{-E_a/RT} g(I) \left(\prod_j a_{H_j^+}^{m_j} \right) \left(\prod_i a_i^{n_i} \right) f(\Delta G_r) \tag{4}$$

where k_0 (moles m^{-2} s^{-1}) is the intrinsic heterogeneous rate constant expressing the pre-exponential factors, such as vibrational state of the transition complex, solid surface dynamics, and entropic factors. A_{min} (m^2) is the reactive surface area of the solid. E_a is the apparent activation energy of the complete reaction. The $\prod_j a_{H_j^+}^{m_j}$ term represents the dependence of the rate on the activity of the proton; m is the order of the reaction with respect to the aqueous proton. The function $g(I)$ represents the potential for a functional dependence on ionic strength. The product $\prod_i a_i^{n_i}$ introduces the role of all other species, surface and solution, in the dissolution process. The final term, $f(\Delta G_r)$ represents the functional dependence of the overall rate on the equilibrium state of the system; i.e., when $\Delta G_r = 0$, R = 0.

Equation 4 does not explicitly differentiate between surface and solution species. However, any proposed mechanism must reflect the chemistry of the surface species and the solution species. For example, the $a_{H_j^+}^{m_j}$ term includes the activity of the proton at the surface and in solution. If the complete dissolution reaction is examined, it may be the case that there exists a third order dependence of the rate on protons that are adsorbed to the ligand – surface complex, and a separate dependence of the rate on the aqueous metal – ligand complex. Likewise, the $a_i^{n_i}$ term will include ligands that exhibit different adsorptive behavior at different pH's; all the solution and surface states of this ligand are included in this term as separate species. In the case of a multidentate ligand such as a siderophore, the adsorbed species may take multiple forms. The functional

groups of the actively complexed 'teeth' may vary along the length of the ligand, or the denticity may differ from mono- to multi-dentate. All these differences are represented, again, in the terms, $a_i^{n_i}$.

In terms of the set of experiments that is presented in this thesis, the two functions $g(I)$ and $f(\Delta G_r)$ will be held relatively constant. The systems will be kept far from equilibrium initially, and will approach equilibrium only if the reaction approaches completion over the time scale of the experiment. By changing the temperature at various pH's, the Arrhenius term is examined, although insufficient material was synthesized for a complete elucidation of this term. It may be the case that the activation energy is not a constant over the whole range of pH, but rather, depends on the pH: $E_a = h(\{H^+\})$. In terms of activated complex theory (ACT), the reactive intermediate may have a strong pH dependence. This dependence should be recognized by varying the temperatures and pH, and analyzing the dependence of R on these parameters. Temperature variation will also affect the surface and solution speciation. However, it is reasonable to suppose that the enthalpic contribution to the activation energy will dominate.

One can propose reactive intermediates that would be consistent with a mechanism that leads from reactants to final products. For example, a reasonable proposition for the mechanism of a trihydroxamate siderophore induced dissolution event is as follows. There is an initial adsorption event, whereby a bidentate surface complex is formed, displacing the adsorbed water (note that charges have been left out of the surface complexes for simplicity):

$$\equiv Fe(-O-)_4(OH_2)_2 + sid \underset{k_{b,1}}{\overset{k_{f,1}}{\rightleftarrows}} \equiv Fe(-O-)_4(sid_1) + 2H_2O \qquad (5)$$
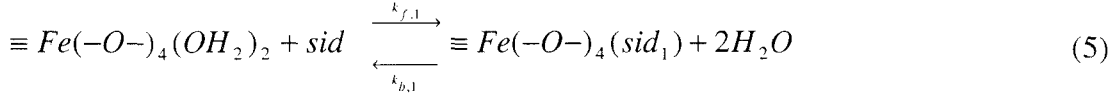
where $(-O-)$ represents the oxygens bound to the bulk solid, and sid_1 represents the first siderophore hydroxamate to bind to the solid surface. This siderophore–surface complex facilitates the sequential protonation of two of the remaining oxygens, thereby weakening their bonds with the distal bulk $-$ Fe and enabling a relatively facile nucleophilic attack by one of the remaining hydroxamate functionalities or hydrolytic attack by water or hydroxide from the solvent phase:

(i.) Attack by second hydroxamate group:

$$\equiv Fe(-O-)_4(sid_1) + 2H^+ \underset{k_{b,2}}{\overset{k_{f,2}}{\rightleftarrows}} \equiv Fe(-O-)_2(sid_1)(-OH-)_2 \qquad (6)$$

$$\equiv Fe(-O-)_2(sid_1)(-OH-)_2 + sid_2 \underset{k_{b,3}}{\overset{k_{f,3}}{\rightleftarrows}} \equiv Fe(-O-)_2(sid_1)(sid_2) + 2(-OH)_2 \qquad (7)$$

or

(ii.) Hydrolytic attack:

$$\equiv Fe(-O-)_2(sid_1)(-OH-)_2 + 2H_2O \underset{k_{b,3}}{\overset{k_{f,3}}{\rightleftarrows}} \equiv Fe(-O-)_2(sid_1)(OH_2)_2 + 2(-OH)_2$$

$$(8)$$
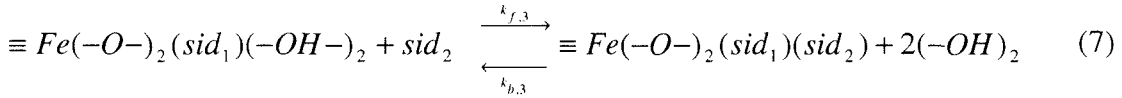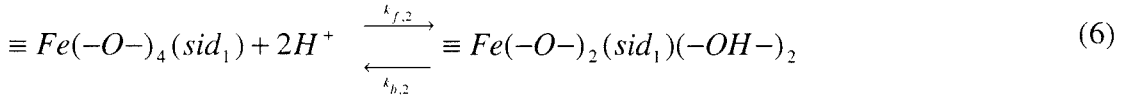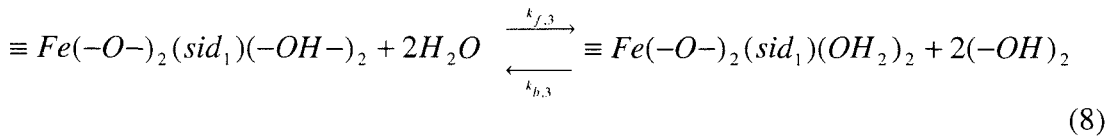
where the $(-OH)_2$'s represent hydroxides that are either in solution or bound to a neighboring surface Fe in the solid; regardless, the bond has broken between these molecules and the surface Fe bound to the siderophore. Reaction 7 or 8 is then followed by the third and final (most likely irreversible) event. This event may be proton mediated hydrolysis of the final two surface bonds, or a repeat of reaction 7 with the third and final hydroxamate functionality. For example,

$$\equiv Fe(-O-)_2(sid_1)(sid_2) + sid_3 \xrightarrow{k_{f,3}} Fe(sid[octahedral])(aq) + \tag{9}$$
$$(hydrated - surface)$$
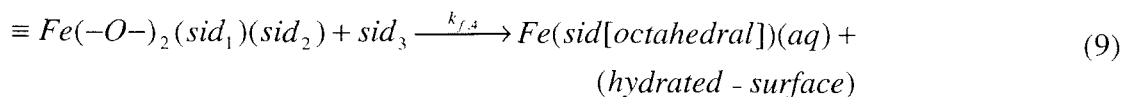
These proposed mechanisms can be complicated by multinuclear interactions wherein more than one hydroxamic acid functionality interacts with metal centers at the solid surface. For example, upon the adsorption event posited in equation 6, one of the remaining two hydroxamic acids has the potential to bind with a neighboring surface Fe, generating a binuclear interaction with respect to the siderophore. It is expected that multinuclear interactions will decelerate the rate of dissolution.

Finally, it is important to note that the nature of the siderophores is such that there will be significant non-bonding interactions with the surface. Some preliminary molecular dynamics simulations of hydrated DFA with a model hematite surface are presented that show strong electrostatic and van der Waals interactions of the ligand with the surface. A number of initial geometries are explored and their energies minimized.

The chapters are organized in the following matter: Chapter 2 reviews some of the solution and surface chemistry of the metal – DFA complex, using Fe as the representative metal; Chapters 3, 4, and 5 describe experiments that examine the dissolution of two different synthetic hematite phases in the presence of DFA; Chapter 6 examines the dissolution of γ-MnOOH and MnO_2 by DFA; Chapter 7 shows results for the dissolution of goethite and lepidochrosite by DFA.

Chapter 2

The Chemistry of Deferrioxamine B (DFA) with Iron and Manganese

In this chapter the physical and chemical parameters of the experimental system will be described. Most of the focus will be on describing the physical chemistry of the iron-DFA system, because this is the area where much of the prior work has been performed. However, except for the values of the equilibrium constants, many of the characteristics apply to the Mn(III) – DFA interactions.

2.1 Characteristics of DFA and Fe(III) – , Mn(III) – DFA

I have chosen to model the process of siderophore mediated dissolution of Fe(III)(hydr)oxides and Mn(III)-Mn(IV)(hydr)oxides with well-defined experimental systems. The solid phases were chosen to be crystalline and easily synthesized in the laboratory. The siderophore that is used in all experiments was chosen to be representative of the trihydroxamic acid class of siderophores and to be available in analytical amounts. To this end deferrioxamine B (DFA) was chosen as the model siderophore. Figure 1 shows the molecular structure of DFA and ferrioxamine B (FA), the ferrated analog of DFA, Fe(III) – DFA. The Mn(III) – DFA complex is analogously pseudooctahedral in geometry (Faulkner et al., 1994).

DFA is a trihydroxamic acid siderophore of molecular weight 656.79 g mol^{-1}, as received from Ciba Pharmaceutical Co., having the addition of a coordinate CH_3SO_3H functionality as a synthesis adduct. If the mass of the CH_3SO_3H moiety is subtracted, the remaining mass is 545.49 g mol^{-1}; addition of Fe to the structure renders a molecular weight of 601.34 g mol^{-1}.

The naturally occurring DFA has the structure depicted in figure 1 (a.) The stability of the aqueous FA complex arises in part from the efficacy of the hydroxamate functionality as a Lewis base, donating electron density to the central Fe(III). Figure 2 diagrams a molecular orbital description of the interaction of the hydroxamate moiety with the Fe(III) center, and assumes a pseudo-octahedral symmetry. The molecular orbital
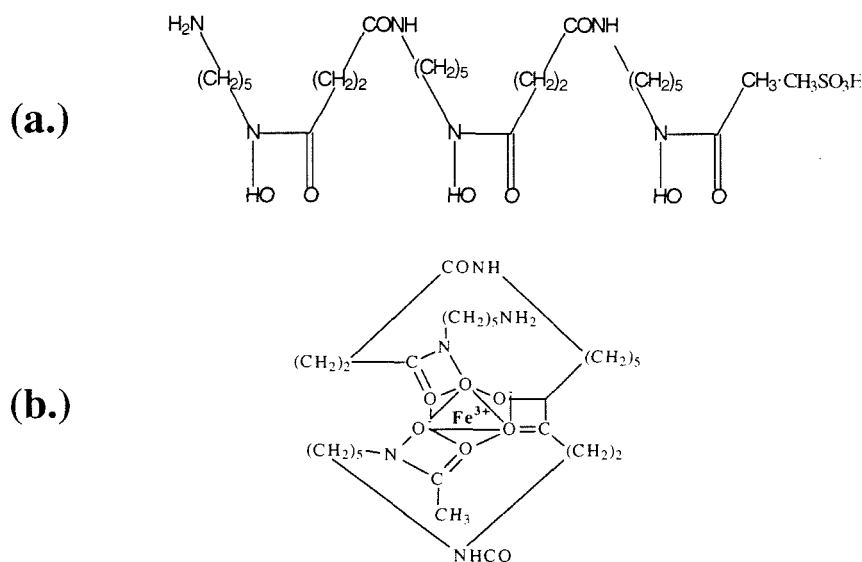
Figure 1

Structures of (a.) deferrioxamine B (DFA) and (b.) ferrioxamine B (FA). Structure (b.) describes the pseudo-octahedral symmetry of the metal-ligand center.

diagram points out the excellent ligand-to-metal charge transfer by the hydroxamate functionalities to the Fe(III), resulting from the π-symmetry ligand orbitals interacting with the T_{2g} symmetry metal orbitals. The electronic configuration of the FA complex is high spin and the UV-vis spectrograph is shown in figure 3. Steric interactions further stabilize the ligand-metal bond, inhibiting the potential for hydrolysis.
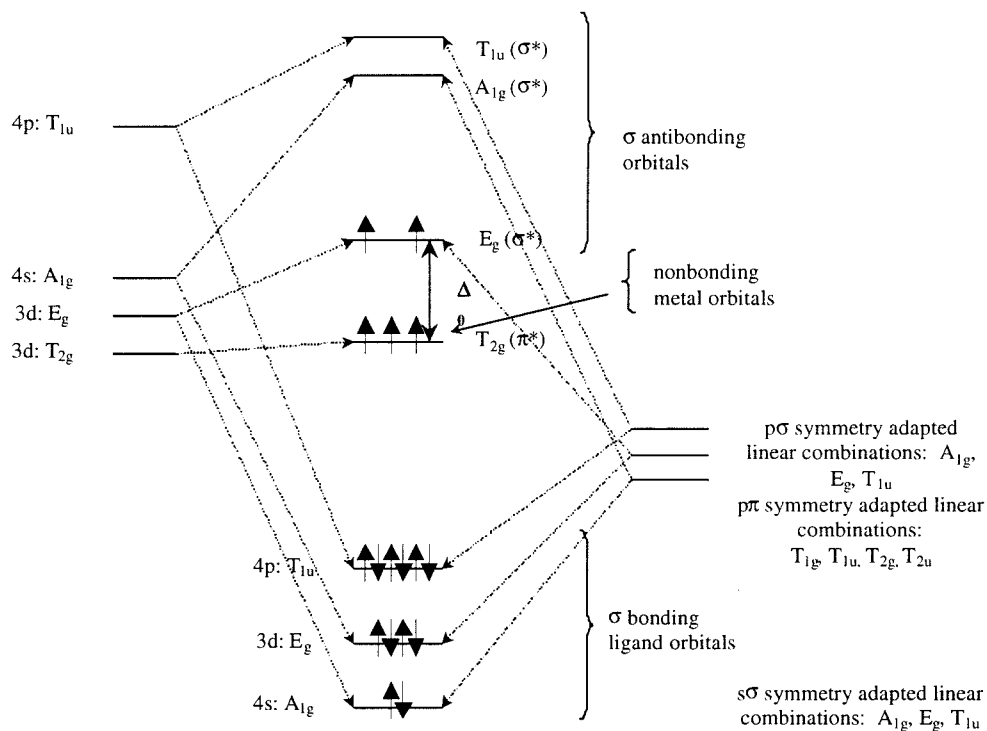
Figure 2

Molecular orbital diagram for FA, where the metal center is Fe(III). The symmetry is considered to be pseudo-octahedral. The analogous Mn(III) complex would have one fewer electron in the E_g orbital.

That the qualitative test for the presence of hydroxamic acids requires severe hydrolysis conditions of sulfuric acid at high temperature and pressure for the degradation of a secondary to a primary hydroxamic acid (Gillam, 1981) supports the interpretation of steric inhibition of hydrolysis. In aqueous solution, DFA forms a highly stable one-to-one octahedral complex with Fe(III), described by the reaction

$$Fe^{3+}(aq) + DFA^{3-} = FA \qquad \log \beta = 30.6 \quad \text{(Wawrousek and McArdle, 1982)} \qquad (1)$$
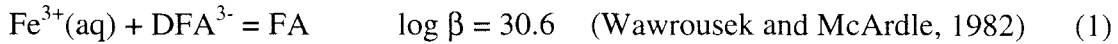
The stability of the one-to-one complex can be compared to an equivalent reaction with acetohydroxamic acid (represented as A^-), a monohydroxamic acid:

$$Fe^{3+}(aq) + 3A^- = FeA_3 \qquad \log \beta_3 = 28.29 \text{ (Wawrousek and McArdle, 1982)} \qquad (2)$$
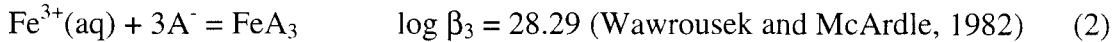
The ratio of complexed Fe(III) to free Fe(III) is

$$[FeA_3]/[Fe^{3+}(aq)] = [A^-]^3 \beta_3$$

$$= [A^-]^3 \, 10^{28.29} \qquad (3)$$

for acetohydroxamic acid, and

$$[FA]/[Fe^{3+}(aq)] = [DFA^{3-}] \beta = [DFA^{3-}] \, 10^{30.6} \qquad (4)$$

for the DFA complex. For these ratios to be equal there must be a significantly greater molar amount of dihydroxamic acid than DFA. For example, for the ratio of complexed iron to uncomplexed iron to be 10^3,

$$[A^-] = 10^{-8.43} \qquad (5)$$

$$[DFA^{3-}] = 10^{-27.6} \qquad (6)$$
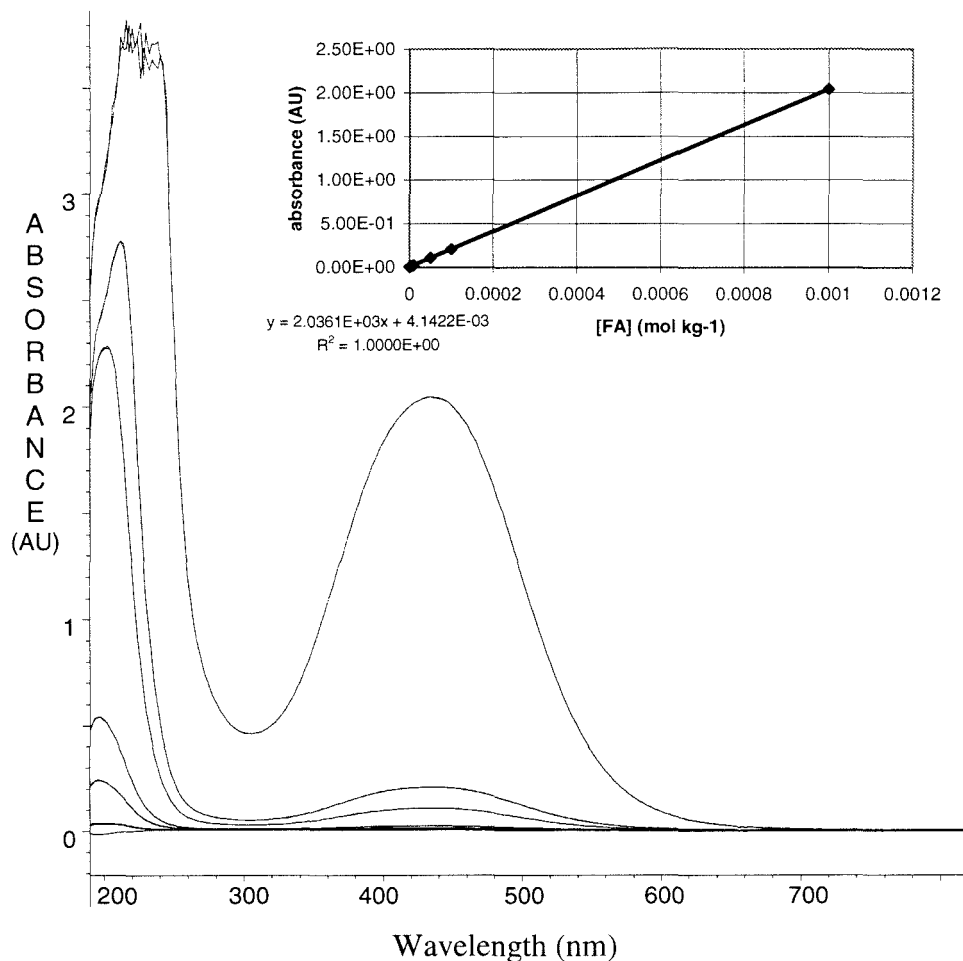
Figure 3

Spectra of varying concentrations of FA. Path-length = 0.01 m, referenced to water. Inset is a graph of the absorbance at 436 nm as a function of [FA] (mole kg^{-1}), giving a molal absorptivity of 2.0361×10^3 m^{-1} cm^{-1}.

and

$$[A^-]/[DFA^{3-}] = 10^{19.7}. \qquad (7)$$

This example illustrates the chelate effect for the FA complex; a monohydroxamic acid is highly ineffective relative to the molar equivalent of a trihydroxamic acid such as DFA.

Figure 4 shows the Fourier-transform infrared spectra of the Fe(III)-bound and the unbound complexes in a KBr pellet. Table 1 shows the peak assignations for the DFA spectrum.

DFA has three pKa's that correspond to the following reactions:

$$H_4DFA = H_3DFA + H^+ \qquad\qquad pKa_1 = 8.39 \qquad\qquad (8)$$

$$H_3DFA = H_2DFA^- + H^+ \qquad\qquad pKa_2 = 9.03 \qquad\qquad (9)$$

$$H_2DFA^- = HDFA^{2-} + H^+ \qquad\qquad pKa_3 = 9.70 \qquad\qquad (10)$$

(Schwarzenbach and Schwarzenbach, 1963)
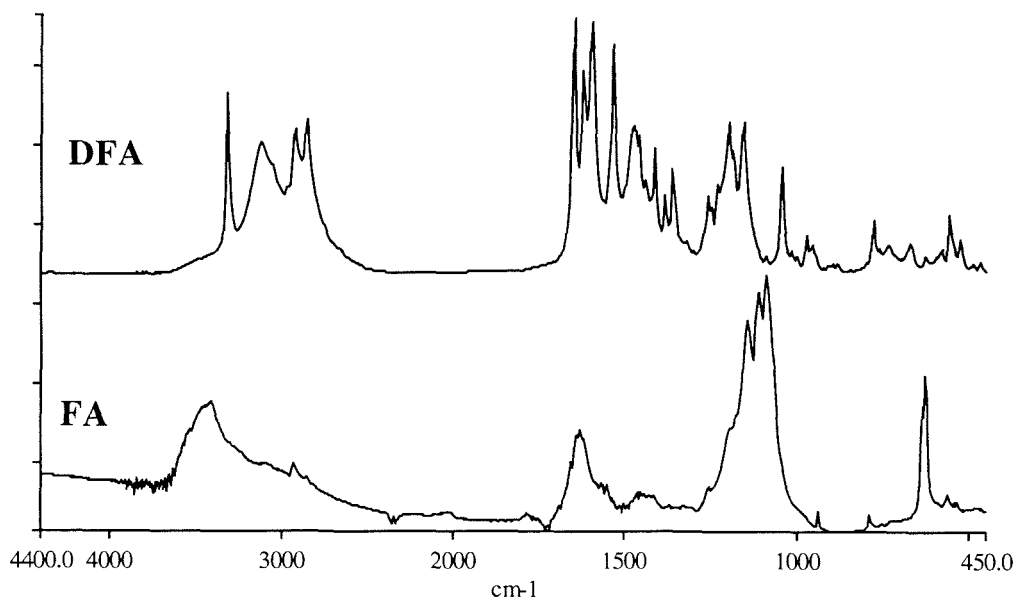
Figure 4

Fourier transform infrared (FTIR) spectra of DFA and FA

Table 1

Peak assignments for the DFA FTIR spectrum

cm^{-1}	band
3324.84	bonded N-H stretch 2° amine
2931.77	Antisymmetric CH_2 stretch
2862.2	symmetric CH_2 stretch
1650.06	C=O stretch
1622.35	C=O stretch
1537.32	N-H bending
1460.01	CH_3 deformations
1385.96	CH_3 deformations
1363.93	NOH bending
1261.55	CH_2 twist
1159	C-C stretches
1046.82	CH_3 bending

Figure 5 shows an equilibrium calculation of the solution speciation of aqueous DFA and

FA, using the constants listed in table 2.

The equilibrium solution chemistry of DFA and FA is well understood, as indicated in

table 2. When an oxide surface is introduced into the system, however, the chemical

picture becomes more complicated. In the experiments presented in this thesis, DFA and

FA are in the presence of an (hydr)oxide surface: hematite (α-Fe_2O_3), goethite (α-

FeOOH), lepidochrosite (γ-FeOOH), manganite (γ-MnOOH), or pyrolusite (MnO_2.)

Table 2

Thermodynamic constants for DFA and FA. Data taken at 20°C, I = 0.1 M $NaNO_3$. (From (Schwarzenbach and Schwarzenbach, 1963))

$H_4\text{-DFA}^+$	=	$H^+ + H_3\text{-DFA}$	pK_{a1}	=	8.39
$H_3\text{-DFA}$	=	$H^+ + H_2\text{-DFA}^-$	pK_{a2}	=	9.03
$H_2\text{-DFA}^-$	=	$H^+ + H\text{-DFA}^{2-}$	pK_{a3}	=	9.70
$H\text{-DFA}^{2-}$	=	$H^+ + DFA^{3-}$	pK_{a4}	>	11
$Fe^{3+} + H_2\text{-DFA}^-$	=	$Fe(H_2\text{-DFA})^{2+}$	Log K	=	21.84
$Fe^{3+} + H\text{-DFA}^{2-}$	=	$Fe(H\text{-DFA})^+$	Log K	=	30.60
$Fe(H_2\text{-DFA})^{2+}$	=	$H^+ + Fe(H\text{-DFA})^+$	pK	=	0.94
$Fe(H\text{-DFA})^+$	=	$H^+ + Fe(DFA)$	pK	>	10
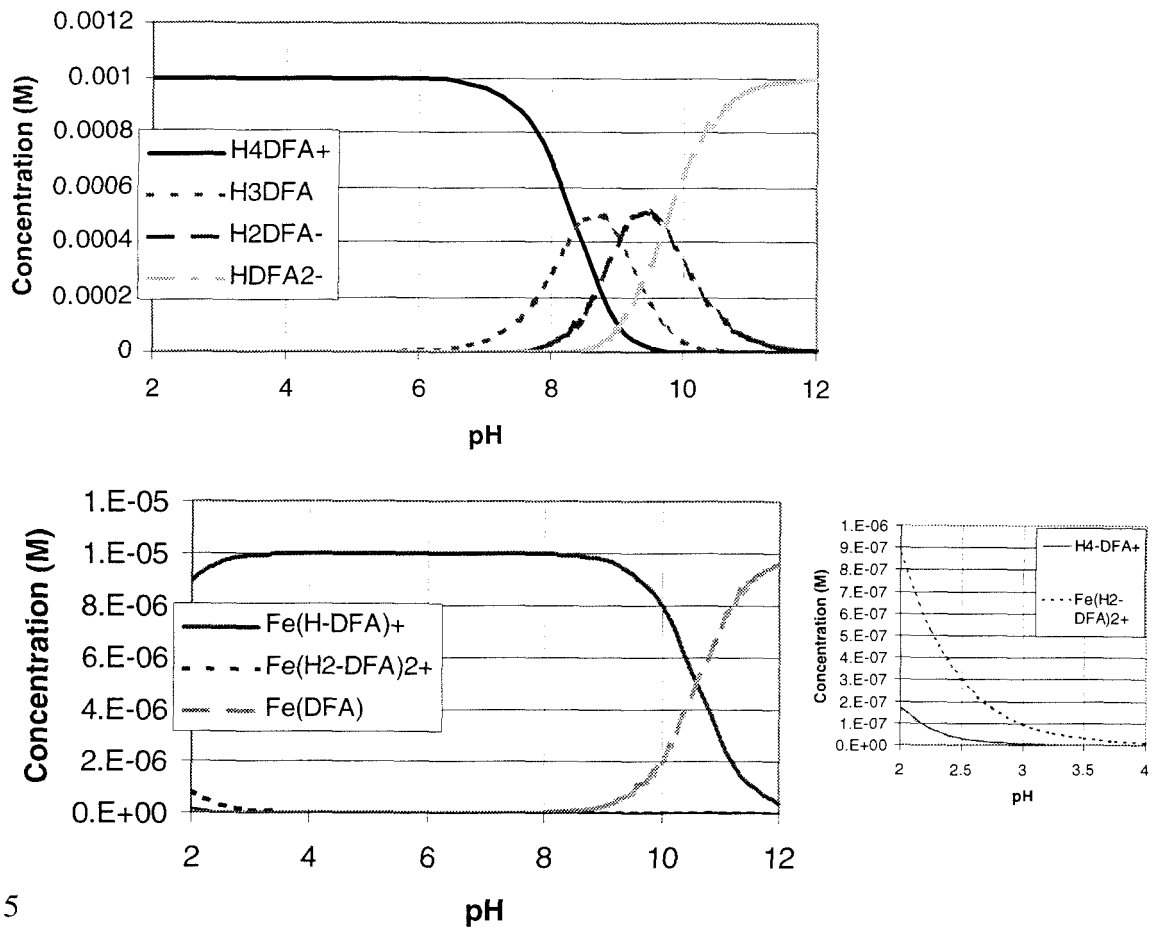
Figure 5

Equilibrium calculation of the aqueous speciation of DFA and FA as a function of pH; inset depicts the low pH region of the FA figure. Constants are taken from table 1. $[Fe]_{tot} = [DFA]_{tot} = 10^{-5}$ M.

2.2 DFA and Oxide Suspensions

Upon the addition of DFA to an aqueous oxide suspension, the system is placed far from equilibrium, with the thermodynamic driving force pushing towards the dissolution of the solid phase. One expects the following set of interactions to govern the evolution of this system in time:

(i) DFA with surface

(ii) M-DFA with surface

(iii) DFA with metal (aq).

The DFA molecule is expected to interact with the (hydr)oxide surface. The extent of interaction will depend on pH, ionic strength, temperature, pressure, and [DFA]. As the system evolves towards equilibrium, FA will appear in solution, affecting the solution and surface speciation. At equilibrium it is expected that a complete description of the system will include the constants listed in table 2, combined with experimentally derived surface partition constants for DFA and FA and (hydr)oxide surface protonation constants. Experimental adsorption isotherms were generated only for one preparation of hematite. The rate of dissolution for the manganite was prohibitively great for accurate determination of adsorbed DFA.

The surface–DFA interaction will be governed by a number of factors. It is expected that there will exist significant non-specific bonding forces of DFA with the (hydr)oxide surface, such as London dispersion forces and electrostatic forces. Over the range of

pH's used in this study, the terminal amino ($-NH_3^+$) group of DFA and FA will be protonated, and exhibit a positive charge; the terminal amino group deprotonates at pH > 11. The pK_a's that are clustered about pH 9 refer to the sequential deprotonation of the hydroxamic acid moieties, and the concentrations of the conjugate acids and bases will depend on the pH of the system.

The DFA molecule is approximately 2 nm in length when stretched to its full linear extent, maintaining the sp^3 configuration of the C-centers. If a distance of 0.4 nm from the nearest charged hydroxamate to the protonated amino group is assumed (see figure 1), then the electrostatic interaction of the amino group with the hydroxamates will most likely be highly attenuated by the aqueous electrolyte medium. The fact that DFA is as large as it is suggests that complicated behavior must be expected upon interaction with the (hydr)oxide surface. It is expected that the surface interaction of the terminal amino group to be governed by its ionic character: there should be a positive correlation between the free energy of the interaction of the amino group with the increased negative charge density of the (hydr)oxide surface; i.e., as the surface becomes more negatively charged, the free energy of interaction becomes more negative.

However, there exist competing interactions that may counter this particular interaction. For one of the phases of synthetic hematite used in the experiments, the point of net zero proton charge (pnzpc) is approximately 8. As the pH of the system approaches 8 from the acidic regime, the solution speciation of DFA becomes complicated. The hydroxamic acids of the DFA molecule sequentially deprotonate (see figure 5.) The average distance

between metal centers on the 001 surface of hematite is 0.29 nm, while there is a bimodal distribution of O-O distances on the surface, centered at 0.265 nm and 0.305 nm (Eggleston and Hochella, 1992). The approximate distance between hydroxamic acid functionalities is 0.7 nm. Thus, the DFA molecule is large enough that it can span a number of oxide surface sites, and a simple one-to-one DFA-surface site interaction model is insufficient to capture the richness of interactions. Thus, simple DFA-surface interaction trends as a function of pH are not necessarily expected.

Work by Eisenlauer and Matijevic (1980) examined the interaction of DFA with a synthetic hematite surface over a similar range of pH's as examined in this study. They found that uptake of DFA onto the surface for pH < pH_{pznpc} was relatively small and independent of pH, while for pH > pH_{pznpc} specific adsorption increased, particularly upon deprotonation of the first hydroxamic acid group. Their experiments suggest that the orientation of DFA on the surface depends primarily on the electrostatic interactions between the DFA and the surface. They attribute the increase in adsorption density at higher pH to the changed orientation of the DFA molecule at the surface, where the positively charged amine interacts favorably with the negatively charged surface, while the sequentially deprotonated hydroxamic acids are repelled. Eisenlauer and Matijevic suggest that this phenomenon allows for an orthogonal orientation of the linear DFA with respect to the plane of the surface (Eisenlauer and Matijevic, 1980).

It is also expected that the FA molecule will interact with the surface of the (hydr)oxide. Figure 5 shows that the solution speciation of the FA molecule is dominated by the singly

charged species, with the charged moiety being the terminal amine. The FA should interact with the surface through a combination of Coulombic interaction of the terminal amine with the surface, and non-specific interactions such as van der Waals and hydrophobic.

To understand the interactions that govern the dissolution of the (hydr)oxides examined in this study, it is necessary to characterize the interactions of the FA and DFA molecules with the surface of the (hydr)oxides. It is reasonable to hypothesize that as effective a Lewis base as the hydroxamic acid should have significant covalent interactions with the surface metal centers. However, the energetics of this interaction may be more or less severely moderated by other factors such as steric interactions. Therefore, the extent and type of interaction must be determined.

It must also be determined whether the DFA and FA molecules are labilized in the presence of the (hydr)oxides. DFA has a finite lifetime in aqueous solution, and is subject to hydrolysis (Bickel et al., 1963). However, over the time scale of the experiments reported in this work, the observed loss of DFA in solution due to hydrolysis is less than 5% of the total. FA is extremely stable in aqueous solution, with no loss of compound detectable by measuring absorbance at 436 nm over the course of six months at room temperature. The conservation of DFA_{tot} can be determined experimentally by maintaining a mass balance of DFA_{tot} as a function of time during the dissolution experiments.

2.3 Ligand-mediated Dissolution

As stated above, it is reasonable to hypothesize a model whereby the DFA-mediated dissolution is affected by covalent interactions between the DFA hydroxamic acid functionalities and the surface metal centers. In this model, the metal-ligand bond forms at the surface, increasing the probability of a dissolution event. In other words, the forming of the metal ligand bond at the surface destabilizes the interaction of that particular metal center with the bulk solid, facilitating the removal of the metal from the solid. Figure 6 depicts an idealized representation of the ligand-mediated dissolution event.

2.3.1 Ligand-surface Interactions

Figure 6 isolates a single hydroxamic acid – surface interaction, making the assumption that a quadra-dentate interaction is unlikely at the surface, although at adatom and edge sites this type of interaction is a possibility. This particular schematic includes a proton dependence that may or may not be real. It is not inconsistent to suggest that the protonated surface site would be susceptible to an increased probability of an effective ligand substitution reaction, wherein the hydroxamic acid acts as a more effective Lewis base than the water molecule, displacing the water from the surface. If this is the case, it may be postulated that as the pH increases and the surface becomes more negatively charged, the surface oxides will become more competitive as Lewis bases. Although, as the pH increases, the hydroxamic acid moieties start to deprotonate at the same pH that the surface begins to become more negatively charged; and, the hydroxamate may increase its Lewis basicity as a result of deprotonation to the same degree as the adsorbed

water. Thus, even ignoring surface charge effects does not allow for a simple view of the surface-DFA interactions.

2.3.2 Adsorption Leading to Dissolution

For the actual dissolution step to occur, figure 6 depicts the addition of six water molecules: four to satisfy the coordination of the Fe(III), and two to satisfy the remaining metal center on the surface. Two scenarios can be postulated. First, the reaction occurs as presented in figure 6, where the destabilized $Fe_{surface}$-solid bond is hydrolyzed. Or, one of the two remaining hydroxamic acid moieties on the DFA molecule overcomes steric hindrance and participates by direct interaction in the removal of the $Fe_{surface}$, as illustrated in chapter 1, equation 7. At higher pH there will exist a greater concentration of hydroxide ions in solution available for interaction with the surface metal centers; while at lower pH, the surface oxides that fulfill the coordination demand of the hydroxamic acid bound $Fe_{surface}$ will be protonated and catalyze the hydrolysis of the $Fe_{surface}$. Thus, the basic and the acidic interactions have the potential to accelerate the dissolution event that is depicted in figure 6. Note, however, that in figure 6, the first step is illustrated as having a proton dependence. For this particular illustration of the dissolution process, the proton dependence is a result of having two water molecules leave the surface, displaced by the hydroxamic acid.
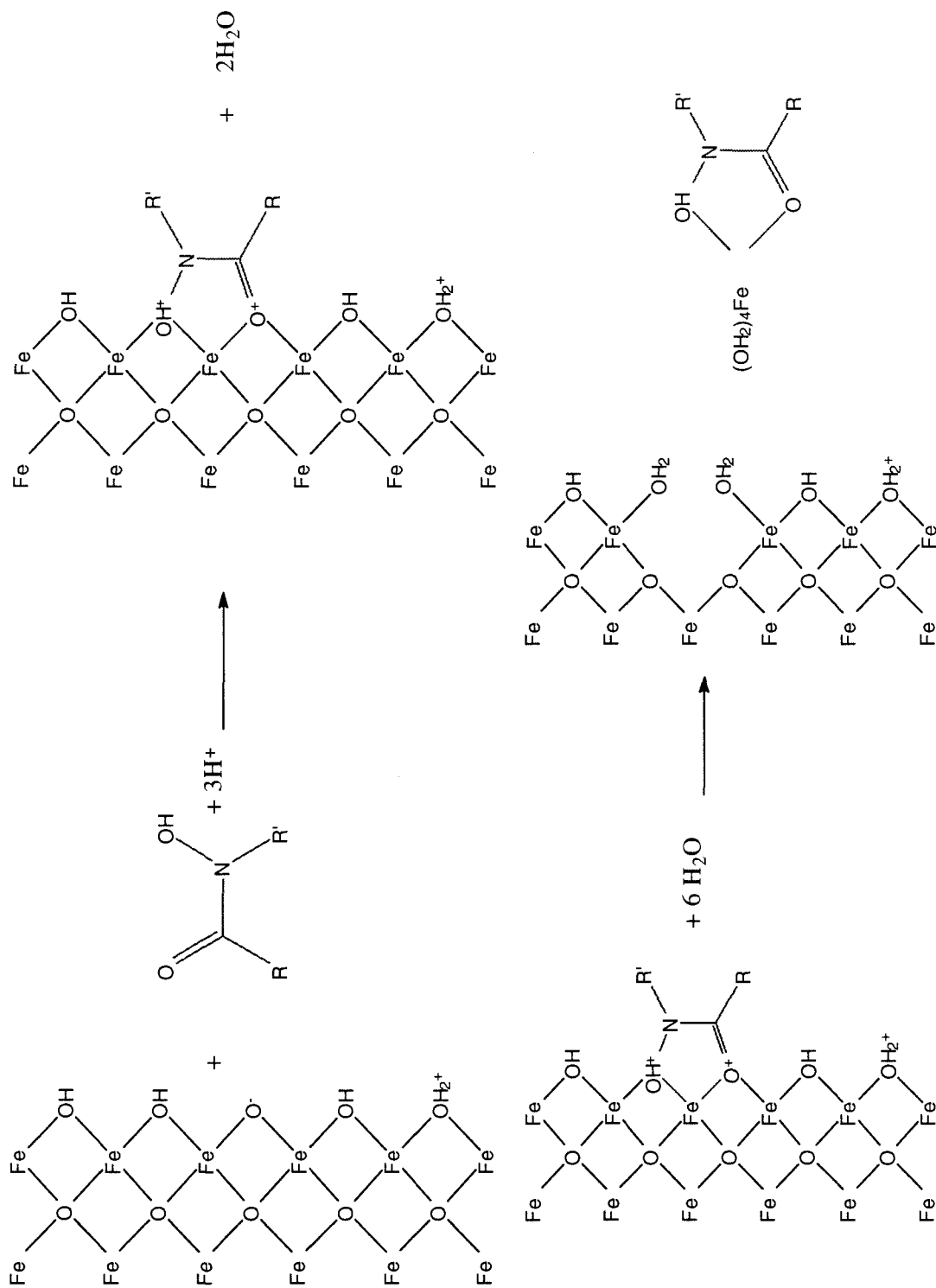
Figure 6

Hypothetical hydroxamic acid mediated dissolution of Fe(III)-(hydr)oxide at pH < 8. The first step is the inner-sphere adsorption of a single hydroxamic acid moiety onto the surface of the solid, with the concomitant removal of water. The second step depicts the hydrolysis of the ligand-metal surface complex and the ensuing removal of the complex into solution.

2.3.3 Mechanism of Dissolution

To examine the mechanism of dissolution of the Mn and Fe (hydr)oxides, it is necessary to attempt to sort through as many of the surface interactions as possible. The following questions must be asked: (1) Does DFA bind covalently with the surface? (2) What is the pH dependence of the DFA-surface binding? (3) Does DFA bind to the surface with a multidentate multinuclear interaction?

2.3.4 Experimental Approaches

A number of experimental approaches have been utilized to address these questions. The most effective approach would be the direct observation of the DFA-surface complex. Diffuse reflectance Fourier transform infrared spectroscopy (DR-FTIR) is utilized to probe for the formation of DFA-surface bonds. Indirect approaches are also used. To examine the effect of pH on the binding of FA and DFA on the surface, adsorption isotherms are generated as a function of pH. If the isotherm is pH independent and exhibits a simple linear partitioning behavior, then it is expected that the surface interaction is neither covalent nor electrostatic. If the isotherm exhibits trends that can be simply explained by mapping onto the pH-dependent electrostatic interactions, then it is expected that the electrostatics dominate the interaction. If the isotherm exhibits a morphology that is consistent with a site binding model, and whose pH dependence is not simply mapped onto the electrostatics of the system, it is reasonable to hypothesize that the interaction has significant covalency. In the ligand-mediated dissolution model posed in figure 6, it is assumed that the surface interaction is covalent. If electrostatic and covalent surface interactions are important with respect to the dissolution event, then

increasing the ionic strength of the electrolyte medium should affect the rate of dissolution.

To attempt to determine the potential for multidentate multinuclear interactions of DFA with the surface, the following approach was taken. A series of dihydroxamic acids of the following form were synthesized:

$$
\begin{array}{ccccccc}
 & \overset{\displaystyle OH}{|} & \overset{\displaystyle O}{\parallel} & & & \overset{\displaystyle O}{\parallel} & \overset{\displaystyle OH}{|} \\
H\!-\!\!-\!\! & N & -C & -(CH_2)_n & -\!\!-\! & C & -N-H
\end{array}
$$
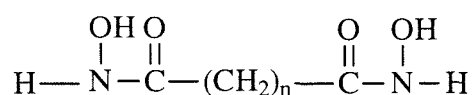
where n varies from 0 to 6. Each compound is reacted with the solid and the behavior of the system is observed. It is expected that the potential for multinuclear interaction of the ligand with the surface will depend on n, the chain length between the hydroxamic acid functionalities. The effect of this interaction should be observable.

2.4 Molecular Dynamics Simulations of DFA – Hematite Interactions

For further insight into the DFA-surface interactions, a set of calculations was performed. These calculations utilize a classical approach to characterize the non-covalent interactions between the DFA molecule and a model hematite surface. Essentially, the calculations involve defining the forces with which the atomic centers interact. Having defined the forces that determine the energy of the molecular system, including electrostatic, van der Waals, torsion, and angular, the total energy of the system is minimized. The total energy includes the bond energies. However, in the system utilized

in these simulations any chemical bond that is formed cannot be broken. Bond lengths and angles are free to change during the energy minimization process, within the constraints imposed by the description of the interactions; i.e., a carbon-carbon bond cannot become infinitely short, as the energy of this interaction goes to infinity as the bond length goes to zero. The total energies measured by the solution of the Hamiltonian of the system mean nothing without a reference energy. Therefore, the meaningful energies are the differences in energy between two system configurations.

2.4.1 Model Results

Newtonian model calculations

In this section a set of calculations is presented that attempts to explore the interaction of DFA with a model hematite surface. The calculations are based on the Universal Force Field (UFF) model that describes the potential energies of the molecular system. With the appropriate boundary conditions, the UFF establishes a set of equations

$$M_i \frac{d^2 x}{dt^2} = F_i = -\frac{\partial V}{\partial x_i} \tag{1}$$

that must be solved to generate a trajectory of the molecular system in time. The program BIOGRAF, and dynamics and minimizer modules in Cerius2, were used on the Silicon Graphics platform to solve the system of equations for the model DFA-hematite system. In the set of calculations presented below, covalent bonds are conserved; i.e., no formation of inner-sphere coordination bonds between DFA and the hematite surface is allowed.

In examining a molecular system of this scale one is confronted with a number of fundamental problems with respect to design of the system in a manner consistent with a force field approach.

First, DFA is a large molecule (figures 8 and 9), MW = 560.69 (in the form used here), and it participates in H-bonding, so implicitly incorporating the water solvent as a continuous dielectric medium is difficult to justify. To deal with this problem, the minimized energies of the system were computed using the Dreiding2 force field (Mayo et al., 1990), in vacuum and with a solvation shell of water, both at the surface and isolated in solution. The solvent shell approach does not capture the effects of long-range solvent interactions because the effect of the bulk water is ignored. However, by focussing on the energy differences between adsorbed and non-adsorbed DFA, the effect of ignoring the bulk water was minimized, and for this set of calculations the approach was deemed sufficient for understanding the interaction trends. Atomic charges were assigned using the qEQ routine (Rappe and Goddard, 1991) after determining the initial structure with no electrostatic interactions, with only van der Waals contributing to the non-bonding energies.

Establishing the force field parameters of the hematite surface is a non-trivial task. The surface of a solid in solution is often taken to be an infinite plane fronting an infinitely extending crystal matrix. In the case examined in this set of simulations, the bare hematite surface was modeled by a (110) surface generated by geometric parameters

developed by Sunder Ramachandran (personal communication). Here, the iron is tetrahedrally coordinated rather than in the typical octahedral coordination. The purpose of the tetrahedral coordination approach is to optimize the electrostatic accuracy of the surface interactions, i.e., to reproduce with the force field the known energetics of the electrostatics of the metal centers at the surface. A qEQ approach was used to optimize the charge distribution in the matrix. For the hematite, a six layer cell was used that was extended to a six by six unit cell in order to be extensive enough to allow the DFA to bind. For the purposes of calculation, the hematite was not treated as a large molecule. Periodic boundary conditions were not used to minimize errors resulting from the incorporation of DFA-DFA interactions. However, the DFA molecule was still large with respect to the extent of the surface, so that edge effects are a concern in the results generated by this study. That is, the fully extended DFA molecule approached the edges of the hematite surface defined above. A force field parameter file developed by Sunder Ramachandran (personal communication) to capture the Fe-C interactions was used to model the interactions with the surface. In this force field a Morse potential[*] with off-diagonal terms in the Hamiltonian matrix is used to capture the short range bonding behavior. The DFA molecules were re-minimized with this parameter file (energies reported in tables 2 and 3) before docking at the surface. Although inaccuracies exist in the absolute values of the numbers reported, by examining differences in energies between the surface and the solution species it is assumed that the correct energetic trends will be observed.

---

[*] The Morse potential is defined as $U(x) = D\{\exp(-2a(x - x_0)) - 2\exp(-a(x - x_0))\}$, where D = depth of the potential well; x_0 = equilibrium distance; and a determines the width of the potential well.

There are two major conformations of an aqueous DFA molecule: first, the uncomplexed molecule in solvent (DFA); second, the molecule complexed to Fe(III) (FA). In the first case, it is expected that the hydrogen bonding would force the hydrophilic groups to the outside to face the aqueous environment, leaving the carbon back-bone inside. Figure 9(B) shows an initial configuration that is fully unraveled, whereas figures 8(A) and 9(A) illustrate configurations that were arrived at through energy minimization algorithms that utilized simulated annealing and Nosé dynamics respectively (Nose, 1991). It can be seen that for the structures in figures 8(A) and 9(A), the molecule has tended to fold into a pseudo-helix, with the carboxyl and hydroxyl groups pointing outward toward the solvent. This type of helical configuration was attained from a number of different initial conditions. The spiraling form of figures 8(A) and 9(A) also supports what one would expect for the FA molecule, with the exception that the hydroxamate groups would be expected to face inward, in octahedral coordination with the central Fe atom. An attempt was made to introduce Fe(III) to the DFA system using the UFF force field; a molecular dynamics run was performed to search for an optimal configuration. However, the time scale of the search was on the order of 10^{-15} s, such that the formation of one tridentate loop in the DFA was observed. It is assumed that the molecule is in the process of zipping up into its final form, where the carbon backbone surrounds the metal center in a sterically stable shell, having the hydroxamate functionalities facing inward towards the metal center. This information, combined with the spiral configuration observed above, leads to the hypothesis that this form is consistent with that which one expects for the Fe(III)–DFA complex. However, further work needs to be done to examine the FA system.

In order to gain some insight into the system, the change in vibrational energies of particular modes of the system in going from solution to the surface was examined. However, since DFA is such a large molecule, it contains many degrees of freedom resulting in a set of vibrational modes that is difficult to analyze conclusively. The general trend observed was that upon binding to the surface a number of the lower energy modes ceased to contribute to the energy of the system (i.e., became negative) while the remaining modes became quite a bit more energetic, with the greatest energy difference at mode 261 with a ΔE (in cm^{-1}) of about 2000 cm^{-1}. This result is not surprising as the docking to the surface would reduce the degrees of freedom of certain motions (due to the presence of an immutable plane) while the strong electrostatic interactions with the surface would shift many of the modes to higher energies. Thus, it is expected that both a shift to higher wave numbers in an adsorption experiment and the loss of some set of vibrational modes resulting from the loss in degrees of freedom will be observed.

The main results of the simulations performed in this study are found in tables 3, 4 and 5. It can be seen that for the isolated DFA, the main energy difference between solvated and unsolvated forms is the favorable van der Waals interaction, the remaining energies differ little from one state to another. This energy difference is due to the added energy of the DFA-water interaction. For this reason, of the energies presented the main focus will be on the change in electrostatic interactions upon docking at the surface, reasoning that anything else will be affected by the fact that the water is treated as part of the DFA system. Upon docking at the surface, a pronounced stabilization due to the favorable

electrostatic interactions is seen. The average unsolvated distance between the DFA and the surface is on the order of 2.9 Å. There is no obvious trend between the energies of the solvated surface species and the unsolvated one. It is true that, as in the isolated case, the van der Waals interactions increase due to the added interaction of the water with the surface. However, the interesting story is in the electrostatic interactions; in all experiments except experiment 9, the electrostatic interactions are severely attenuated by the introduction of solvent, with experiment 8 showing a decrease in electrostatic interactions on the order of 1674 kJ mole^{-1}. This is predominantly a distance effect, and the magnitude of the effect is most likely an artifact of the manner in which the program *calculates the electrostatic interactions in the case that was used. Because of time* constraints, the geometry of the hematite surface was treated as fixed while minimizing the total energy of the system. Thus, only the DFA and water molecules were allowed to relax. In this mode the electrostatic interactions are computed with an algorithm that allows the interactions to fall off as r^{-2}. Although the increased stability of the surface complex over the isolated compound is most likely significant, the magnitude of the differences may be too high.

It is important to note, however, that the difference in energy between the DFA-surface interaction with an intervening layer of water and the DFA-surface interaction without the intervening layer of water suggests that there is a strong energetic tendency to exclude water from the region between the DFA and the surface. The ΔE's presented in table 5 *suggest that the DFA does interact strongly with the surface, mainly as a result of the* electrostatic interactions, and that it is expected that DFA will be bound to the surface

through non-specific interactions in aqueous solution. The proximity of the hydroxamic acid groups to the surface suggests the potential for inner sphere complexation upon displacement of water (or surface hydroxyls). Figure 8(A) shows a space filling model of experiment 7, indicating an overlapping of the van der Waals radii and the potential for covalent interactions between DFA and the surface to occur.

One notes that in experiment 7 two docking configurations were examined. Both were quite stable with respect to the isolated system, yet they exhibit very different energetics with respect to each other (table 5). Although configuration 1 has more stable electrostatic and van der Waals interactions than configuration 2, the trend for the angles is opposite. This illustrates the fact that the molecule will have a large number of different stable interactions with the surface.

A

B
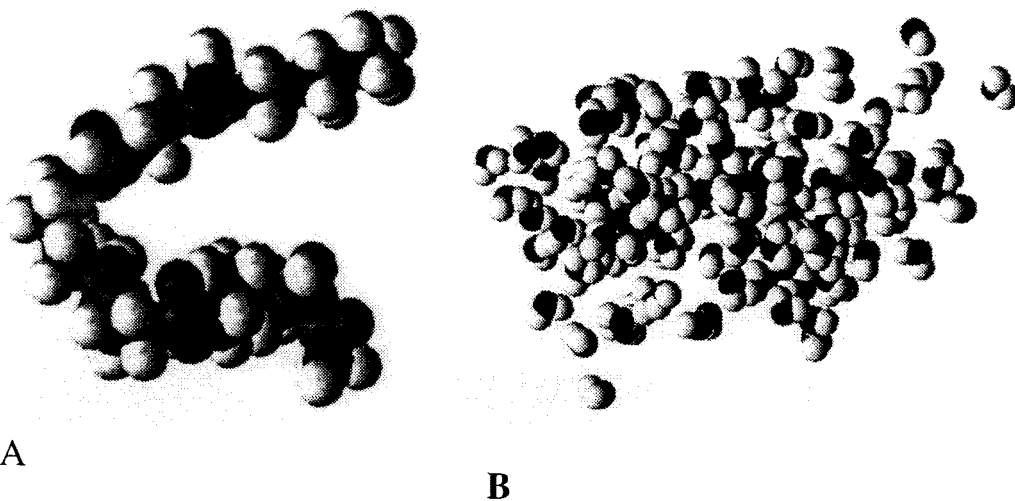
Figure 7

(A) Experiment 2, unsolvated. This picture shows the energy-minimized structure of the unsolvated DFA in a vacuum.

(B) Experiment 6. This picture shows the energy-minimized structure of the solvated DFA in vacuum.

A

Figure 8

B
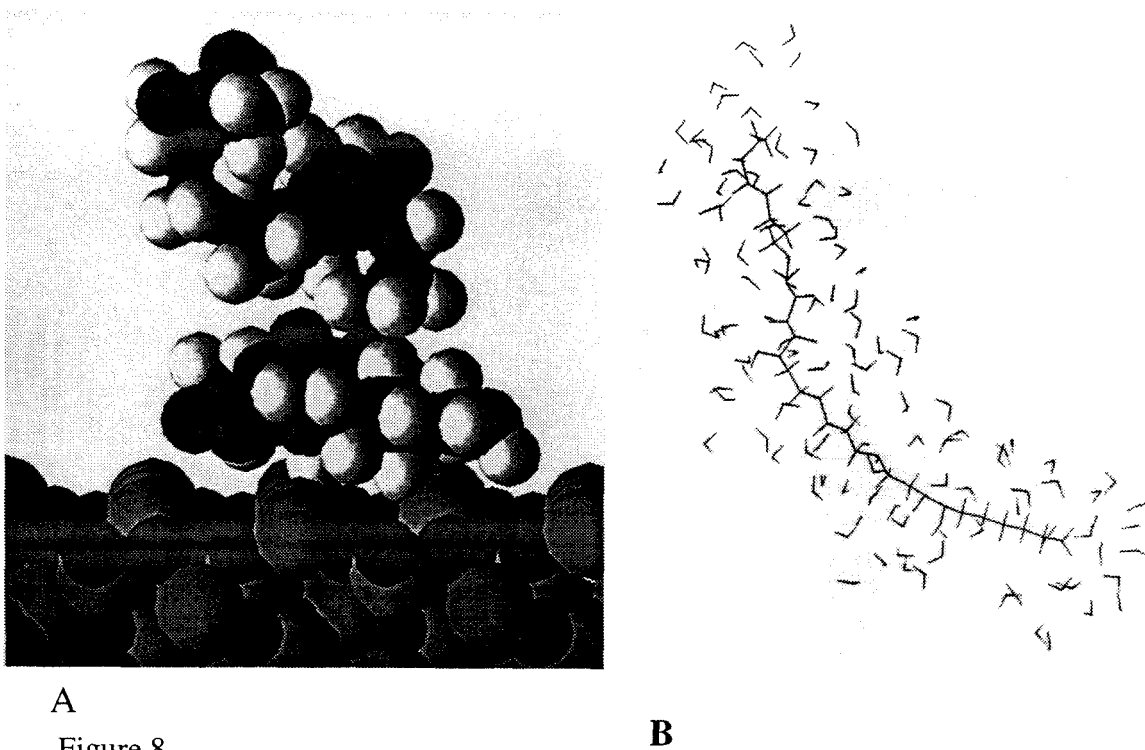
(A) Experiment 7. The figure depicts the energy-minimized structure of the docked unsolvated DFA onto the model hematite surface.

(B) Experiment 9. The figure depicts a stick model of the energy-minimized structure of the solvated linear DFA molecule.

Table 3

Energy distributions for various initial conditions for DFA in solution.

Experiment (in solution)	Total E kJ mole[-1]	RMS Force	Bonds	Angles	Torsions	Electro- static	van der Waals
2	105.27	0.96	39.66	108.49	73.85	-272.30	155.52
2 (solvated)	-112.26	0.88	36.82	106.52	75.14	-280.91	-49.83
6	235.35	0.96	31.71	113.60	50.79	-75.02	114.27
6 (solvated)	45.44	1.13	23.85	86.82	54.02	-104.43	-14.85
7	-141.34	0.40	44.35	240.29	104.10	-688.60	158.53
7 (solvated)	-309.99	1.42	43.64	241.79	104.01	-690.36	-9.08
8	-511.20	1.00	46.19	124.22	101.75	-951.11	167.74
8 (solvated)	-701.66	1.97	45.40	133.68	101.67	-988.18	5.77
9	120.16	1.00	20.42	72.22	42.01	-156.06	141.54
9 (solvated)	-146.36	1.05	23.01	77.24	43.76	-167.03	-123.39

Table 4

Energy distributions for various initial conditions for DFA at the surface of a model hematite.

Experiment (at surface)	Total E kJ mole^{-1}	RMS Force	Bonds	Angles	Torsions	Electro- static	van der Waals
2	-3475.44	1.88	223.97	695.51	101.80	-4841.72	345.05
2 (solvated)	-4206.34	2.05	166.65	470.49	93.68	-4338.72	-598.44
6	-4407.68	2.05	213.68	620.03	114.35	-5642.79	287.11
6 (solvated)	-4197.68	2.01	186.98	424.13	97.07	-4528.09	-377.82
7	-3014.28	0.96	211.75	644.29	112.05	-4070.95	88.62
7 (solvated) config. 1	-3460.42	1.55	141.63	601.70	106.36	-3876.48	-433.59
7 (solvated) config. 2	-3315.03	1.97	123.18	458.69	109.91	-3657.53	-349.28
8	-3927.02	1.84	168.45	440.24	102.72	-5050.42	412.04
8 (solvated)	-3086.29	1.88	177.07	426.43	119.24	-3460.59	-348.44
9	-3723.43	1.88	143.64	914.58	92.59	-5194.98	320.79
9 (solvated)	-5013.19	1.8828	248.2786	755.4212	116.901	-5310.58	-823.16

Table 5

Energy difference Δ = (isolated – surface)

Experiment (at surface)	ΔE kJ mole⁻¹	ΔBond	ΔAngle	ΔTorsion	ΔElectro-static	Δvan der Waals
2	3580.71	-184.31	-587.02	-27.95	4569.43	-189.54
2 (solvated)	4094.09	-129.83	-363.97	-18.54	4057.81	548.61
6	4643.03	-181.96	-506.43	-63.56	5567.77	-172.84
6 (solvated)	4243.12	-163.13	-337.31	-43.05	4423.66	362.96
7	2872.94	-167.40	-404.01	-7.95	3382.35	69.91
7 (solvated) config. 1	3150.43	-97.99	-359.91	-2.34	3186.12	424.51
8	3416.15	-122.26	-316.02	-0.96	4099.32	-244.30
8 (solvated)	2384.63	-131.67	-292.75	-17.57	2472.41	354.22
9	3843.59	-123.22	-842.37	-50.58	5038.92	-179.24
9 (solvated)	4866.83	-225.27	-678.19	-73.14	5143.56	699.77

2.5 Conclusion

The interactions of DFA and FA with the (hydr)oxide surface are expected to be varied and complicated. The experiments described in the ensuing chapters will examine the contributions of the various interactions to the dissolution reaction. Although there exist very few data on the Mn(III) – DFA system, it can be expected that the interactions will be analogous to the Fe(III) – DFA system. Only qualitative work has been performed on characterizing the physical chemistry of the aqueous Mn(III) – DFA complex (Faulkner et al., 1994), and some of the characterizations of the complex in aqueous solution presented in this thesis are the first of their type.

Chapter 3

Interaction of DFA and FA with the Surface of a Synthetic Hematite

3.1 Introduction

3.1.1 Adsorption and Dissolution

The first question asked in chapter 1 is, "How do siderophores interact with the (hydr)oxide surface?" The molecular dynamics simulations presented in chapter 2 suggest that interactions do occur. Thus, it is reasonable to hypothesize that siderophore-surface interactions do occur and are significant with respect to the dissolution process. To test this hypothesis, adsorption isotherms were generated to examine the pH-dependent interaction of DFA and FA with the hematite surface. If the DFA – mediated dissolution is governed by the surface interaction, then the relevant intensive parameter of the system is the surface concentration of DFA. The experiments presented in this chapter will address the character of the surface interactions of DFA and FA with a synthetic hematite phase.

To understand the dissolution behavior of hematite in the presence of DFA, it is necessary to explore the equilibrium interactions between the DFA molecule and the hematite surface. The experimentally elucidated DFA – surface interactions will constrain the proposed mechanism of the dissolution reaction to be consistent with the observed adsorption behavior. If adsorption is fast relative to the rate of dissolution and if the rate-limiting step for the dissolution depends predominantly the adsorbed DFA

species, then a characterization of the adsorbed DFA will be necessary to describe the dissolution process.

Table 1 lists the equations governing dissolution in the system under investigation. In this analysis, the surface coordination approach to modeling the interaction of the DFA and FA with the hematite surface is taken. Although it cannot be assumed a priori that the interaction of the DFA with the hematite surface involves covalent interactions, data presented in this chapter and in chapter 5 support this mechanism. As proposed in chapter 2, it is also expected that DFA interacts with the surface with significant non-covalent interactions. Electrostatic interactions resulting from the positively charged terminal amine of DFA will occur over the entire p_aH range studied. In all the experiments presented in this work p_aH is defined as the negative logarithm of the proton activity in aqueous solution. As the p_aH of the system traverses the range between $p_aH = 7$ and $p_aH = 9$, the protonation state of the hydroxamic acids on the DFA molecule changes, generating an amphiprotic species with a positive charge centered at the terminal amine and negative charge distributed over the hydroxamate functionalities. This zwitterionic species has the potential to interact variously with the hematite surface. The large number of carbon atoms in the structure of DFA implies that one should expect a significant van der Waals interaction between the DFA and the hematite surface.

It is proposed that the dissolution of the hematite is a surface-mediated event in the sense that for the dissolution to occur, the DFA must interact with the solid surface. It is also proposed that the rate-limiting step is the removal of the covalently bound $\equiv Fe-H_iDFA$

complex from the hematite surface. It must be pointed out that this rate limiting step is probably not a single step, but rather a set of elementary steps that involve the breaking of Fe – O bonds of the surface Fe with the bulk oxygen atoms. The reactions governing the adsorption of the DFA and FA onto the surface, the surface protonation state, and the solution speciation of DFA and FA are assumed to be rapid with respect to the dissolution event. These assumptions lead to the hypothesis that, at a given temperature, pressure, and ionic strength (I),

$$R = f([\equiv Fe\text{-}H_iDFA], p_aH) \tag{1}$$

where R = the rate of dissolution. In the simplest case, R is the superposition of a set of independent dissolution reactions (Stumm and Wollast, 1990):

$$R = \sum_i R_{L_i} + R_{H^+} + R_{hydrolysis} \tag{2}$$

where R_i's represent the contributions of the ligand-, proton- and hydrolysis- mediated pathways to the observed dissolution rate. Writing the rate as in equation 2 assumes that negligible non-linear interactions exist between reacting components that contribute to the rate. However, recent work (Kraemer, 1997) suggests the potential for nonlinear effects resulting from the interaction of hydroxide with the adsorbed ligand that have the potential to enhance the dissolution. In the experiments presented in this work, the data will show that the contribution of the R_{OH^-}, R_{H^+}, and $R_{hydrolysis}$ are negligible with respect to R_{L_i}. Therefore, we expect

$$R = \sum_i R_{L_i} \tag{3}$$

or

$$R = \frac{d[Fe]_{tot}}{dt} = \sum_i k_i [\equiv Fe - H_i\text{-}DFA^{(i-3)}] \tag{4}$$

where i sums over all the surface species of DFA, and $[Fe]_{tot}$ is defined as the sum of the

concentrations of the dissolved Fe species. In this case, the p_aH dependence is captured

in the surface speciation of DFA, and k_i is valid for a particular p_aH. If $[\equiv Fe\text{-}H_iDFA]$ is

constant over the course of the dissolution experiment, i.e., the solution concentration of

DFA is in enough excess to fix the concentration of the surface species, the surface

configuration remains constant over the course of the reaction, and the removal of

material from an average particle is negligible, for a particular p_aH the rate of reaction

can be written as a pseudo zero[th] order reaction:

$$R_i = k' \tag{5}$$

where k' incorporates the steady state value of the DFA surface concentrations. This

zero[th] order model predicts a dissolution curve that is a straight line, where the dissolution

curve is defined as the graph of $[Fe]_{tot}$ as a function of time.

Table 1
Equations governing the reaction of DFA with the iron oxide surface

outer sphere adsorption

$H_4\text{-}DFA^+(aq) + \equiv FeOH_j$	$= \equiv Fe\text{-}OH_j\text{-}H_3\text{-}DFA^j + OH_j$	$K_{os}{}^1{}_{eq}$
where $j = 0, 1, 2$		
$H_3\text{-}DFA(aq) + \equiv FeOH_j$	$= \equiv Fe\text{-}OH_j\text{-}H_2\text{-}DFA^{(j-1)} + OH_j$	$K_{os}{}^2{}_{eq}$
$H_2\text{-}DFA^-(aq) + \equiv FeOH_j$	$= \equiv Fe\text{-}OH_j\text{-}H\text{-}DFA^{(j-2)} + OH_j$	$K_{os}{}^3{}_{eq}$

dissolution

$\equiv Fe\text{-}H_i\text{-}DFA^{(i-3)} + OH^{j-2}{}_j$	$\rightarrow \equiv FeOH\text{-}(Fe\text{-}H_i\text{-}DFA)^{(i-4)}$	k_i
where $i = 1, 2, 3; j = 1, 2$		
$\equiv FeOH\text{-}(Fe\text{-}H_i\text{-}DFA)^{(i-4)}$	$\rightarrow \equiv FeOH_j + (Fe\text{-}H_i\text{-}DFA)^{(i-3)}$	k_i
where $i = 1, 2, 3; j = 1, 2$		

inner sphere adsorption

$H_4\text{-}DFA^+(aq) + \equiv FeOH_j{}^{(j-1)}$	$= \equiv Fe\text{-}H_3\text{-}DFA^+ + OH_j{}^{(j-2)}$	$K_{is}{}^1{}_{eq}$
where $j = 0, 1, 2$		
$H_3\text{-}DFA(aq) + \equiv FeOH_j{}^{(j-1)}$	$= \equiv Fe\text{-}H_2\text{-}DFA + OH_j{}^{(j-2)}$	$K_{is}{}^2{}_{eq}$
$H_2\text{-}DFA^-(aq) + \equiv FeOH_j{}^{(j-1)}$	$= \equiv Fe\text{-}H\text{-}DFA^- + OH_j{}^{(j-2)}$	$K_{is}{}^3{}_{eq}$
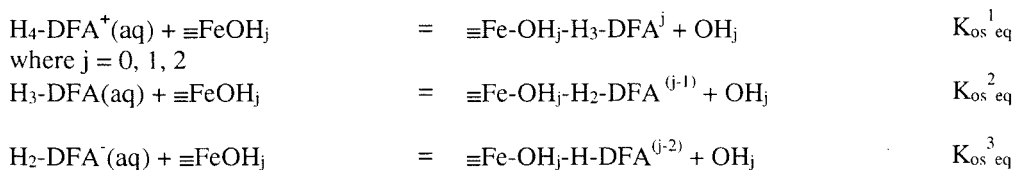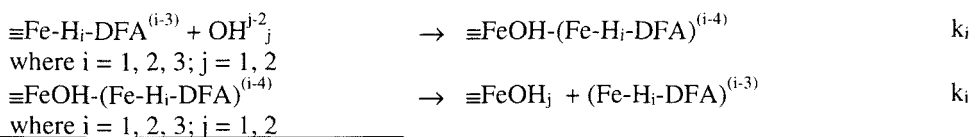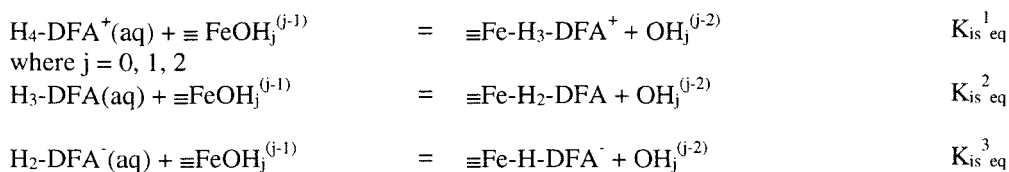
other surface reactions

$\equiv FeOH_j\text{-}(Fe\text{-}H_i\text{-}DFA)^{(i+j-4)}$	$= \equiv FeOH_j{}^{(j-1)} + Fe\text{-}H_i\text{-}DFA^i(aq)$	$K^i{}_{partition}$
$\equiv FeOH + H^+$	$= \equiv FeOH_2{}^+$	K_1
$\equiv FeOH$	$= \equiv FeO^- + H^+$	K_2
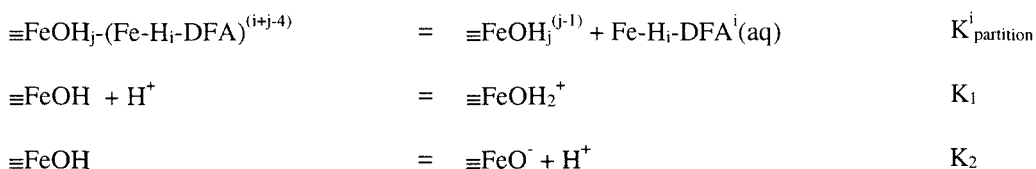
solution reactions
(From [Schwarzenbach, 1963 #206])

$H_4\text{-}DFA^+$	$= H^+ + H_3\text{-}DFA$	pK= 8.39
$H_3\text{-}DFA$	$= H^+ + H_2\text{-}DFA^-$	pK = 9.03
$H_2\text{-}DFA^-$	$= H^+ + H\text{-}DFA^{2-}$	pK = 9.70
$H\text{-}DFA^{2-}$	$= H^+ + DFA^{3-}$	pK > 11
$Fe^{3+} + H_2\text{-}DFA^-$	$= Fe(H_2\text{-}DFA)^{2+}$	Log K = 21.84
$Fe^{3+} + H\text{-}DFA^{2-}$	$= Fe(H\text{-}DFA)^+$	Log K = 30.60
$Fe(H_2\text{-}DFA)^{2+}$	$= H^+ + Fe(H\text{-}DFA)^+$	pK = 0.94
$Fe(H\text{-}DFA)^+$	$= H^+ + Fe(DFA)$	pK > 10
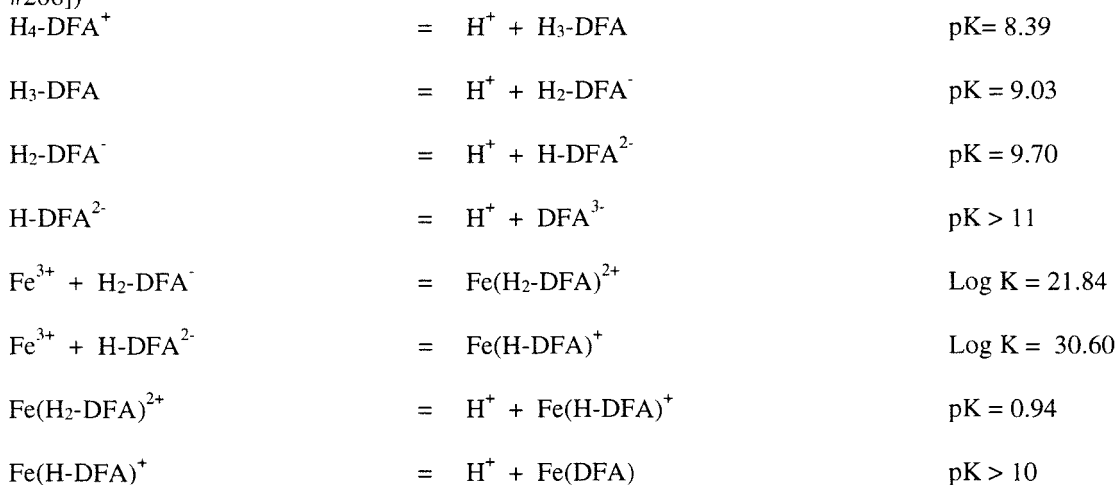
From equations 1 through 5 it is clear that to understand the mechanism of dissolution, the chemistry of the surface interactions must be explored. To this end, adsorption isotherms of DFA and FA were generated over a range of pH's; surface proton titrations were performed on the hematite phase; and photon correlation spectroscopy was used to examine the effects of adsorbed DFA and p_aH on the stability of hematite suspensions.

In the following section the particular hematite phase utilized in this set of experiments is characterized and the experimental methods are described.

3.2 Hematite Synthesis

Sol-gel method

The synthesis of the hematite used in this set of experiments follows the method of Sugimoto and Sakata (Sugimoto and Sakata, 1992). A solution of 2.00 m (mole kg^{-1}) Fe(Cl)$_3$ (EM Science) was prepared in acid-washed Pyrex bottles. To 250.0 ml of this preparation was added 100.0 ml of 6.00 $\pm$ 0.03 N NaOH (VWR Science) while agitating the container by hand. The container was tightly sealed with a screw-on cap, placed in an ultrasonic bath for 10 minutes, and then set in an oven preheated to 100.0°C. The suspension remained in the oven for eight days prior to cleaning.

3.3 Hematite Cleaning

After synthesis, the solid suspension was cleaned in the following manner. The suspension was brought to a p_aH of approximately 8.5 by the addition of 0.10 M NaOH,

whereupon the particles quickly aggregated and settled. The supernatant was discarded and the particles were resuspended in the purest available water (MQW) (18.2 Mohm cm water (MilliQ purification system)). This process was repeated five times. After the final resuspension, the p_aH was not adjusted, rather the suspension was placed in EDTA-rinsed dialysis bags (Spectra/Por Molecularporous Dialysis membrane; molecular weight cut-off = 6-8000). The dialysis bags were suspended in MQW and the water was stirred. The conductance of the MQW surrounding the dialysis bag was monitored. The MQW was replaced continuously until the conductance was less than 10^{-6} siemens cm^{-1} (Orion conductivity meter model 126; conductivity cell model c12210). The dialyzed product was lyophilized to a dry powder and refrigerated.

3.4 Particle Characterization

Figure 1 is a set of two transmission electron micrographs (TEM) of these particles (a.)

prior to and (b.) post dissolution. Samples for TEM analysis were prepared by dispersing

in water, with mortar and pestle, and placing a drop of solution on the surface of a holey

(a.)

(b.)
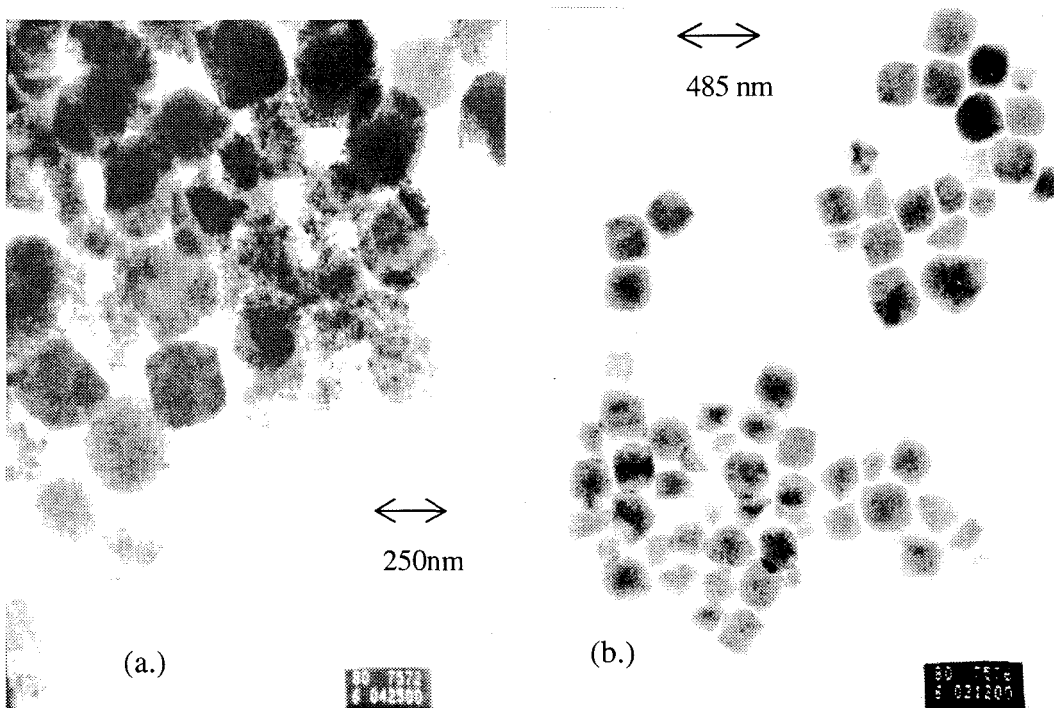
Figure 1

Transmission electron micrographs (TEM) of hematite (sg2g). (a.) Pre dissolution. (b.)
Post dissolution. Actual magnification (a.) 40,400X (b.) 20,600X. Note the bimodal
distribution of cuboidal and fine particles in the sample.

carbon substrate that was covering a Cu grid. The excess solution was wicked away after

30 seconds and the grid was allowed to air dry. The microscope that was used was a

Philips EM430 transmission electron microscope. The analysis was carried out at 300

keV. The micrograph (figure 1 (a.)) clearly shows a bimodal sample, with a set of

uniformly distributed fine particles with an average radius of approximately 12-25 nm,

coupled with a set of cuboidal particles having an average radius of approximately 250-350 nm. A calculation of the surface area generated from sampling particles from the micrograph gives an average surface area of approximately 22 m^2 g^{-1} hematite, taking into account the approximate number density of particles in a sample of six micrographs. Figure 2 shows that the BET analysis of this sample generates a BET surface area of 23.00 ± 0.22 m^2 g^{-1} (Micromeritics ASAP 2000, Adsorptive: N_2 gas). Powder x-ray

BET surface area of sg2g hematite

$y = 0.1868x + 0.0015$
$R^2 = 0.9996$
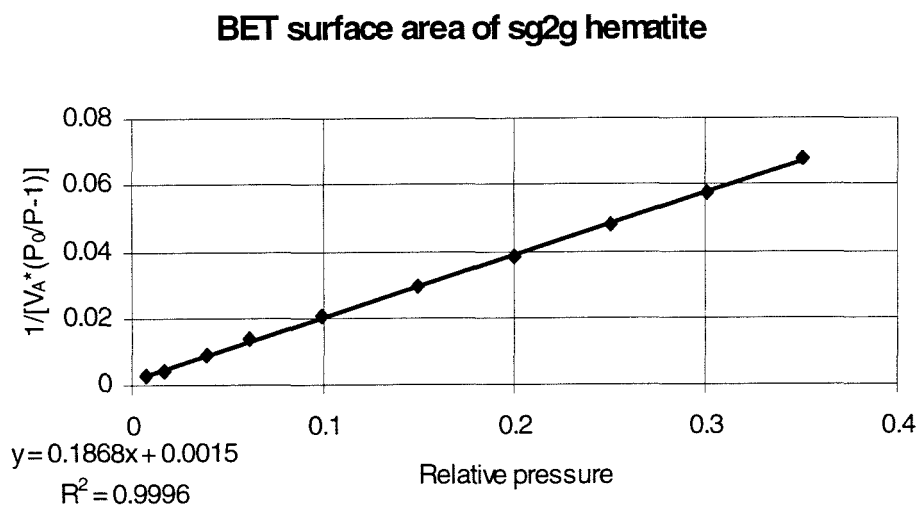
Figure 2
BET plot for hematite, pre-dissolution. 0.7429 g of sample were used, generating a BET surface area of 23.00 ± 0.22 m^2 g^{-1}.

(a.)

```
FN:TL1206B.NI      ID:HEMATITE, SG-31 TL1206B 10-70 S DEG   SCINTAG/USA
DATE:12/ 6/96    TIME:14:46       PT: 1.000   STEP:0.050    WL:1.54059
FULL-COPY  PCOPY  PAGE  TITLE  CYCLE  D ANGLE  END  OVERLAP  REPOS  CURSOR  LABEL
```
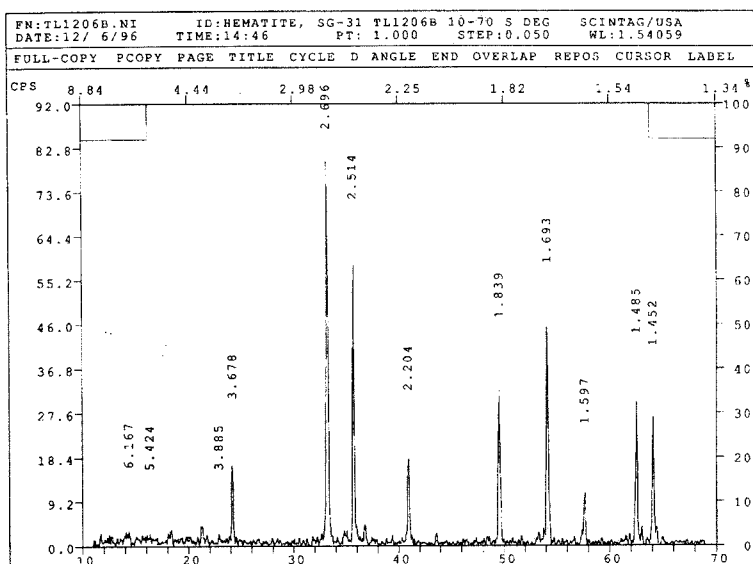
(b.)
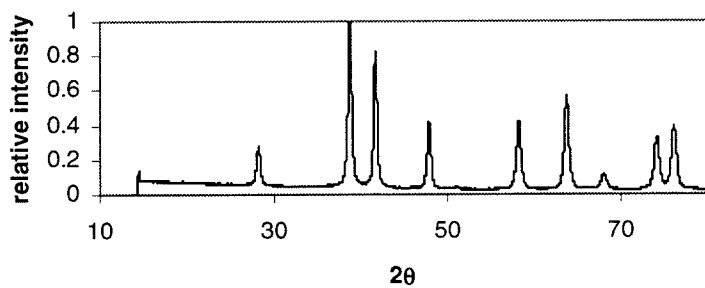
(c.)
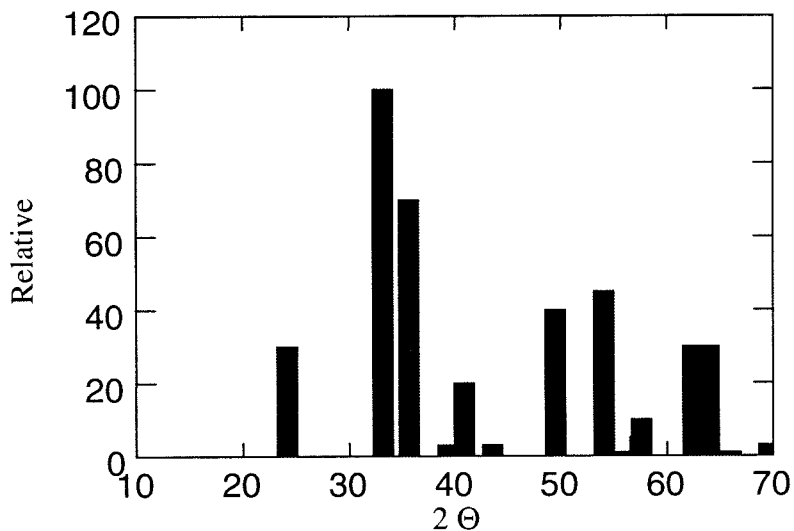
Figure 3

XRD of sol-gel prepared hematite, exhibiting characteristic diffraction pattern for a pure hematite phase. (a.) Scintag Cu-radiation; (b.) Inel with Co-radiation; (c.) Bar graph depicts expected lines for Cu-radiation.

diffraction (XRD) measurement (Scintag PAD-V diffractometer with Cu K_α; and Inel CPS-120 diffractometer with Co K_α (lambda = 1.7902Å) radiation) gives the spectra in figure 3, and shows that the phase is pure hematite. Visual analysis of the diffraction patterns for the fine and the cuboidal particles during the TEM analysis confirmed the monocrystallinity of both particle types.

Fourier transform infrared (FTIR) spectroscopy (Perkin Elmer 1600 Series FTIR for KBr pellet spectra and Nicolet 60SX FTIR for diffuse reflectance spectra) confirmed that the synthesized phase was hematite. Figure 4(a.) depicts the FTIR spectrum of the hematite utilized in these experiments. Figure 4(b.) shows the ratio of the diffuse reflectance spectrum of DFA adsorbed to hematite to the diffuse reflectance spectrum of the pristine hematite. The spectra of DFA and FA are pictured as references. It can be seen that in the finger print region of DFA, 500 cm^{-1} to 1700 cm^{-1}, there is evidence that DFA is interacting with the surface in an analogous way to its interaction with Fe(III) in solution. The ratio peak at 1460 cm^{-1} seems to correspond with the FA peak at 1632 cm^{-1}. This is strong evidence for the inner sphere interaction of DFA with hematite.

(a.)

(b.)
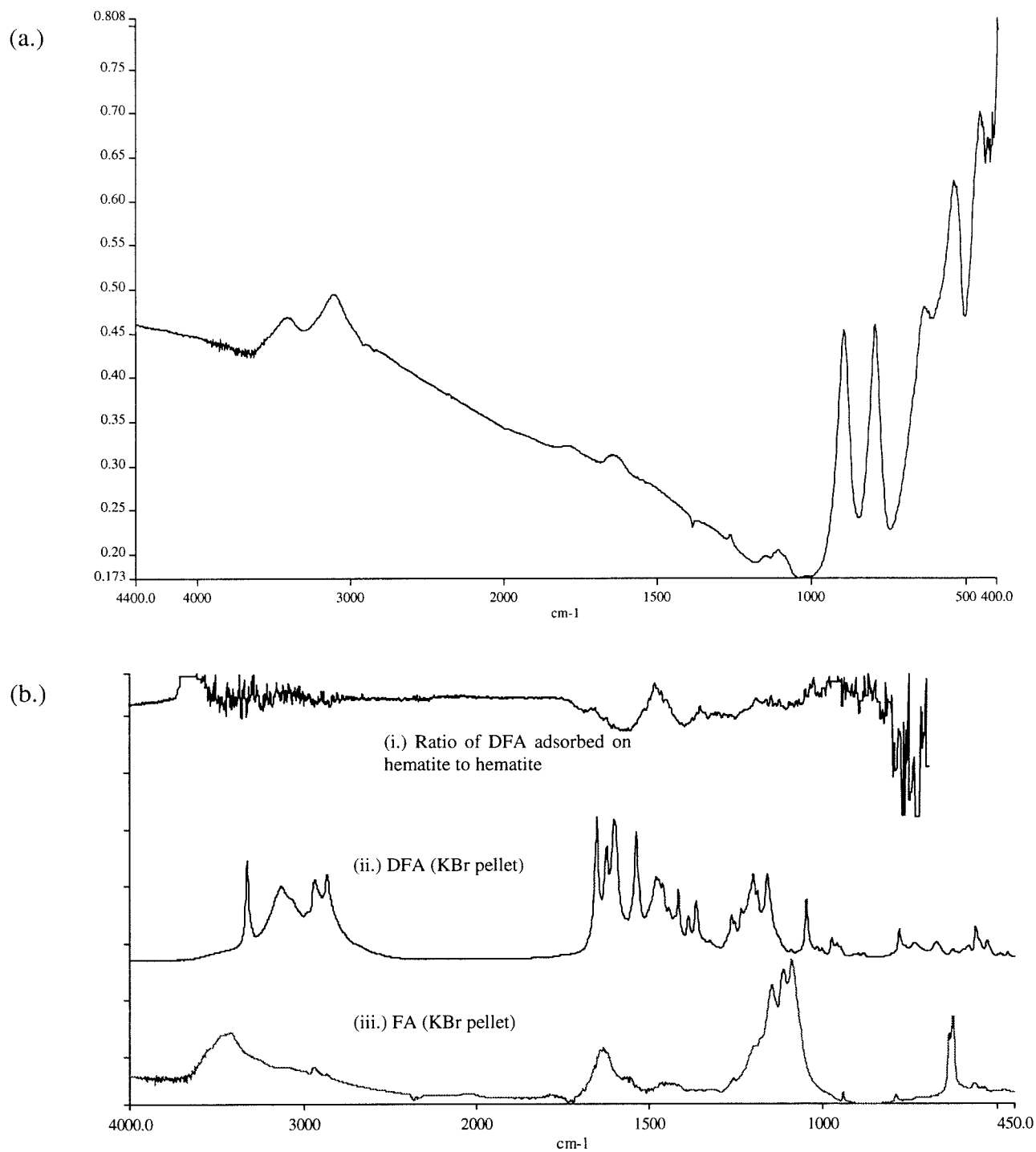
Figure 4

(a.) FTIR spectrum of hematite (sg2g); KBr pellet, 0.01 g hematite, 0.2 g KBr.

(b.) Diffuse reflectance FTIR spectrum showing (i.) the ratio spectrum of hematite with adsorbed DFA to pristine hematite. Spectra of (ii.) DFA and (iii.) FA are shown for reference.

Fluoride adsorption was performed under constant ionic strength (0.01 N NaNO$_3$) in order to determine the anion adsorption site density of this particular preparation of hematite. Figure 5 shows the results of this measurement (Orion 9409 BN solid state fluoride electrode; Radiometer ref201 Ag/AgCl reference electrode; Radiometer PHM 84 pH meter.) Table 2 lists the physical characteristics of this hematite preparation. The F$^-$ – adsorption results in an average anion adsorption site density of 1.73 x 10^{-6} mol m$_{hematite}$$^{-2}$.

Figure 5

Fluoride adsorption on a suspension of hematite. [hematite] = 1.00 g kg^{-1}, 0.01 mole kg^{-1} NaNO$_3$, p$_a$H = 5.65. The line in the graph is generated by fitting a Langmuir isotherm to the data with Γ_{max} = 1.73 x 10^{-3} mol kg^{-1} and K$_{ads}$ = 1.89 x 10^3 kg mole^{-1}.

Table 2

Charateristics of hematite

Particle diameter (fines)	12-20 nm
Particle diameter (cuboidal)	150-350 nm
Calculated average diameter	50 nm
BET surface area	$23.00 \pm 0.22 \ m^2 \ g^{-1}$
Fluoride adsorption density from Langmuir model, Γ_{max}	$3.98 \times 10^{-5} \ mol \ g_{hematite}^{-1} \ (r^2 = 0.907)$
	$1.73 \times 10^{-6} \ mol \ m_{hematite}^{-2}$
K_{ads} (F^- adsorption; Langmuir model)	$1.89 \times 10^3 \ kg_{solution} \ mol^{-1}$

3.5 Experimental Methods

3.5.1 Photon Correlation Spectroscopy (PCS)

The particles size distribution as a function of p_aH and [DFA] was determined by PCS. (The PCS apparatus used was the following: Spectrum Physics model 127 HeNe laser, emitting at 632 nm; Brookhaven Instrument Corporation (BIC) Laser light Scattering System, with a BIC 9000 AT digital correlator and a BIC 200 SM goniometer.) The ionic strength was maintained at 0.01 m $NaClO_4$. The p_aH was adjusted by additions of 0.01 m NaOH and $HClO_4$. The scattering intensity was recorded at 60° and 90°.

The PCS data were taken to characterize the effect of [DFA] on the stability of the hematite suspensions as a function of p_aH. Rather than assuming a log-normal particle

size distribution, which would lose information about the potential for a multimodal size distribution, a least squares fitting approach was used that is resident in the BIC software. In this approach no a priori assumption is made regarding the distribution, rather a distribution is determined that best fits the data.

3.5.2 Titrations

Acidimetric and basimetric titrations were performed on an automatic titrating system. A radiometer autoburette (Radiometer ABU 80 attached to a PHM 85 Precision pH meter, Radiometer pHG201 glass pH electrode, Radiometer Ref201 Ag/AgCl reference electrode with saturated KCl) was controlled through LabView running on the Windows 95 platform. $HClO_4$ was standardized against a known amount of TRIS buffer that had been dried in a $100°$ oven overnight. Titrations were performed at $I = 0.01, 0.1$, and 1.0 m, fixed with $NaClO_4$. Suspensions were deaerated with N_2 prior to titration, and a positive pressure of N_2 was maintained throughout the experiments. The electrode response was standardized by fitting the tails of the solid titration curves to a corrected Nernstian equation: $r = (E_0 - E)/59.1 +$ intercept, where E_0 was measured as 293 mV for the reference electrode (-40 mV versus a calomel electrode). Solutions were stirred with a magnetic stirrer. NaOH, standardized against a known mass of NaHPhthalate, was introduced into the suspension at a rate of $< 4.3 \times 10^{-6}$ l min^{-1}. The combined precision of the meter and the electrode set-up was 0.2 mV, with the stability checked every 7 s.

3.5.3 Adsorption Isotherms

Adsorption isotherms for the adsorption of DFA and FA on hematite were generated. Suspensions of the solid were prepared in 0.01 m NaClO$_4$ having a concentration of hematite of 10.00 g kg^{-1}. For the DFA system three suspensions were prepared in 10^{-5}, 10^{-4} and 10^{-3} m DFA. For each datum the p$_a$H of the suspension was fixed by additions of 0.10 m NaOH and 0.1 m HClO$_4$; approximately 5-7 g of the suspension were removed and filtered at each p$_a$H value. A record of the total mass of the system was tracked at each point to within $\pm 10^{-5}$ g. To analyze for the concentration of DFA in the filtrate, known concentrations of Fe(III)(aq) were added and the [FA] was determined by measuring the absorbance at 436 nm. The stock solution of Fe(NO$_3$)$_3$ was freshly prepared for each concentration of DFA. The concentration of the Fe(NO$_3$)$_3$ stock was fixed at approximately an order of magnitude greater than [DFA]. For the 10^{-3} m DFA system, the Fe(NO$_3$)$_3$ stock was stabilized with a one:one molal addition of NaF.

For adsorption of FA, the suspensions were maintained at a constant p$_a$H and the [FA] was varied. The filtrate was analyzed by measuring the absorbance at 436 nm.

3.8 Results

3.8.1 Proton Titrations of the Hematite Surface

Titrations were performed to characterize the pH dependent charge of the hematite surface. In these data, pH is defined as the negative logarithm to the base ten of the concentration of aqueous protons, and termed p$_c$H. Three titrations were done at I = 0.01, 0.1, and 1.0 m. To analyze the titration data, it was assumed that a single surface-site

model holds. In this model the following equations are assumed to capture the protonation behavior of the surface:

$$\equiv Fe - OH_2^+ = \; \equiv Fe - OH + H^+ \qquad\qquad K_{a1}(int) \qquad\qquad\qquad (6)$$

$$\equiv Fe - OH = \; \equiv Fe - O^- + H^+ \qquad\qquad K_{a2}(int)$$

where the $K_{ai}(int)$ are the intrinsic surface deprotonation constants. Figures 6-8 show the results of the titrations.

At each point on the titration curve, the following equation can be written:

$$C_a - C_b - [H^+] + [OH^-] = [\equiv FeOH_2^+] - [\equiv FeO^-] \qquad\qquad (7)$$

where C_a and C_b are the concentrations of added acid and base in the solution (Stumm and Morgan, 1996), and the remaining species are in concentration. The right hand side of equation 7 is the molar concentration of charge on the surface of the oxide. If equation 7 is multiplied by $F \; (a \; s)^{-1}$, where F = Faraday's constant (96,490 C mol^{-1}), a = mass of solid (kg liter^{-1}), and s = specific surface area (m^2 kg^{-1}), the resulting quantity is the net surface charge density, σ, of the solid at the particular p$_c$H and ionic strength. Since the observed equilibrium constant for the surface protonation reaction depends on the ionic strength, the intrinsic constants from equation 6 must be multiplied by a Boltzmann factor, which is the electrostatic correction resulting from the surface potential:

$$K_{a1} = K_{a1}(int)\exp\left(\frac{F\Psi}{RT}\right) \qquad\qquad\qquad (8)$$

At the pznpc, the surface potential $\Psi = 0$, and $K_{a1} = K_{a1}(int)$. Therefore, the lines of surface charge density, σ, as a function of p_cH at the different ionic strengths should converge at the pznpc.

Figures 6 through 9 show the data from a set of three titrations of hematite. The titration curves are reported and the surface charge density, σ $(C\ m^2)$, is depicted as a function of p_cH for $I = 0.01, 0.1$, and $1.0\ m$ $NaClO_4$. Figure 9 shows that the pznpc of the hematite is approximately 8, although the data exhibits some instability around this point, except for $I = 1.0$. The value of 8 for the pznpc for a clean hematite surface agrees with literature values (e.g., (Kosmulskim et al., 1993).)

(a.)

(b.)

Figure 6

Surface titration of hematite at I = 0.01 m NaClO$_4$. (a.) Titration data, p$_c$H as a function of total added base; (b.) σ (C m^{-2}) as a function of p$_c$H.

(a.)

(b.)

Figure 7

Surface titration of hematite at I = 0.1 m NaClO$_4$. (a.) Titration data, p$_c$H as a function of total added base; (b.) σ (C m^{-2}) as a function of p$_c$H.

Figure 8

Surface titration of hematite at I = 1.0 *m* NaClO$_4$. (a.) Titration data, p$_c$H as a function of total added base; (b.) σ (C m^{-2}) as a function of p$_c$H.

Figure 9

Surface charge density as a function of p_cH for I = 0.01, 0.1, and 1.0 m NaClO4. Note common intersection of the curves at $p_cH \approx 8.1$.

3.8.2 Adsorption of DFA and FA on Hematite

To extract the effect of surface density of DFA on the rate of dissolution, it is necessary to have an understanding of the surface loading of DFA on the hematite particles as a function of p_aH and [DFA]; i.e., p_aH -dependent adsorption isotherms must be generated. Figures 10 and 11 depict the adsorption of FA and DFA, respectively, on hematite as a function of p_aH, and [DFA] or [FA].

3.8.2.1 Adsorption of FA on Hematite

The data in figure 10 show that that the adsorption of FA on hematite is linear over the concentration range tested, and that adsorption is relatively insensitive to p_aH. These observations are consistent with a simple partition coefficient treatment of adsorption:

$$[FA]_{surface} = K_p [FA]_{solution} \qquad (9)$$

where K_p is the partition coefficient defined for a given p_aH. Table 3 lists the experimentally derived K_p values.

It is convenient to express the free energy of the bulk FA – surface interaction as $\Delta G_{ads} = \Delta G_{vdW} + \Delta G_{Coul} + \Delta G_{covalent}$, where the total free energy of the adsorption reaction has been divided into contributions from van der Waals interactions, Coulombic interactions and covalent interactions, respectively. It is instructive to analyze the data relative to such a partitioning of the reaction.

Figure 10

Adsorption of FA on hematite. Inset shows the partition coefficients, K_p, as a function of pH.

Table 3

Adsorption Constants for FA on Hematite

pH	K_p
6	0.144
7	0.167
7.5	0.100
8	0.102
8.5	0.114
9	0.113

van der Waals Interactions

The FA molecule has a total of 20 -CH_2- moieties distributed over its extent. These affect the extent of the stabilization of interactions with the surface by the van der Waals or London dispersion forces. From table 5 in chapter 2, it can be seen that the van der Waals interactions estimated for the solvated DFA interacting with the hematite surface are favorable with respect to an estimate of the self interaction of the purely solvated molecule (i.e., self interaction). Although this energy is merely a gross estimate, it is reasonable to suppose that the combination of the reorganization energy of the water molecules around the FA molecule and the van der Waals interactions would increase the stability of the surface species relative to the aqueous species.

Coulombic Interactions

FA has a single positive charge (on the terminal amine) over the range of p_aH in this experiment. If the FA interacts predominantly through Coulombic interactions, then it is expected that the interaction of the terminal amine with the surface would become more attracting at higher p_aH, as the mean surface charge density of the oxide becomes more negative, given that the net charge of FA is +1 over the p_aH range of the experiments. This phenomenon is not observed, suggesting that the Coulombic interactions are insignificant relative to the other attractive interactions. Moreover, the maximum K_p's observed were at p_aH 6 and 7, where the surface is expected to have a net positive charge. Besides the terminal amine, the only non-CH_2 groups on the FA molecule are two amides that are not expected to participate in covalent interactions with the surface. The dipolar

character of the carbon – oxygen bond may participate in Coulombic interactions. The negative charge resides on the oxygen in this case, and may contribute to the slight increase of stability of the surface complex at p_aH 6 and 7.

Covalent Interactions

No covalent interactions are expected between FA and the surface.

Thus, in the case of FA van der Waals and hydrophobic interactions are proposed to dominate the energetics of the FA – surface bonding.

3.8.2.2 Adsorption of DFA on Hematite

Figure 11 shows the adsorption isotherms of DFA on hematite at varying p_aH's. These curves are well modeled by the Langmuir isotherm:

$$\Gamma = \frac{\Gamma_{max} K_{lang}[DFA]}{1 + K_{lang}[DFA]} \tag{7}$$

where Γ = concentration of adsorbate on surface (mole g^{-1})

Γ_{max} = maximum surface concentration of adsorbate (mole g^{-1})

K_{lang} = equilibrium constant for adsorption of adsorbate onto adsorbent (m^{-1}).

Table 4 lists the parameters generated by fitting the model to the data set, while figure 12 depicts these same parameters as a function of p_aH.
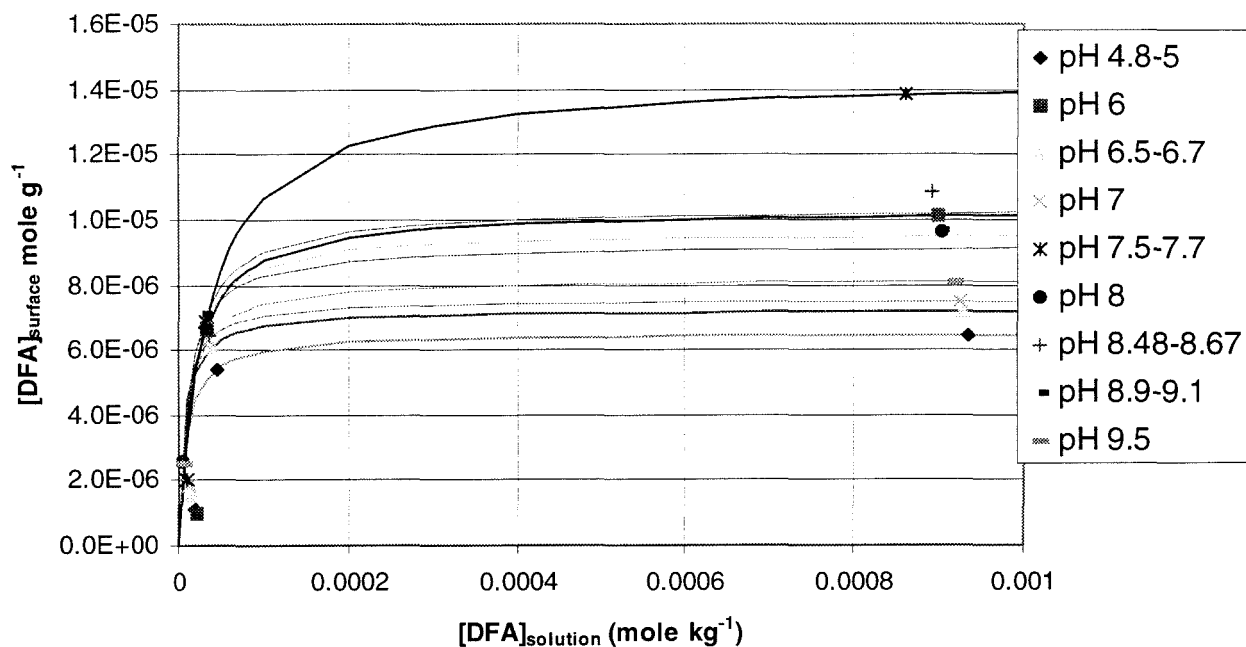
Figure 11

Adsorption of DFA on hematite. Lines are drawn utilizing the parameters generated from the Langmuir model of the adsorption isotherm given in table 4.

The concentrations used in the adsorption experiments were chosen to match those used in the dissolution experiments. The data in figure 12 indicate that the Γ_{max} vary by a factor of about 2.3. Γ_{max} becomes greatest at p_aH 7.5, at which point the concentration of the singly deprotonated solution species, H_3DFA, begins to appear. This species is neutrally charged, but one of the hydroxamic acids is deprotonated and in the hydroxamate form. Because of the charge separation on the DFA molecule, it is likely that the DFA – surface interaction is affected by the negative charge of the hydroxamate

(a.)

(b.)

(c.)

(d.)
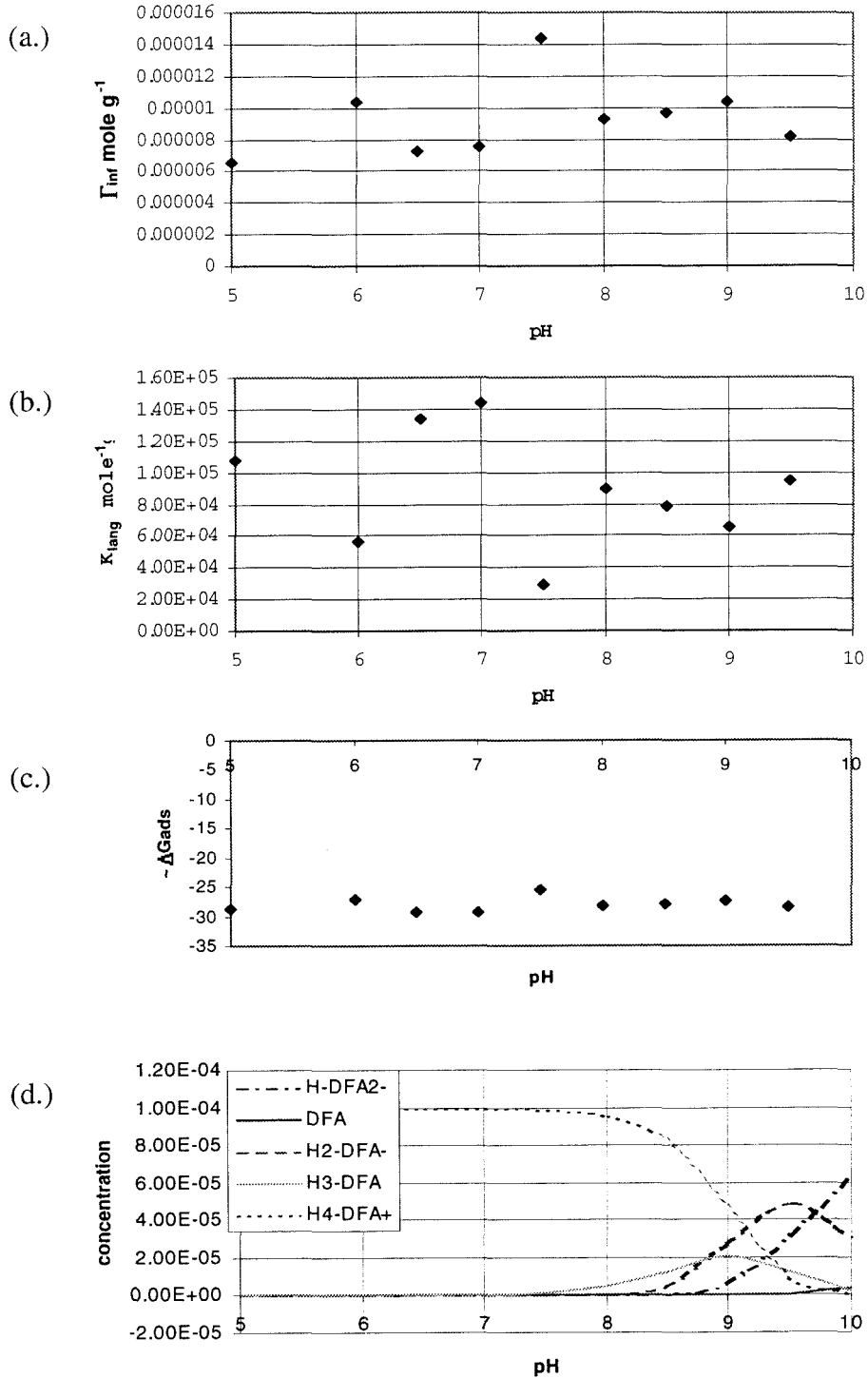
Figure 12

Langmuir parameters for adsorption of DFA onto hematite.   (c.) shows the approximation of $\Delta G^0 = -RT \ln K$; (d.) depicts the solution speciation of DFA over the same pH range.

that is well separated from the positively charged terminal amine. Other than the point at p_aH 7.5, the Γ_{max} remain relatively constant over a wide range of p_aH's, again indicating that the non-specific interactions may govern the adsorption of DFA onto hematite. The behavior of the system becomes more complicated as the p_aH approaches the pH_{pznpc} and the pK_{a1} of the first hydroxamic acid deprotonation. As the DFA and the hematite surface become increasingly deprotonated with increasing p_aH, it is expected that electrostatic repulsion might become significant in reducing the affinity of the DFA to the surface. This effect is not observed. In fact the affinity of the DFA to the surface, measured by K_{ads}, varies by a factor of five, with the greatest difference being between p_aH 7 and p_aH 7.5. This difference can be attributed to the increased concentration of the H_3DFA species in solution. The values of K_{lang} and Γ_{max} at $p_aH = 7.5$ suggest that there is a possibility for change in surface interaction occurring between $p_aH = 7$ and $p_aH = 7.5$. That is, the surface loading increases and the affinity decreases, suggesting that there might exist an altered orientation of the molecule on the surface, allowing an increased density of DFA on the surface at saturation. This could be a function of the increased negative charge of the surface interacting with the positively charged terminal amine, with the remaining DFA molecule minimizing its interaction with the surface. However, if it is assumed that the interaction between the H_3DFA and the surface is predominantly an inner sphere bidentate mononuclear interaction, then the H_3DFA would have to displace a surface oxo group in a nucleophilic attack on a surface Fe(III), and the interaction at $p_aH = 7.5$ would be a complicated mixture of the increasingly stable electrostatic interaction of the terminal amine with the increasingly negative surface, the

repulsive electrostatic interaction of the singly deprotonated H_3DFA, and the increasingly

effective Lewis base – nucleophile of the single hydroxamate functionality.

Table 4

Adsorption parameters for the Langmuir model of the adsorption of DFA onto hematite

p_aH	Γ_{max} (mole g^{-1})	K_{ads} (m^{-1})	$\sim\Delta G^0$ (kJ mole^{-1})
5	6.52×10^{-6}	1.07×10^5	-12.47
6	1.03×10^{-5}	5.63×10^4	-11.78
6.5	7.23×10^{-6}	1.34×10^5	-12.71
7	1.17×10^{-5}	1.44×10^5	-12.79
7.5	2.44×10^{-5}	2.88×10^4	-11.05
8	9.21×10^{-6}	8.92×10^4	-12.27
8.5	9.62×10^{-6}	7.88×10^4	-12.14
9	1.04×10^{-5}	6.58×10^4	-11.94
9.5	8.19×10^{-6}	9.50×10^4	-12.34

It is reasonable to assume that the energetics of DFA – surface interaction are affected by $\{H^+\}$ and $\{OH^-\}$, and by the protonation state of the surface. At p_aH 8, the net charge on the surface is circum-neutral, and H_3DFA is present in solution, but in low concentrations relative to DFA_{tot}. It is reasonable to suppose that the inner sphere adsorption of the H_4DFA^+ is less efficient than that of the H_3DFA as a result of the lower nucleophilicity of the hydroxamic acid form relative to the hydroxamate form; but that it is a better

nucleophile than H_2O, increasing the adsorption efficiency at lower p_aH. For example, in solution once the DFA interacts with $Fe^{3+}(aq)$ the waters of hydration are rapidly displaced from the coordination sphere, and the three hydroxamic acids quickly deprotonate. As the surface becomes more negatively charged, the H_4DFA^+ must begin to compete with OH^- for surface sites. However, as the p_aH becomes greater than p_aH 8, the solution speciation of DFA becomes a mix of the mono-, di-, and tri-hydroxamate states, which are expected to be excellent nucleophiles with respect to interaction with Fe(III) and, by implication, with the hematite surface. These species may compete effectively with OH^- for surface sites.

Table 4 and figure 12 show an estimate of the ΔG^0 of the adsorption reaction, where $\Delta G^0 \approx -RTln\ K_{ads}$. It can be seen that the values of ΔG^0 vary by 1.73 kJ at most, suggesting little variation in the energetics of bonding of DFA at the surface.

Comparison with the DFA-hematite adsorption study by Eisenlauer and Matijevic (1980) is complicated by the difference in reported values of the pH_{pznpc}, the value reported for the hematite used in their study being 7. On a per gram basis, the adsorption data agree for $p_cH < pH_{pznpc}$. However, on a per unit surface area basis, the data presented in this work exhibit an adsorption maximum that is approximately half of that observed in the Eisenlauer and Matijevic work. They observe an adsorption maximum at $p_aH = 9.8$, whereas the data in this work indicate an adsorption maximum at $p_aH = 7.5$. Eisenlauer and Matijevic argue that the increased adsorption at $p_aH = 9.8$ results from the DFA – surface interaction being primarily based on the favorable electrostatic interaction of the

terminal amine with the negatively charged surface. As a result, the adsorbed DFA reorients itself in a geometry that approaches an orthogonal orientation of the linear DFA with respect to the plane of the surface. The results from the work with hematite presented here suggest that the use of a simple electrostatic argument for the DFA – surface interaction is insufficient to capture the complexity of the bonding of DFA to the hematite surface.

Most importantly for this study, the generation of the adsorption isotherms for the range of p_aH's, over which the dissolution experiments have been performed, allows the determination of the rate constant for the surface mediated dissolution step described in equation 4. The data describing the dissolution of this preparation of hematite by DFA are presented in the chapter 4.

3.8.3 Photon Correlation Spectroscopy (PCS)

PCS was utilized to examine the effect of DFA adsorption on the stability of colloidal suspensions of hematite with respect to coagulation. If the DFA adsorbs to the hematite in significant amounts, it is hypothesized that the surface properties would change, affecting the interparticle interactions. Figures 13 through 18 show the results of the PCS measurements for $p_aH = 4, 6, 7, 8$, and 9. The $[DFA]_{tot}$ varies from 0 to 10^{-3} m. The data shown are from measurements of scattering taken at 90 degrees. This is a three-dimensional data set, in the sense that there are two independent variables, p_aH and $[DFA]_{tot}$, and the particle size distribution is examined as a function of these two variables.

Looking at the data for which $[DFA]_{tot} = 0$ and the p_aH varies, it can be seen that the distributions vary insignificantly for $p_aH < 8$. At $p_aH = 8$ and $p_aH = 9$ a significant volume of particles appears at around 5000 nm, while the distribution between 50 and 500 nm has shifted to larger sizes, suggesting the onset of coagulation. These observations are consistent with the observation that $pH_{pznpc} = 8$.

As the $[DFA]_{tot}$ varies for constant p_aH, little occurs to the distribution until the $[DFA]_{tot}$ reaches 10^{-4} or 10^{-3} m. This observation is consistent with observations made by Holmen and Casey characteristics (Holmén and Casey, 1996) wherein the effect of adsorption of acetohydroxamic acid onto goethite had an insignificant effect on the proton surface charging. However, at $[DFA]_{tot} = 10^{-3}$ m, a skewing of the distribution towards larger particles size can be seen, suggesting that there exists a change in surface characteristics as the surface becomes saturated with DFA. The change in surface characteristics results in a decrease of the stability of the suspension. Formation of greater than monolayer coverage of DFA, defined here as surface precipitation, may occur as a result of DFA(aq) interacting with the DFA – saturated surface, significantly altering the characteristic of the surface.
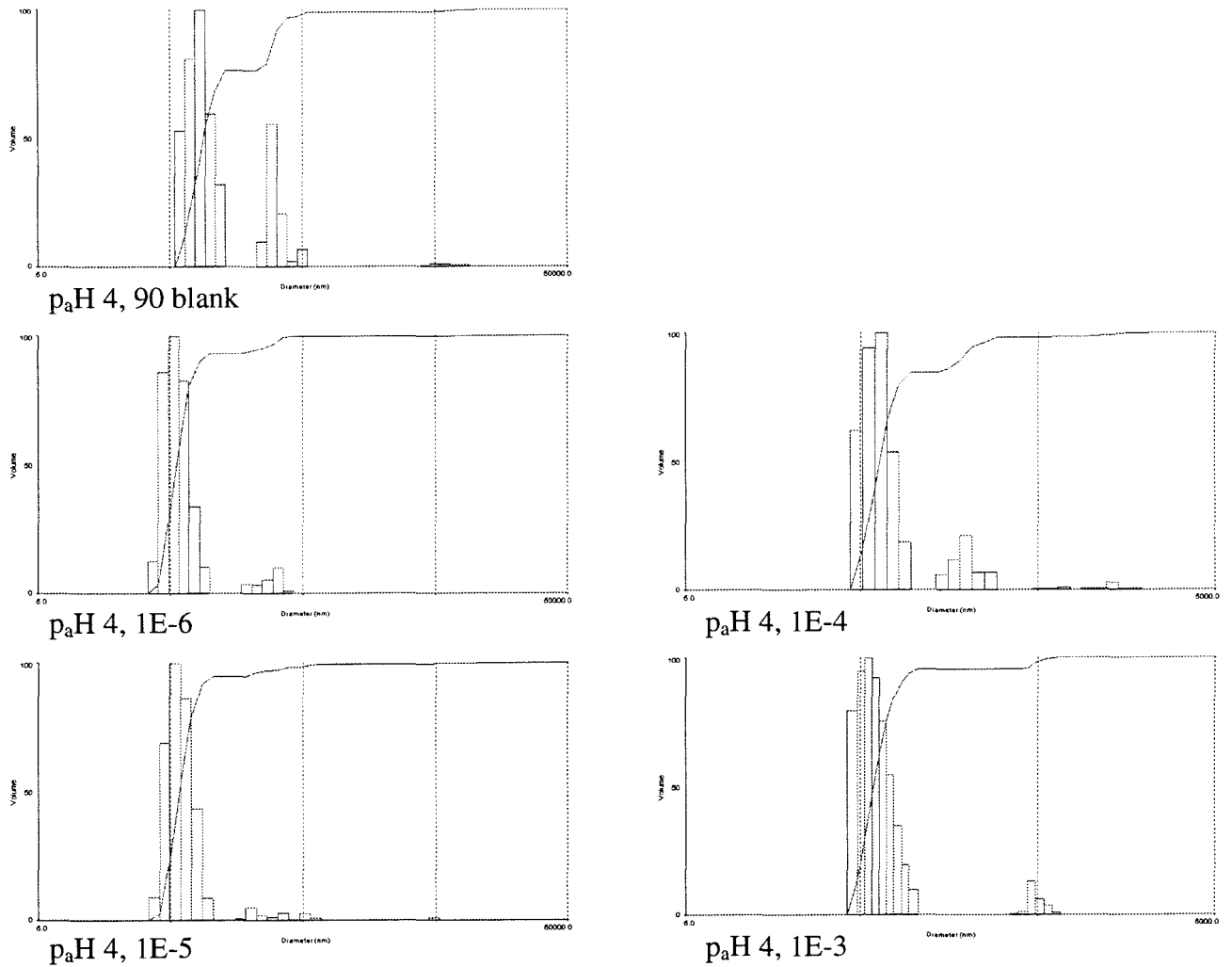
Figure 13

PCS particle size distributions for $p_aH = 4$; [DFA] varies as indicated. Signal reported is percent of total volume of particles. The line shows the cumulative distribution. Note that the scale of the x-axis varies among the plots.

p_aH 6, 90 blank

p_aH 6, 1E-6

p_aH 6, 1E-4

p_aH 6, 1E-5

p_aH 6, 1E-3
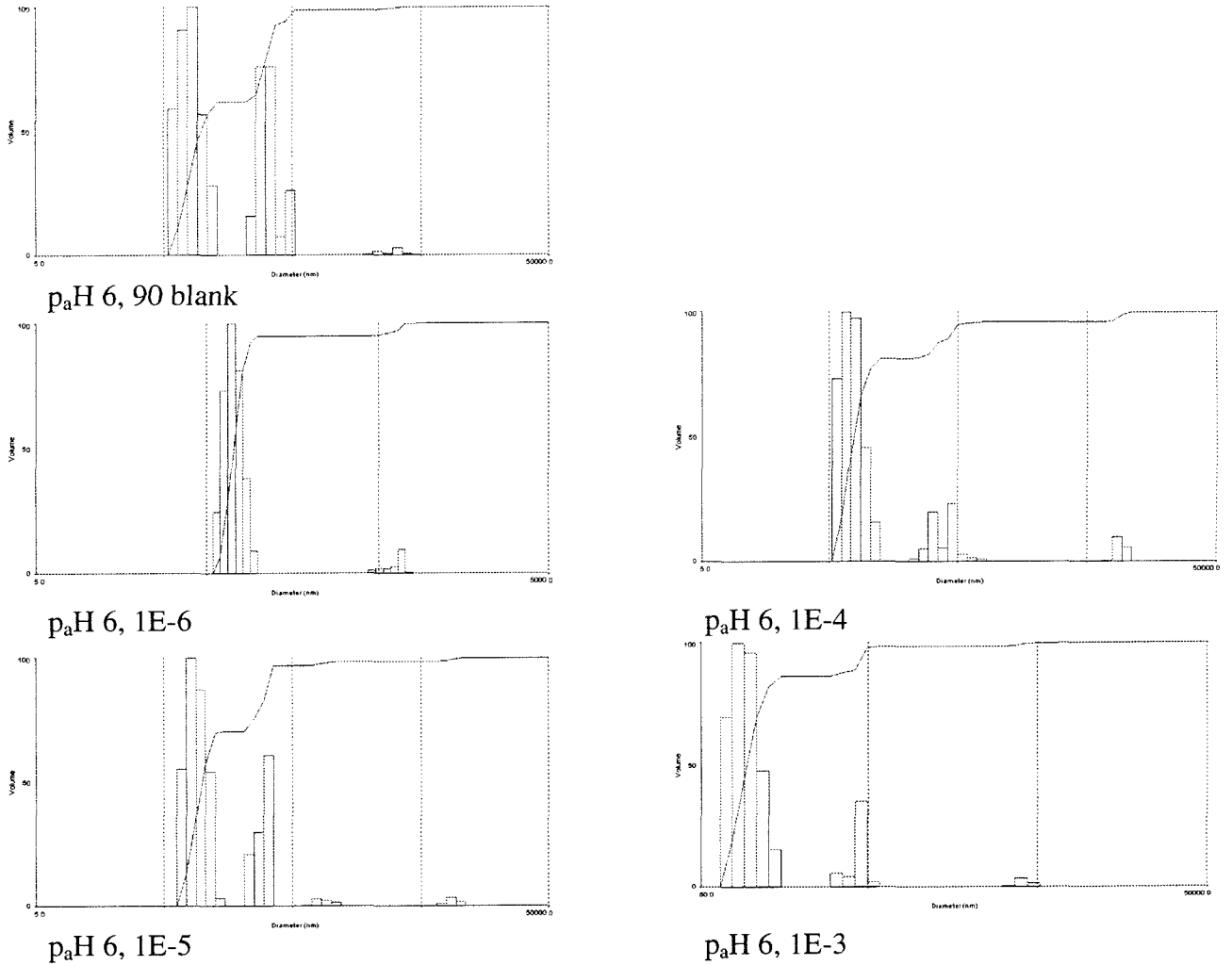
Figure 14

PCS particle size distributions for $p_aH = 6$; [DFA] varies as indicated. Signal reported is percent of total volume of particles. The line shows the cumulative distribution. Note that the scale of the x-axis varies among the plots.
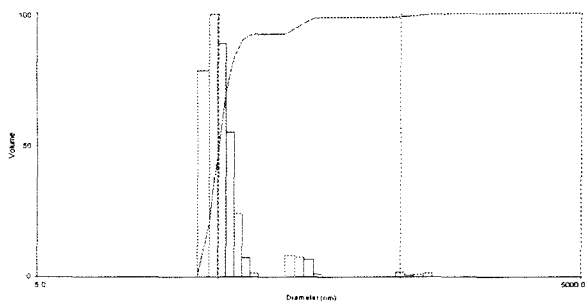
p_aH 7, 90 blank
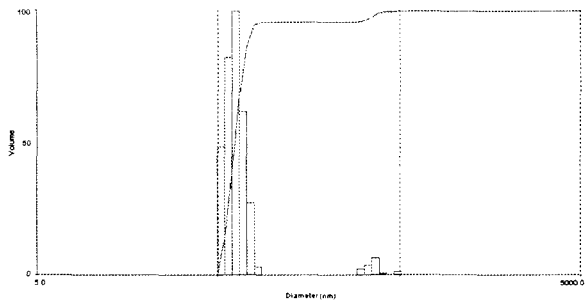
p_aH 7, 1E-5
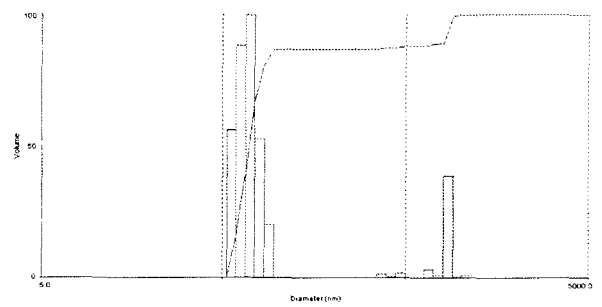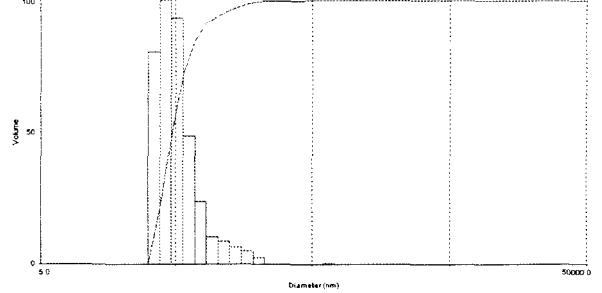
p_aH 7, 1E-6

p_aH 7, 1E-4

Figure 15

PCS particle size distributions for p_aH = 7; [DFA] varies as indicated. Signal reported is percent of total volume of particles. The line shows the cumulative distribution. Note that the scale of the x-axis varies among the plots.
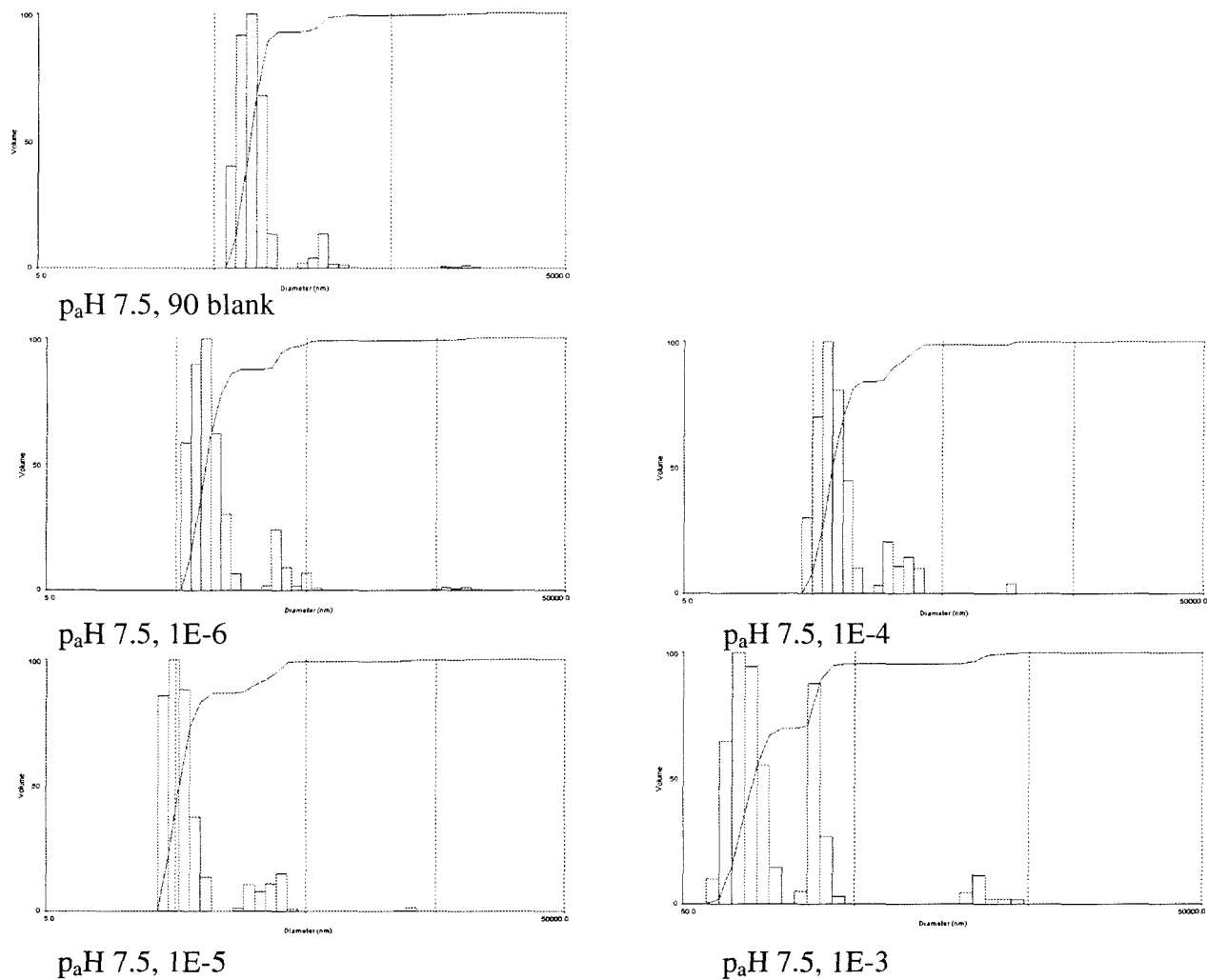
Figure 16

PCS particle size distributions for $p_aH = 7.5$; [DFA] varies as indicated. Signal reported is percent of total volume of particles. The line shows the cumulative distribution. Note that the scale of the x-axis varies among the plots.
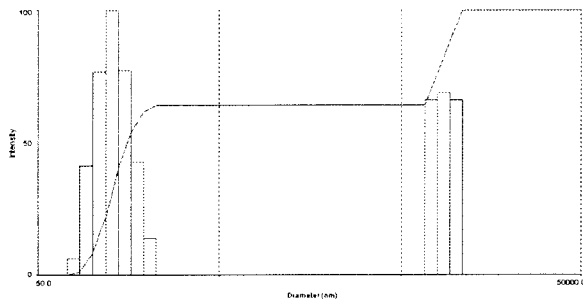
p$_a$H 8, 90 blank
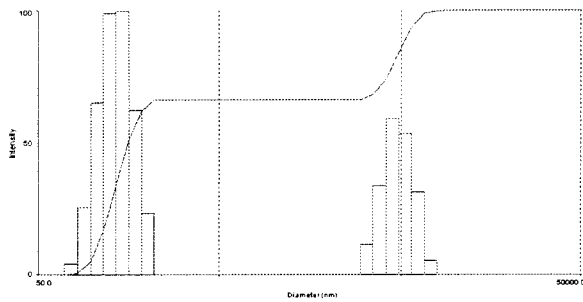
p$_a$H 8, 1E-6
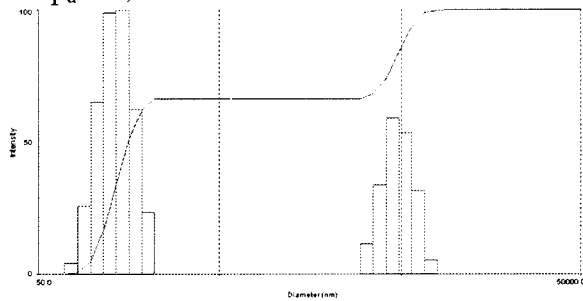
p$_a$H 8, 1E-4
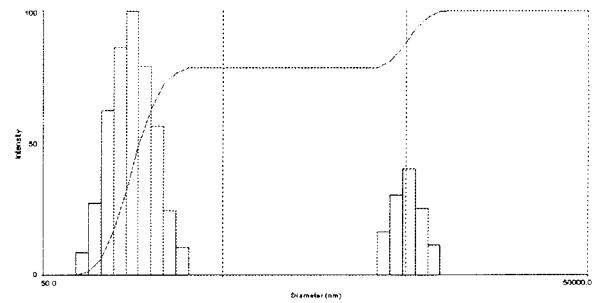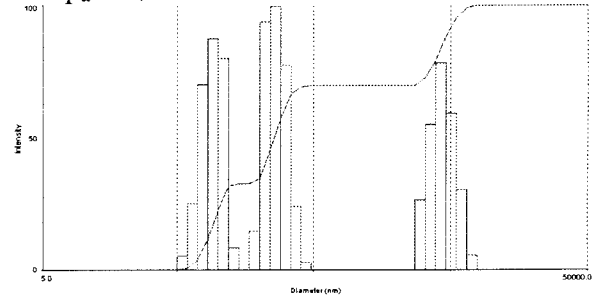
p$_a$H 8, 1E-5

p$_a$H 8, 1E-3

Figure 17

PCS particle size distributions for p$_a$H = 8; [DFA] varies as indicated. Signal reported is percent of total volume of particles. The line shows the cumulative distribution. Note that the scale of the x-axis varies among the plots.
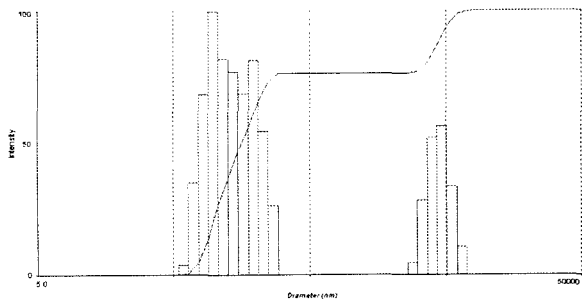
p_aH 9, 90 blank
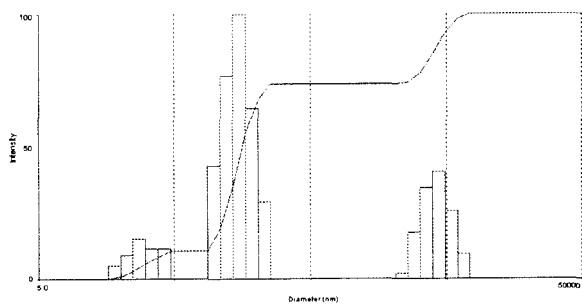
p_aH 9, 1E-5
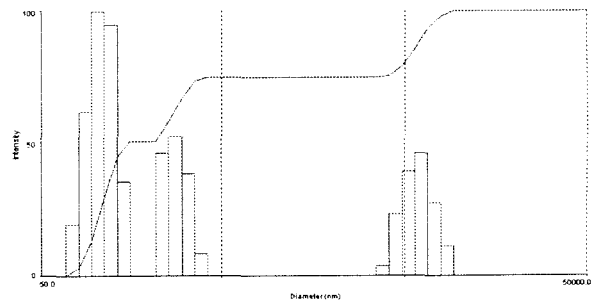
p_aH 9, 1E-3

Figure 18

PCS particle size distributions for $p_aH = 9$; [DFA] varies as indicated. Signal reported is percent of total volume of particles. The line shows the cumulative distribution. Note that the scale of the x-axis varies among the plots.

Figure 19 shows the mean particle diameters of the hematite, assuming a log-normal particle distribution. It is interesting to note that there appears to be coagulation at $p_aH = 8$, $[DFA]_{tot} = 0$, consistent with the observed pH_{pznpc} from the surface proton titrations presented above. The remaining data suggest that there is little effect of addition of DFA on the particle size distribution, illustrating the value of using the least square fitting method presented above.
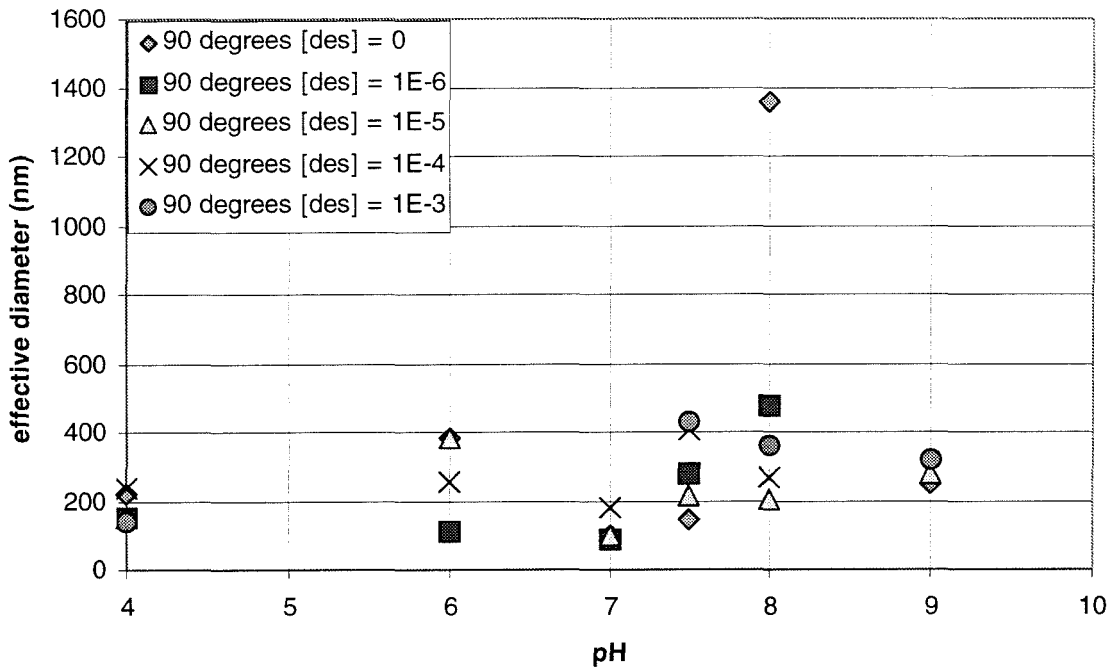
Figure 19

PCS data of sg2g hematite taken at a 90 ° angle. The reported mean diameters assume that the particles are log normally distributed. Note that there appears to be coagulation at $p_aH = 8$ for [DFA] = 0, as expected from the calculated pH_{pznpc} reported above.

3.9 Conclusion

In this chapter data have been presented that illustrate the interactions of the DFA molecule with the hematite surface. Strong evidence exists that a combination of covalent and non-covalent interactions is implicated in the surface binding. The binding of DFA to the surface is complicated and results from the sum of a number of separate interactions. The data presented here agree in general but not in detail with the data presented by Eisenlauer and Matijevic (Eisenlauer and Matijevic, 1980); the differences arise because of the difference in surface interactions resulting from the differences in hematite preparations. Their hematite preparation exhibited very different charging characteristics than the hematite preparation in this work. Specifically, they observe a pH_{pznpc} of 7 whereas the hematite in this work has a pH_{pznpc} of 8. The main differences in the interpretation of the surface bonding interactions comes from the observations of Eisenlauer and Matijevic at $p_aH = 9.6$, 2.6 pH units above the pH_{pznpc}. The highest p_aH observed in the data presented here is $p_aH = 9.4$, only 1.4 pH units above the pH_{pznpc}. Because of the p_aH dependent charge distribution of DFA and the hematite surface in the same p_aH range, it is expected that the electrostatic interactions will be complicated.

Chapter 4

The Dissolution of Hematite

4.1 Introduction

Hematite is found as one of the end products of weathering in soil pedogenesis (Bolt and Bruggenwert, 1976). Hematite is the thermodynamically stable Fe(III) oxide at standard temperature under ambient oxygen concentrations. As a model of the pool of naturally occurring Fe(III)-(hydr)oxides, hematite represents the more stable end of the reactivity spectrum.

The data presented in this chapter describe the dissolution of a pure synthetic hematite phase, the preparation of which is described in chapter 3. The data will characterize the appearance of FA in solution as a function of time. These data combined with the adsorption data presented in chapter 3 will lead to a proposed mechanism for the interaction of DFA with the surface of the hematite particles and the resultant dissolution as a function of [DFA], p_aH, ionic strength and temperature.

4.2 Experimental Methods

$NaClO_4$ was utilized as an inert electrolyte in all experiments. The hematite concentration was 1.00 g hematite (kg solution)$^{-1}$. Prior to introduction of DFA to the system, the suspension was placed in an ultrasonic bath (Bransonic 220) for

approximately two minutes. After sonication the suspension was stirred for 3 to 14 days. N_2 was bubbled through the suspension for at least two hours prior to the introduction of DFA; the bubbling was maintained through the duration of the experiments.

DFA was dissolved in MQW prior to introduction to the hematite suspension. Two stock DFA solutions were maintained: 10^{-1} m and 10^{-4} m. These were stored at $4°C$ when not in use, and freshly prepared if stored for more than three weeks. UV-visible spectroscopy of the stock solution showed negligible degradation of the stock solution over the time scale of the storage period.

For all the dissolution experiments, p_aH is defined as the negative logarithm to the base ten of the activity of the aqueous proton and termed p_aH. A combination pH electrode (Corning 476390 High performance Ag/AgCl; Beckman Futura Plus 5712A Ag/AgCl) was used for monitoring the p_aH of the rotary-stirred reactor (see below). Two pH meters were used: a Corning pH/ion analyzer 350 and a Radiometer ion 83 ion meter.

A pH-stat was designed and built to maintain a constant p_aH in the jacketed beaker system described below. Control was maintained through a MacIntosh Computer housing a National Instruments data acquisition board (Lab-NB) controlling two stepper motors (Superior Electric Slo-Syn MO61-FC02) that were attached to two micrometer burettes (2.5 ml, Gilson). A two-channel digital pH meter (Corning pH/ion analyzer 350) fed a digital signal through the RS232 port directly into the serial port of the PC. A program was written in the LabView environment (National Instruments) that tested for user-

determined p_aH stability (≤ 0.005 p_aH units min^{-1}), and injected acid or base to maintain solution p_aH to within 0.005 p_aH units. A record of addition of acid and base as a function of time was stored on the PC hard disk. For this system a glass electrode (Radiometer pHG201) and either a glass frit reference electrode (Radiometer Ref 201; Ag/AgCl, saturated KCl) or a glass sleeve reference electrode (Radiometer Ref 261 Ag/AgCl, saturated KCl) was used. A second pH-stat was utilized for the p_aH adjustment of experiments whose Δ p_aH was monotonic. In this case, an auto burette (Radiometer ABU 12 or ABU 80, connected to a Radiometer PHM 84 Research pH meter) was set up with strong acid (0.01 m $HClO_4$) or base (0.01 m NaOH), and only a record of the integrated amount of acid or base additions was kept.

Two experimental systems were used.

The first consisted of jacketed beakers connected to a re-circulating constant temperature bath (Haake FK) (See figure 1.) The beakers were closed to the atmosphere, kept under a positive pressure of CO_2-scrubbed N_2 gas that had been hydrated with electrolyte solution, and constantly agitated with either magnetic or propeller stirring (Metrohm 722 stirrer). Temperature was fixed at 25.0°C. Two to six jacketed beakers could be connected in series; at most two of these could be maintained at constant p_aH. Each reaction vessel was wrapped with aluminum foil to minimize the flux of laboratory light into the system.
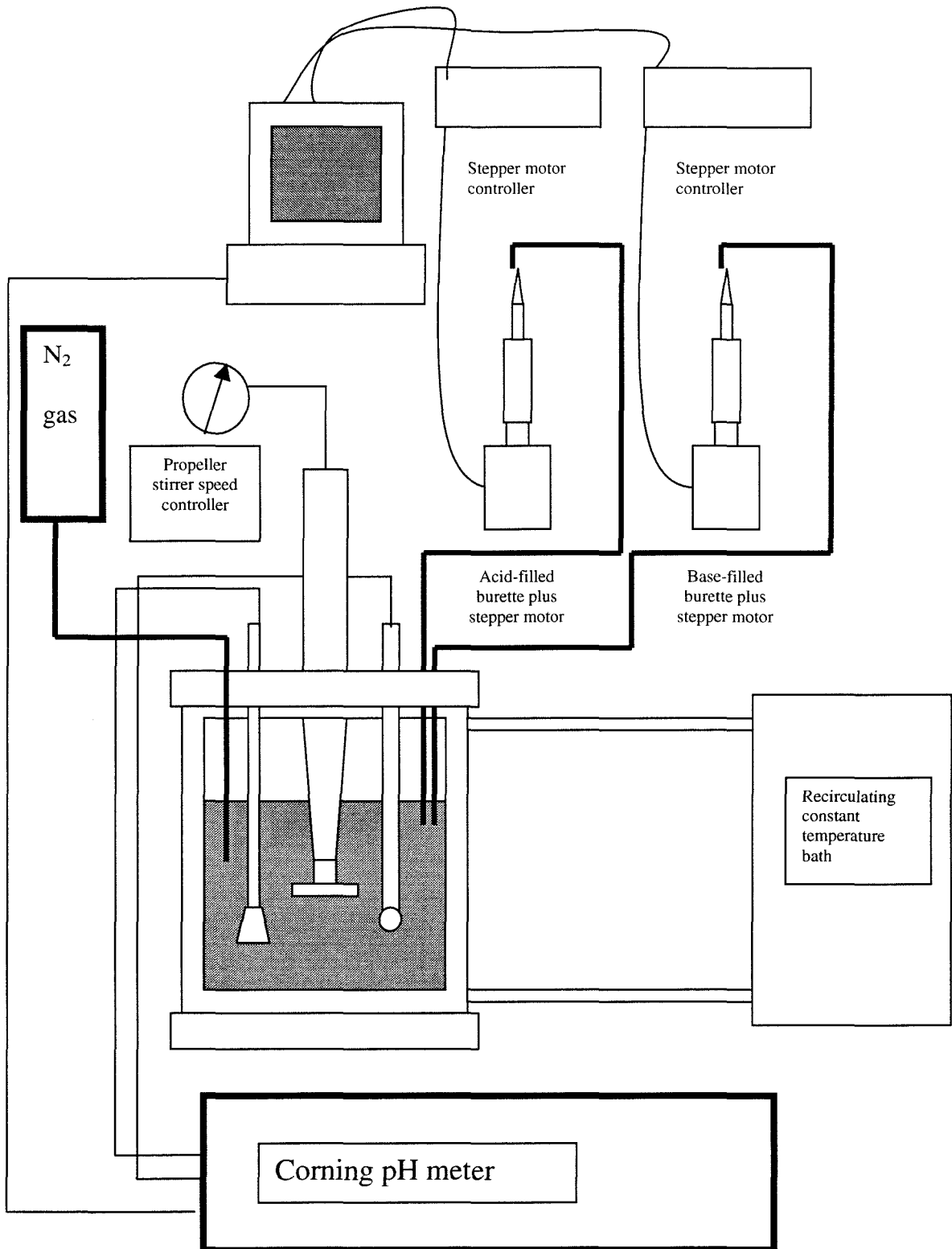
Figure 1

Experimental setup for pH-stat dissolution experiments.

The second system, depicted in figure 2, consisted of a set of nine 500 ml Erlenmeyer flasks placed in an environmental rotary stirrer (Labline Environmental Shaker). Air blowing over a water cooled copper coil, whose temperature was maintained with a refrigerated recirculating bath (Neslab RTE-110), combined with a feedback controlled heating coil, maintained an air environment of constant temperature (25.0°C). The rotation rate was maintained at 200 rpm. The flasks were kept under a positive pressure of CO_2-scrubbed N_2 gas that had been hydrated with electrolyte solution. For experiments performed with this system, p_aH was adjusted at every sample time through small additions of either 0.01 or 0.1 m $HClO_4$ or NaOH. The vessels were wrapped in
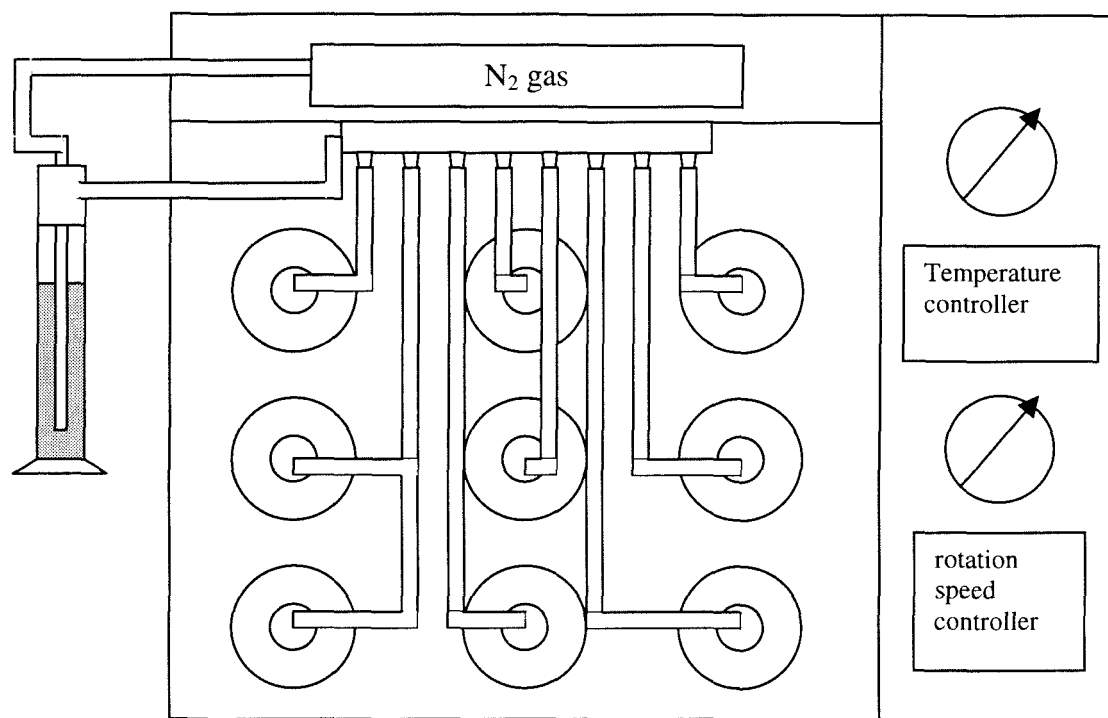
Figure 2

Rotary stirrer reactor.

aluminum foil to prevent influx of light.

DFA was introduced into the containers with a calibrated pipette (Gilson or Eppendorf) at time = 0.

For both systems, samples were removed by pulling suspension through a Teflon tube into a glass, nylon, or high-density polyethylene (HDPE) syringe. At no time did the solution contact metal. The samples were filtered through 0.2 μm cellular micropore acetate filters into HDPE centrifuge tubes and stored at 4°C.

The filtrate was stored in the cold room (4°C) prior to and post analysis. The filtrate was analyzed for total Fe with a Hewlett Packard 4500 inductively coupled plasma mass spectrometer (ICPMS). Standard curves were obtained periodically through each analysis, resulting in a new standard curve generated after the analysis of each set of samples for a given kinetic experiment. Concentrations of standards were achieved by the dilution of purchased ICPMS standards (High Purity Standards). Each datum consisted of the average of three measurements. Mass 57 was utilized for Fe measurement, referenced to an internal standard of Tl to correct for instrumental drift. Measurements were discarded and retaken if the percentage residual error exceeded 7%.

The remaining filtrate was stored in the cold room for further analysis with high performance liquid chromatography (HPLC) (Hewlet Packard Series II 1090 liquid chromatograph). An HPLC method was developed to independently confirm the

observed concentration of FA, and to attempt to determine the residual DFA. A 12.5% acetonitrile-87.5% 0.02 M p_aH 3.00 phosphate solution was used as the mobile phase. The temperature was maintained at 28°C. The column used was from Alltech (Allosphere ODS-2, 5 μm, 150 mm x 4.6 mm, PEEK). The diode array UV-visible detector was monitored at 220 nm and 436 nm, referenced to the average of 560 to 600 nm. The flow rate was 0.800 ml min^{-1}, and the pressure maintained itself at approximately 100 bar throughout the run.

4.2 Experimental Results

4.2.1 Dissolution as a Function of p_aH and [DFA]

The results of the dissolution of the hematite are shown in figure 3. The graphs in figure 3 show the data for the appearance of Fe in solution as a function of time. Each point represents the average of two or three data and the error bars indicate $\pm$ two standard deviations. These experiments were performed in the rotary stirred reactor. Figures 3 (I) (a.), (b.), and (c.) show the dissolution curves at pH = 5, 6, and 7 respectively; while (d.), (e.) and (f.) show the relationship between the ICPMS measurements of [Fe]$_{tot}$ and the HPLC measurements of [FA]. The accuracy of the HPLC measurements is hampered by the tendency of the DFA to bind to the tubing in the HPLC apparatus, resulting in poor peak separation and high peak asymmetry. However, the measurements show that the Fe measured by ICPMS can be equated with [FA]. These measurements combined with the blanks confirm that the Fe in solution is in the form of FA. Figure 3 (II) (g.) and (h.) shows the analogous dissolution curves measured by ICPMS for pH = 8 and 9, respectively.

It is hypothesized that the rate of production of FA is a function of [DFA], p_aH,

[hematite], T, I (ionic strength), and P. Since the stability of the aqueous FA complex is

so great, it is assumed that the Fe observed in solution is bound by FA, as confirmed by

(a.)
p_aH

(b.)
p_aH

(c.)
p_aH

(d.)
[DFA]$_0$ = 10$^-$

(e.)
[DFA]$_0$ = 10^{-4}

(f.)
[DFA]$_0$ = 10^{-3} m
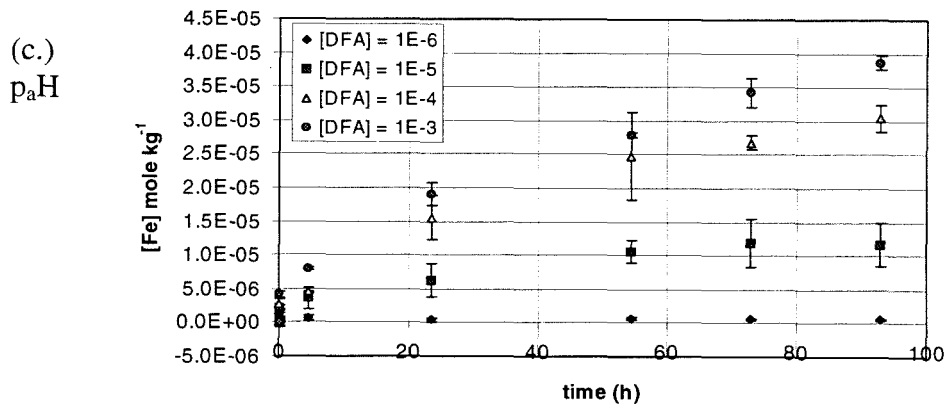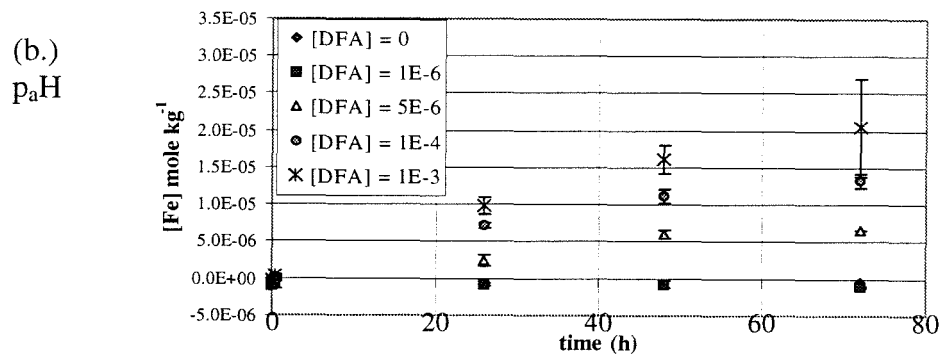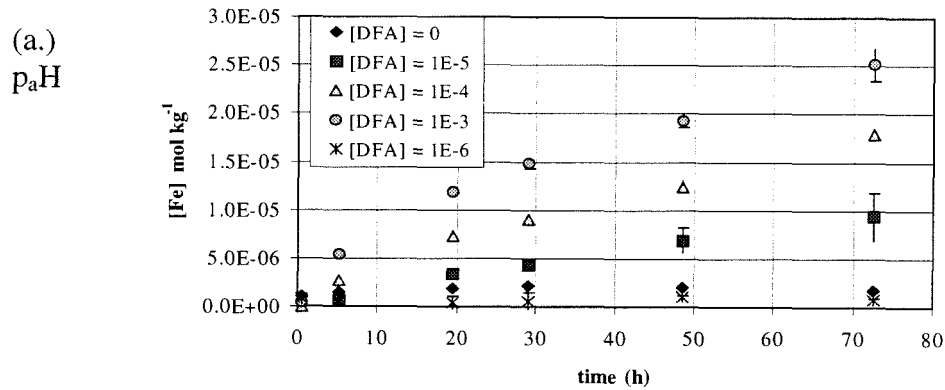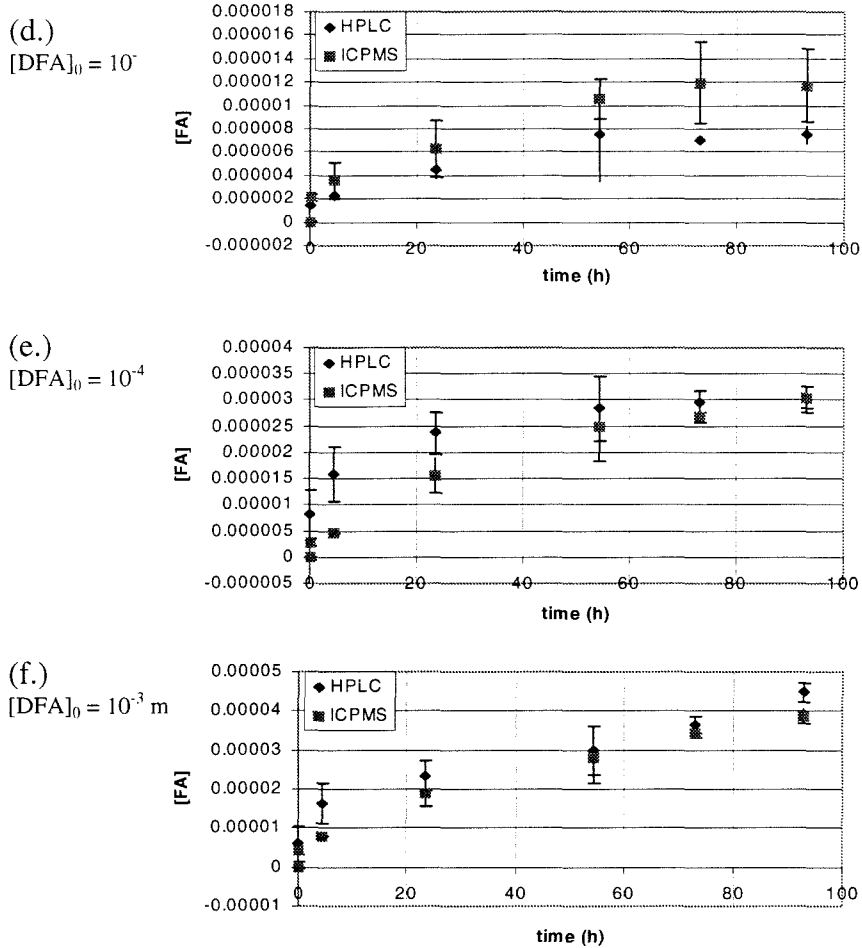
Figure 3 (I)

Dissolution of hematite at (a.) p$_a$H = 5, (b.) p$_a$H = 6, and (c.) – (f.) p$_a$H = 7. [DFA]$_0$ = 0, 10^{-6}, 10^{-5}, 10^{-4}, and 10^{-3} mol kg^{-1}. [Hematite] = 1.00 g kg^{-1}. For figures (d.), (e.), and (f.) the graphs compare the HPLC analysis with the ICPMS analysis.

HPLC analysis. Over the p$_a$H range and time scale examined in this work, the dissolution mediated by the aqueous proton or hydroxide ions is less than the random errors generated by the analytical methods used, and therefore cannot be resolved. The presence of the fine size fraction in the freshly prepared hematite sample suggests that there might be incomplete filtration by the 0.2 μm filters; if this were the case, the

(g.)

(h.)
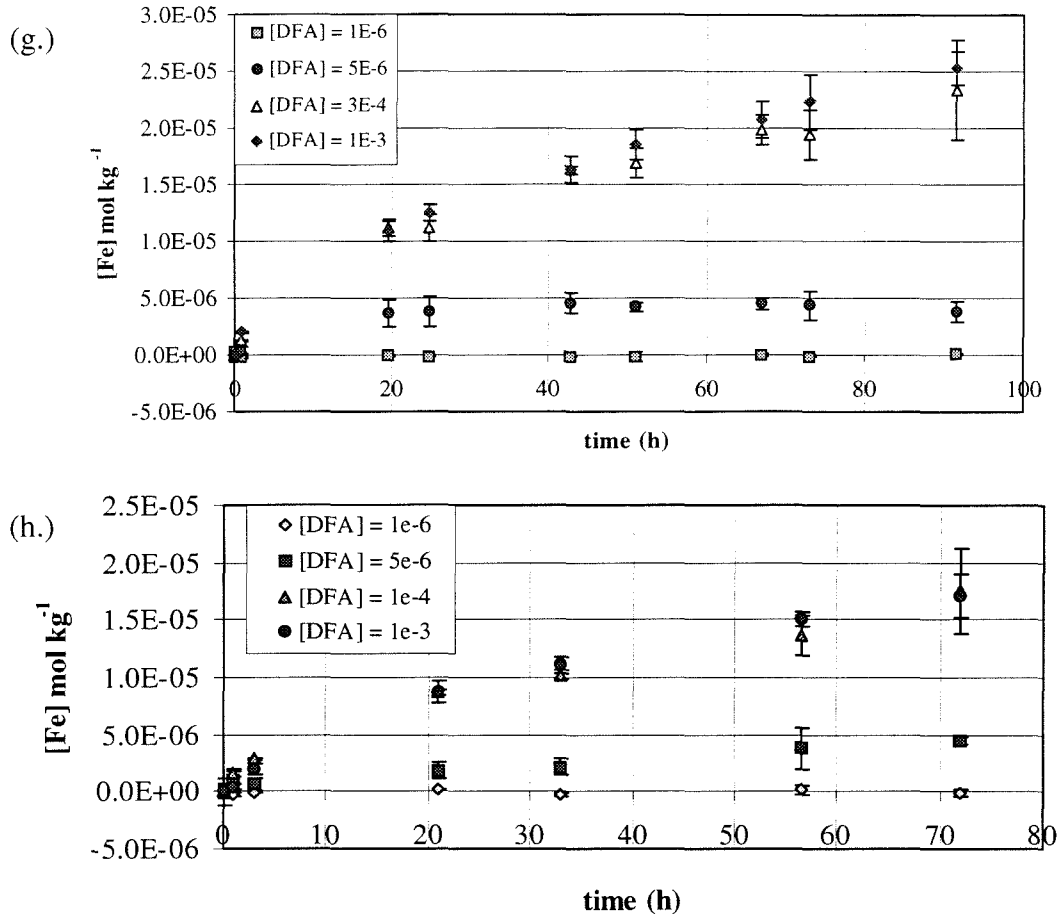
Figure 3 (II)

Dissolution of hematite at (g.) $p_aH = 8$ and (h.) $p_aH = 9$.
$[DFA]_0 = 10^{-6}$, 10^{-5}, 10^{-4}, and 10^{-3} mol kg^{-1}.

presence of these fines in the filtrate should be observed in the blank experiments. The

lack of fines in the filtrate is confirmed by the observation of negligible [Fe] in blank

dissolution experiments performed at the various p_aH's. The limit of accurate detection

by the ICPMS was between $1-10 \times 10^{-7}$ mol$_{Fe}$ kg$_{solution}^{-1}$, which was within the range of

the Fe sampled from the reaction vessel prior to the addition of DFA (defined as time =

0.)

The morphology of the dissolution curves for each p_aH value studied indicates a non-constant rate over the time scale of these experiments. In the near time regime (t < 24 h) the rate of dissolution is greater than in the far time regime (t > 24 h), resulting in a convex dissolution curve. Other investigators have generated dissolution curves with this morphology (e.g., Eisenlauer and Matijevic, 1980; Holmén and Casey, 1996; Ludwig et al., 1995; and Zinder et al., 1986.) The morphology indicates that the rate of dissolution is not a constant with respect to time, as would be expected from the pseudo-zero[th] order process defined by equation 5 in chapter 3, and, in the DFA-hematite system, points to two hypotheses concerning its origin.

4.2.2 The Presence of Fine Particles

First, the existence of the fine fraction in the pre-dissolved hematite and absence in the post-dissolved hematite samples (see chapter 3, figure 1) suggest that the fine fraction might preferentially dissolve at a greater rate than the larger size fraction.

The total dissolution reaction of the small particle size fraction can be written as follows:

$$\equiv Fe - OH_{small\ particle} + DFA \rightarrow \equiv Fe - DFA_{small\ particle} + OH^-$$
$$\equiv Fe - DFA_{small\ particle} + H_2O \rightarrow FA + \equiv Fe - OH_{small\ particle} + H^+ \qquad (1)$$
$$R_2 = k_2[\equiv Fe - DFA]_{small\ particle}$$
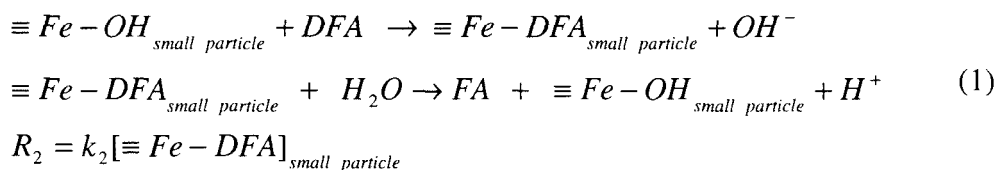
where the $[\equiv Fe-H_iDFA]$ small particle represents the adsorbed DFA molecule and the protonation state of the DFA molecule has been left off for convenience and k_2 is valid for a particular p_aH and [DFA]. In this case, DFA is in excess over the $[\equiv Fe-H_iDFA]$ small

particle and the concentration of the fine fraction goes to zero over the course of the reaction. It is assumed that the reaction is surface mediated, and that the rate is dependent on the adsorbed ligand concentration. Thus the rate of disappearance of the [$\equiv$Fe-H$_i$DFA]$_{small\ particle}$ goes as

$$R_2 = \frac{-d[\equiv Fe-H_i\text{-}DFA^{(i-3)}]_{small\ particle}}{dt} = \sum_i k'_{2i}[\equiv Fe-H_i\text{-}DFA^{(i-3)}]_{small\ particle} \qquad (2)$$

where the protonation states are explicitly included and

$$k'_{2i} = [H^+]^n_{surface}\, k_{2i} \qquad (3)$$

In this case, n is the order of the reaction with respect to the concentration of adsorbed protons (see equation 4, Chapter 1) (Furrer and Stumm, 1983). At a given [$\equiv$Fe-H$_i$DFA], p$_a$H, and [DFA] it can be assumed that the surface configuration of the DFA species is well defined, in the sense that the distribution of variously configured dissolution-active surface species is fixed. Moreover, this distribution is independent of the total number of surface sites in the fine fraction: as the concentration of the fine fraction goes to zero over the course of the dissolution reaction, the site distribution remains constant. Thus, equation 2 reduces to

$$R_2 = \frac{-d[\equiv Fe-H_i\text{-}DFA^{(i-3)}]_{small\ particle}}{dt} = k'_2[\equiv Fe-DFA]_{small\ particle} \qquad (4)$$

4.2.3 High and Low Energy Sites

The second hypothesis (e.g., Holmén and Casey, 1996) invokes the existence of two pools of reactive sites, a high energy site and a low energy site, where the energy refers to the energetics of the kinetic process; i.e., a low energy site is a site for which the activation energy for the dissolution reaction with DFA is low relative to the high energy site. Thus, the rate constant of the low energy site exceeds that of the high energy site. It is assumed that the concentration of this site is limited and is depleted as the reaction progresses. The rate of disappearance of the low energy site can be written as in equation 4:

$$R_3 = \frac{-d[\equiv Fe - H_i\text{-}DFA^{(i\text{-}3)}]_{low\ energy}}{dt} = k_3'[\equiv Fe - DFA]_{low\ energy} \tag{5}$$

where the primed k again indicates that the system is at a set p_aH, with the distribution of surface sites remaining constant over the course of the reaction, and the *[≡Fe-DFA]* represents the set of all surface species at the given p_aH.

4.2.4 Large Particle Dissolution

As set forth in equation 5, chapter 3, the dissolution of the large particle fraction is assumed to proceed via a pseudo-zero[th] order surface-mediated dissolution process. This assumption relies on the fact that the concentration of surface sites remains relatively constant over the course of the reaction, that the concentration of DFA remains in excess relative to the concentration of surface sites and therefore relatively constant over the course of the reaction. The assumption also relies on the constancy of the configuration

and distribution of dissolution-active surface sites remain constant over the course of the reaction. Given these assumptions, the rate of reaction is expected to be constant.

4.2.5 Mathematical Expression of the Three-Site Kinetic Model

Dividing the dissolution reaction into three reactions results in the definition of three independent dissolution reactions. These three dissolution processes are assumed to occur in parallel, with no interdependence, and can be treated independently. If it is assumed that the form and distribution of the dissolution-active adsorbed DFA remain constant over the entire extent of the small particle and the low energy reactions, then equations (1), (4) and (5) may easily be integrated; i.e., the variable of integration, $\equiv Fe\text{-}DFA$, is well defined. It is also recognized that there is a one-to-one correspondence between the appearance of a molecule of FA in solution and the disappearance of a surface group. Thus, the following set of equations are arrived at:

$$
\begin{aligned}
[Fe]_1 &= k't \\
[Fe]_2 &= [\equiv Fe - DFA]_0^{low\ energy}(1 - e^{-k_2't}) \\
[Fe]_3 &= [\equiv Fe - DFA]_0^{small\ particle}(1 - e^{-k_3't}) \\
[Fe]_{tot} &= k't + [\equiv Fe - DFA]_0^{low\ energy}(1 - e^{-k_2't}) + [\equiv Fe - DFA]_0^{small\ particle}(1 - e^{-k_3't})
\end{aligned}
\tag{6}
$$

where $[\equiv Fe - DFA]_0^i$ represents the initial concentrations of the surface species in the low energy and small particle pools; and $[Fe]_1$, $[Fe]_2$, $[Fe]_3$ correspond to the contributions of the large particle, low energy, and small particle sites respectively to the total $[Fe]$ observed in the dissolution reaction.

In order to test the validity of the kinetic model presented in equation 6, one further experiment was performed. Hematite particles that had already been utilized in DFA dissolution experiments were re-cleaned by the same cleaning procedure developed for newly synthesized particles. These particles were then dissolved in the presence of 10^{-4} m DFA over a range of p_aH's. Figure 4 shows the results from these experiments. Figure 1 in chapter 3 shows that the large particles have not changed size significantly as a result of the initial dissolution experiments. Thus, comparison of these data with the data from the dissolution of the freshly prepared particles is valid.

Three observations are immediately apparent. First, the nonlinear nature of the dissolution curve is preserved: the rate of dissolution decreases monotonically with time. However, the total amount of FA in solution at 23 h is about half as much as that observed in the experiment that used freshly-prepared hematite, which may be accounted for by the absence of the small particles in this preparation. Secondly, the $[FA]_{solution}$ must be normalized by the concentration of surface sites, a quantity not measured experimentally. Finally, the dependence of the dissolution on p_aH is not resolvable in the data presented in figure 4. These three observations suggest that: (i) the low energy sites reappear upon cleaning of the hematite particles, and have a dissolution time scale on the order of 8 h; (ii) the lack of the fine fraction results in a decreased rate of dissolution on the 24 h time scale, with the overall rate of the dissolution of the large particles being on the order of one half of the rate of dissolution observed in the system that includes both fines and large particles, a phenomenon that may be accounted for by a decrease in the per mass surface site concentration.
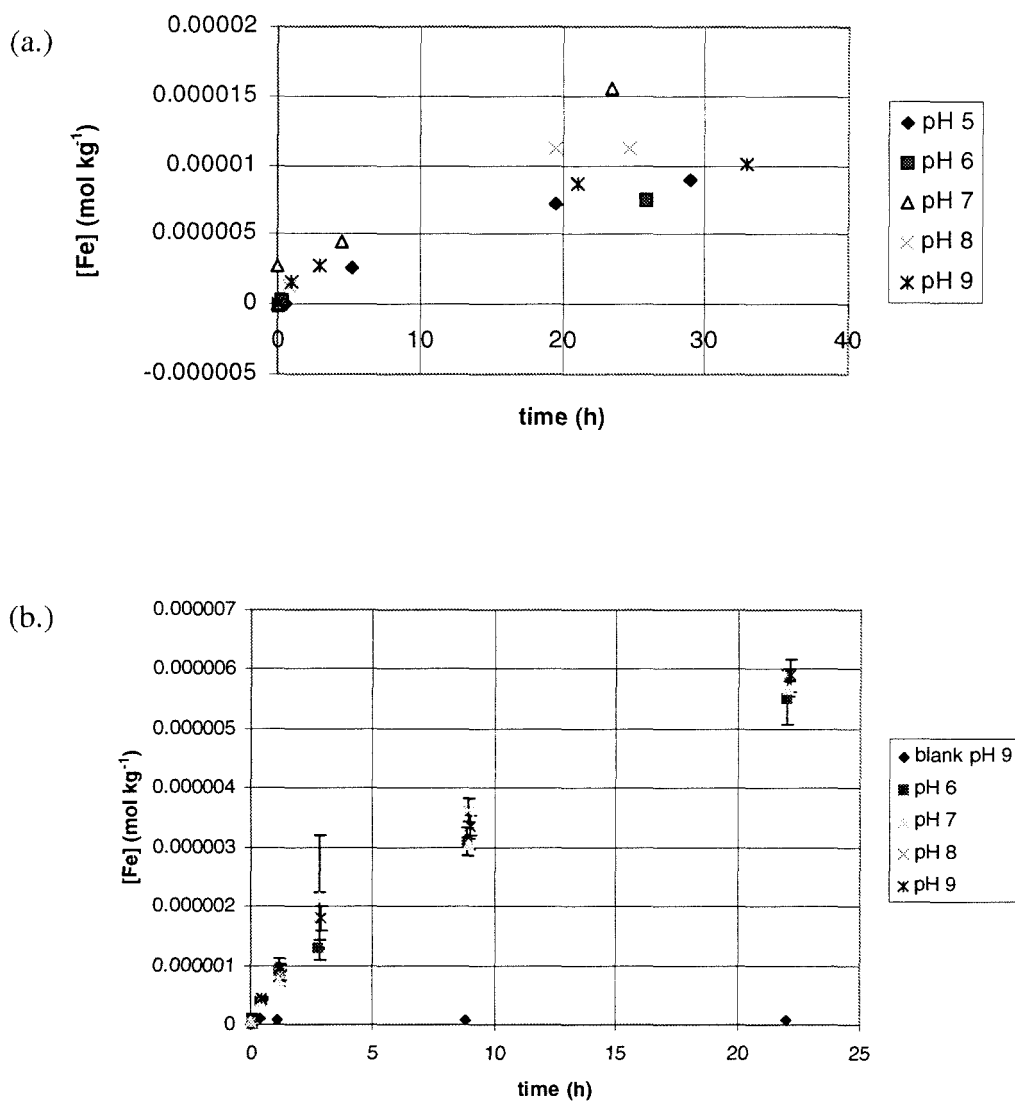
Figure 4

Dissolution of hematite; [hematite] = 1.00 g kg^{-1}, [DFA]$_0$ = 10^{-4} m. (a.)

Freshly prepared particles; (b.) re-cleaned particles: the particles used in

(b.) had been dissolved once in the presence of DFA and re-cleaned.

4.2.6 Determination of Optimal Model Parameters for Re-cleaned Particles

To extract the parameters of the kinetic model described in equation 6, the data set depicted in figure 4 will be modeled with the following equation:

$$[Fe] = [FA] = C^0_{low\ energy}(1 - e^{-k'_3 t}) + k't \tag{7}$$

The results of the model are shown in figure 5, with the parameters used to generate the line listed in table 1.
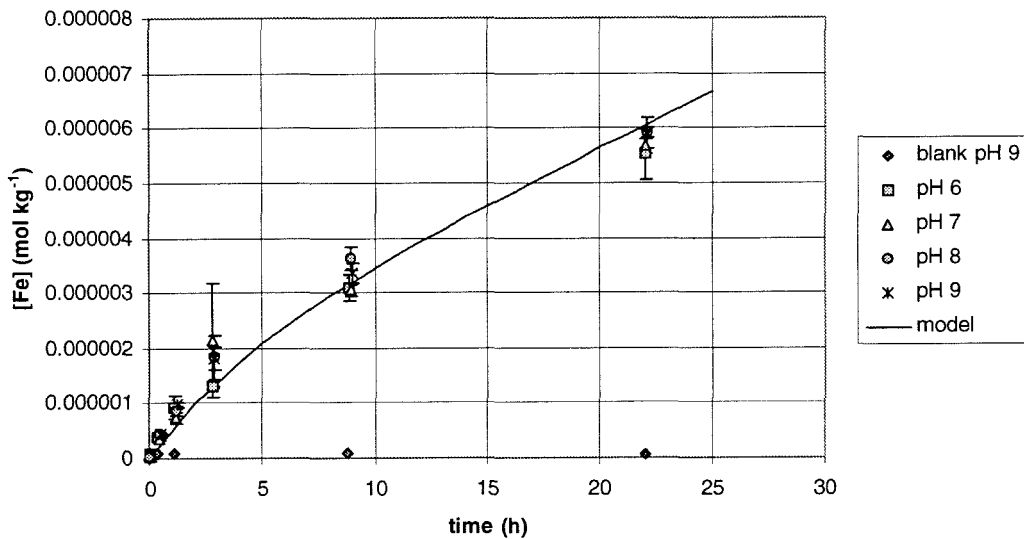
Figure 5

Dissolution of re-cleaned hematite; $[DFA]_0 = 10^{-4}$ m, [hematite] = 1.00 g kg^{-1}. Parameters used to generated model line were determined from the long time linear assumption and the short time exponential assumption. C_0 was generated by residual error minimization.

Table 1

List of parameters used to generate the model line in figure 5

$C^0_{low\ energy}$	1.58×10^{-6} mole surface sites (g solid)$^{-1}$
k_3'	$0.220\ m\ \mathrm{h}^{-1} \pm 0.067$
k'	$2.04 \times 10^{-7}\ \mathrm{h}^{-1} \pm 1.25 \times 10^{-8}$
mean fitting error:	6.96201×10^{-7}

$\sigma = (1/(n-p)\Sigma_i(C_i^{obs} - C_i^{pred})^2)^{1/2}$

where n = number of observations (6)

and p = number of parameters (3)

The parameters listed in table 1 were determined in the following manner. At t > 8 h, it assumed that the linear term in equation 7 dominates and that the parameter k' can be generated from fitting a line through the last three points of the data set. Performing this operation and averaging over the four data sets generates the k' in table 1. At t < 8 h the exponential term dominates and a line can be drawn through a plot of log [Fe] vs. time; the slope of this line is an estimate of k₃' for each p_aH value. Averaging over the four data sets in this manner generates the value reported in table 1. The value of C₀ is chosen such that σ is minimized, keeping the values of k' and k₃' fixed; note that this value agrees with the value of 3.98×10^{-5} mole g^{-1} determined from F$^-$ adsorption.

Comparing the model to the data, it can be seen that the model fits the observed concentration relatively well over the time scale of the experiment. If a parameter-fitting approach is taken that only seeks to minimize the residual error, then we arrive at the

parameters listed in table 2, the results shown in figure 6. In this approach, the parameter values are chosen such that the total error is minimized, with no constraints on the values. A sensitivity analysis, shown in figure 7, indicates that the residual error is most sensitive to k' and C_0. This result is expected because of the exponential dependence of the sensitivity on $-k_3'$. The error due to $\Delta k'$ depends linearly on k'.
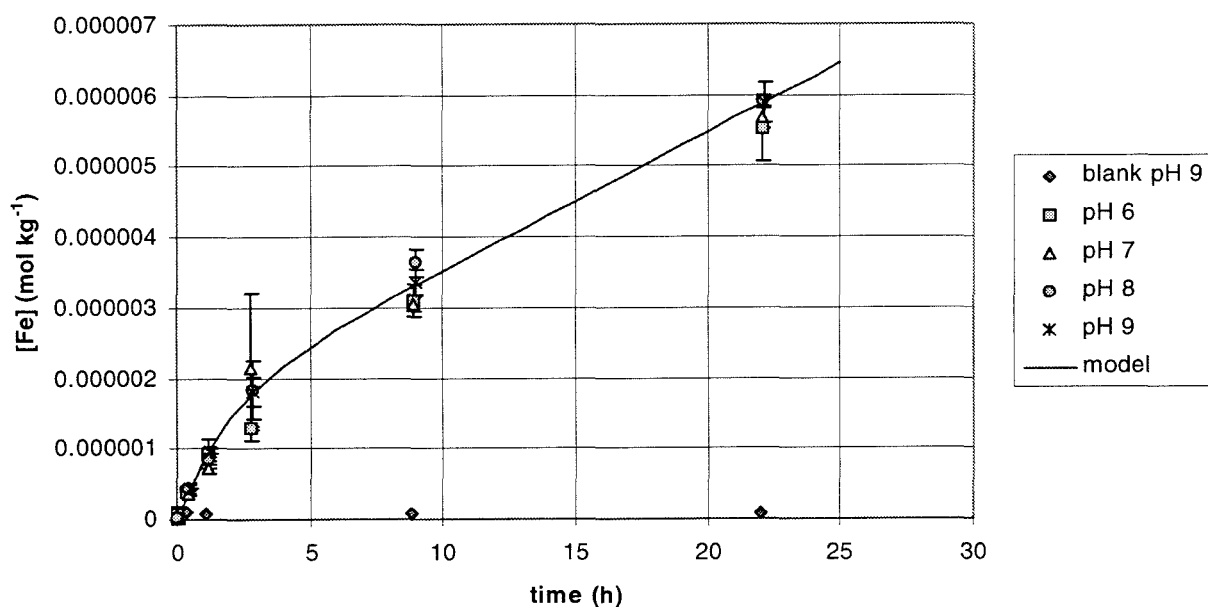
Figure 6

Dissolution of re-cleaned hematite. [DFA] = 10^{-4} m; [hematite] = 1.00 g kg^{-1}; line generated from optimized parameters.

Table 2

List of parameters used to generate the model line in figure 6

$C^0_{low\ energy}$	1.58×10^{-6} mole surface sites (g solid)$^{-1}$
k_3'	0.525 h^{-1}
k'	1.95×10^{-7} h^{-1}
mean fitting error	2.65133×10^{-7}

$$\sigma = (1/(n\text{-}p)\Sigma_i(C_i^{obs} - C_i^{pred})^2)^{1/2}$$

where n = number of observations (6)

and   p = number of parameters (3)
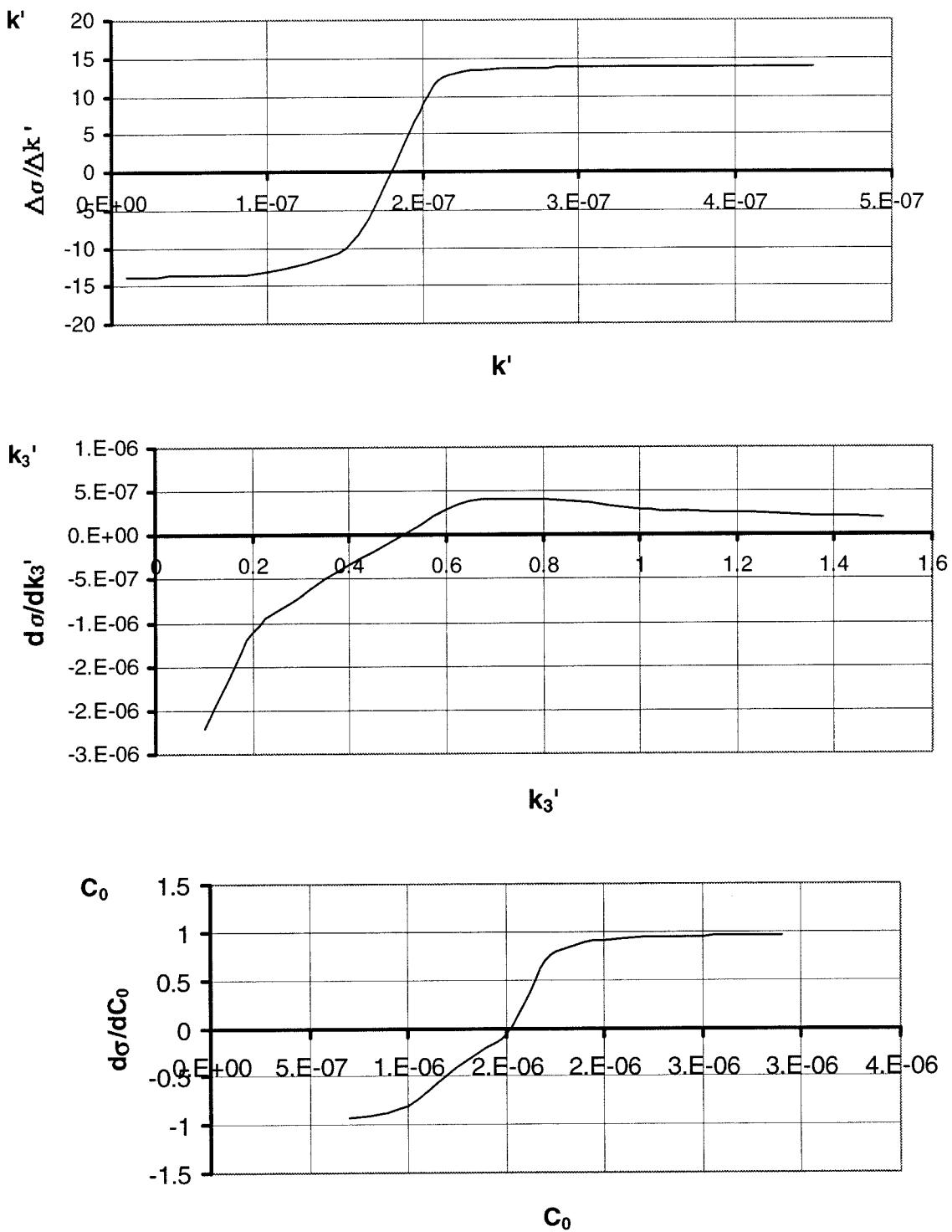
Figure 7

Sensitivity analysis of the three parameters introduced in equation 12.

4.2.7 Application of Optimized Parameters to Newly Synthesized Particles

The parameters from table 2 are applied to the dissolution experiments of the freshly prepared particles; i.e., it is assumed that $C^0_{low\ energy}$ and k_3' remain constant for all the experiments. By fixing $C^0_{low\ energy}$ and k_3' the parameters for the dissolution of the small particle fraction found in equations 6 are generated by a least squares fitting algorithm. The data are modeled in the following manner: (1) The low energy parameters are kept constant for all the dissolution data, and are derived from the data in figure 6; (2) The slope and intercept of the linear long time regime is determined for each data set. For experiments wherein [DFA] remains relatively constant over the whole course of the reaction, i.e., for reactions that do not go to completion, the slope is taken as the pseudo-zero[th] order rate constant. The intercept gives the total concentration of low energy and small particle sites. Subtracting the total low energy sites (kept constant for all data sets) from the total generates the total number of small particle sites. In the cases in which the reaction goes to completion over the examined time scale, the large particle term is treated as resulting from a pseudo-first order process, giving the total reaction:

$$[Fe]_{tot} = [\equiv Fe-DFA]_0^{large\ particle}(1-e^{-k't}) +$$
$$[\equiv Fe-DFA]_0^{low\ energy}(1-e^{-k_2't}) + [\equiv Fe-DFA]_0^{small\ particle}(1-e^{-k_3't}) \qquad (8)$$

where the first term on the right-hand side captures the dissolution of the large particle fraction. For systems in which [DFA]$_{solution}$ remains relatively constant, the reaction can be written as

$$[Fe]_{tot} = k''t + [\equiv Fe-DFA]_0^{low\ energy}(1-e^{-k_2't}) + [\equiv Fe-DFA]_0^{small\ particle}(1-e^{-k_3't}) \qquad (9)$$

In the case where $[DFA]_{solution}$ is not in excess with respect to surface sites during the course of the reaction, as expressed in equation 8, the concentration of dissolution-active surface sites is in excess relative to $[DFA]_{solution}$ throughout the reaction, therefore $[DFA]_{solution} \rightarrow 0$ as the reaction goes to completion.

(3) The parameter k_2' is adjusted to minimize the total error of the model. Figures 8 through 12 show the results of the above process.
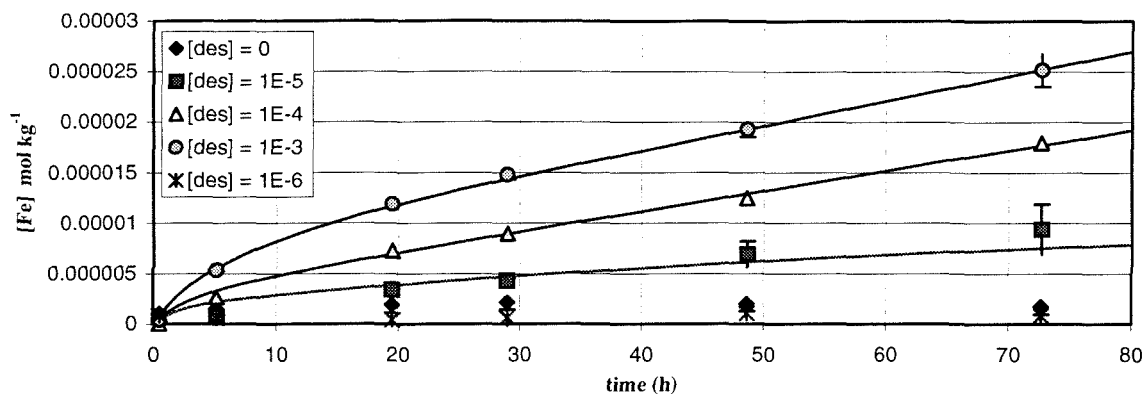
p_aH 5 Model

$[DFA]_0 = 10^{-5}$ m

$[FA] = C_{0,\text{low energy}} (1 - \exp(-k_{0,\text{low energy}} t)) + C_{0,\text{small particle}} (1 - \exp(-k_{0,\text{small particle}} t)) +$
$\quad C_{0,\text{ large particle}} (1 - \exp(-k't))$

$C_{0,\text{low energy}}$	=	1.58×10^{-6} m
$k_{\text{low energy}}$	=	0.525 h^{-1}
$C_{0,\text{small particle}}$	=	2.50×10^{-7} m
$k_{\text{small particle}}$	=	0.127 h^{-1}
$C_{0,\text{large particle}}$	=	1.00×10^{-5}
k'	=	1.15×10^{-2} h^{-1}
Error	=	1.55809×10^{-6}

$[DFA]_0 = 10^{-4}$ m

$[FA] = [FA] = C_{0,\text{low energy}} (1 - \exp(-k_{\text{low energy}} t)) + C_{0,\text{small particle}} (1 - \exp(-k_{\text{small particle}} t)) + k't$

$C_{0,\text{low energy}}$	=	1.58×10^{-6} m
$k_{\text{low energy}}$	=	0.525 h^{-1}
$C_{0,\text{small particle}}$	=	1.57×10^{-6} m
$k_{\text{small particle}}$	=	0.127 h^{-1}
k'	=	2.00×10^{-7} $m\,h^{-1}$
Error	=	5.84255×10^{-7}

$[DFA]_0 = 10^{-3}$ m

$[FA] = [FA] = C_{0,\text{low energy}} (1 - \exp(-k_{\text{low energy}} t)) + C_{0,\text{small particle}} (1 - \exp(-k_{\text{small particle}} t)) + k't$

$C_{0,\text{low energy}}$	=	1.58×10^{-6} m
$k_{\text{low energy}}$	=	0.525 h^{-1}
$C_{0,\text{small particle}}$	=	5.78×10^{-6} m
$k_{\text{small particle}}$	=	0.127 $m\,h^{-1}$
k'	=	2.45×10^{-7} $m\,h^{-1}$
Error	=	4.00631×10^{-7}

Figure 8

Model fit to the data for dissolution of freshly prepared hematite at $p_aH = 5$. Parameters are generated as described in the text.

p$_a$H 6 Model

$[DFA]_0 = 6 \times 10^{-6} \; m$

$[FA] = C_{0,low \; energy} (1 - \exp(-k_{0,low \; energy} \; t)) + C_{0,small \; particle} (1 - \exp(-k_{0,small \; particle} \; t)) + C_{0,slarge \; particle} (1 - \exp(-k't))$

$C_{0,low \; energy}$	=	$1.58 \times 10^{-6} \; m$
$k_{low \; energy}$	=	$0.525 \; h^{-1}$
$C_{0,small \; particle}$	=	$1.50 \times 10^{-6} \; m$
$k_{small \; particle}$	=	$0.095 \; h^{-1}$
$C_{0,large \; particle}$	=	$6.00 \times 10^{-7} \; m$
k'	=	$9.28 \times 10^{-3} \; h^{-1}$
Error	=	1.21994×10^{-6}

$[DFA]_0 = 10^{-4} \; m$

$[FA] = [FA] = C_{0,low \; energy} (1 - \exp(-k_{low \; energy} \; t)) + C_{0,small \; particle} (1 - \exp(-k_{small \; particle} \; t)) + k't$

$C_{0,low \; energy}$	=	$1.58 \times 10^{-6} \; m$
$k_{low \; energy}$	=	$0.525 \; h^{-1}$
$C_{0,small \; particle}$	=	$2.83 \times 10^{-6} \; m$
$k_{small \; particle}$	=	$0.095 \; h^{-1}$
k'	=	$1.30 \times 10^{-7} \; m \, h^{-1}$
Error	=	4.98598×10^{-7}

$[DFA]_0 = 10^{-3} \; m$

$[FA] = [FA] = C_{0,low \; energy} (1 - \exp(-k_{low \; energy} \; t)) + C_{0,small \; particle} (1 - \exp(-k_{small \; particle} \; t)) + k't$

$C_{0,low \; energy}$	=	$1.58 \times 10^{-6} \; m$
$k_{low \; energy}$	=	$0.525 \; h^{-1}$
$C_{0,small \; particle}$	=	$2.93 \times 10^{-6} \; m$
$k_{small \; particle}$	=	$0.095 \; h^{-1}$
k'	=	$2.29 \times 10^{-7} \; m \, h^{-1}$
Error	=	5.3577×10^{-7}

Figure 9

Model fit to the data for dissolution of freshly prepared hematite at p$_a$H = 6. Parameters are generated as described in the text.
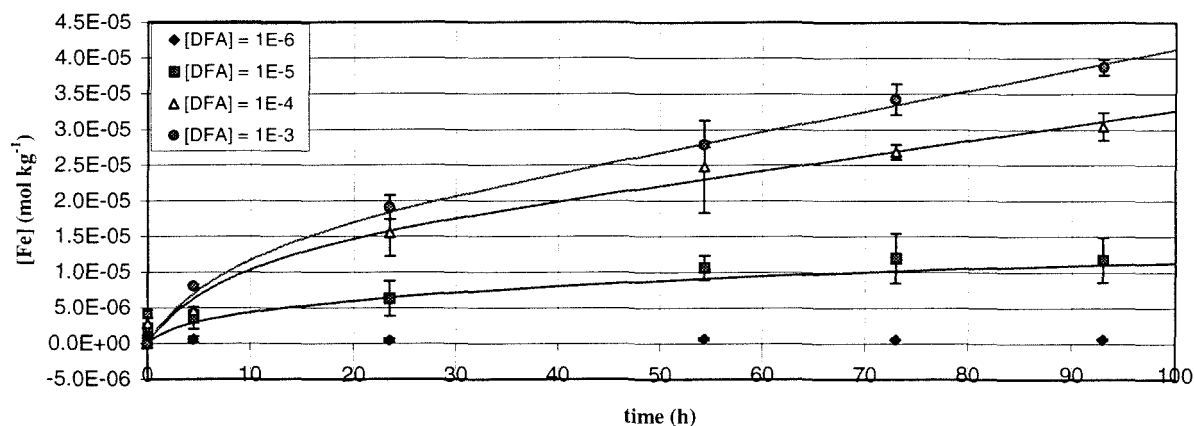
p_aH 7 Model

$[DFA]_0 = 10^{-5}\ m$

$[FA] = C_{0,\text{low energy}} (1 - \exp(-k_{\text{low energy}}\ t)) + C_{0,\text{small particle}} (1 - \exp(-k_{\text{small particle}}\ t)) +$
$\quad C_{0,\text{large particle}} (1 - \exp(-k't))$

$C_{0,\text{low energy}}$	=	$1.58 \times 10^{-6}\ m$
$k_{\text{low energy}}$	=	$0.525\ h^{-1}$
$C_{0,\text{small particle}}$	=	$5.00 \times 10^{-6}\ m$
$k_{\text{small particle}}$	=	$0.110\ h^{-1}$
$C_{0,\text{large particle}}$	=	1.00×10^{-5}
k'	=	$1.40 \times 10^{-2}\ h^{-1}$
Error	=	1.87694×10^{-6}

$[DFA]_0 = 10^{-4}\ m$

$[FA] = [FA] = C_{0,\text{low energy}} (1 - \exp(-k_{\text{low energy}}\ t)) + C_{0,\text{small particle}} (1 - \exp(-k_{\text{small particle}}\ t)) + k't$

$C_{0,\text{low energy}}$	=	$1.58 \times 10^{-6}\ m$
$k_{\text{low energy}}$	=	$0.525\ h^{-1}$
$C_{0,\text{small particle}}$	=	$9.92 \times 10^{-6}\ m$
$k_{\text{small particle}}$	=	$0.110\ h^{-1}$
k'	=	$2.11 \times 10^{-7}\ m\ h^{-1}$
Error	=	2.15743×10^{-6}

$[DFA]_0 = 10^{-3}\ m$

$[FA] = [FA] = C_{0,\text{low energy}} (1 - \exp(-k_{\text{low energy}}\ t)) + C_{0,\text{small particle}} (1 - \exp(-k_{\text{small particle}}\ t)) + k't$

$C_{0,\text{low energy}}$	=	$1.58 \times 10^{-6}\ m$
$k_{\text{low energy}}$	=	$0.525\ h^{-1}$
$C_{0,\text{small particle}}$	=	$1.08 \times 10^{-5}\ m$
$k_{\text{small particle}}$	=	$0.110\ h^{-1}$
k'	=	$2.88 \times 10^{-7}\ m\ h^{-1}$
Error	=	2.54313×10^{-6}

Figure 10

Model fit to the data for dissolution of freshly prepared hematite at $p_aH = 7$. Parameters are generated as described in the text.
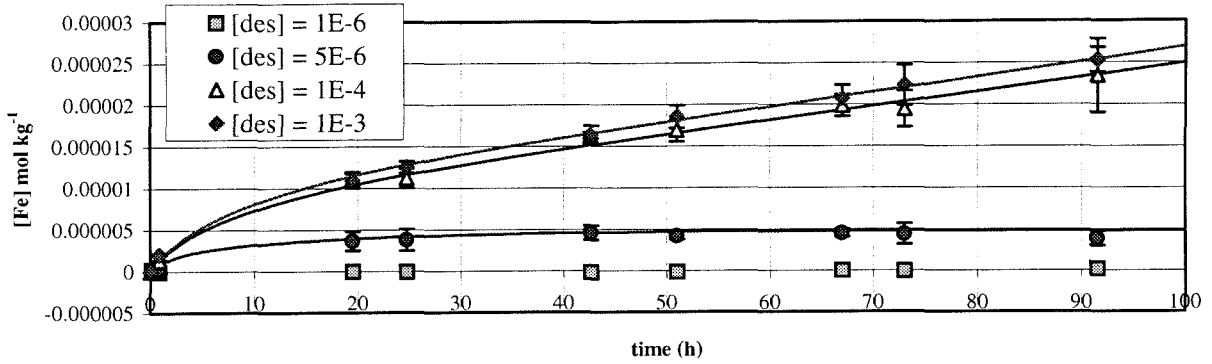
p_aH 8 Model

$[DFA]_0 = 5 \times 10^{-6} \, m$

$[FA] = C_{0,low\ energy} (1 - \exp(-k_{0,low\ energy}\ t)) + C_{0,small\ particle} (1 - \exp(-k_{0,small\ particle}\ t)) + C_{0,slarge\ particle} (1 - \exp(-k't))$

$C_{0,low\ energy}$	=	$1.58 \times 10^{-6} \, m$
$k_{low\ energy}$	=	$0.525 \, h^{-1}$
$C_{0,small\ particle}$	=	$1.24 \times 10^{-6} \, m$
$k_{small\ particle}$	=	$0.100 \, h^{-1}$
$C_{0,large\ particle}$	=	$2.00 \times 10^{-6} \, m$
k'	=	$5.21 \times 10^{-2} \, h^{-1}$
Error	=	4.70318×10^{-7}

$[DFA]_0 = 10^{-4} \, m$

$[FA] = [FA] = C_{0,low\ energy} (1 - \exp(-k_{low\ energy}\ t)) + C_{0,small\ particle} (1 - \exp(-k_{small\ particle}\ t)) + k't$

$C_{0,low\ energy}$	=	$1.58 \times 10^{-6} \, m$
$k_{low\ energy}$	=	$0.525 \, h^{-1}$
$C_{0,small\ particle}$	=	$6.36 \times 10^{-6} \, m$
$k_{small\ particle}$	=	$0.100 \, h^{-1}$
k'	=	$1.70 \times 10^{-7} \, m\,h^{-1}$
Error	=	8.91378×10^{-7}

$[DFA]_0 = 10^{-3} \, m$

$[FA] = [FA] = C_{0,low\ energy} (1 - \exp(-k_{low\ energy}\ t)) + C_{0,small\ particle} (1 - \exp(-k_{small\ particle}\ t)) + k't$

$C_{0,low\ energy}$	=	$1.75 \times 10^{-6} \, \text{mole} \, g_{solid}^{-1}$
$k_{low\ energy}$	=	$0.525 \, h^{-1}$
$C_{0,small\ particle}$	=	$7.45 \times 10^{-6} \, \text{mole} \, g_{solid}^{-1}$
$k_{small\ particle}$	=	$0.100 \, h^{-1}$
k'	=	$1.78 \times 10^{-7} \, m\,h^{-1}$
Error	=	6.53965×10^{-7}

Figure 11

Model fit to the data for dissolution of freshly prepared hematite at $p_aH = 8$. Parameters are generated as described in the text.

Legend:
◇ [DFA] = 1E-6
■ [DFA] = 1E-5
▲ [DFA] = 1E-4
● [DFA] = 1E-3

x-axis: time (h)
y-axis: [Fe] mol kg^{-1}
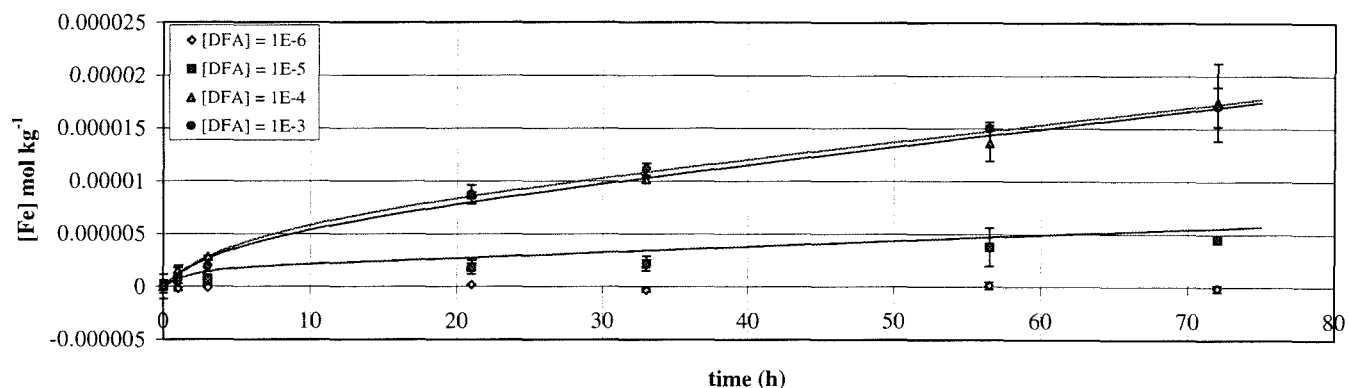
p$_a$H 9 Model

$[DFA]_0 = 10^{-5}$ m

$[FA] = C_{0,\text{low energy}} (1 - \exp(-k_{\text{low energy}} t)) + C_{0,\text{small particle}} (1 - \exp(-k_{\text{small particle}} t)) + k't$

$C_{0,\text{low energy}}$	=	1.58×10^{-6} m
$k_{\text{low energy}}$	=	0.525 h^{-1}
$C_{0,\text{small particle}}$	=	1.24×10^{-6} m
$k_{\text{small particle}}$	=	0.108 h^{-1}
k'	=	5.52×10^{-8} m h^{-1}
Error	=	1.39082×10^{-6}

$[DFA]_0 = 10^{-4}$ m

$[FA] = [FA] = C_{0,\text{low energy}} (1 - \exp(-k_{\text{low energy}} t)) + C_{0,\text{small particle}} (1 - \exp(-k_{\text{small particle}} t)) + k't$

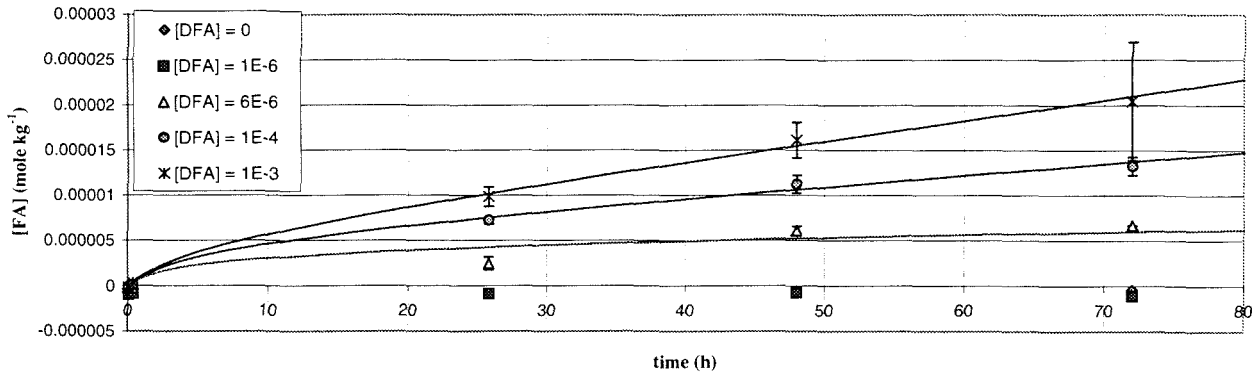|		
$C_{0,\text{low energy}}$	=	1.58×10^{-6} m
$k_{\text{low energy}}$	=	0.525 h^{-1}
$C_{0,\text{small particle}}$	=	3.17×10^{-6} m
$k_{\text{small particle}}$	=	0.108 h^{-1}
k'	=	1.70×10^{-7} m h^{-1}
Error	=	6.43975×10^{-7}

$[DFA]_0 = 10^{-3}$ m

$[FA] = [FA] = C_{0,\text{low energy}} (1 - \exp(-k_{\text{low energy}} t)) + C_{0,\text{small particle}} (1 - \exp(-k_{\text{small particle}} t)) + k't$

$C_{0,\text{low energy}}$	=	1.58×10^{-6} mole g$_{\text{solid}}^{-1}$
$k_{\text{low energy}}$	=	0.525 h^{-1}
$C_{0,\text{small particle}}$	=	3.95×10^{-6} mole g$_{\text{solid}}^{-1}$
$k_{\text{small particle}}$	=	0.108 h^{-1}
k'	=	1.63×10^{-7} m h^{-1}
Error	=	7.45375×10^{-7}

Figure 12

Model fit to the data for dissolution of freshly prepared hematite at p$_a$H = 9. Parameters are generated as described in the text.

As can be seen by the residual errors reported, the proposed model explains the observations with a high degree of accuracy. Although this correlation is not proof of mechanism, the experimental data show that the assumptions are reasonable. The results from the experiments with low initial concentrations of DFA suggest that a different experimental setup is required to resolve the steady state rates of dissolution. The low energy material seems to be sufficient to account for almost all the FA in solution for $[DFA]_0 \approx 10^{-6}$ m. These data imply that a flow-through system would be required for an estimate of the steady state dissolution rates for the large-particle fraction. In such a system the [DFA] remains constant and the solid is in excess, so once the low energy sites and the small particle fraction had dissolved, steady state dissolution would be observed. However, for greater $[DFA]_0$ in the batch experiments, the [DFA] remains in excess throughout the reaction, and the concentration of the surface sites on the large particle fraction remains relatively unchanged. Thus, the batch experiment can be assumed to be a good estimate of the steady state results, assuming that the accumulation of products does not interfere significantly with the dissolution reaction.

Table 3 lists the pseudo-zeroth order parameters from the dissolution experiments for the freshly prepared hematite particles. The data for the $p_aH = 6$ dissolution experiments have greater error than for the other data sets because of the sparseness of points. Therefore, if that datum is ignored in table 3, it the general trend of the data is that the rate remains relatively constant between $p_aH = 5$ and $p_aH = 7$, then falls off as the p_aH rises through pH $= 8$. However, figure 4 indicates that in the time region between $t = 0$

and t = 24 h, the data are noisy, indicating that there may be very little real difference among the data at various pH's in this time period.

Table 3

Pseudo-zero[th] order rate constants (mol kg^{-1} h^{-1}) for freshly prepared hematite; $5 \leq pH \leq 9$.

[DFA]$_0$	pH				
(m)	5	6	7	8	9
10^{-4}	2.00×10^{-7}	1.30×10^{-7}	2.11×10^{-7}	1.70×10^{-7}	1.70×10^{-7}
10^{-3}	2.45×10^{-7}	2.29×10^{-7}	2.88×10^{-7}	1.78×10^{-7}	1.63×10^{-7}

4.3 Pseudo-First Order Rates of Dissolution

The data derived from the adsorption isotherms presented in chapter 3 allow for an estimation of pseudo-first order rate constants for those experiments for which the reaction does not go to completion. To perform this operation the linear sections of the dissolution curves are isolated; i.e., the short time regime data is ignored. The first-order rate constant is derived from the zero[th]-order rate constant, which is the slope of the linear portion of the curve, by determining the adsorption density of DFA at each datum in the curve and dividing the zero[th]-order rate constant by the determined surface concentration value. For [DFA]$_0 \geq 10^{-4}$ m it is assumed that [DFA]$_{solution}$ remains approximately constant and in excess in the linear portion of the curve. For [DFA]$_0 < 10^{-4}$ m the region of the curve is taken for 10 h $< t <$ t$_{saturation}$, where t$_{saturation}$ is the time at which [FA] = [DFA]$_0$. It must be noted that the curves generated by these data include the effect of the

low energy sites and the small particle fraction, and therefore will not be truly representative of the pseudo-first order rate constant. The parameters from the adsorption isotherms of FA allow for the determination of the total [FA] produced in the dissolution reaction.

As discussed in chapter 3, it is assumed that the dissolution reaction can be described by the following rate equation:

$$R = \frac{d[Fe]}{dt} = \sum_i k_i [\equiv Fe - H_i\text{-}DFA^{(i-3)}]$$

(10)

or, at a particular pH:

$$R = \frac{d[Fe]}{dt} = k' [\equiv Fe - H_i\text{-}DFA^{(i-3)}]$$

(11)

$[\equiv Fe - H_i\text{-}DFA^{(i-3)}]$ has been measured directly for the $[DFA]_0$'s used in the dissolution experiments. Therefore, the pseudo-zero[th] order rate constants can be divided by this measured value, and the pseudo-first order constants then determined.

Since FA is adsorbed onto the surface, the measured $[FA]_{solution}$ underpredicts the actual rate of dissolution. The rate can be corrected by utilizing the isotherm from chapter 3, equation 11:

$$[FA]_{tot} = [FA]_{solution}(1 + K_p) \qquad (12)$$

Equation 12 implies that the rate should be multiplied by the factor $1 + K_p$. The results of

the determination of the pseudo-first order rate constant and the correction for the

adsorbed FA are shown in table 4 and figure 13. The rates are reported both on a g^{-1} and

a m^{-2} basis, and differ by the conversion factor of 23 m^2 of surface area per gram

hematite.
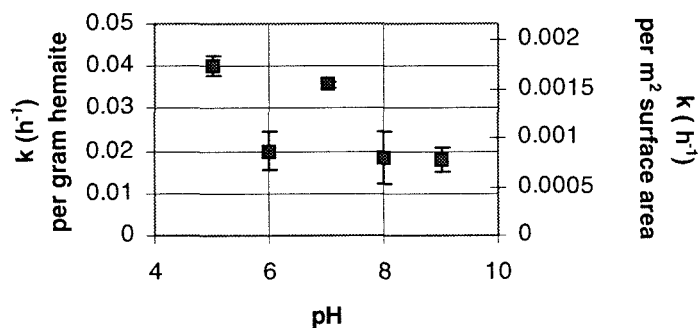
Figure 13

First order rate constants for the dissolution of hematite in the presence of DFA. The units on the y-axes are reported on a per gram hematite (l.h. side) and on a per m^2 surface area (r.h. side), and differ by a factor of 23 m^2 (g hematite)$^{-1}$.

Table 4

Pseudo-first-order rate constants for surface mediated dissolution of hematite. The reported values are corrected for adsorbed FA.

p_aH	k_{mean} (h^{-1})	S_d	k_{mean} (h^{-1})	S_d
	per gram hematite		per m^2 surface area	
5	4.03×10^{-2}	2.37×10^{-3}	1.75×10^{-3}	1.03×10^{-4}
6	2.00×10^{-2}	4.44×10^{-3}	8.67×10^{-4}	1.93×10^{-4}
7	3.58×10^{-2}	7.44×10^{-4}	1.56×10^{-3}	2.40×10^{-4}
8	1.82×10^{-2}	6.14×10^{-3}	7.92×10^{-4}	2.67×10^{-4}
9	1.79×10^{-2}	2.73×10^{-3}	7.80×10^{-4}	1.19×10^{-4}

4.4 Mass Balance

To achieve a mass balance for DFA_{tot} at each point in time, it is assumed that the system is in pseudo-equilibrium with respect to solution and surface speciation of the DFA and FA species. Thus, at each point in time on the dissolution curve, the solution and adsorption reactions are assumed to be fast relative to the dissolution reaction. To solve for speciation, the system of equations listed in table 1, chapter 3 must be augmented by the conservation and mass action equations governing the system.

4.5.1 Conservation Equations

$$[DFA]_{tot} \quad = \quad [FA(aq)] + \Sigma_i \left([H_i\text{-}DFA^{(i-3)}(aq)] + \right. \tag{13}$$

$$[\equiv Fe\text{-}H_i\text{-}DFA^{(i-3)}] + [\equiv FeOH\text{-}(Fe\text{-}H_i\text{-} DFA)^{(i-4)}])$$

$$[Fe]_{tot} \quad = \quad [FA(aq)] + \Sigma_i \, [\equiv FeOH\text{-}(Fe\text{-}H_i\text{-}DFA)^{(i-4)}] \tag{14}$$

$$[\equiv FeOH]_{tot} \quad = \quad [\equiv FeOH] + [\equiv FeOH_2^+] + [\equiv FeO^-] + \tag{15}$$

$$\Sigma_i \left([\equiv Fe\text{-}H_i\text{-}DFA^{(i-3)}] + \right.$$

$$[\equiv FeOH\text{-}(Fe\text{-}H_i\text{-}DFA)^{(i-4)}])$$

In this discussion it will be assumed that surface diffusion of nonspecifically adsorbed species is fast relative to the dissolution event, and thus will be ignored.

4.5.2 Mass Action Equations

For the adsorption of DFA onto the surface of the hematite, a Langmuir form for the adsorption isotherm is assumed.

$$[\equiv Fe\text{-}H_iDFA] \quad = \quad \Gamma_{max} K_i[H_iDFA]/(1 + K_i[H_iDFA]) \tag{16}$$

And, for FA, a linear partitioning is assumed.

$$[\equiv FeOH\text{-}(Fe\text{-}DFA)] \quad = \quad K_p[Fe\text{-}DFA] \tag{17}$$

The mass action equations for the solution species are generated from chapter 3, table 1.

So, if it is assumed that the rate of dissolution is proportional to the adsorbed surface species, then it follows that

$$R = \frac{d[Fe]}{dt} = \sum_i k_i[\equiv Fe - H_i\text{-}DFA^{(i-3)}] \tag{18}$$

where the sum is over all the protonation states of all the DFA surface. If the analysis is continued by choosing one of the protonation states for simplicity, then

$$\frac{d[Fe]}{dt} = k[\equiv Fe - DFA] = k\frac{\Gamma_{max}K'[DFA]}{1 + K'[DFA]} \tag{19}$$

for a given temperature, p_aH and pressure; and where [DFA] represents the distribution of protonation states of DFA at a particular p_aH.

From the conservation equations listed above, we have

$$[DFA] = [DFA]_{tot} - [Fe - DFA] - \frac{\Gamma_{max} K_1^{'} [DFA]}{1 + K_1^{'} [DFA]} - K_p [Fe - DFA] \tag{20}$$

If the above equation is solved for [DFA], then

$$[DFA] = \frac{1}{2K_1^{'}} \left[\begin{array}{l} -\left(1 - K_1^{'} DFA_{tot} + K_1^{'}[Fe - DFA] + K_p K_1^{'}[Fe - DFA] + K_1^{'} \Gamma_{max}\right) + \\ \left(\left(1 - K_1^{'} DFA_{tot} + K_1^{'}[Fe - DFA] + K_p K_1^{'}[Fe - DFA] + K_1^{'} \Gamma_{max}\right)^2 - \right)^{\frac{1}{2}} \\ \left(4K_1^{'}\left([Fe - DFA](1 + K_p) - [DFA]_{tot}\right)\right) \end{array} \right]$$

$$\equiv \zeta \tag{21}$$

and

$$\frac{d[Fe - DFA]}{dt} = k[\equiv Fe - DFA] = k\frac{\Gamma_{max} K_1^{'}[DFA]}{1 + K_1^{'}[DFA]} = k\frac{\Gamma_{max} K_1^{'} \zeta}{(1 + K_1^{'} \zeta)} \tag{22}$$

Using this calculation, the self-consistency of the various models can be checked with the data. Figure 14 shows the results of applying the adsorption isotherm parameters to equation 21. The intrinsic first-order surface rate constants are taken from table 3, and the maximum rate is chosen; i.e., the reported rate is that of maximum surface coverage of DFA.

Figures 15 through 19 show the solution and surface speciation as a function of time for the linear portion of the dissolution curve. The concentrations are calculated using the parameters reported above. Since the $p_a H$ of the system is constant, the speciation is

reported as total concentrations, with no differentiation among the protonation states of the particular species. Mass balance is achieved by definition, because the parameters are self-consistant. As expected, the [FA] increases at a constant rate that is proportional to the adsorbed DFA. The [DFA](aq) has been left off the graphs for $[DFA]_0 = 10^{-3}$ m because of the scale of the concentrations; [DFA] remains relatively constant over the course of the reaction.
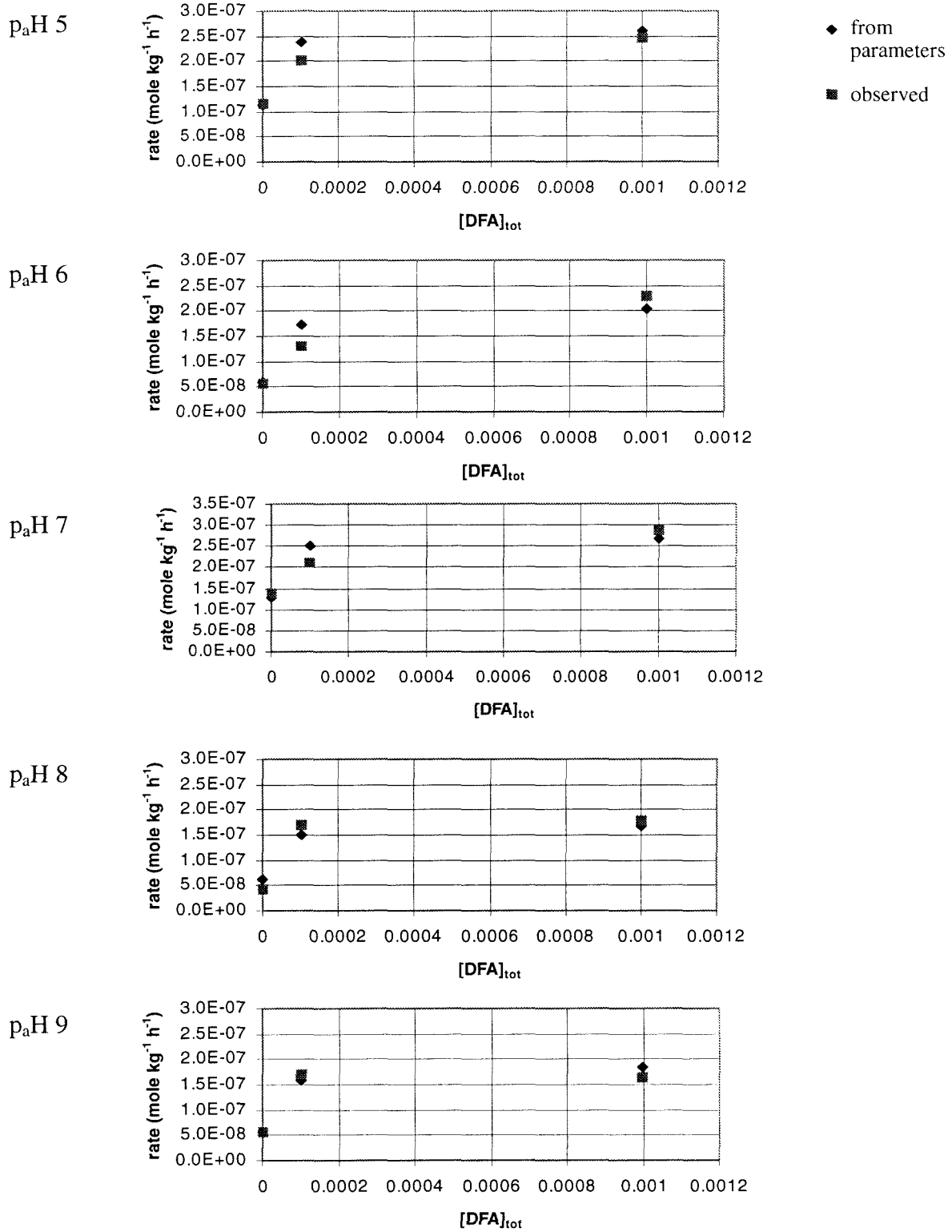
Figure 14

A comparison of observed zero[th]-order dissolution rates to those determined by adsorption parameters.

(a.)

(b.)

(c.)
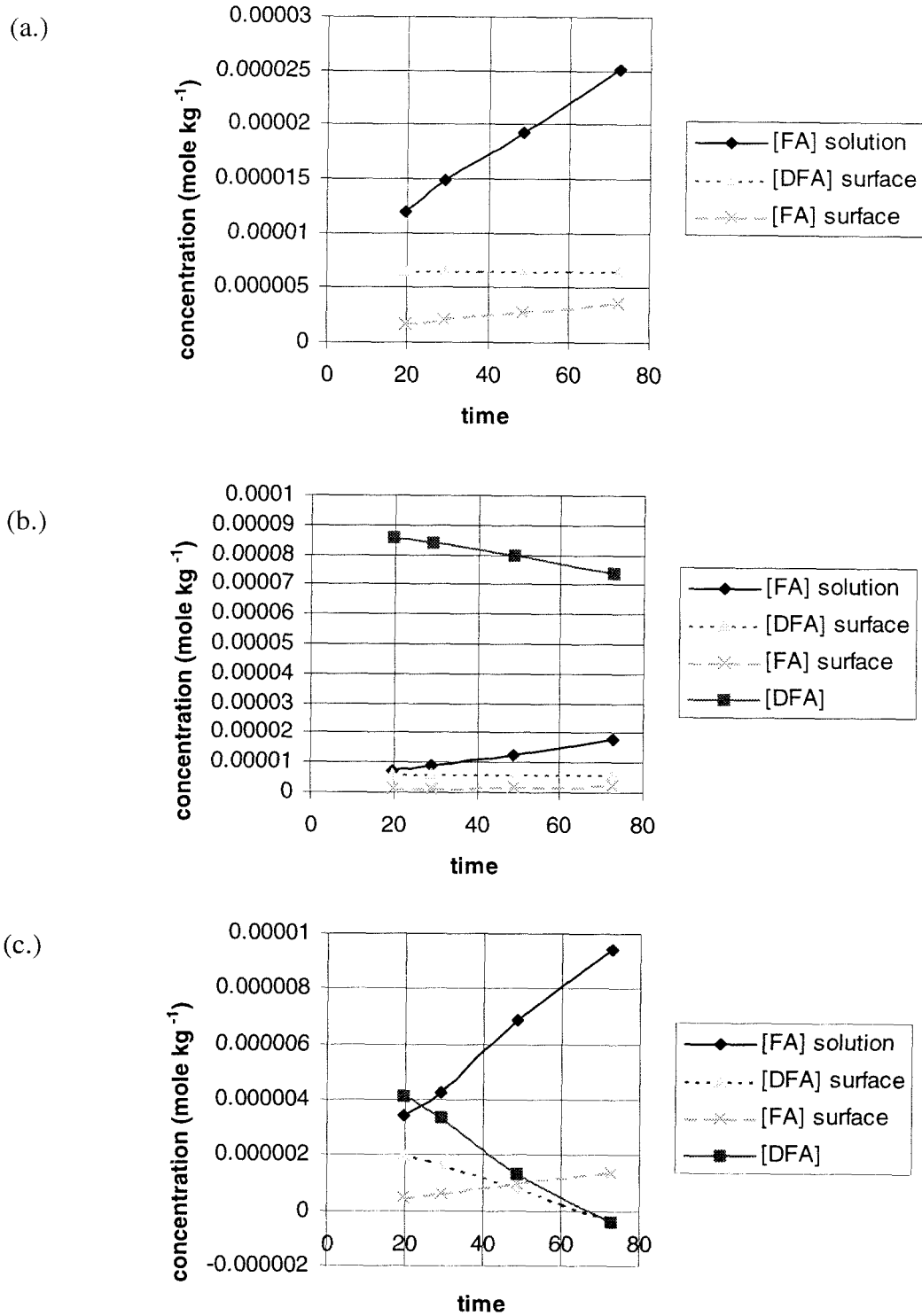
Figure 15

p_aH 5 speciation. (a.) $[DFA]_0 = 10^{-3}$ m; (b.) $[DFA]_0 = 10^{-4}$ m;

(c.) $[DFA]_0 = 10^{-5}$ m.

(a.)

(b.)

(c.)
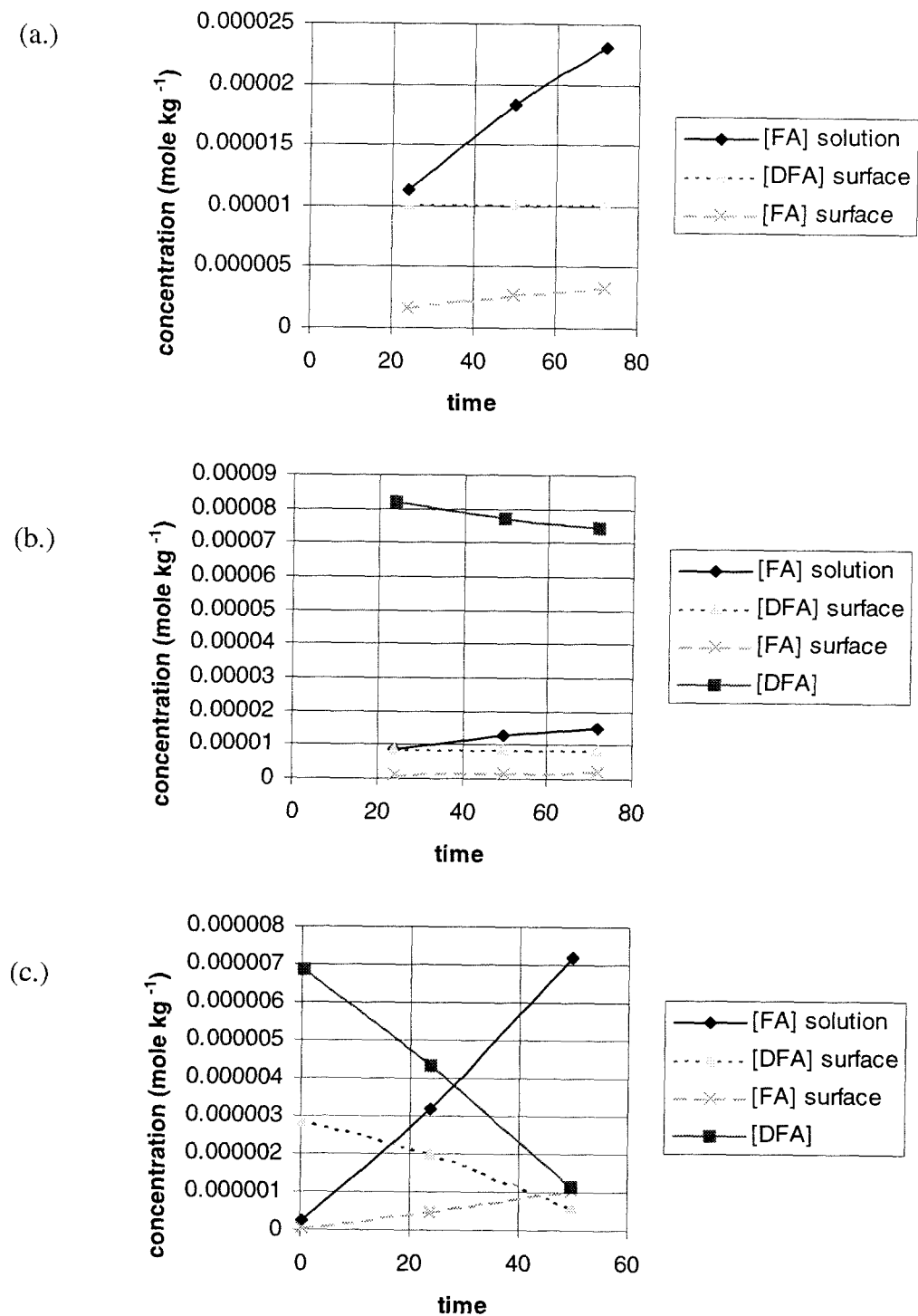
Figure 16

p_aH 6 speciation. (a.) $[DFA]_0 = 10^{-3}$ m; (b.) $[DFA]_0 = 10^{-4}$ m;

(c.) $[DFA]_0 = 10^{-5}$ m.

(a.)

(b.)

(c.)
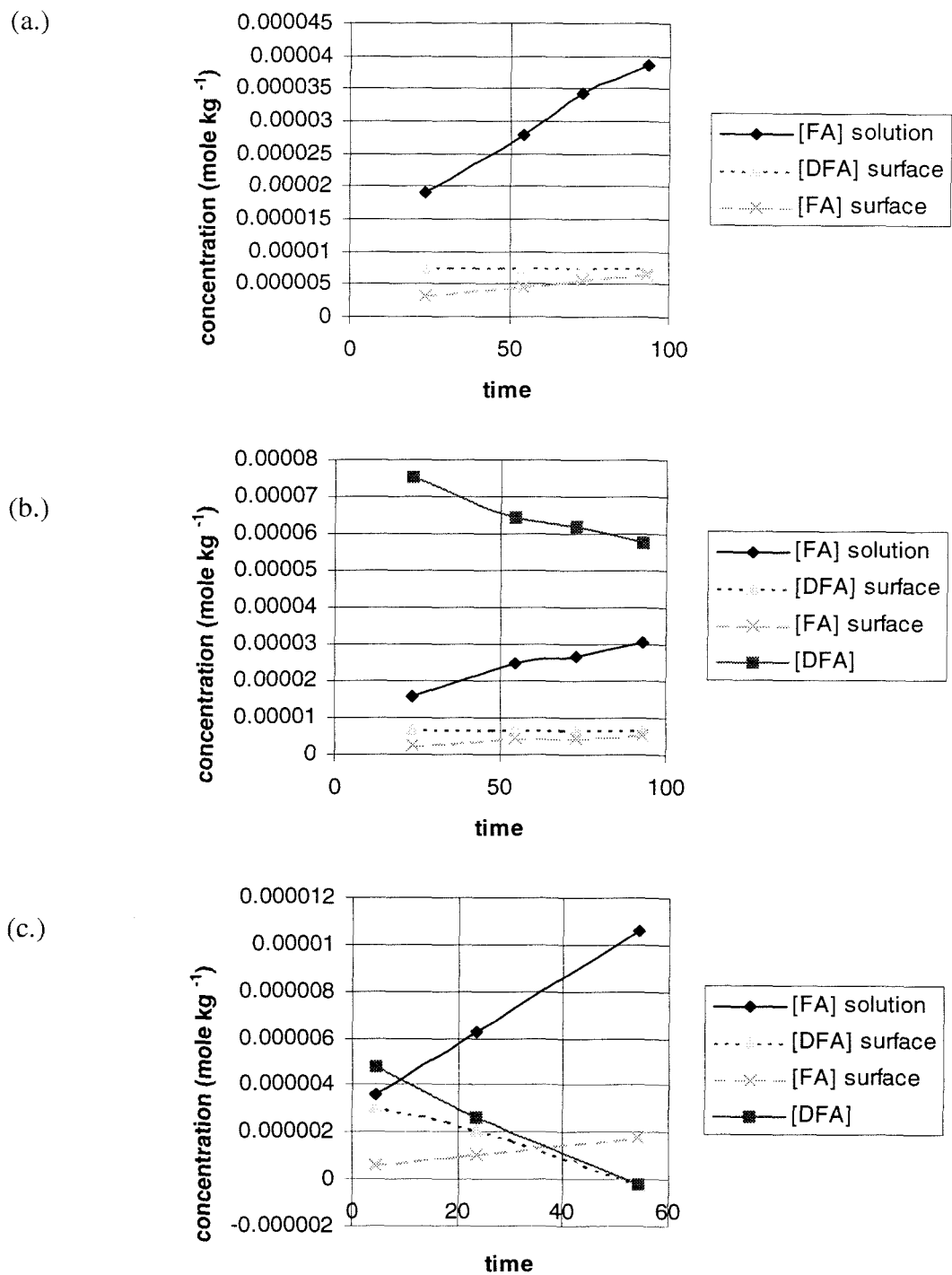
Figure 17

p_aH 7 speciation. (a.) $[DFA]_0 = 10^{-3}$ m; (b.) $[DFA]_0 = 10^{-4}$ m;
(c.) $[DFA]_0 = 10^{-5}$ m.

(a.)

(b.)

(c.)
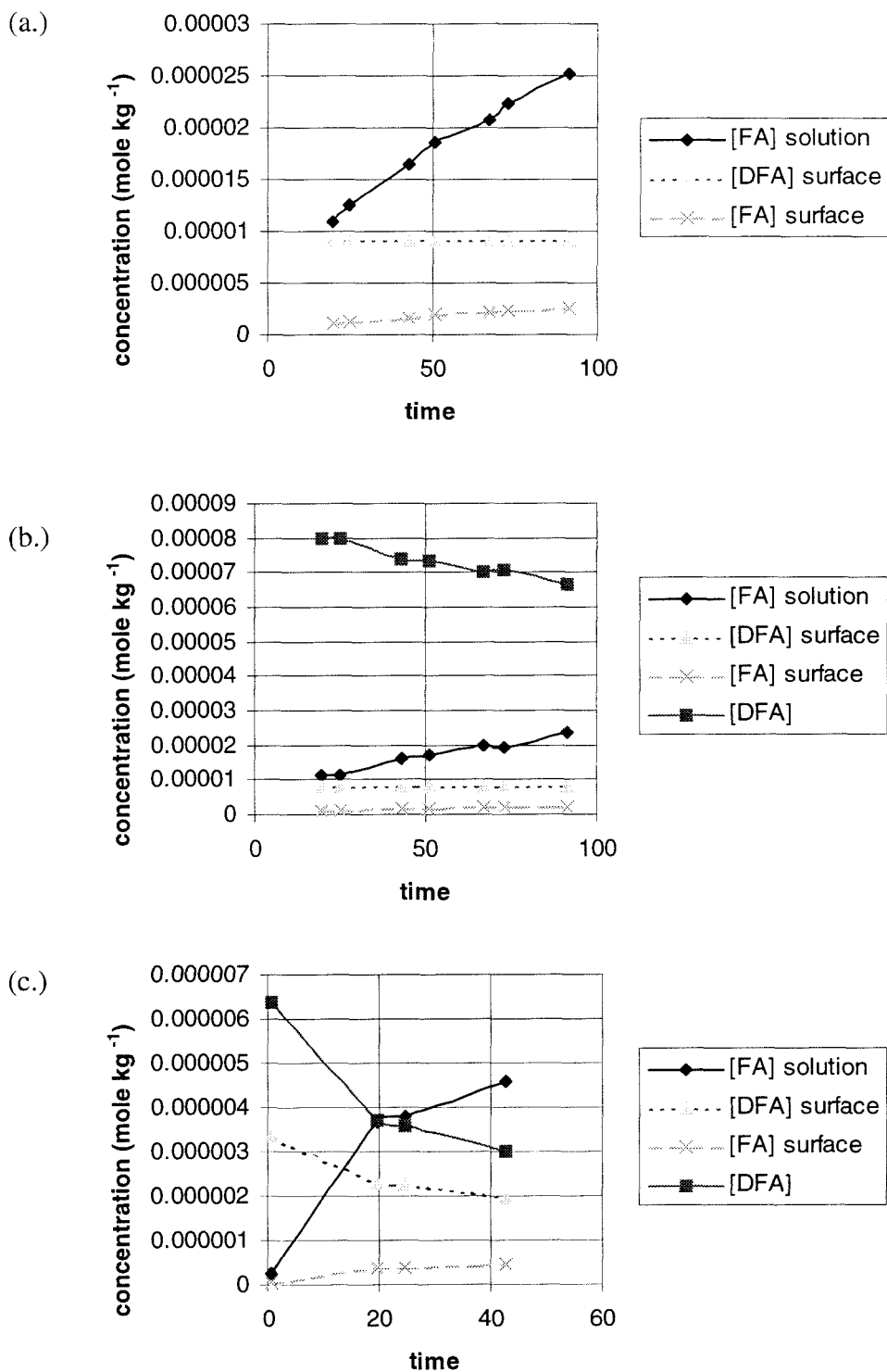
Figure 18

p_aH 8 speciation. (a.) $[DFA]_0 = 10^{-3}$ m; (b.) $[DFA]_0 = 10^{-4}$ m;

(c.) $[DFA]_0 = 10^{-5}$ m.

(a.)

(b.)

(c.)
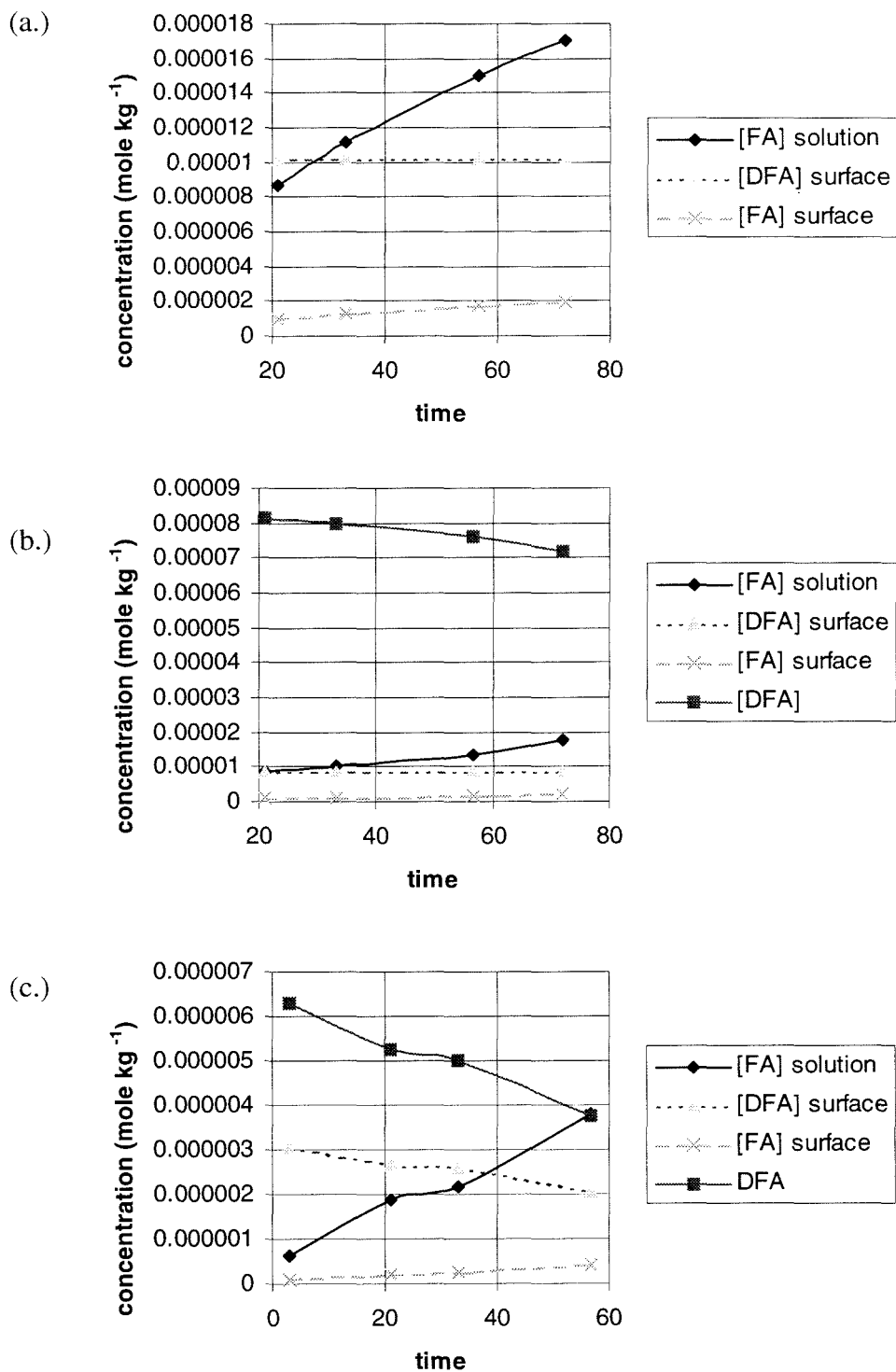
Figure 19

p_aH 9 speciation. (a.) $[DFA]_0 = 10^{-3}$ m; (b.) $[DFA]_0 = 10^{-4}$ m;
(c.) $[DFA]_0 = 10^{-5}$ m.

4.6 Effect of Ionic Strength

The effect of the concentration of electrolyte on the dissolution has the potential to take a number of forms. The ionic strength of the medium (I) will affect the equilibrium concentration of aqueous and surface species by altering the electrostatic correction to the activity coefficient. As ionic strength increases, charge shielding by the electrolyte medium increases, and the non-equilibrium interactions between charged particles in the system will be altered. If the transition state complex of the dissolution-active DFA − surface species involves the interaction of charged groups, then it is expected that a change in ionic strength will affect the rate of reaction.

4.6.1 Equilibrium Effects

For the reaction

$$HA = A^- + H^+ \qquad K = \{A^-\}\{H^+\}/\{HA\}$$

$$= \gamma_{A^-} \gamma_{H^+} [A^-][H^+]/[HA] \qquad (23)$$
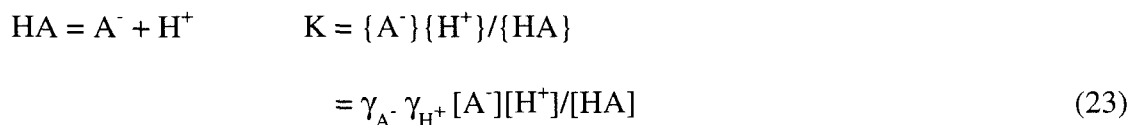
$$K_c = [A^-][H^+]/[HA]$$

where K_c is the conditional equilibrium constant referenced to a defined ionic strength, and γ_i are the activity coefficients for the charged species, i, the effect of increasing the ionic strength is to decrease the values of γ_i. Over the range of ionic strength examined in the these experiments, $\gamma_i < 1$, $K_c > K$, and increasing I, where I is the ionic strength of the solution, increases K_c. The activity coefficient of the charge-neutral HA is assumed to be

unity. Thus, for example, at I > 0, a greater concentration of protons is needed to achieve the same p_aH, defined as $-\log\{H^+\}$, than at I = 0, where $\{H^+\} = [H^+]$.

4.6.2 Non-equilibrium Effects

For the overall reaction

$$Fe_2O_3(s) + H_iDFA^{i-3}(aq) \leftrightarrow Fe - DFA(aq)^+ + (i-1)H^+ \qquad (24)$$
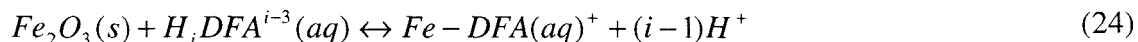
where the solid is in excess and i = 1, ..., 4 , the ionic strength can affect a number of different species that are intermediate in the reaction. For example, the resultant FA species is singly charged over most of the p_aH range of the dissolution experiment, while the DFA species varies in charge from +1 to –2, with integer increments. This condition generates a varying effect on the value of K_c:

$$K = \frac{[Fe - DFA^+]\gamma_{FA}[H^+]^{i-1}\gamma_{H^+}^{i-1}}{[H_iDFA^{i-3}]\gamma_{DFA}} \qquad (24)$$

$$K_c = \frac{\gamma_{DFA}}{\gamma_{FA}\gamma_{H^+}^{i-1}}K$$

It is assumed that γ_{H+} and γ_{FA} have similar values, although the aqueous proton will have a greater ionic potential than FA because of the size difference, but the value of γ_{DFA} will vary as a function of p_aH. Table 5 shows the effect of I on K_c using the Debye-Hückel limiting law for the activity coefficients, recognizing that their validity is limited for high ionic strength media and assuming $\gamma_{H+} = \gamma_{FA}$. However, the effect is captured for illustrative purposes. The values in the table are based on the assumption that a single species of DFA dominates the effect at a particular p_aH.

Table 5

Ionic strength effect on K_c.

approximate p_aH range	charge of DFA	$\gamma_{DFA}/\ \gamma_{Fe-DFA}\ \gamma_{H^+}$
I = 0.01		
<8	1	1.41
8 to 9	0	1.41
9 to 9.5	-1	1.12
>9.5	-2	0.71
I = 0.1		
<8	1	2.98
8 to 9	0	2.98
9 to 9.5	-1	1.44
>9.5	-2	0.34
I = 1		
<8	1	31.62
8 to 9	0	31.62
9 to 9.5	-1	3.16
>9.5	-2	0.03
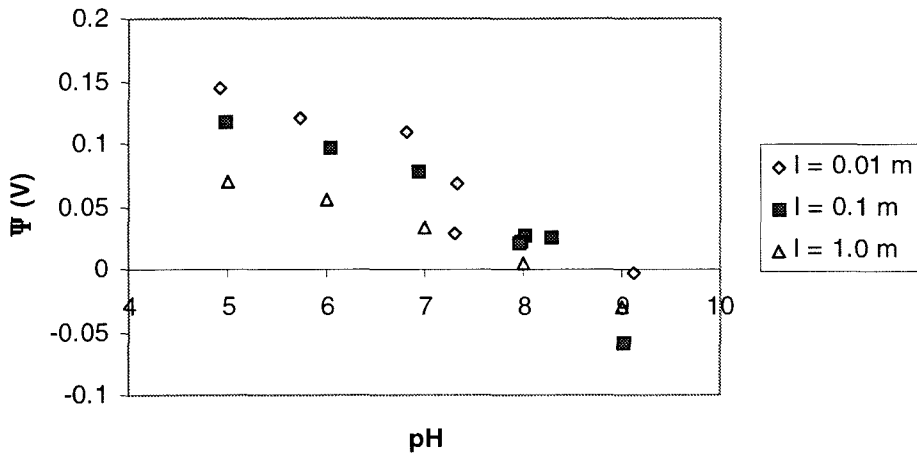
Figure 20

Potential at the hematite surface as a function of p_aH for $I = 0.01$, 0.1 and 1.0 m. Data are calculated from observed surface charge densities using Gouy-Chapmann theory.

For $p_aH < 9.5$ the net effect of increasing ionic strength on the value of the equilibrium constant for the FA dissociation constant is an increased stability of the FA complex. Likewise, the surface association constants of the DFA-surface complexes would be correlated with ionic strength. Thus, the concentration of the DFA-surface complexes is expected to be greater for a given solution concentration as the ionic strength increases. Figure 20 shows the calculated potential at the hematite surface as a function of p_aH. The data are calculated from Gouy-Chapman theory, where $\sigma = (8\ RT\varepsilon\varepsilon_0 c \times 10^3)^{1/2}$ $\sinh(Z\Psi_0/2\ RT)$, where σ is the surface charge density and Ψ_0 is the potential at the surface (Stumm and Morgan, 1996).

Table 6 illustrates a thermodynamic representation of the hematite – DFA system using the tableau formalism, where four mononuclear DFA surface species have been hypothesized. They differ in their proton-dependent surface charge. The surface constants have not been determined, therefore they are omitted. Table 7 shows the effect of the surface charge correction on log K, with the values calculated from the observed σ from the titration curves.

Table 6

Stoichiometric matrix for hematite surface – DFA system

Components	$\equiv$FeOH	H_3DFA	$f(\Psi)$	H^+	log K
Species					
$\equiv$FeOH	1	0	0	0	0
$\equiv$FeOH$^+$	1	0	1	1	
$\equiv$FeO$^-$	1	0	-1	-1	
$\equiv$Fe - HDFA^{2-}	1	1	-2	-4	
$\equiv$Fe - HDFA$^-$	1	1	-1	-3	
$\equiv$Fe – HDFA	1	1	0	-2	
$\equiv$Fe - HDFA$^+$	1	1	1	-1	
H_3DFA	0	1	0	0	0
H_4DFA^+	0	1	0	1	8.39
H_2DFA^-	0	1	0	-1	-9.03
$HDFA^{2-}$	0	1	0	-2	-18.73

An increase in ionic strength results in an increased shielding of the surface charge. The shielding can be expressed through the application of a double-layer approach to characterizing the interaction of the charged surface with the surrounding electrolyte. The shielding is characterized by the Debye parameter, $\kappa = (2F^2 \, I \times 10^3/\varepsilon\varepsilon_0 \, RT)^{1/2}$ (m^{-1}) at 25°C (Stumm and Morgan, 1996). The extent of the double layer can be expressed as κ^{-1} (m). So, the double layer thickness is proportional to $I^{-1/2}$.

Thus, it is expected that an increase in ionic strength would effect an increase in rate of the overall reaction if the rate limiting step, or set of steps, involves the interaction of like-charged moieties, e.g., $\equiv FeOH^+$ with H_4DFA^+ and $\equiv FeO^-$ with H_2DFA^-. The increased ionic strength would effectively shield the interaction, potentially reducing the activation energy for the formation of the activated complex in the transition state. If the dissolution reaction depends on the energetics of the reaction of a charged DFA molecule with the like-charged surface, then the increase in ionic strength, resulting in a decrease of the Debye length, might be expected to exhibit a positive correlation with the rate of dissolution. Likewise, if the interactions of oppositely charged moieties govern the rate limiting steps, then it is expected that an increase in ionic strength might decrease the rate of reaction.

Table 7

$P = \exp(-F\Psi/RT)$

I = 0.01

p_aH	$f(\Psi)$	$f(\Psi)^{-1}$	$f(\Psi)^{-2}$
4.91	0.00	281.11	79023.26
5.73	0.01	110.87	12292.33
6.81	0.01	69.48	4827.35
7.32	0.07	14.34	205.77
7.31	0.33	3.03	9.21
9.11	1.13	0.88	0.78

I = 0.1

p_aH	$f(\Psi)$	$f(\Psi)^{-1}$	$f(\Psi)^{-2}$
4.98	0.01	98.37	9677.47
6.04	0.02	44.60	1988.87
6.94	0.05	20.49	420.00
8.01	0.34	2.94	8.65
8.28	0.36	2.74	7.51
7.97	0.41	2.43	5.89
7.97	0.45	2.20	4.84
9.02	10.08	0.10	0.01

I = 1

p_aH	$f(\Psi)$	$f(\Psi)^{-1}$	$f(\Psi)^{-2}$
5.00	0.07	15.16	229.77
6.00	0.12	8.48	71.87
7.01	0.27	3.72	13.86
8.00	0.85	1.18	1.38
9.00	3.33	0.30	0.09

Figure 21 depicts a set of experiments designed to examine the effects of ionic strength on the rate of dissolution of hematite. The initial concentration of DFA was set at 10^{-4} m, and the p_aH was varied from 6 to 9. The rates are depicted in figure 22 and as the data show, there exists a monotonic increase of pseudo-zero[th] order rate with increasing ionic strength at each p_aH. Since no adsorption isotherms were generated at varying ionic strengths, it is impossible to deconvolute these data in the same manner as performed above, where the first-order rate constants were extracted from the pseudo-zero[th]-order constants through the determination of $\equiv Fe - DFA$. Therefore, it is not possible to determine the mechanistic difference that causes the variation in rate.

The greatest effect on the rates comes at $p_aH = 6$ and $p_aH = 8$. At $p_aH = 6$ the dominant solution species of DFA is H_4DFA^+. It is expected that the surface has a mean positive charge at $p_aH = 6$, and it can be hypothesized that the increased rate is a result of the increased shielding of the positively charged amine from the positively charged surface. At $p_aH = 8$, the dominant solution species is still H_4DFA^+, but there exists a significant proportion of H_3DFA. Although the surface has a net neutral charge at this p_aH, there will exist a significant number of surface groups having negative charge, and it may be that the increased shielding of charge allows the singly deprotonated hydroxamate to interact more effectively with the like-charged surface. However, this argument would suggest that the trend should be obvious at $p_aH = 9$. At $p_aH = 9$, the change in rate as a function of ionic strength is small and it may be that the presence of the dihydroxamate
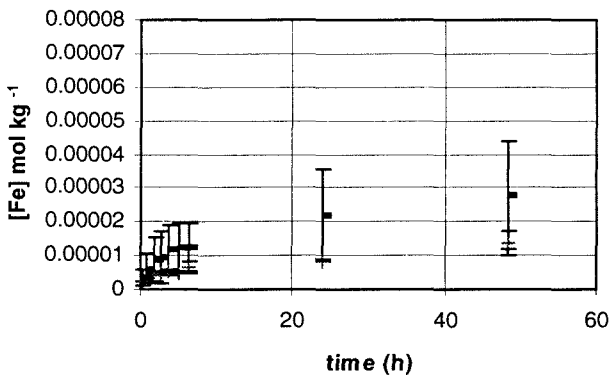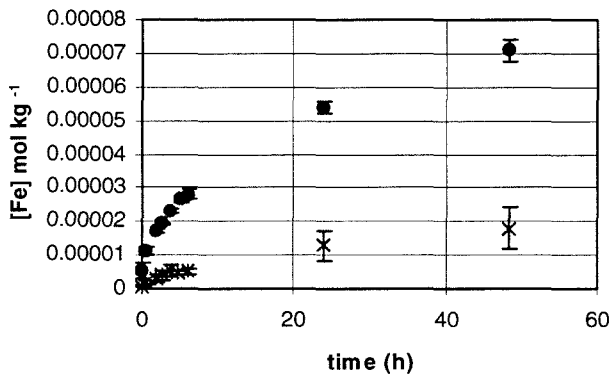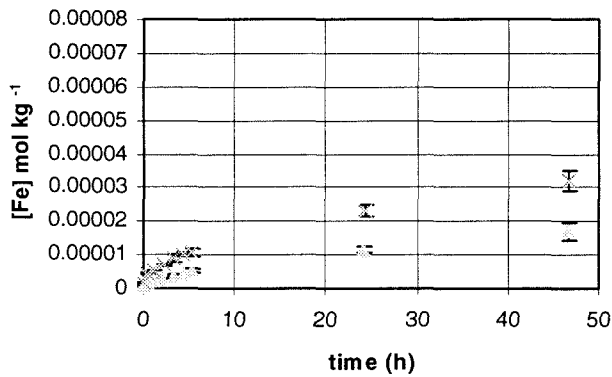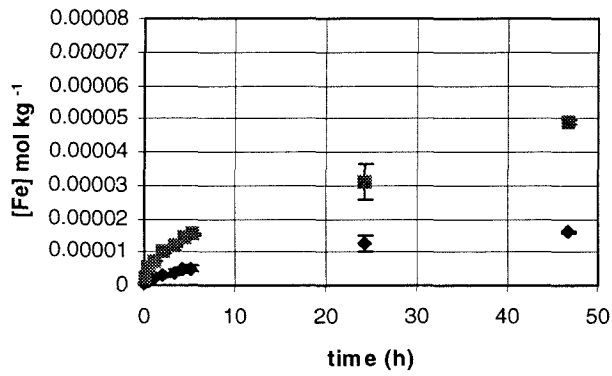
Figure 21

Dissolution of hematite as a function of ionic strength and p_aH. [DFA] = 10^{-4} m.

form of DFA, H_2DFA^-, in equiproportion to H_3DFA, and the increased net negative charge of the surface prevents the effect from being observed. It may also be the case that the activated complex at $p_aH = 9$ is uncharged.

The ionic strength data support the hypothesis that the dissolution reaction is surface mediated. If the rates of dissolution were a simple linear function of κ^{-1}, then we would expect log(R) to be proportional to $\log(I^{-1/2})$. Figure 23 shows this treatment. It is clear that the data do not fall on a straight line for any of the p_aH's examined except for $p_aH = 9$. Thus, the relationship between R and I is not completely straightforward, and may have contributions from the effect of I on the configuration of the DFA-surface complex.
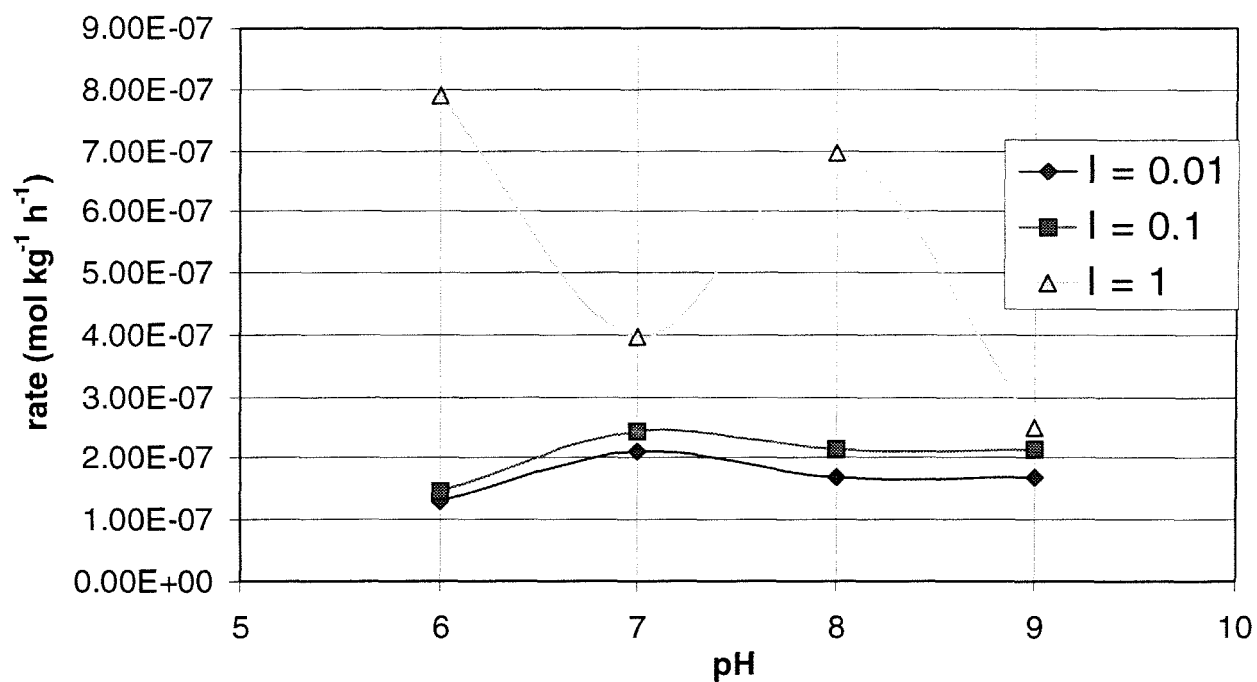
Figure 22

Pseudo-zero[th] order rates as a function of ionic strength and p_aH. $[DFA]_0 = 10^{-4}$ m. Rates are taken as the slope of the line connecting the final two data points for each curve in figure 30.
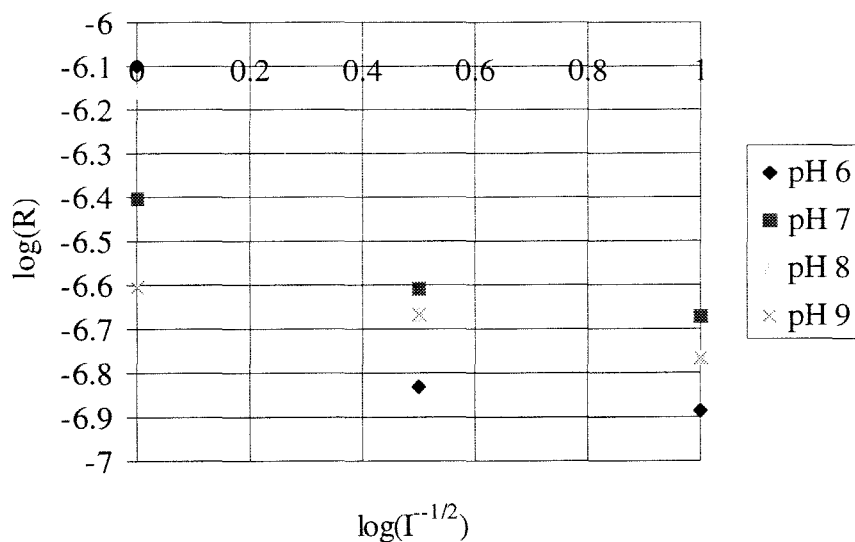
Figure 23

Graph of log(R) as a function of $\log(I^{-1/2})$ and p_aH.

4.7 Effects of Temperature

To complete the study of this hematite preparation, the effect of temperature on the rate of dissolution was explored. Figure 24 illustrates the results of increasing the temperature to 35°C. Notice that the morphology of the dissolution curve is less convex than the curves observed at 25°C. On average, the initial [Fe] measured by ICPMS, taken at t = 0, is 4.61×10^{-7} $m \pm 1.75 \times 10^{-7}$ m. This observable initial [Fe] suggests that the more labile surface sites are dissolved more effectively at higher temperatures over the range of p_aH's studied. Also, the initial dissolution of the low energy sites is more rapid at 35°C than at 25°C.

148

Figure 25 shows the pseudo-zeroth order rate constants extracted from the data depicted in figure 24. As can be seen from the data, an increase of temperature of 10°C results in an increase in the pseudo-zeroth order rate constant. Again, it is difficult to deconvolute the effect of temperature on the reaction mechanism because the effect of temperature on adsorption behavior was not examined. Also, at 35°C the stability of the DFA in solution over the time scale of days is questionable. The rates are taken from data within the first 8 hours of dissolution, an action that is justified by the apparent linearity of the data in the region 0.3 h < t < 8 h. The data after this point exhibit some anomalous behavior that is attributed to the degradation of the DFA molecule by hydrolysis. Thus, given the complicated nature of the dissolution process, i.e., the existence of multiphasic dissolution events, a simple Arrhenius or transition state theoretical approach may not be warranted. In addition, without the ability to generate a third temperature point because of insufficient material, determining the applicability of the Arrhenius plot to the data is inappropriate.

It may be reasonable to correlate the observation that the difference in rates as a function of temperature is the greatest at $p_aH = 8$ with the similar observation of the rate increase in the ionic strength data. If the rate increase is related to the conformation of a transition state complex, then these data would suggest that the complex involves a like-charge interaction that is moderated by the increase of temperature and the increase in ionic strength.
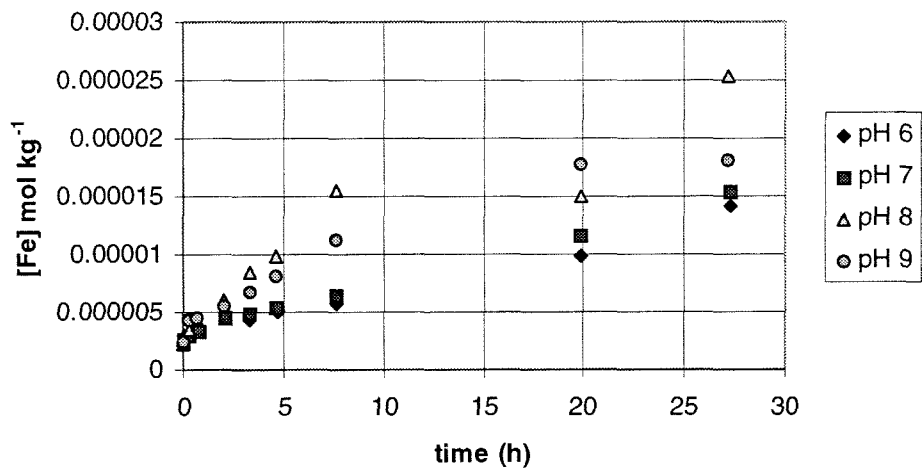
Figure 24

Dissolution of hematite at 35°C as a function of pH. $[DFA]_0 = 10^{-4}$ m.
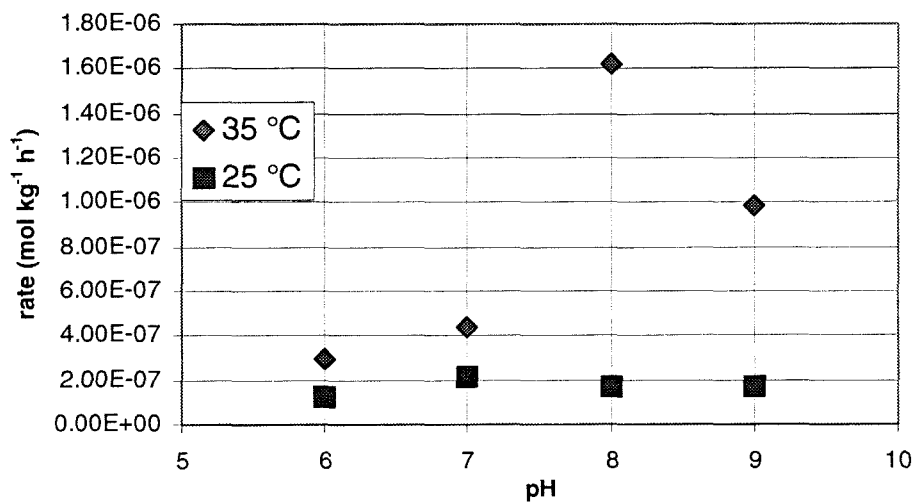
Figure 25

Pseudo-zero[th] order rates as a function of temperature. $[DFA]_0 = 10^{-4}$ m.

4.8 Discussion

The above approach for extracting the pseudo-first order rate constants from the pseudo-zero[th] order constants and the adsorption isotherms assumes that there is a one-to-one correspondence between the molar amount of FA formed and the adsorbed surface species. As previously mentioned, it is hypothesized that the rate of the dissolution reaction is limited by the removal step. However, there exists a number of potential complications with respect to the details of the rate limiting step that are not resolved in the data.

For example, if there exists one surface configuration of the adsorbed DFA molecule that defines the configuration of the adsorbate in the rate-limiting step for the dissolution event, and if such a configured adsorbed DFA results in the removal of one FA molecule from the surface, then the one-to-one correspondence is the expected result. However, assume that there exists a set of surface configurations of the adsorbed DFA molecule in the rate-limiting step. Assume further that all members of the set have the potential to result in a dissolution event, and each member has a different energetic barrier for reaction. Each surface configuration will have a different concentration and a different rate of reaction. The experimentally observed dissolution rates will integrate over all these rates and will therefore generate no information about the detailed distribution of concentrations and rates. An example of this is the existence of the low energy sites, whose dissolution rate is greater than that of the large particle sites. This particular difference is resolvable in the data. In fact, however, there is no guarantee that each

configuration will result in a one-to-one correspondence between a DFA molecule adsorbed to a particular site and the appearance of a molecule of FA in solution.

It is instructive to test the hypothesis that there exists a resolvable reaction order for the DFA-induced dissolution of hematite. If the reaction is written as

$$R = k^{'}[\equiv Fe - DFA]^{n}$$
$$or$$
$$\log R = n\log[\equiv Fe - DFA] + \log k^{'}$$

(25)

where n is the order of the reaction, n would be expected to have an integer value if the reaction is a simple function of the adsorbed DFA. Figure 26 shows a plot of $\log R$ as a function of $\log [\equiv Fe^- DFA]$; table 8 lists the parameters generated from the plot. Note that the parameters are generated from a fit through three points and the $[\equiv Fe^- DFA]$ spans a range of 3.4 x 10^{-6} to 1.0 x 10^{-5} mole g^{-1}. The variance of the slope and intercept is a function of the combined uncertainty of the adsorption isotherm data and the rate data. Since the adsorption isotherm was performed only once, it is difficult to estimate the uncertainty of these data. However, most of the uncertainty of the slope will be derived from the uncertainty in the rate data. It can be argued that the largest contribution to the error comes from the high concentration data, where the surface saturated with ligand. Examining the data, it can be seen that for p_aH = 5, 6, and 7, the data at [DFA] = 10^{-3} seems to suggest that the regression suggests a greater slope than the actual, while at p_aH = 8 and 9, the opposite holds. It is interesting to note that the curvature of the data changes from convex at p_aH = 5, 6, and 7 to concave at p_aH = 8 and 9. This observation

indicates that the effect of concentration on reaction order may change as a function of p_aH.

The intercept, log k', should correspond to the pseudo-first order rate constants listed in table 8, and should be on the order of –2. As can be seen in table 5, the log k' values vary significantly from this value, indicating that the surface mediated reaction is the result of a complicated set of surface configurations. It must also be observed that the data included in figure 26 include the data for which $[DFA]_0 = 10^{-5}$ m. These data include the nonlinear portion of the dissolution curve and may invalidate this approach. However, removing the low concentration data results in a set of lines defined by two points only, and the resulting intercepts vary from –8.4 to 12.8. The variation in the intercepts suggests that a simple reaction order approach to the dissolution mechanism is invalid for the DFA – hematite system, and, moreover, the dissolution-active surface configurations define a complicated set of DFA – surface interactions.
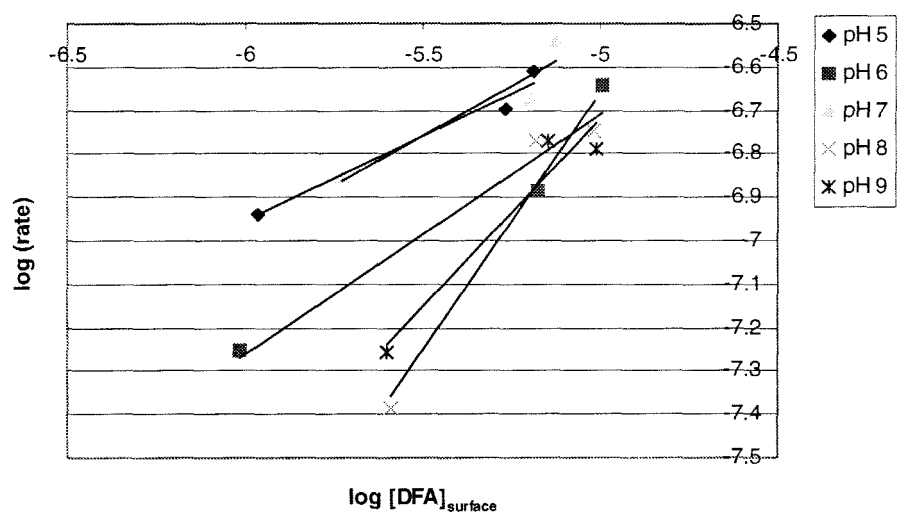
Figure 26

Log *R* as a function of log [≡*Fe⁻DFA*].

Table 8

Parameters generated from a linear fit to equation 10.

p_aH	n	log k	R^2
5	0.39027	-4.6129	0.9702
6	0.54881	-3.9659	0.94128
7	0.44999	-4.282	0.892
8	1.1884	-0.7152	0.93816
9	0.87345	-2.3491	0.93679

The distribution of dissolution-active surface sites need not remain constant as a function of [$\equiv Fe\text{-}DFA$]. This case would result in nonlinearity for the graph of log R vs. log [$\equiv Fe\text{-}DFA$]. The adsorption affinity may differ among sites; or, the forms of the adsorption isotherms themselves may not be equivalent within the set of adsorption sites. If either of these scenarios hold true, then the assumption that all the surface sites are equivalent fails in detail.

On the other hand, assume that the equivalence of the adsorption sites does hold true, and therefore the curves in figure 26 do have some validity with respect to reaction order. How could it be that $n_i \neq 1$? Figure 27 depicts a potential mechanism by which this phenomenon might occur. In this figure, one molecule of DFA adsorbs to the surface, binding in a trinuclear configuration with three surface Fe's, one for each hydroxamate functionality. Each adsorption event has the potential to result in a dissolution event. If all three adsorption events are successful, then the reaction order resulting from this scheme would be 1/3; i.e., three moles of FA are generated for every mole of adsorbed DFA. However, a statistical argument favors the order being greater than 1/3. Under this proposed reaction mechanism, the adsorbed DFA molecule has the potential to leave the surface bound to 0, 1, 2, or 3 Fe atoms originating from the surface. Each of the four configurations has some probability of occurring, with the value of each probability unknown. Define the probability of the DFA molecule leaving the surface with 0 Fe's bound to the molecule as a, the probability of the DFA leaving with 1 Fe molecule as b, and so on. Then, at each p_aH it is expected that n = $(a \cdot 0) + (b \cdot 1) + (c \cdot 2) + (d \cdot 3)$, where $0 \leq a, b, c, d \leq 1$, $a + \ldots + d = 1$, and $a, b, c,$ and d vary as a function of p_aH.
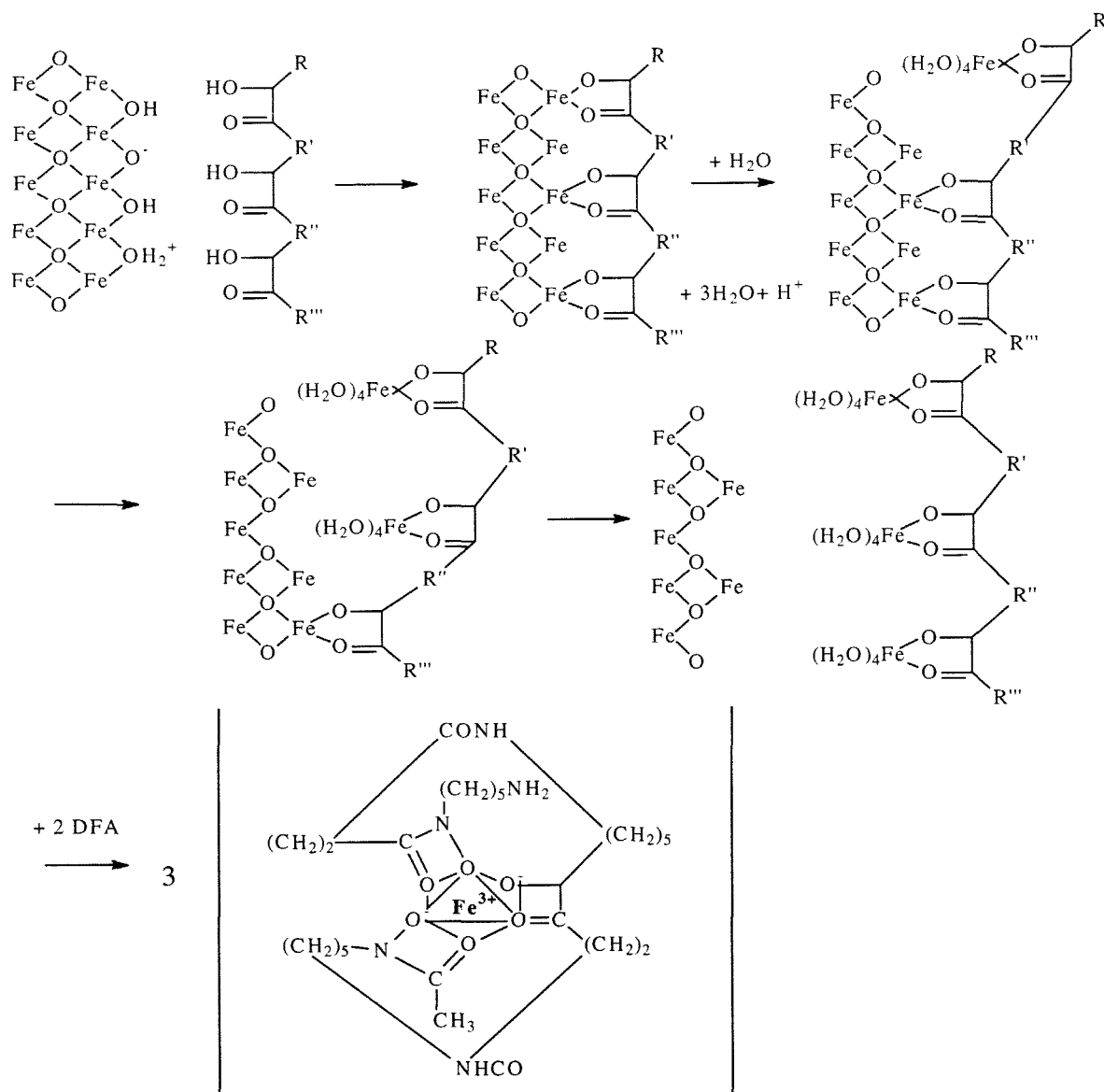
Figure 27

Mechanism for DFA-mediated dissolution of hematite, where $n_i \neq 1$. This sequence depicts one possible scenario in which the adsorption of a single DFA molecule results in the removal of three surface-bound Fe atoms. The expected reaction order of such a sequence is 1/3.

Why should the rate of reaction vary as a function of p_aH? It is hypothesized that this phenomenon is a result of the pH-dependent surface configurations of the adsorbed DFA. In this context a configuration is meant to denote a particular state of the surface complex; i.e., the number of covalent bonds between the DFA and the surface, the proton-dependent charge state, the geometry of the surface complex, etc. As already discussed, the DFA molecule has the potential to have a multinuclear interaction with the surface. The energetics of this interaction will be affected by the pH dependent state of the surface and the DFA molecule.

The following factors have the potential to affect the surface configuration as the p_aH increases:

(1) $[OH^-]$ (aq)

As p_aH increases, $[OH^-]$(aq) increases and competes with the hydroxamic acid functionalities for the surface metal centers. This effect is most likely attenuated by the increased efficacy of the hydroxamate form of the ligand as a result of its Lewis basicity. The net result of this effect is a decreased residence time of all three hydroxamates simultaneously bound to the surface.

(2) Electrostatics

The net negative charge density of the surface increases as the p_aH increases. If the DFA adsorbs initially with a single hydroxamate moiety, the remaining two DFA hydroxamic acids will experience an increased probability of encountering a negatively charged

surface group (recall the distance between hydroxamates on DFA is sufficient to span two surface metal centers.) If either of these two functionalities is in the hydroxamate form, it must overcome the electrostatic repulsion of the interaction with a negatively charged surface group to establish a covalent interaction. The results of the experiments wherein ionic strength is varied suggest that there are two important electrostatic effects in the dissolution mechanism. The first effect is seen in the $p_aH < p_aH_{pznpc}$ region, where the DFA molecule has a positive charge residing on the terminal amine and the hydroxamic acid functionalities in the acidic form. The surface has a net positive charge. The repulsive interaction of the terminal amine with the surface appears to reduce the rate of dissolution. The second effect is seen at $p_aH = 8$, where the surface is net neutrally charged and the DFA has a significant population of the singly deprotonated hydroxamate form. The large increase in rate observed with increase in ionic strength supports the idea that the dissolution-active complex requires the bonding of a hydroxamate in inner sphere coordination with the surface.

The work done by Eisenlauer and Matijevic (Eisenlauer and Matijevic, 1980) also indicates the potential for complicated surface configurations. They suggest that for $p_aH < pH_{pznpc}$ the surface configuration is some subset of the three hydroxamic acid functionalities adsorbed on the surface in a multinuclear configuration. They also suggest that for $p_aH > pH_{pznpc}$ the surface configuration is one-to-one; i.e., there exists one adsorbed DFA per surface group. They invoke the terminal amine as the surface active moiety on the adsorbate, however. This configuration would result in a lower reaction rate and a higher adsorption density. The rate would be lower because of the

electrostatic repulsion creating an energy barrier for the binding of the hydroxamate functionalities to the surface Fe's. The adsorption density would be higher because the bulk of the DFA molecule would not lay on the surface, rather, would be orthogonal to the surface, allowing for a larger number of DFA molecules to access the surface per unit surface area.

The overall rates of dissolution over the p_aH range examined do not differ greatly. This result suggests that the reaction trends that are determined by pH effects are either not significant or are offset by other effects, such as dissolution active DFA – surface configurations that vary as a function of p_aH.

The chemical results of the dissolution generate a mechanistic description of the dissolution process. At the most general level, the DFA molecule moves to the surface where it binds as a mononuclear, inner sphere complex. The configuration of this surface complex then determines the efficacy of the complex with respect to dissolution. The electrostatic interactions between the rest of the DFA molecule and the surface dominate the configuration. Figure 28 shows a cartoon of the effects of the electrostatic and van der Waals interactions on the surface configuration.

The van der Waals interactions are shown in figure 28 (a.); the net effect of these interactions is attractive. Figures 28 (b.) through (e.) depict interactions that are variously attractive and repulsive, with the net effect of altering the surface configuration of the
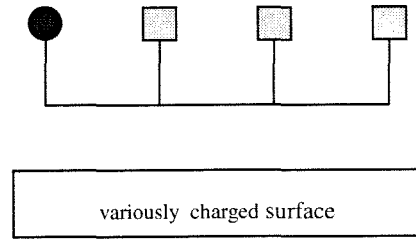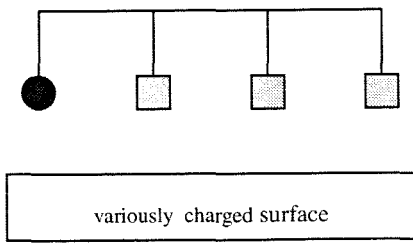
(a.) van der Waals interactions (all pH's)

net effect: attractive
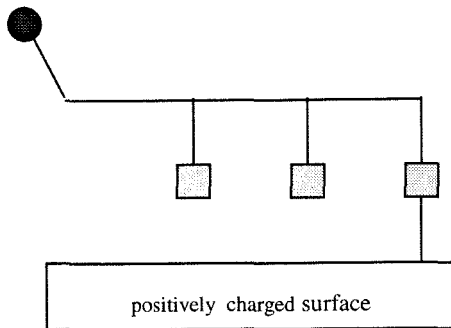
(b.) electrostatic interactions, pH < 8.

net effect: repulsive
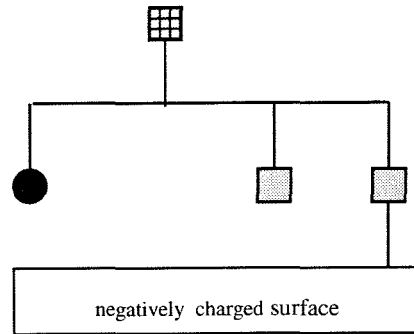
(c.) electrostatic interactions, 8 < pH < 8.7.

net effect: neutral
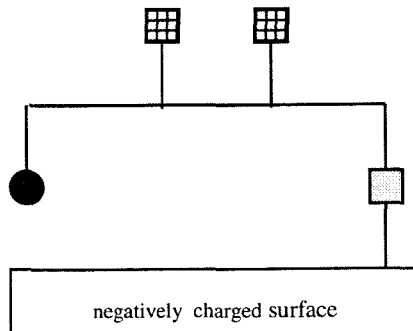
(d.) electrostatic interactions, 8.7 < pH < 9.5.

net effect: repulsive
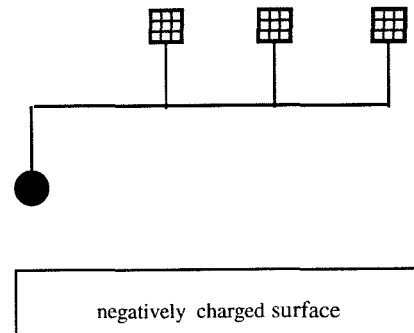
(e.) electrostatic interactions, 9.5 < pH.

net effect: repulsive

Figure 28

Cartoon of non-covalent interactions of DFA with the oxide surface, showing the gross effects of surface charge and molecular charge on the surface – molecule interactions. Bidentate covalent interactions are depicted as a line from the hydroxamate to the surface.

hydroxamic acid (neutrally charged)

hydroxamate (negatively charged)

amine (positively charged)

DFA molecule. The figure shows a bidentate covalent interaction between one hydroxamate and the surface. The DFA molecule is effectively tethered to the surface by this electrostatic interaction. The interaction of the rest of the DFA molecule and the surface will depend strongly on the charge state of the surface and the remaining two hydroxamic acid functionalities, thus defining the surface configuration.

An interesting aspect of the system that was not systematically examined results from the observation that DFA acts as a surfactant in aqueous solution. At the higher concentrations of DFA, foaming was observed in the experimental system. It is not clear whether micelles form in solution at the concentrations used in these experiments. Micellar formation would significantly complicate the interpretations of these results.

4.9 Conclusion

This chapter presents data that clearly show the influence of DFA on the solubility of hematite. DFA adsorbs to the surface and effects the removal of Fe from the surface of the mineral. The result is straightforward, but the mechanism and the nature of the DFA – surface interactions are not. The results indicate that there are very complicated interactions at the surface. The interactions become complicated as the charging behavior of the surface and the DFA molecule change as a function of pH. That their changes track each other increases the complexity of the interactions. However, the net

result of the observations is that the dissolution is relatively insensitive to pH at 25°C and I = 0.01 m.

The insensitivity of the DFA-mediated dissolution to pH means that organisms that use DFA in their iron uptake systems are relatively unrestricted with respect to the pH of their ecosystems, and can inhabit a wide range of waters. Furthermore, since there does exist a positive correlation between [DFA]$_{solution}$ and the rate of dissolution, then increased proximity of the organism to the oxide surface would enhance the *local* concentration effects, and also increase access to the dissolved FA product.

The low [DFA]$_0$ experiments are interesting in that they show that the DFA molecule is highly effective even at low concentrations. The reactions go to completion over the time scale of about 8 h, having successfully scavenged the low energy iron from the surface. Thus, an organism can optimize its energetic catabolic strategy for iron uptake by synthesizing very small amounts of DFA for release.

The chemistry of the DFA – hematite system is a fascinating example of a complex chemical species, DFA, interacting with a surface. The myriad of interactions generate a set of data which points to a rich area for general study of the interaction of complex biomolecules with inorganic surfaces.

Chapter 5

Dissolution of Synthetic Hematite with a Goethite Impurity

5.1 Introduction

In this chapter data will be presented that describe the dissolution of a synthetic preparation of hematite, called SC hematite. The SC hematite has a goethite impurity, as evidenced in the x-ray diffraction pattern presented below. The mixed phase oxide was employed for two reasons. First, the mixed phase aspect can be thought to be more representative of the complexity of naturally occurring oxides. Second, the data from the dissolution of the SC hematite can be compared to a similar oxide preparation and dissolution experiment in the presence of a naturally occurring siderophore by Hersman et al. (Hersman et al., 1995).

5.2 Hematite Synthesis

The synthesis of SC hematite followed the procedure modified from Schwertmann and Cornell (Schwertmann and Cornell, 1991). In a 1 l high density polyethylene (HDPE) bottle 40.00 g $Fe(NO_3)_3 \cdot 9H_2O$ were added to 500.0 g MilliQ water that had been preheated to 90°C. 300.00 g of 1.00 m KOH preheated to 90°C and 50.00 g of 1.00 m $NaHCO_3$ preheated to 90°C were added to this suspension. NaOH(s) was added to this suspension to bring [NaOH]tot to 5 m. The suspension was placed in a 90°C oven for four days.

5.3 Hematite Cleaning

After synthesis, the solid suspension was cleaned in the same manner as described for the sol gel prepared hematite in chapter 3.

5.3.1 Particle Characterization

Figure 1 is a transmission electron micrograph (TEM) of these particles prior to dissolution. Samples for TEM analysis were prepared by dispersing in water, with mortar and pestle, and placing a drop of solution on the surface of a holey carbon substrate which was covering a Cu grid. The excess solution was wicked away after 30 seconds and the grid was allowed to air dry. The microscope that was used was a Philips EM430 transmission electron microscope. The analysis was carried out at 300 keV. The micrographs depicted in figure 1 show a set a of particles with a mixed geometry. The particles are dominated by needle-like crystals that have an average length of approximately 1.5×10^{-6} m, and a radius of 2.4×10^{-8} m. The second set of particles are platelets having a diameter of approximately 2.5×10^{-7} m. A calculation of the surface area generated from sampling particles from the micrograph gives an approximate specific surface area of 15 m^2 g^{-1} hematite. Figure 2 shows that the BET analysis of this sample generates a BET surface area of 13.5 ± 0.3 m^2 g^{-1} (Micromeritics ASAP 2000, Adsorptive: N_2 gas), in excellent agreement with the calculated value.

Powder x-ray diffraction (XRD) measurement (Scintag PAD-V diffractometer) gives the spectra shown in figure 3 and shows that the phase is hematite with a significant goethite

impurity. Visual analysis of the diffraction patterns for the needles and the platelets confirmed their crystallinity.

(a.)

(b.)
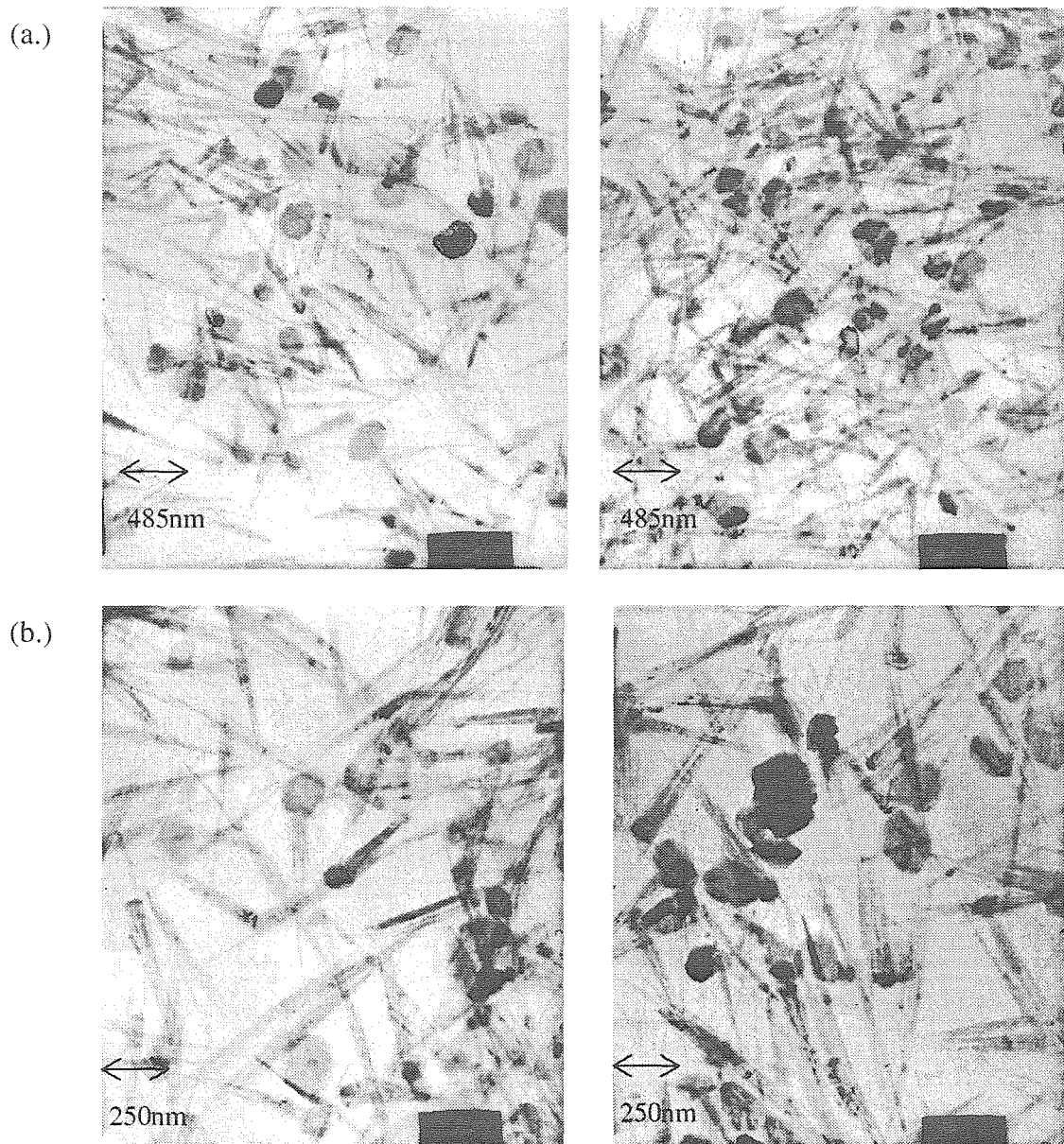
Figure 1

Transmission electron micrographs (TEM) of SC hematite.

(a.) 20,600 X magnification.

(b.) 40,400 X magnification.

y = 0.5174x - 0.0053
R^2 = 0.9899
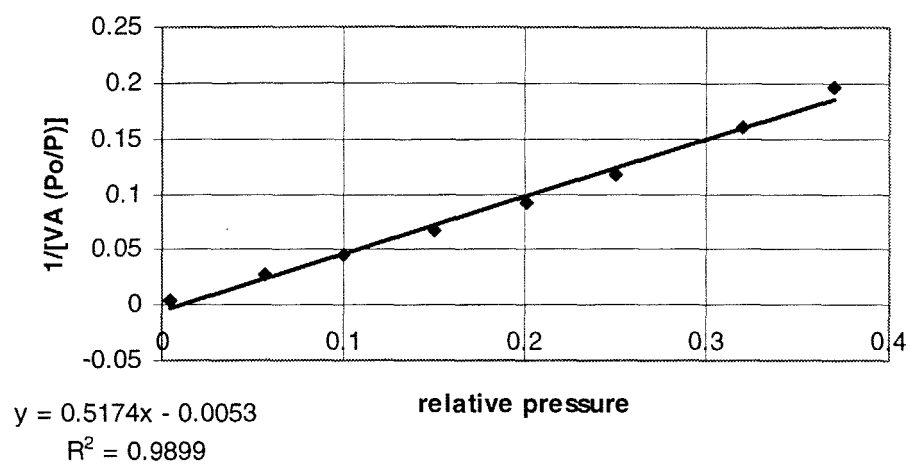
Figure 2

BET adsorption isotherm of SC hematite. BET surface area = 13.5 ± 0.3 m^2 g^{-1}, 0.1134 g of solid used for determination.
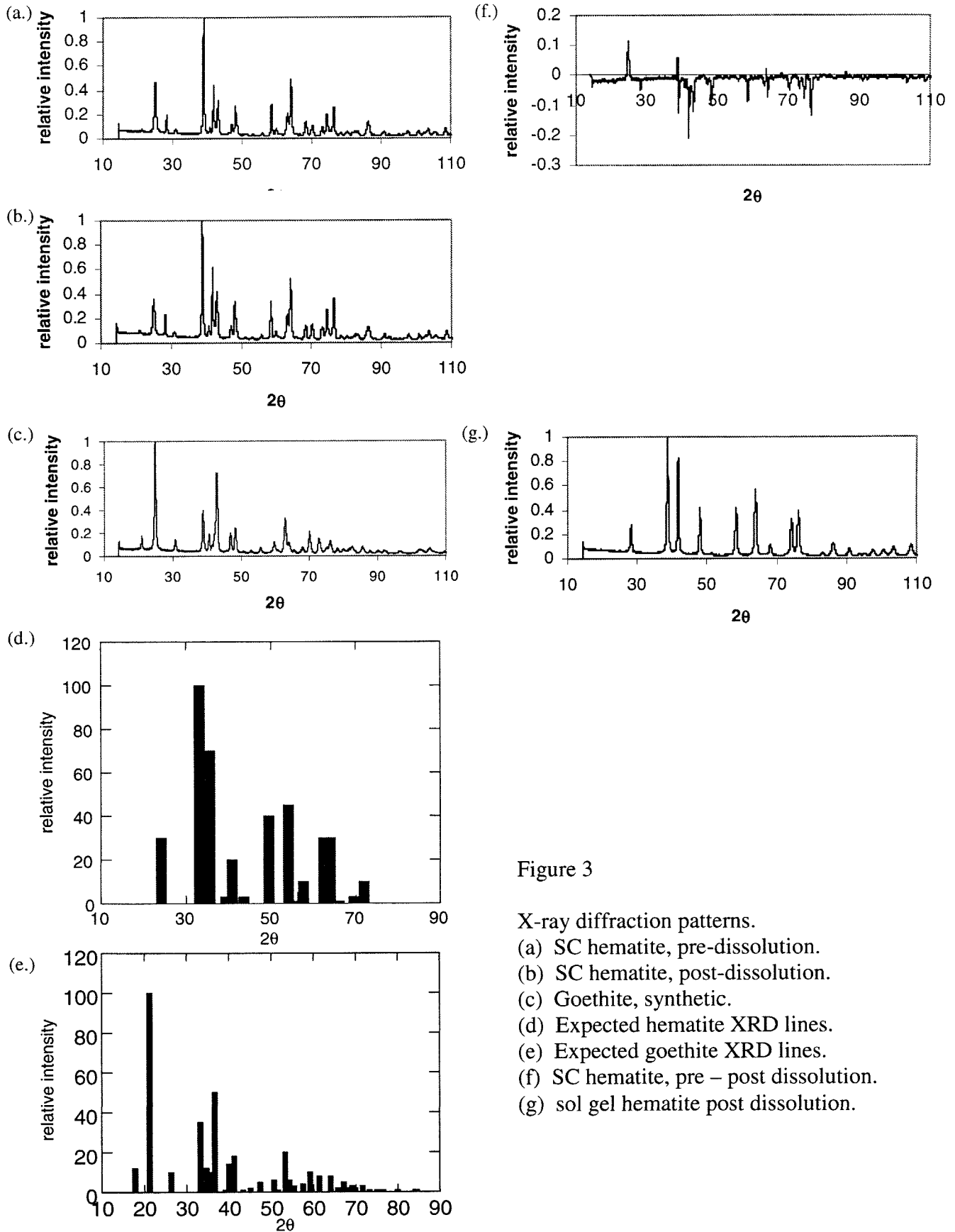
Figure 3

X-ray diffraction patterns.
(a) SC hematite, pre-dissolution.
(b) SC hematite, post-dissolution.
(c) Goethite, synthetic.
(d) Expected hematite XRD lines.
(e) Expected goethite XRD lines.
(f) SC hematite, pre – post dissolution.
(g) sol gel hematite post dissolution.

Figure 3 shows seven different diffraction patterns for comparison. Figure 3(a) depicts the pattern for the SC hematite prior to dissolution. If this figure is compared to the expected intensities of the pattern for hematite (figure 3(d)) and goethite (figure 3(e)), as well as the diffraction patterns for sol gel prepared hematite (figure 3(g)) and a synthetic goethite (figure 3(c)), then it is clear that goethite exists as a crystalline phase in the sample. The presence of needles as a major morphological feature of the sample is consistent with this observation. Because the absolute intensities of the signals at particular diffraction angles will depend on the efficiency of the scattering process, a function of the refractive index of the crystals and the scattering cross section, it is difficult to determine the absolute proportions of goethite to hematite in the sample. In an attempt to determine if there exists a preferential dissolution of a particular phase, figure 3(f) shows the difference in the pre- and post- dissolution SC hematite. Comparing figure 3(b) to figure 3(a) and referencing figure 3(f), there is weak evidence for the increased loss of goethite over hematite. This observation could result from a number of factors, including: (i) goethite is found more dominantly at the surface of the particles; (ii) goethite dissolves more efficiently than hematite. However, there exists no definitive evidence from the above data that can directly determine the cause.

5.4 Dissolution Experiments

The procedures and experimental setup utilized for the dissolution experiments for SC hematite are identical to those outlined for the sol gel prepared hematite. Total organic carbon (TOC) was utilized to monitor the [DFA] for each sample (Shimadzu TOC-5000A with an ASI 5000A auto-sampler).

5.5 Experimental Results

5.5.1 Dissolution Data

The results of the dissolution experiments are shown in figures 4 through 9. The graphs in figures 4 through 9 show the appearance of Fe in solution as a function of time for varying pH and [DFA]. For all the experiments presented in this chapter, [hematite] = 1.00 g kg^{-1}, unless otherwise noted. The data points are the average of at least two experiments and the error bars are ± two standard deviations. Also shown in the figures is [DFA] as a function of time. The [DFA] data taken by TOC measurements has a large error associated with it, with reproducibility of measurements of a single sample exhibiting high variability. The DFA interacted with the plumbing of the TOC apparatus, so adsorption onto the walls of the tubing occurred at higher [DFA] and leaching from the walls occurred at lower [DFA]. Thus, the data should be interpreted as qualitative.

To analyze this set of data, the pseudo-zero[th] order rate constants are extracted from the long time data: t > 6 h. No adsorption isotherms were generated for this material, so no pseudo-first order constants can be extracted from the data. Note that the morphology of the dissolution curves appears somewhat similar to that of the sol gel prepared hematite, in that there is a rapid near-time dissolution, followed by a slowing of the rate. Tables 1 through 6 list the parameters generated from the data. The tables list the weighted average for some of the experiments. In these instances, there are two types of repetitions: one in which the initial conditions are replicated contemporaneously, and the other in which the conditions are replicated for a run performed at another time.

(a.)

(b.)
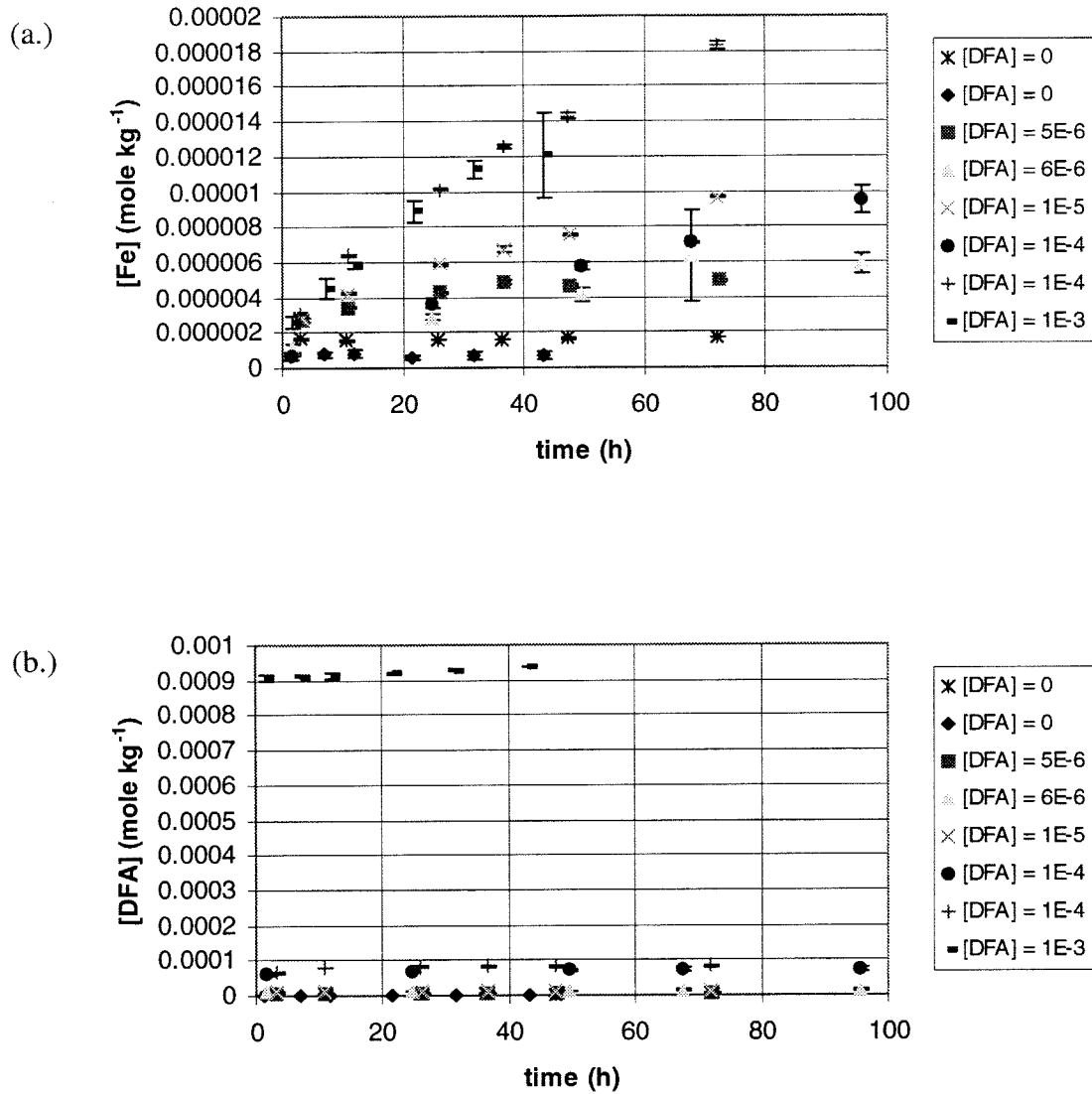
Figure 4

(a.) SC hematite dissolution at pH = 4, [hematite] = 1.00 g kg^{-1}. [DFA]$_0$ varies from 0 to 10^{-3} m.

(b.) [DFA] in solution as a function of time.

(a.)
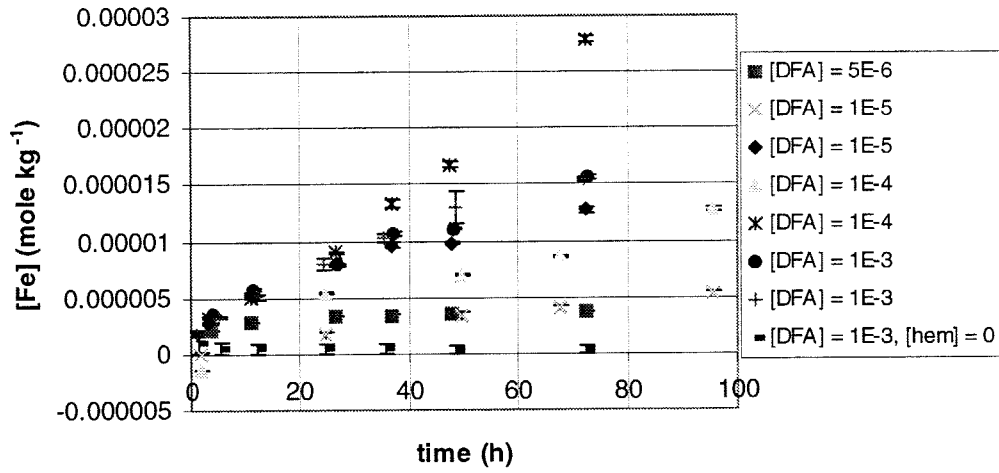
(b.)
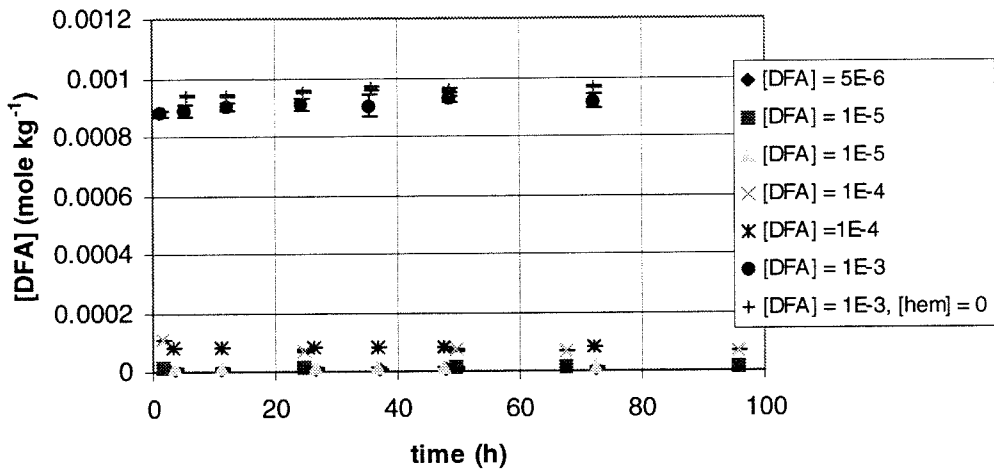
Figure 5

(a.) SC hematite dissolution at pH = 5, [hematite] = 1.00 g kg^{-1}. [DFA]$_0$ varies 5 x 10^{-6} to 10^{-3} m.

(b.) [DFA] in solution as a function of time.

(a.)
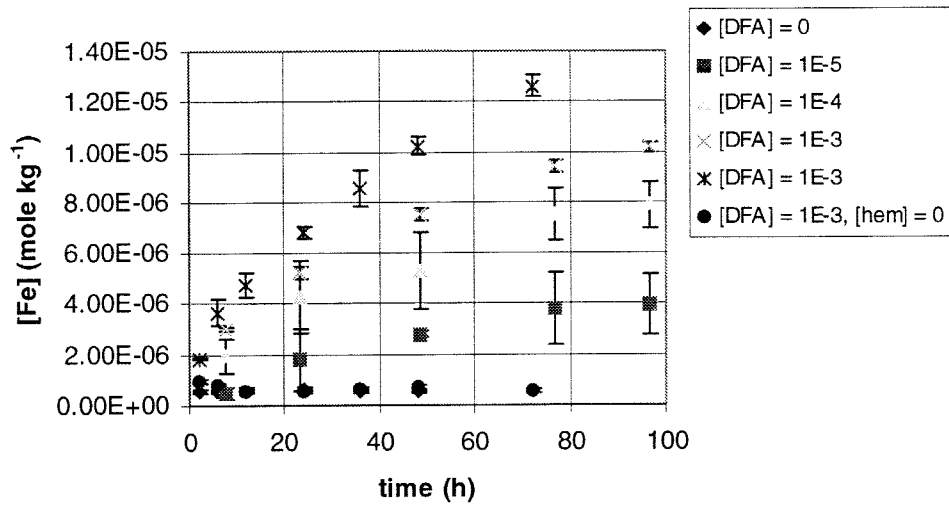
(b.)
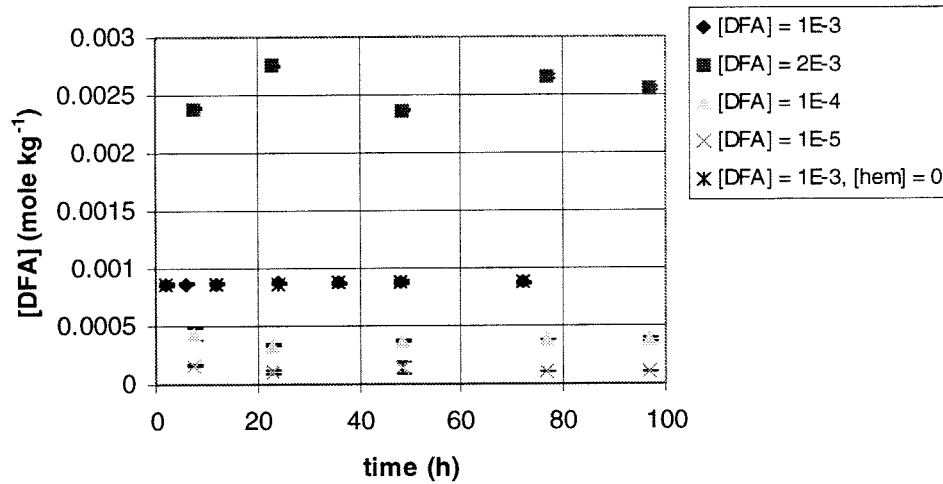
Figure 6

(a.) SC hematite dissolution at pH = 6, [hematite] = 1.00 g kg^{-1}. [DFA]$_0$ varies from 0 to 10^{-3} m.

(b.) [DFA] in solution as a function of time.

(a.)
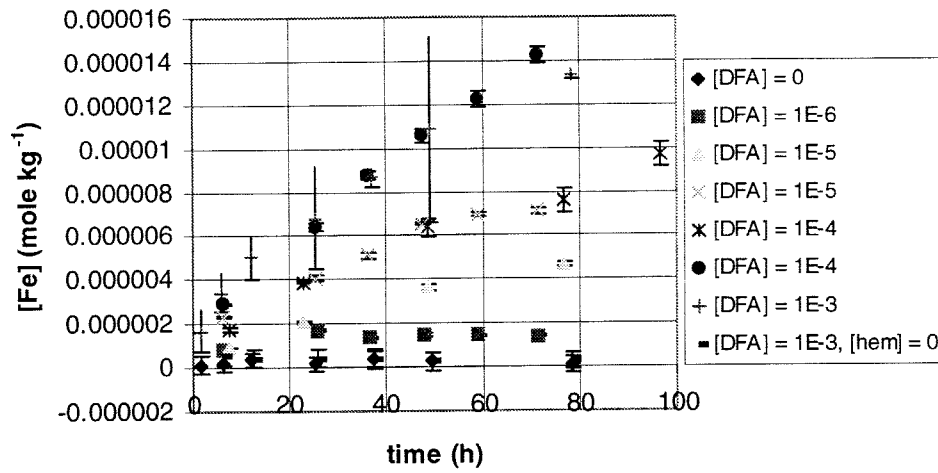
(b.)
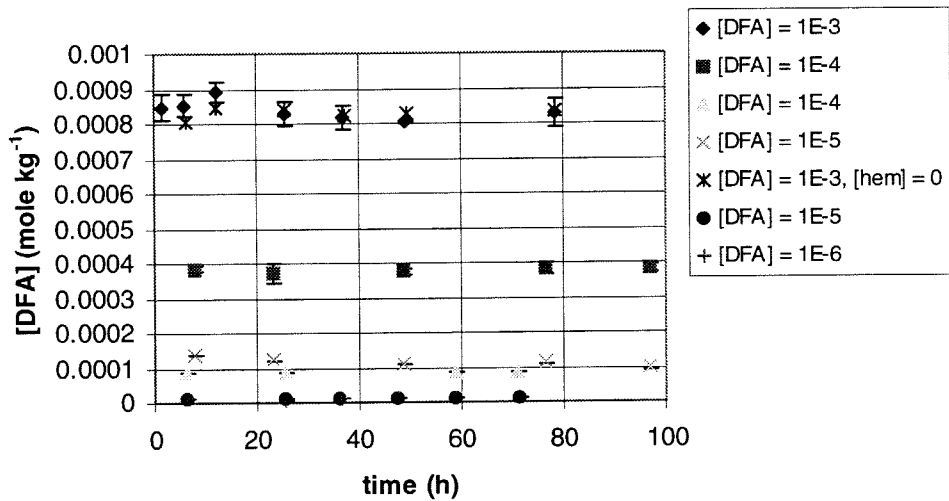
Figure 7

(a.) SC hematite dissolution at pH = 7, [hematite] = 1.00 g kg^{-1}. [DFA]$_0$ varies from 10^{-6} to 10^{-3} m.

(b.) [DFA] in solution as a function of time.

(a.)
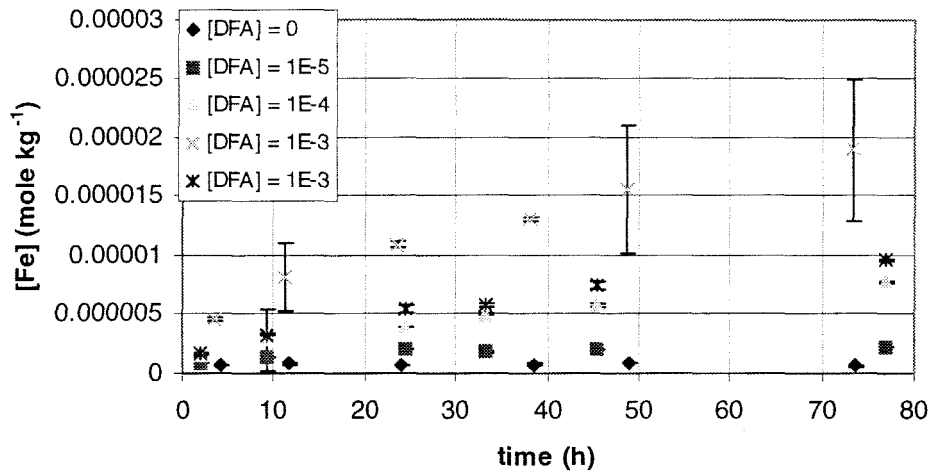
(b.)
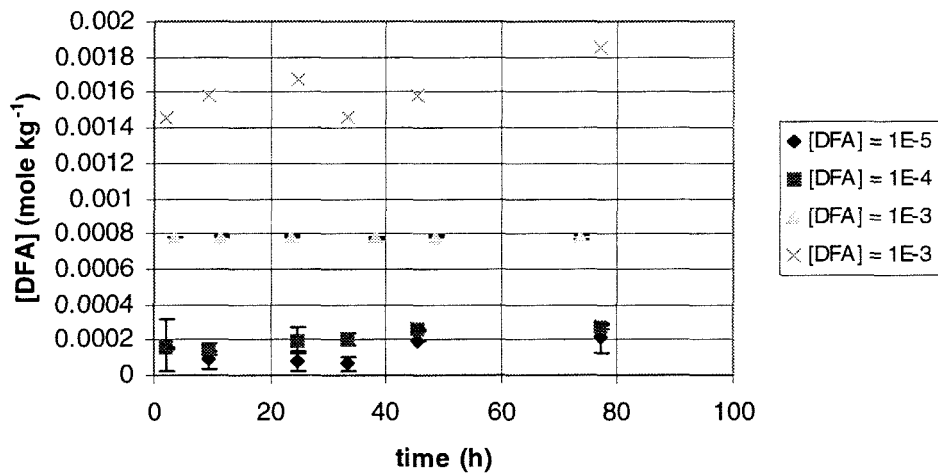
Figure 8

(a.) SC hematite dissolution at pH = 8, [hematite] = 1.00 g kg^{-1}. [DFA]$_0$ varies from 0 to 10^{-3} m.

(b.) [DFA] in solution as a function of time.

(a.)
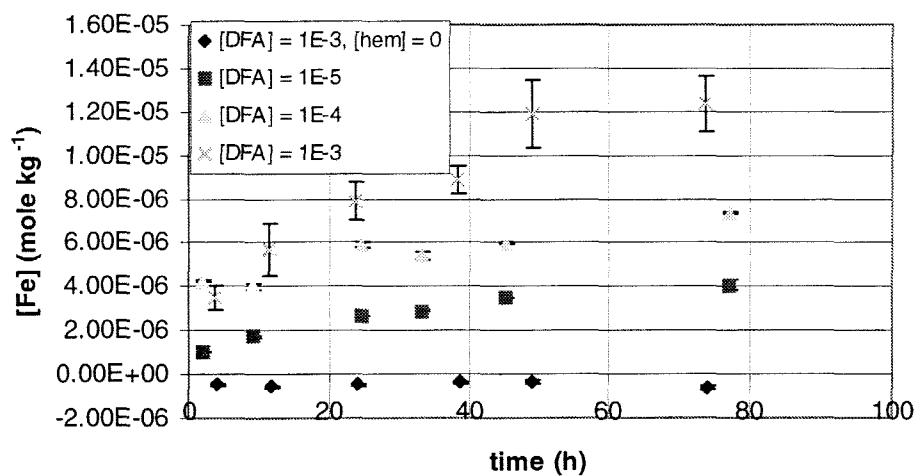
(b.)
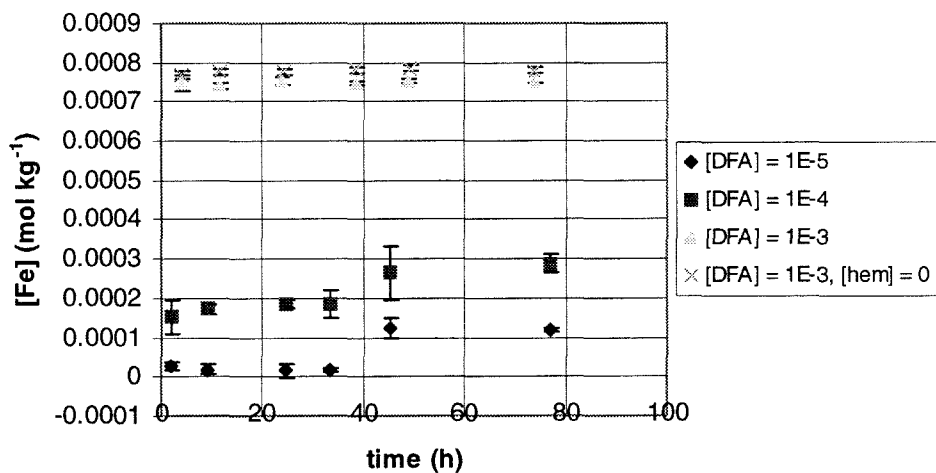
Figure 9

(a.) SC hematite dissolution at pH = 9, [hematite] = 1.00 g kg^{-1}. [DFA]$_0$ varies from 10^{-5} to 10^{-3} m.

(b.) [DFA] in solution as a function of time.

Table 1

Rate constants for pH = 4, SC hematite.

$[DFA]_0$ (m)	pseudo-zero[th] order rate constant (m h^{-1})	weighted average (m h^{-1})	S_d	r^2
0	1.65×10^{-9}			0.41609
0	-2.34×10^{-10}			0.0020652
5×10^{-6}	5.68×10^{-8} (t < 50 h)	5.60×10^{-8}	1.01399×10^{-9}	0.997
6×10^{-6}	5.53×10^{-8} (t < 70 h)			0.876
1×10^{-5}	8.72×10^{-8}			0.997
1×10^{-4}	8.21×10^{-8}	1.13×10^{-7}	5.30827×10^{-8}	0.999
1×10^{-4}	1.74×10^{-7}			0.993
1×10^{-3}	2.01×10^{-7}			0.917

Table 2

Rate constants for pH = 5, SC hematite.

$[DFA]_0$ (m)	pseudo-zero[th] order rate constant (m h^{-1})	weighted average (m h^{-1})	S_d	r^2
5×10^{-6}	not applicable			
1×10^{-5}	5.15×10^{-8}	8.36×10^{-8}	2.77977×10^{-8}	0.990
1×10^{-5}	9.97×10^{-8}			0.965
1×10^{-4}	7.46×10^{-8}	2.99×10^{-7}	1.93967×10^{-7}	0.988
1×10^{-4}	4.11×10^{-7}			0.996
1×10^{-3}	1.60×10^{-7}	1.66×10^{-7}	9.05097×10^{-9}	0.980
1×10^{-3}	1.73×10^{-7}			0.969
1×10^{-3}	-6.48×10^{-9}			0.537

[hematite] = 0

Table 3

Rate constants for pH = 6, SC hematite.

$[DFA]_0$ (m)	pseudo-zeroth order rate constant (m h^{-1})	weighted average (m h^{-1})	S_d	r^2
0	-1.39×10^{-9}			0.465
1×10^{-5}	3.02×10^{-8}			0.957
1×10^{-4}	5.32×10^{-8}			0.962
1×10^{-3}	6.75×10^{-8}	9.91×10^{-8}	4.475×10^{-8}	0.977
1×10^{-3}	1.31×10^{-7}			0.986
1×10^{-3}	1.66×10^{-10}			0.554

[hematite] = 0

Table 4

Rate constants for pH = 7, SC hematite.

[DFA]$_0$ (m)	pseudo-zeroth order rate constant (m h^{-1})	weighted average (m h^{-1})	S$_d$	r^2
0	-6.11 x 10^{-10}			0.0294
1 x 10^{-6}	not applicable			
1 x 10^{-5}	4.86 x 10^{-8}	6.24 x 10^{-8}	1.19991 x 10^{-8}	0.980
1 x 10^{-5}	6.93 x 10^{-8}			0.889
1 x 10^{-4}	7.46 x 10^{-8}	1.37 x 10^{-7}	5.41543 x 10^{-8}	0.976
1 x 10^{-4}	1.68 x 10^{-7}			0.995
1 x 10^{-3}	1.29 x 10^{-7}			0.978
1 x 10^{-3}	-3.24 x 10^{-9}			0.696

[hematite] = 0

Table 5

Rate constants for pH = 8, SC hematite.

[DFA]$_0$ (m)	pseudo-zeroth order rate constant (m h^{-1})	weighted average (m h^{-1})	S$_d$	r^2
0	-5.77 x 10^{-10}			0.0347
1 x 10^{-5}	1.92 x 10^{-8}			0.709
1 x 10^{-4}	7.05 x 10^{-8}			0.978
1 x 10^{-3}	1.64 x 10^{-7}	1.23 x 10^{-7}	5.72488 x 10^{-8}	0.991
1 x 10^{-3}	8.26 x 10^{-8}			0.977

Table 6

Rate constants for pH = 9, SC hematite.

[DFA]$_0$ (m)	pseudo-zeroth order rate constant (m h^{-1})	r^2
1 x 10^{-5}	2.72 x 10^{-8}	0.951
1 x 10^{-4}	4.89 x 10^{-8}	0.991
1 x 10^{-3}	1.03 x 10^{-7}	0.981
1 x 10^{-3}	-5.22 x 10^{-10}	0.0207

[hematite] = 0

The data from these tables elicit a few important observations. As in the sol gel hematite, there is no observable dissolution for the blank experiments in which [DFA] = 0. For 5 < p_aH < 7, the pseudo-zero[th] order rates are greater for $[DFA]_0 = 10^{-4}$ m than for $[DFA]_0 = 10^{-3}$ m. Finally, the variation in rates for a particular set of experimental conditions can be quite large.

That the blank experiments yield no discernible dissolution simply reconfirms that dissolution is dominated by the DFA mechanism. The second observation is more troubling. One expects that the increase in [DFA] would yield an increased dissolution rate. Note that the variance in the reported rates renders the difference between the rates for which the pseudo-zero[th] order rates are greater for $[DFA]_0 = 10^{-4}$ m than for $[DFA]_0 = 10^{-3}$ m statistically insignificant. Nonetheless, even assuming that there is no difference between the rates in these cases, the observation must be examined. This phenomenon is not observed for the sol gel hematite dissolution. However, the BET specific surface area of the sol gel hematite is 23.0 m^2 g^{-1}, whereas that of the SC hematite is 13.5 m^2 g^{-1}. If it is assumed that the dissolution-active surface site density is equivalent for the two hematite preparations, then it is expected that the total number of dissolution-active sites for the SC hematite would be 60% less than for the sol gel preparation. The SC hematite sites may have reached adsorption saturation at [DFA] = 10^{-4} m. If this is the case, there should be no difference in pseudo-zero[th] order rates between $[DFA]_0 = 10^{-4}$ m and $[DFA]_0 = 10^{-3}$ m.

Finally, the large variance in some of the reported data must be addressed. The only variable that was not under control was the composition of the actual hematite sample introduced into each reaction vessel. All the samples were taken from the same hematite preparation, but some internal variation may have existed that was amplified by the lyophilization process. The lyophilized product was divided into powder and some clumped material. The clumped material may have had an intrinsically different sized distribution; or, from figure 1, the material may have preferentially divided into the needles and the platelets. The self-consistency of the data indicates that the systematic errors have been minimized, although a few anomalous points exist on the dissolution curves.

For $[DFA]_0 < 10^{-5}$ m, the dissolution reaction goes to completion over the time scale of the experiments. For these experiments, as in the equivalent experiments for the sol gel hematite, the assumption of excess [DFA] fails, and the expression of rate as a pseudo-zero[th] order constant is inappropriate. The observed FA in solution results predominantly from the dissolution of the kinetically low energy sites, as observed in the sol gel hematite dissolution.

5.5.2 Dissolution Mechanism

As proposed in the discussion of the dissolution of the sol gel prepared hematite, it is hypothesized that the dissolution reaction can be represented by the following reaction scheme:

$$H_i DFA \;\; + \;\; \equiv FeOH_j \;\;\; \leftrightarrow \;\;\; \equiv Fe-H_{i-1}DFA \;\; + \;\; OH_{j+1} \qquad \text{(adsorption)} \qquad (1)$$

$$\equiv Fe-H_{i-1}DFA \;\; + \;\; H_2O \;\;\; \rightarrow \;\;\; Fe-H_{i-1}DFA \;\; + \;\; \equiv FeOH_2^+ \qquad \text{(dissolution)} \qquad (2)$$

where reaction (1) is assumed to be fast relative to the time scale of the dissolution reaction. There will exist a distribution of protonation states of the surface and the solution species. These are assumed to attain pseudo-equilibrium states relative to the time scale of dissolution. Thus, it is assumed that equation 2 describes the rate-limiting step for the dissolution reaction. As in the case of the sol gel hematite, the rate expression can be written as a pseudo-first order reaction:

$$R = \frac{d[Fe]_{tot}}{dt} = \sum_i k_i [\equiv Fe-H_i\text{-}DFA^{(i-3)}] \qquad (3)$$

or as a pseudo-zero$^{\text{th}}$ order reaction:

$$R_i = k' \qquad (4)$$

for the region of the dissolution curve for which [DFA] is in excess.

Figure 10 shows the results from the dissolution experiments expressed as the log of the pseudo-zero$^{\text{th}}$ order rate constant as a function of pH. In this presentation of the data, the anomalously high values for the $[DFA]_0 = 10^{-4}$ m have been removed. When this is done,

the data appear well-behaved, and there is no need to invoke a surface saturation condition. The experiment depicted in figure 11 supports this approach.
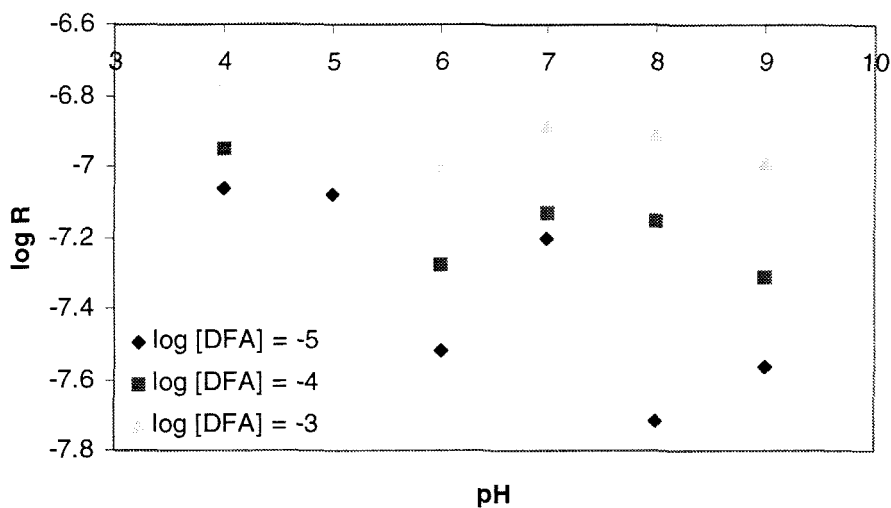
Figure 10

Pseudo-zero[th] order dissolution rates for SC hematite expressed as log R vs. pH, [DFA] = 10^{-5}, 10^{-4}, 10^{-3} m.

One further dissolution experiment was performed to test the hypothesis that the dissolution reaction is a surface mediated reaction. For this experiment, the concentration of hematite was varied from 1.00 g kg^{-1} to 0.10 g kg^{-1}. The concentration of DFA was 0.001 m. If the dissolution reaction is surface mediated, it would be expected that the rate of reaction would correlate positively with the concentration of hematite. If the dissolution-active surface sites are saturated for both of the experiments, then the observed pseudo-zero[th] order rate constant of the 0.1 g kg^{-1} suspension should be directly proportional to that of the 1.00 g kg^{-1} suspension. However, if the dissolution-active

surface sites are saturated for the low [hematite] experiment, yet no for the high [hematite] experiment, then the rates need not be directly proportional. The observed rates vary by a factor of 2.9, not 10. This observation suggests that the surface is saturated for the [hematite] = 0.10 g kg^{-1} case but not for the [hematite] = 1.00 g kg^{-1} case. Thus, it is consistent with this result to ignore the anomalous data for which the pseudo-zeroth order rate does not positively correlate with [DFA].
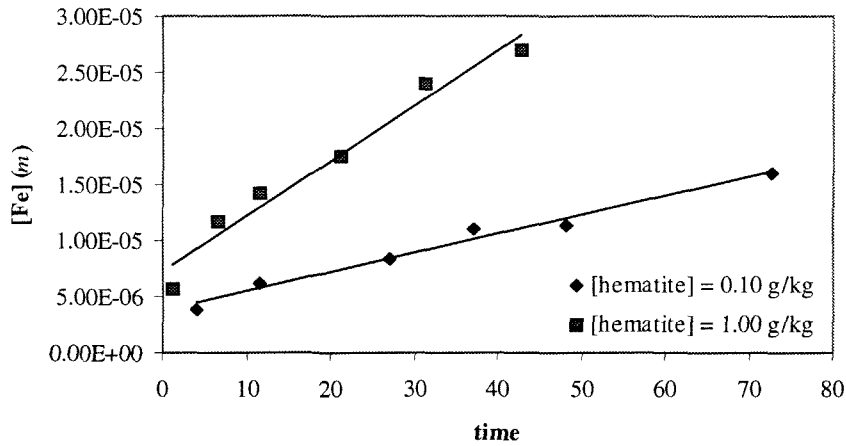
Figure 11

Dissolution of SC hematite with [hematite] varying by a factor of 10. [DFA] = 10^{-3} m. The rates vary by a factor of 2.9.

5.6 pH Data

For one set of experiments wherein the pH varied from pH = 4 to pH = 8 and [DFA]$_0$ = 10^{-3} m, the [OH$^-$] and [H$^+$] required to maintain a constant pH was closely monitored

using the pH stat described in chapter 3. Figure 12 shows the dissolution curves and figures 13 through 17 show the results of these observations. The pH stat data for pH = 9 was lost due to a hard disk error.
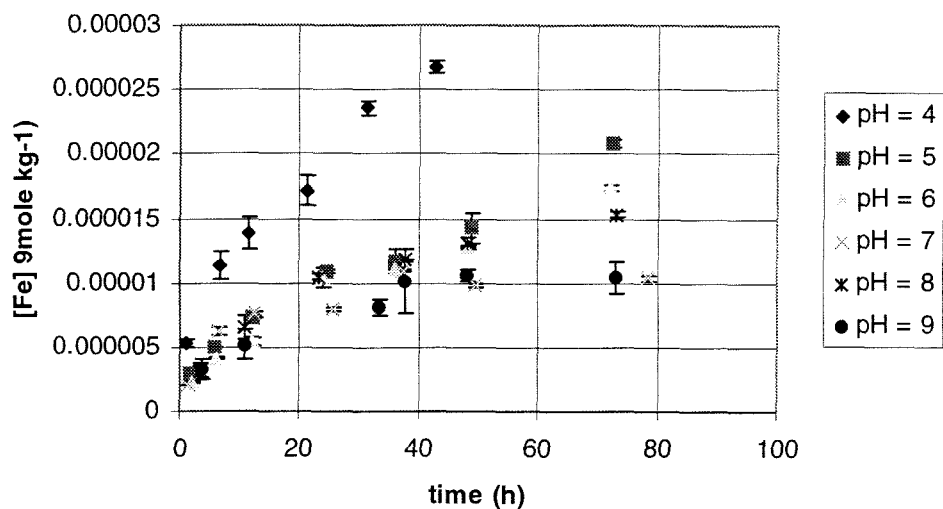
Figure 12

Propeller-stirred, pH-stat dissolution reaction. T = 25°C[DFA]$_0$ = 10^{-3} m, pH varies, [hematite] = 1.00 g kg^{-1}.
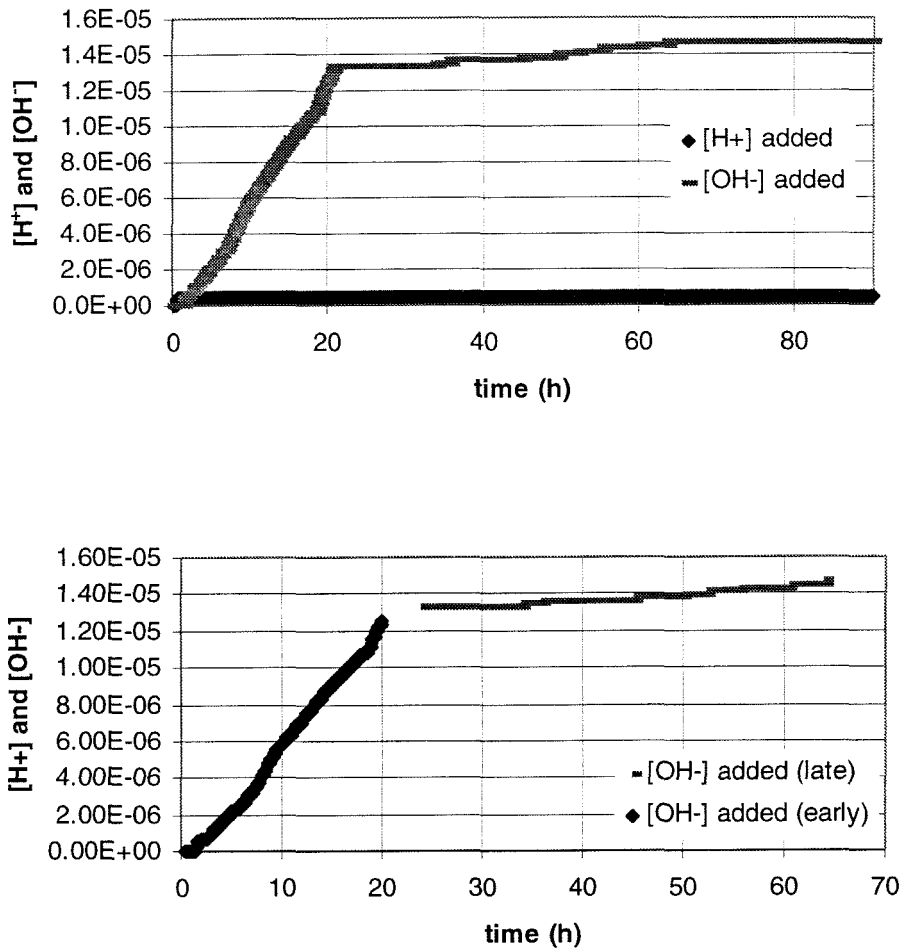
Figure 13

Additions of acid and base as a function of time; pH = 4.

(a.) Raw data.

(b.) Linear fit for early data and late data. $R_{early} = 6.59 \times 10^{-7}$ mol_{OH^-} kg^{-1} h^{-1}; $R_{late} = 3.31 \times 10^{-8}$ mol_{OH^-} kg^{-1} h^{-1}.
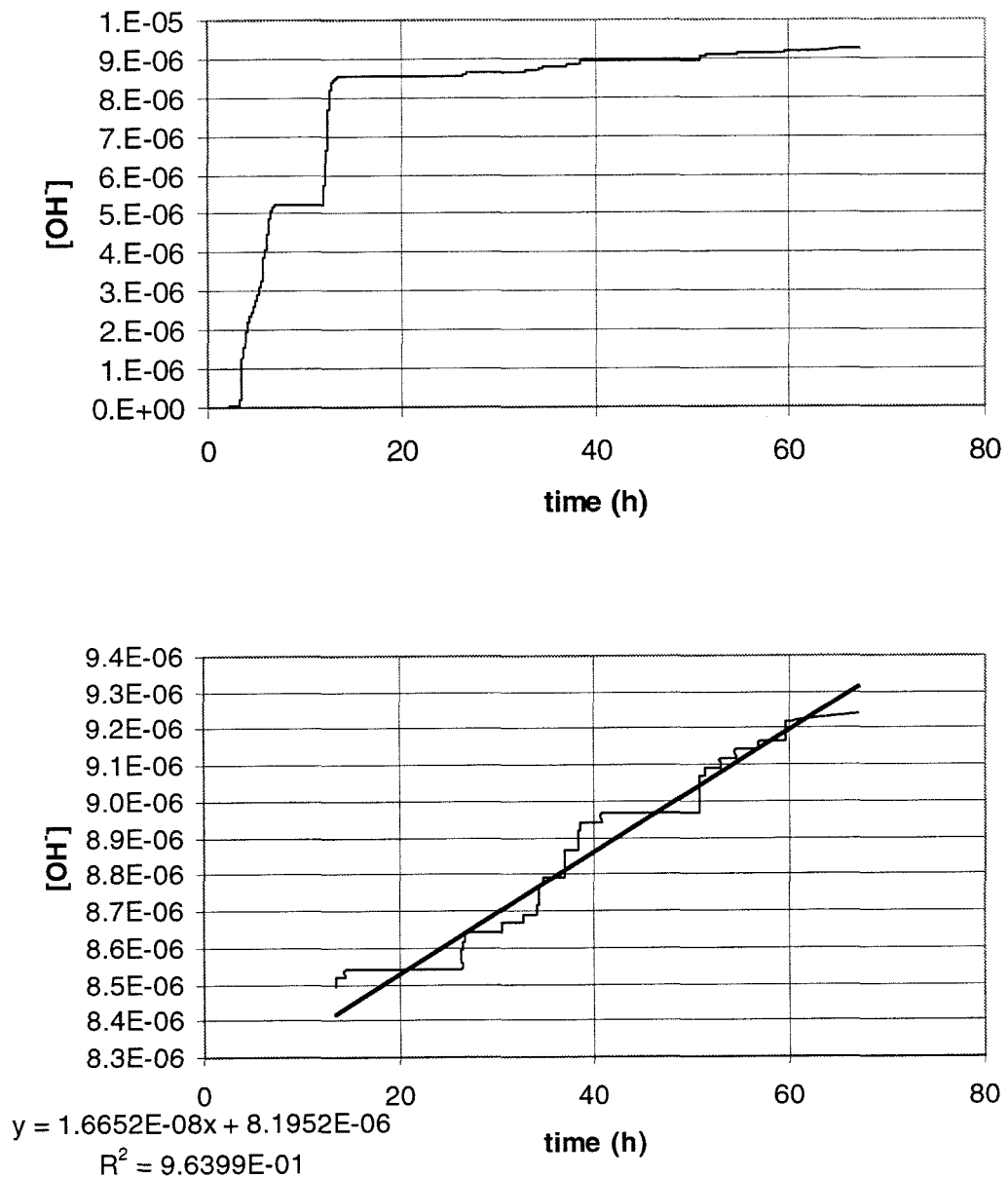
Figure 14

Additions of acid and base as a function of time; pH = 5.

(a.) Raw data.

(b.) Linear fit for early data and late data. R_{early} = undetermined; R_{late} = 1.67 x 10^{-8} mol_{OH^-} kg^{-1} h^{-1}.

(a.)

(b.)

(c.)

(d.)

$y = 2.7039E-05x + 1.3274E-05$
$R^2 = 9.3021E-01$

$y = 1.1415E-07x + 1.0463E-04$
$R^2 = 9.5321E-01$

$y = 0.0331x - 4.0128$
$R^2 = 0.9986$
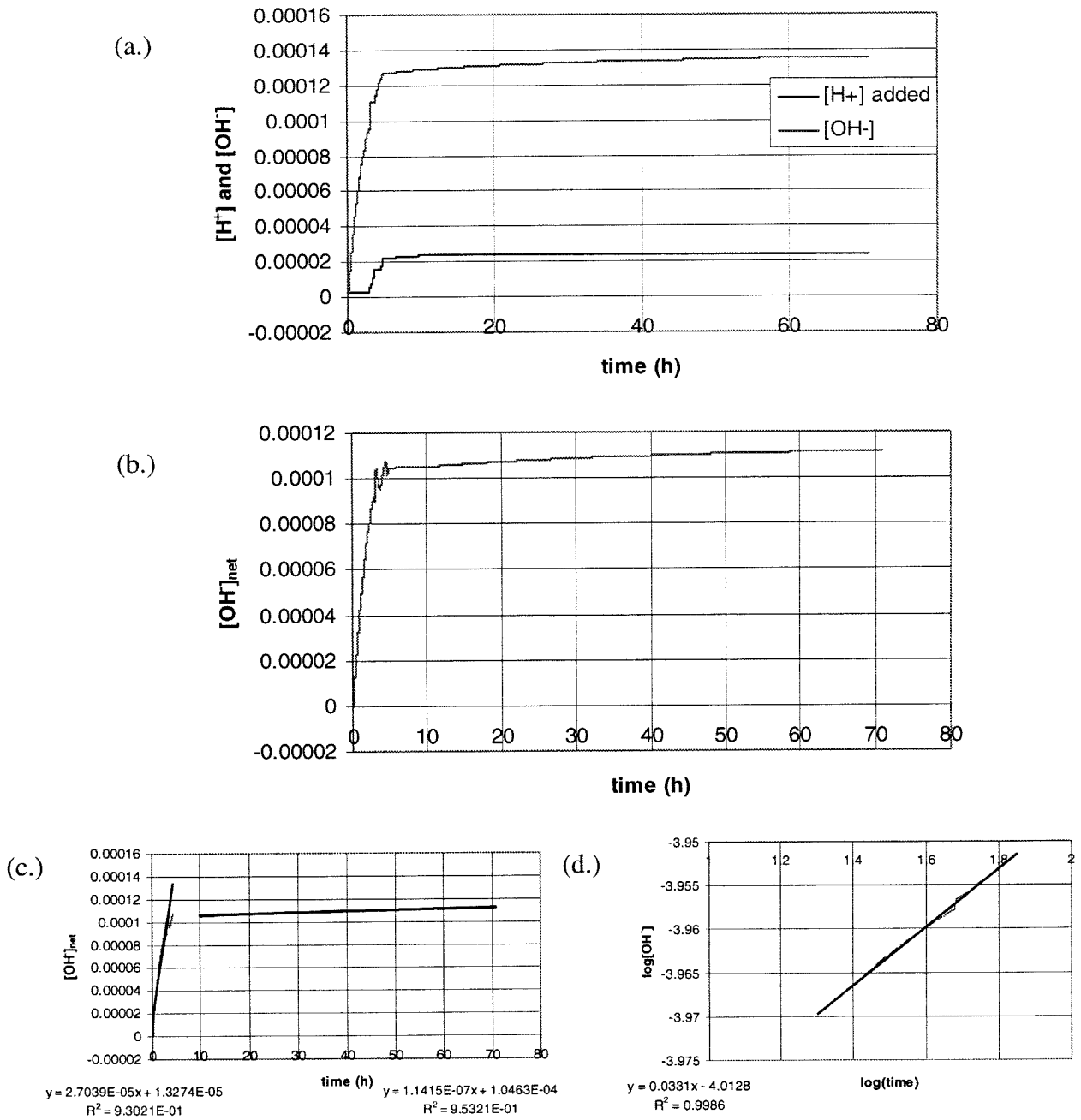
Figure 15

Additions of acid and base as a function of time; pH = 6.

(a.) Raw data.

(b.) $[OH^-]_{net} = [OH^-] - [H^+]$.

(c.) Linear fit for early data and late data. $R_{early} = 2.70 \times 10^{-5}$ mol_{OH^-} kg^{-1} h^{-1};
$R_{late} = 1.14 \times 10^{-7}$ mol_{OH^-} kg^{-1} h^{-1}.

(d.) Fit of the data to $log[OH^-]$ as a function of $log(t)$.

(a.)

(b.)
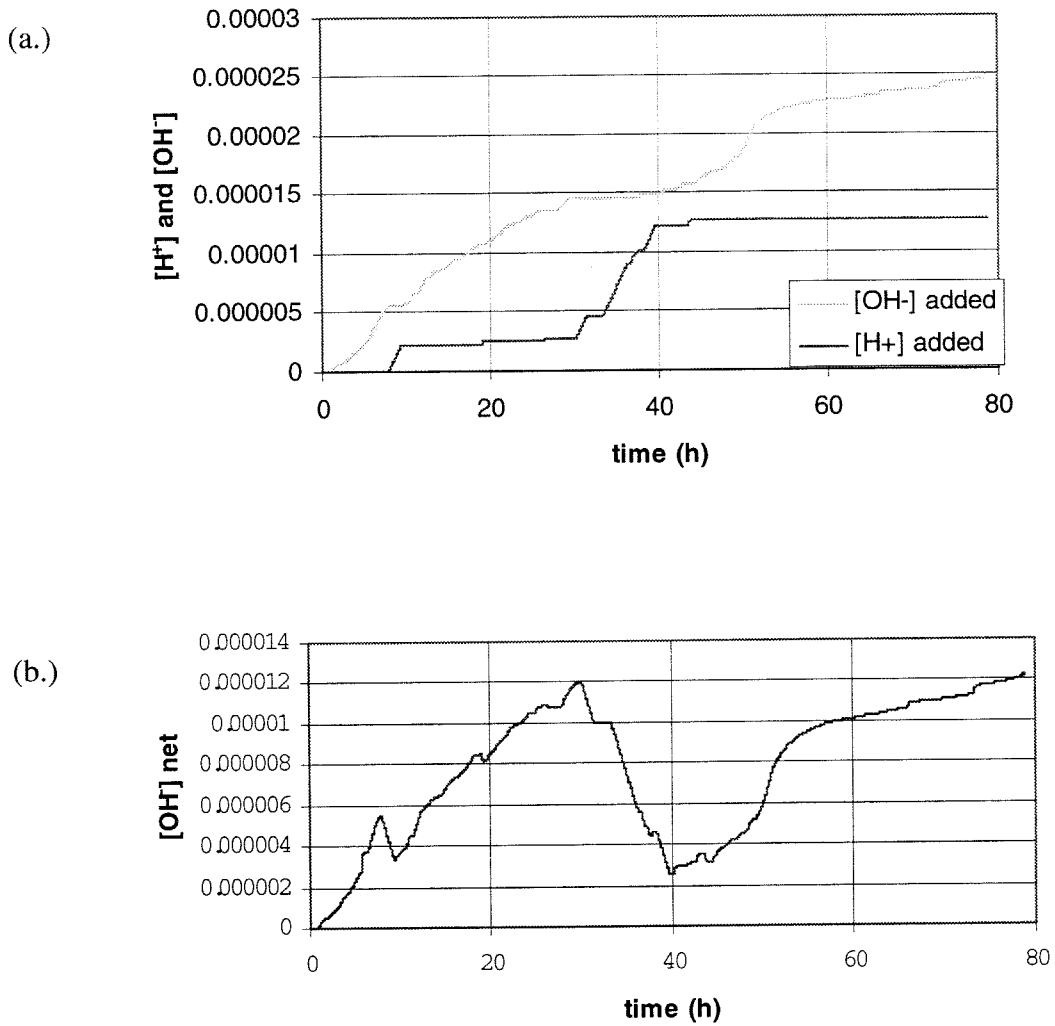
Figure 16

Additions of acid and base as a function of time; pH = 7.

(a.) Raw data.

(b.) $[OH^-]_{net} = [OH^-] - [H^+]$.

No obvious rate relationship can be concluded from the data.

(a.)

(b.)

$y = 5.1331E\text{-}07x + 6.2192E\text{-}06$

$R^2 = 9.9545E\text{-}01$

(c.)

$y = 0.8444x - 5.9044$

$R^2 = 0.9955$
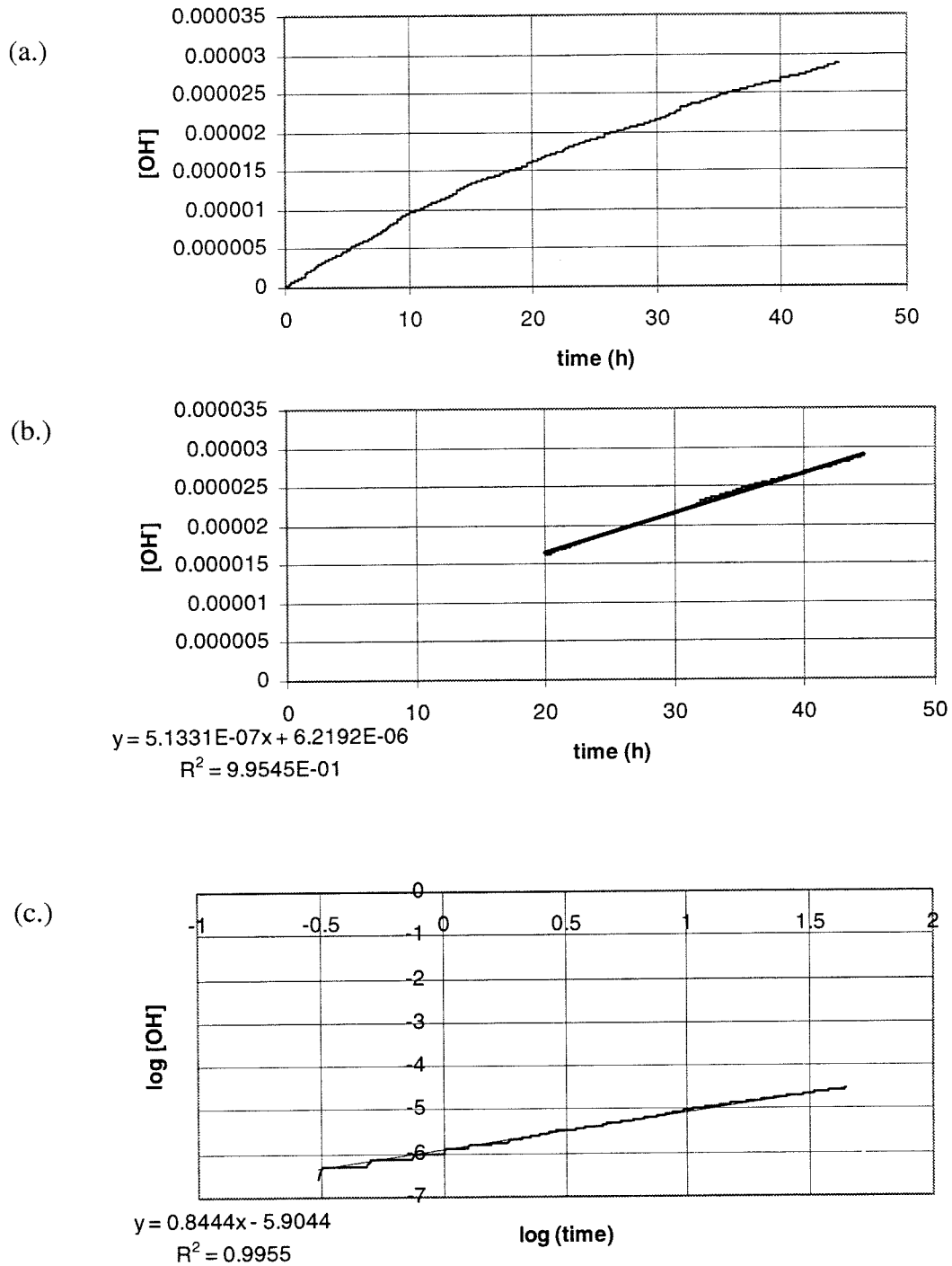
Figure 17

Additions of acid and base as a function of time; pH = 8.

(a.) Raw data.

(b.) Linear fit to late time data; $R_{late} = 5.133 \times 10^{-7}$ mol_{OH^-} kg^{-1} h^{-1}.

(c.) Fit of the data to log [OH⁻] as a function of log (t).

The data exhibit two obvious trends. First, there is a net addition of base, regardless of the pH of the system. Second, for pH = 4, 5, and 6 there exists a fast initial rate of addition of base, followed by a striking leveling off. The data for pH = 7 seem erratic, possibly because of the fact that the system is unbuffered at this pH. The pH = 8 data shows a slight decrease in rate of addition over the time scale of the experiment, but seems to indicate a relatively constant rate of addition. The data are also not corrected for the change in total volume resulting from sample removal. If the error resulting from this were significant, the data would be punctuated with spikes at the sampling times; this is not observed, therefore it can be assumed that the change in total volume is not significant.

Since the first pK_a of DFA is 8.39 and the first pK_a of FA is 0.94, for pH's less than or equal to 7 it is expected that the DFA molecule will give up three protons to the system upon binding Fe(III). The surface Fe(III) is six-coordinate with bulk oxide atoms and surface waters of hydration. Upon adsorption of the DFA, two of these covalent oxide bonds are hypothesized to be displaced by the DFA interaction. However, upon removal of the surface Fe(III) as a result of the dissolution step, shown in equation 2, the surface must reform its hydration state, and the net result will be the removal of two oxide atoms. Depending on the protonation state of the surface, there will be a net gain or loss of protons in solution resulting from the removal of the two oxide atoms. At pH < pH_{pznpc} there will be a net addition of protons to the solution, while at pH > pH_{pznpc} there will be a net loss of protons from solution. However, the protonation state of the surface must

reestablish itself in pseudo-equilibrium. The surface oxides that are bared as a result of the removal of the surface Fe must re-equilibrate with the solution. At a given pH there must be a net addition of protons onto these surface oxides that is sufficient to maintain the average protonation state of the surface as defined by the pH of the system. For example:

$$\equiv Fe(-O-)_2 H_2 + H_3 DFA \quad \rightarrow \quad \equiv Fe - HDFA + 2H_2 O$$

$$\equiv Fe - HDFA \quad \rightarrow \quad \equiv \quad + \quad Fe - DFA + H^+ \tag{5}$$
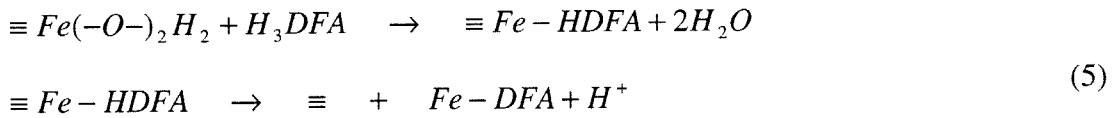
where the notation (-O-) refers to the surface oxides bound to the dissolution-active surface Fe, and "$\equiv$" refers to the surface that remains upon removal of the oxide; i.e.,

$$\equiv \quad = \quad \equiv Fe(-O-)_2 \tag{6}$$

and the protonation state of these remaining oxides must be energetically consistent with the pH of the system. Thus, for example, at pH = 8, it is expected that

$$\equiv Fe(-O-)_2 + 2H^+ \quad = \quad \equiv Fe(-O-)_2 H_2 \tag{7}$$
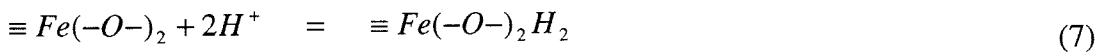
As the pH approaches 8.40, the aqueous speciation of DFA becomes dominated by the H_3-DFA species, which generates a net loss of one proton as illustrated in equations 5 through 7. As the surface charge density becomes more positive with decreasing pH, it is expected that the demand by the system for OH^- will increase.

Figure 18 compares the rate of hydroxide utilization to the rate of dissolution as a function of pH. The rates appear to be anticorrelated, with the rate of hydroxide utilization increasing with increasing pH. There is no clear relationship generated from these data. In particular, by examining the hydroxide data above, it is clear that there are at least two regions in the dissolution time frame that indicate different mechanisms for reaction. The initial fast rate of hydroxide utilization is followed by a much slower rate, indicating that there may be two completely different surface configurations involved in the dissolution reaction, the early time configuration being more labile than the late time configuration.

(a.)

(b.)
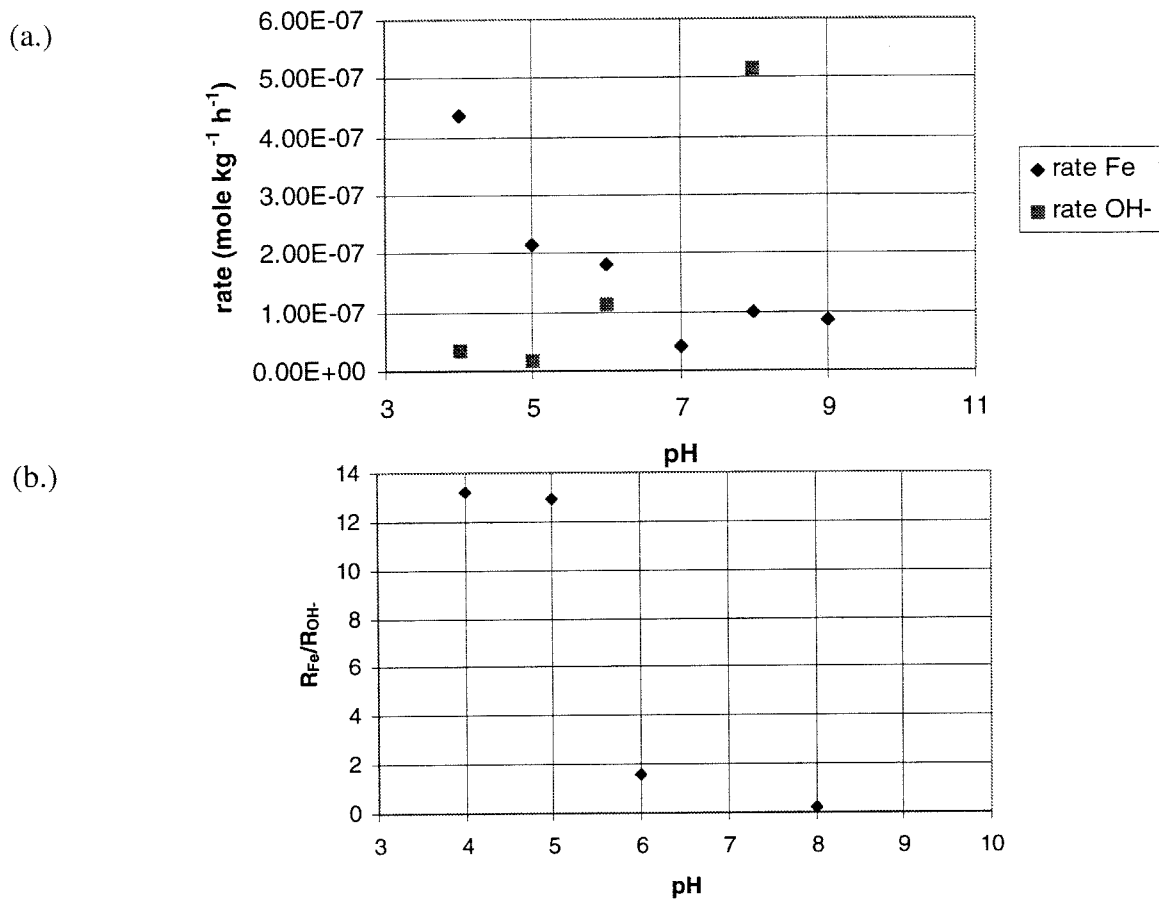
Figure 18

Comparison of the rate of hydroxide utilization to the pseudo zero[th] order dissolution rate constant for SC hematite by DFA. (a.) Rates compared; (b.) ratio R_{Fe} to R_{OH^-}.

5.7 Conclusion

The rates of dissolution of SC hematite are comparable to the sol gel hematite dissolution rates when corrected for surface area. The dissolution of SC hematite also varied little as a function of pH. Some data indicate that the rates plateau at $[DFA]_0 = 10^{-4}$ m, suggesting that the surface becomes saturated at this concentration. However, the data from the low [hematite] experiment contradicts this suggestion. Therefore, the plateau at $[DFA]_0 = 10^{-4}$ is considered to be an anomaly.

Further work needs to be performed to elucidate the detailed proton dependence of the reaction. It is not clear what role the goethite impurity plays in the dissolution reaction. However, data presented in chapter 6 indicates that the rates of dissolution of goethite are less than for hematite, suggesting that perhaps the hematite is preferentially mined during the dissolution reaction. The XRD spectra in figure 3 show no definitive proof of this, however.

The area-based rates of dissolution at pH = 4 for the SC hematite are comparable to the rates observed by Hersman et al. for their pseudomonad (11C) siderophore (Hersman et al., 1995). They observe a pseudo-zero[th] order are-based rate of dissolution of 10^{-8} mole m^{-2} h^{-1} at pH = 3, for a siderophore concentration of 0.24 mmol kg^{-1}. The rate for the SC hematite and DFA is 1.3 x 10^{-8} mole m^{-2} h^{-1} at pH = 4. The 11C siderophore is also a hydroxamic acid siderophore, and the agreement of rates suggests a similar dissolution activity as DFA.

Chapter 6

Dissolution of Synthetic Manganite and Pyrolusite

6.1 Introduction

In environments where the rate of vertical mixing is slow with respect to the time scale of microbial metabolism, such as lake and marine sediments and stratified water columns, microorganisms establish a characteristic steady-state profile of electron donors and acceptors. As oxygen is depleted in aerobic respiration, other electron acceptors are utilized in a sequence defined by the free energy of the particular donor-acceptor pair, starting preferentially with the most exergonic couple. The oxidants, O_2, NO_3^- and SO_4^{2-}, are observed, and are utilized by microorganisms as terminal electron acceptors in cellular respiration. Mn(II) and Fe(II) are also observed, suggesting the utilization of Fe(III) and Mn(IV) as electron acceptors for respiration. A large number of organisms have been identified that utilize the oxidized form of at least one of these metals as terminal electron acceptors ((Ehrlich, 1996), (Nealson and Little, 1997)).

In order to utilize Mn(IV) for respiration, the organism must first access the Mn that is bound in $MnO_2(s)$. Equation (1) shows that the solubility of $MnO_2(s)$ as Mn^{2+} depends strongly on the p_aH and the reducing potential of the system.

$MnO_2 + 4H^+ + 2e^- = Mn^{2+} + 2H_2O$ log K = 41.38 (Stumm and Morgan, 1996)
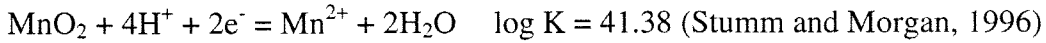
$$K = \frac{\{Mn2+\}}{10^{-4pH}10^{-2p\varepsilon}}$$ (1)

$log\{Mn^{2+}\} = 41.38 - 4pH - 2p\varepsilon$

It is this reducing potential that is captured by the bacteria through the oxidation of organic electron donors.

Besides being an important electron acceptor in anoxic microbial systems, Mn plays a significant role in intracellular processes. Mn is found as an activator in many enzymes, and occurs in certain superoxide dismutases and photosystem (II), generating a nutritional requirement for soluble Mn in oxic environs. If a ligand-free model is created wherein $[Mn^{2+}]$ is controlled by $MnO_2(s)$ and $[O_2]$ is fixed by atmospheric P_{O_2}, and the p_aH is fixed at 10, then log $[Mn^{2+}] = -20$ at equilibrium. This vanishingly small concentration suggests that there exists approximately 6 x 10^3 atoms of Mn per liter of water, hardly sufficient to support an actively reproducing microbial population for whom the average [Mn] is on the order of 30 ppm$_{mass\ per\ dry\ weight}$ (3 x 10^{17} molecules Mn per gram bacteria) (Beck (1978)). Thus, it is clear that mechanisms must have evolved to solubilize Mn in alkaline waters.

It thus becomes important to ask about the role of biogenic molecules in the redox cycling of manganese in natural waters: do there exist microbially produced compounds that stabilize Mn(III) or Mn(IV)? Can a biogenic compound solubilize Mn-oxyhydroxides at environmentally significant p_aH's such as $p_aH \geq 7$? This chapter presents data that illustrates the dissolution of a synthetic manganite phase in the

presence of DFA at $7 \geq p_aH \geq 9.5$. The data will show that the dissolution occurs rapidly relative to hematite dissolution, and results in a highly stable Mn(III) – DFA complex in solution.

6.2 Manganite Synthesis

Manganite (γ-MnOOH) was synthesized according to the Giovanoli procedure (A. Stone, personal communication). The recipe is as follows: 20.4 g 8.82 M H_2O_2 was sparged with N_2, and added to 1000.0 g of N_2 sparged 6.0 x 10^{-2} m $MnSO_4$ at 25°C. While rapidly stirring with a magnetic stirrer, 300.0 g of N_2 - sparged 2.0 x 10^{-1} m NH_3 was then added. The solution was placed in a 95°C water bath for rapid heating and then in a 95°C oven for six hours. The solution was cleaned by washing the solid with 2.0 l of 95°C MQW in a vacuum filter apparatus. The product was lyophilized, kept tightly sealed and stored in the freezer.

6.3 Particle Characterization

Figure 1 is a TEM of the MnOOH; samples were prepared as described above. The dimensions of the particles from the TEM micrographs are 500-750 nm x 50 nm x 25 nm. The surface area calculated by sampling the particle sizes and geometries on the set of micrographs generates a surface area of approximately 28 m^2 g^{-1}. The manganite particles are fine fibrous needles that seem to be highly aggregated before sonication. The TEM diffraction pattern indicated that the needles were monocrystalline.

Powder x-ray diffraction (XRD) (Siemens D500 with Cu K_α (λ = 1.542Å) radiation)
generates the pattern exhibited in figure 2. As can be seen by comparing the observed
spectrum with the expected diffraction lines, the product is a very pure crystalline
preparation of γ-MnOOH, as expected.

(a.)   (b.)
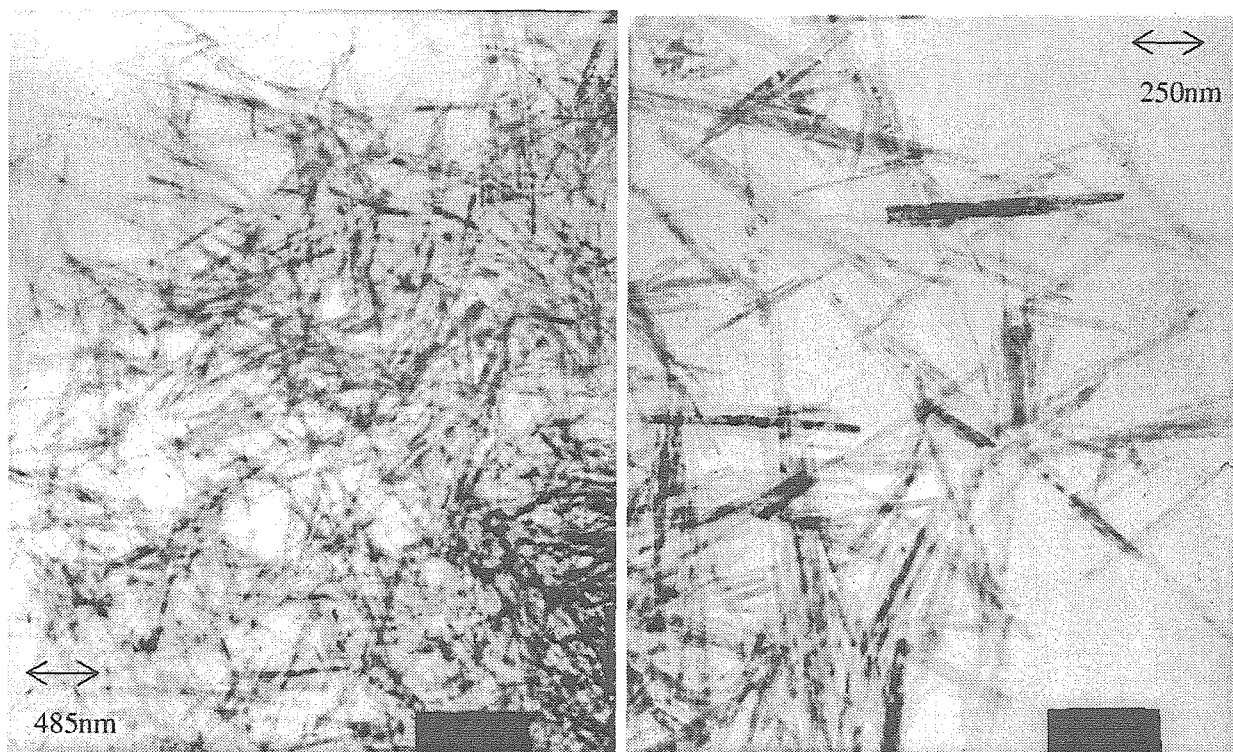
Figure 1

TEM micrograph of manganite.

(a.) 20,600 X magnification

(b.) 40,400 X magnification.
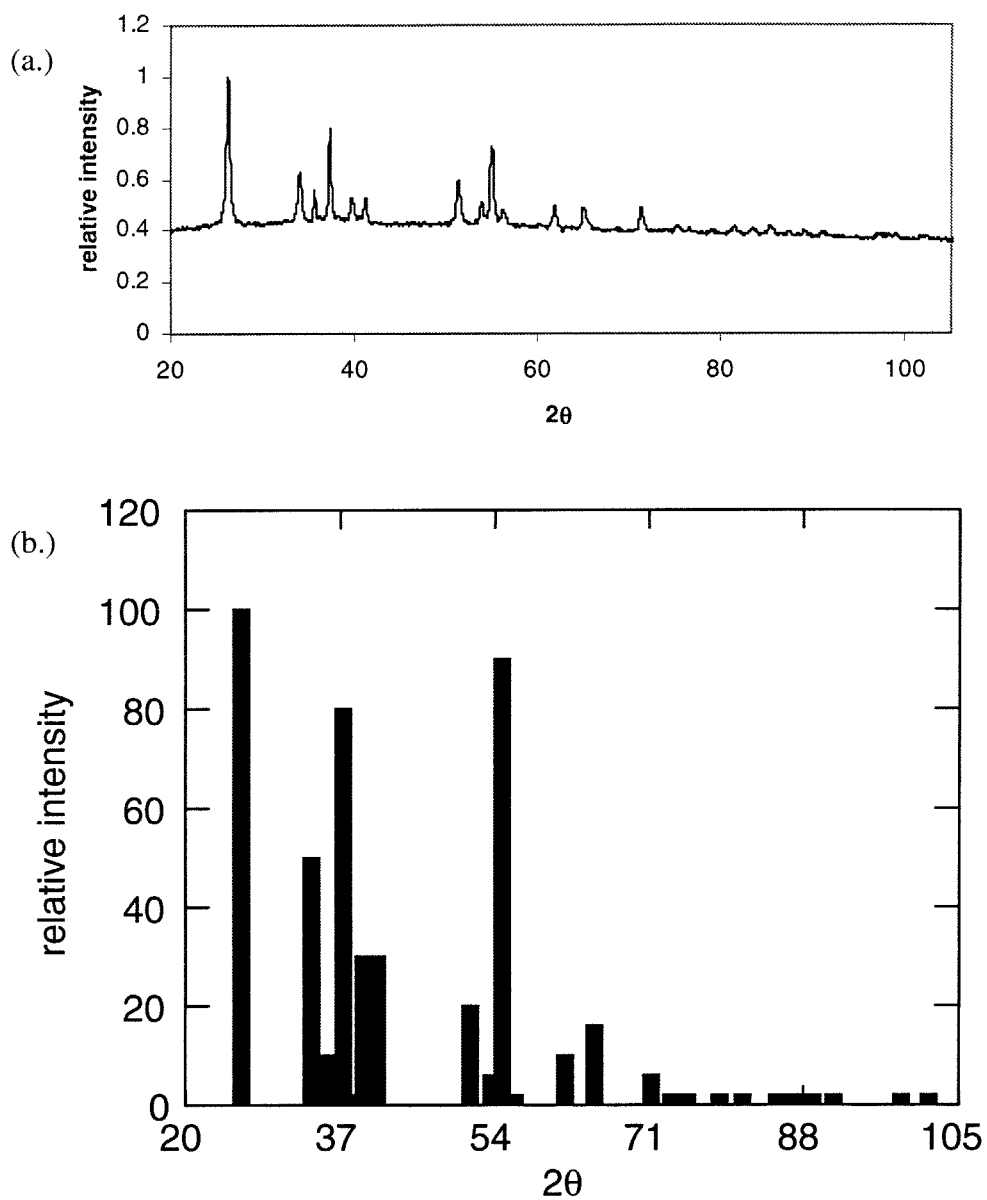
Figure 2

(a.) XRD measurement of γ-MnOOH, measured spectrum compared to

(b.) expected lines.

Figure 3 depicts the diffuse reflectance FTIR spectrum of manganite, a ratio spectrum of manganite – DFA to manganite where the values at each wavelength for the manganite – DFA spectrum are divided by the values at the same wavelength for the manganite spectrum. If DFA has adsorbed to the surface of the manganite to a significant extent, then a signal should be observed in the region in which DFA absorbs light in the infrared. The KBr spectrum of DFA is shown for reference. There is evidence in the ratio spectra that DFA adsorbs onto the surface of manganite, as shown by observing the regions centered at 3000 cm^{-1} and 1500 cm^{-1}. For preparation of the manganite – DFA sample, manganite was saturated with a solution of 10^{-4} m DFA followed by rapid vacuum filtration of the solution through the solid with an 0.2 μm cellulose acetate filter. The manganite – DFA solid material was then lyophilized and stored in the freezer until the spectra were obtained.

For the two preliminary experiments that examine the dissolution of MnO_2 by DFA, two preparations were used. One preparation was the standard prepared for the leuco crystal violet method described below, the other was purchased from Aldrich and used as prepared.
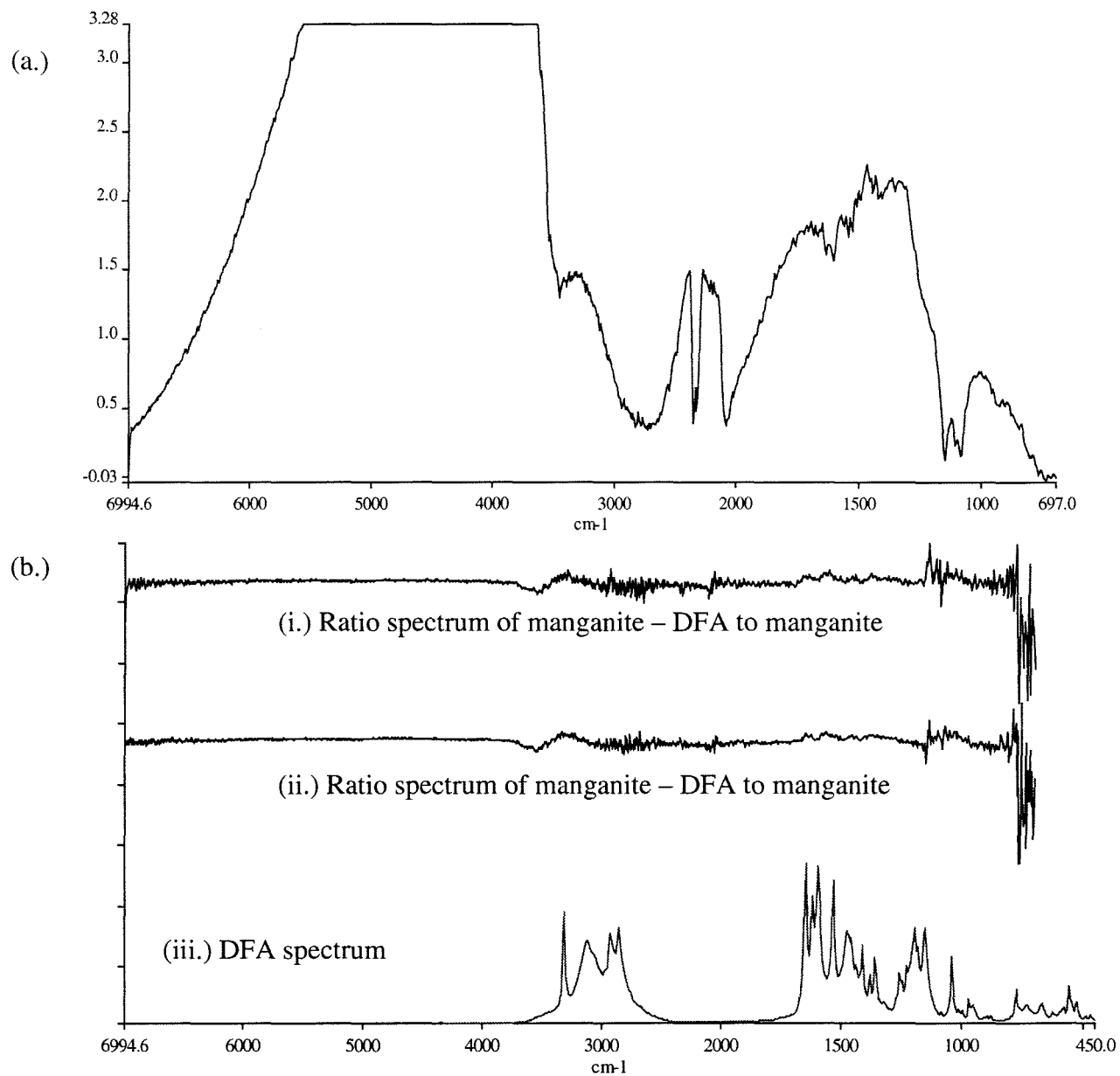
Figure 3

(a.) FTIR transmittance spectrum of γ-MnOOH.

(b.) (i.) and (ii.) Ratio spectra of manganite – DFA to manganite, with reference to

(iii.) DFA KBr pellet spectrum.

6.4 Synthesis of Mn(III) – DFA

Three approaches were developed to synthesize Mn(III) – DFA complexes. The first method relied on the stoichiometric oxidation of a solution of Mn(II) and DFA by Mn(VII). A 1.0×10^{-3} m solution of DFA with 9.80×10^{-4} m $MnCl_2$ was prepared. To this solution $KMnO_4$ of known concentration was added drop-wise. The solution was monitored by UV-visible spectroscopy, observing at 530 nm where MnO_4^- absorbs strongly. When this peak was observed to form, additions of MnO_4^- were ceased. Figure 4 shows the resulting UV-visible spectrum of the product and the absorbance at three wavelengths as a function of addition of MnO_4^-. The complex forms a yellow-green color, caused by the weak absorbance at 625 nm. Figure 5 depicts a UV-visible calibration curve for the complex, generating a molal extinction coefficient of

1.94×10^3 $m^{-1}cm^{-1}$ at 312 nm.

The second approach relied on the efficacy of DFA in dissolving Mn(III) oxides. A suspension of synthetic Mn_2O_3 (Aldrich) was prepared, to which was added DFA to bring the solution to $[DFA]_{tot} = 0.10$ m. This solution was agitated in the rotary stirrer at 200 rpm for three days, after which the suspension was filtered through Whatman 0.02 μm filters. The product of this reaction exhibited exactly the same spectrum as the Mn(III) – DFA prepared by oxidation of Mn(II) by Mn(VII) in a DFA solution.

The third approach was a simple ligand exchange reaction between Mn(III) – acetate and DFA. Mn(III) acetate dihydrate (Aldrich) was opened in an Ar atmosphere glove box and 0.38 g was transferred to a tared container. MQW was added to bring the

concentration to 2.83 x 10^{-2} *m*. 51.87 g of 3.028 x 10^{-2} *m* DFA was added to the Mn(III)

– acetate solution, generating an acetate-DFA molar ratio of 1.107.

(a.)

(b.)
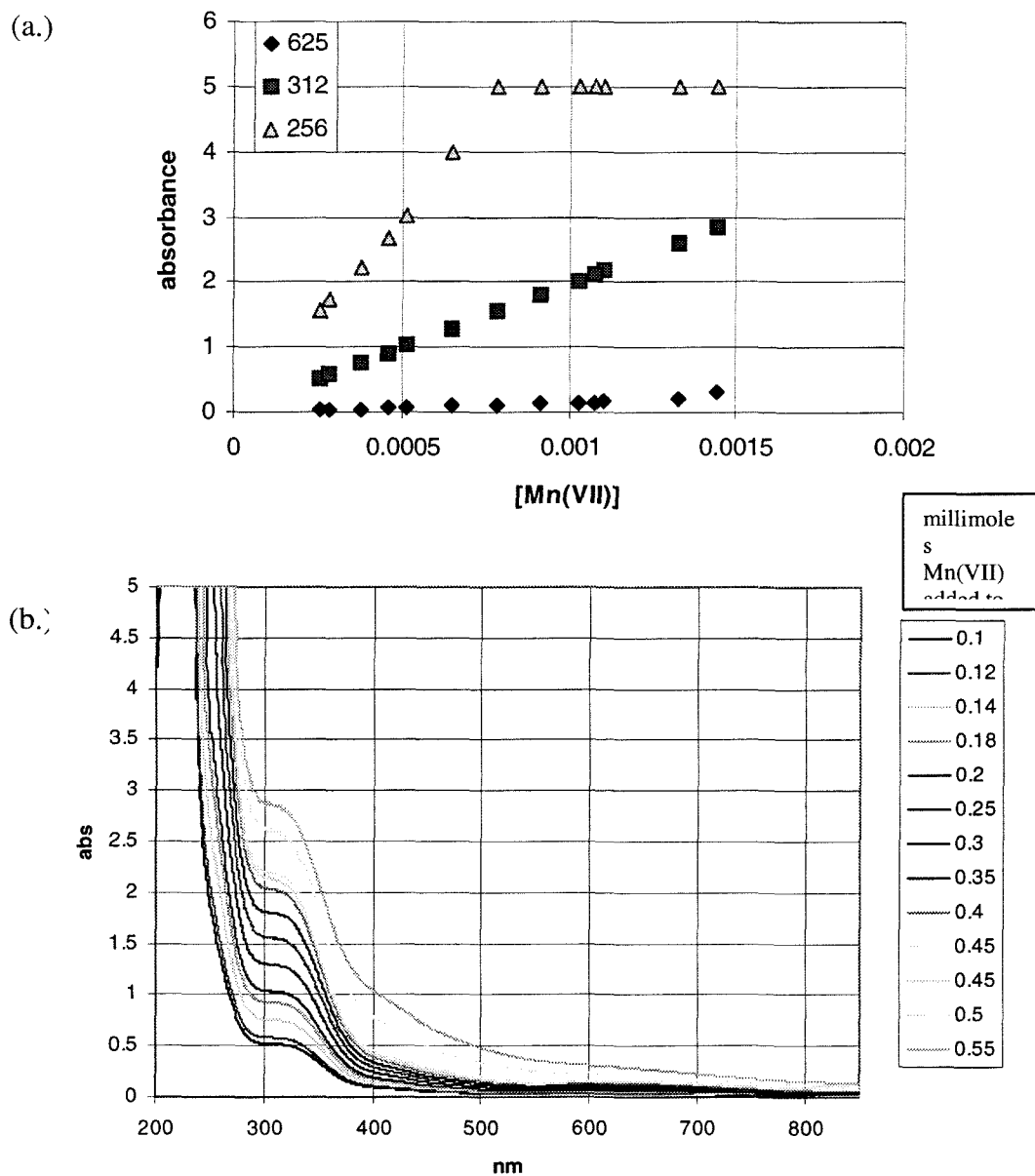
Figure 4

(a.) Absorbance of Mn-des complex at various wavelengths as a function of additions of Mn(VII) oxidizing equivalents.
(b.) Spectra showing the formation of Mn(III) – DFA complex as MnO_4^- is added to a Mn(II) – DFA solution.

Except for the acetate preparation, solutions of Mn(III) – DFA were found to be stable at room temperature and exposed to laboratory light over the time scale of months. The acetate preparation was not stable over a time scale of weeks.

Previous work characterizing the Mn(III) – DFA complex has indicated that the complex was not stable to equimolar concentrations of ethylenediaminetetraacetic acid (EDTA); also, the Mn(III) – DFA complex was bleached by Chelex-100 within minutes (Faulkner et al., 1994). In the work of Faulkner et al. work cyclic voltammetry indicated a negative shift in oxidation potential of the complexed Mn(III) (Faulkner et al., 1994). The authors also identify the complex as a one-to-one complex of DFA with Mn(III).

$y = 1.93886E+03x + 2.18794E-02$
$R^2 = 9.99259E-01$
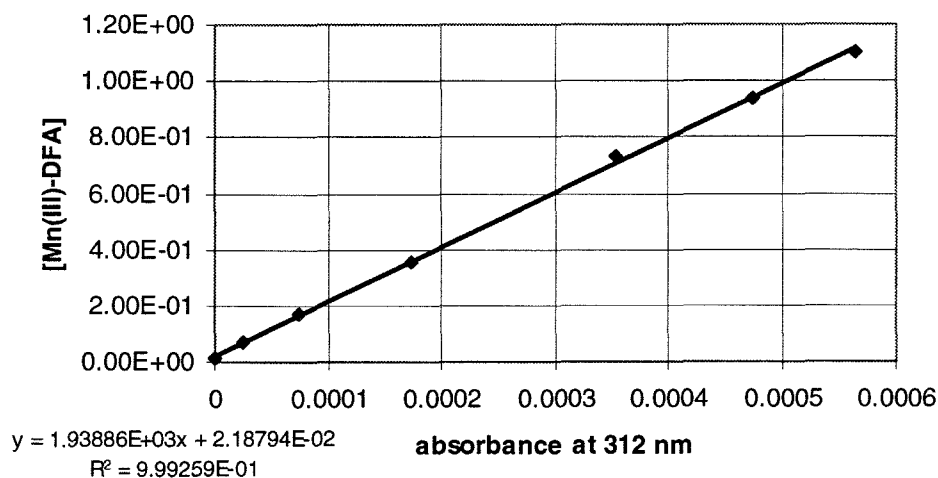
Figure 5

UV-visible calibration curve of Mn(III) – DFA at 312 nm, showing an extinction coefficient of $1.93886 \times 10^3 \ m^{-1} \ cm^{-1}$.

6.5 Leuco Crystal Violet Determination of Manganite Average Oxidation State

The leuco crystal violet (LCV) method (Kessick et al., 1972) was used for the determination of oxidized Mn titer of the manganite as the dissolution of manganite by DFA progressed. A standard suspension of MnO_2 was prepared to calibrate the method. 400.0 g of MQW and 25.0 g of 0.2 m NH_3 were combined in a 500 ml erlenmeyer flask. The solution was purged with N_2 for approximately 1 h, after which time 6.00 g of 0.12 mm $KMnO_4$ and 2.00 g of 0.10 m $MnCl_2$ were added to the solution. A brown precipitate was observed. The suspension was purged with N_2 for approximately 0.5 h, followed by the addition of 25.0 g of 0.80 m p_aH 7 phosphate buffer. The suspension was diluted to 1.00 l with MQW. The final p_aH of the suspension was fixed at 7.3 by the addition of HCl. The stock suspension contained 3.15 x 10^{-4} m Mn_{tot} and 5.92 x 10^{-4} N oxidizing equivalents.

Figure 6 depicts the calibration curve of the LCV method for the absorbance at 592 nm. In this method a 3.0 x 10^{-2} m stock solution of LCV in 0.10 m $HClO_4$ was prepared. 12.5 g of 0.001 m HCO_3^- was placed in an HDPE flask to which was added a known mass of MnO_2 suspension, 1.00 g of LCV stock solution and 1.25 g 4.0 6.0 m acetic acid – acetate stock whose p_aH was fixed at 4.0. This mixture was brought to 25.0 g with MQW. The solid was observed to have dissolved. The absorbance was measured at 592 nm on a UV-visible spectrophotometer.
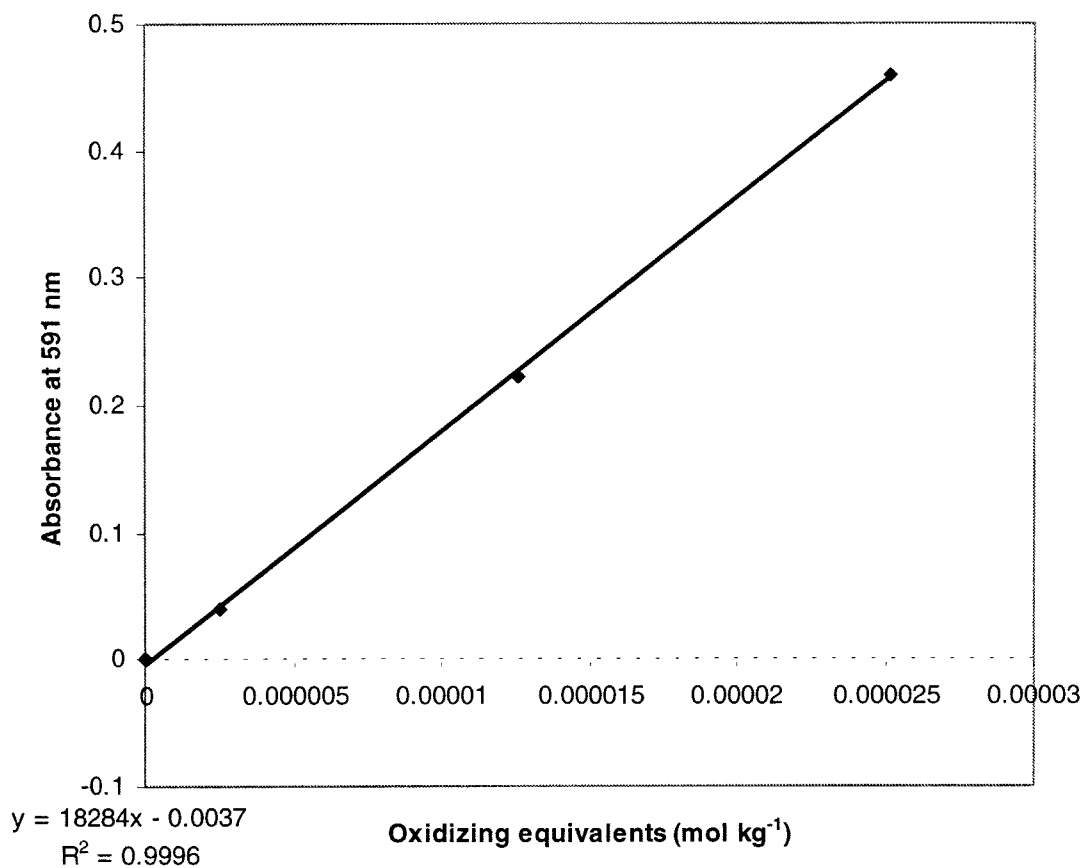
Figure 6

LCV absorbance at 592 nm as a function of dissolved [MnO$_2$].

This method was followed for the dissolution experiments for manganite, to determine whether there existed significant reduction of Mn(III) by DFA during the course of the reaction.

6.6 Dissolution Experiments

The dissolution of manganite was carried out in the jacketed beaker system described above for the sg2g hematite experiments. All reactions were carried out in the dark, and some were carried out with magnetic stirring as opposed to propeller stirring. No difference in rates of dissolution was observed due to the different stirring method. All experiments were performed under a positive pressure of N_2 and at constant temperature of 25°C. Initial experiments were performed in an unbuffered system to monitor the p_aH change of the system as a function of time or rate of dissolution. The p_aH change was rapid and extensive, resulting in a Δp_aH of > one p_aH unit over 6 h. This result suggested that a buffering system should be chosen to limit the $\Delta p_aH/\Delta t$ to negligible amounts. TRIS buffer (Baker Bio-Analyzed Ultrapure Bioreagent, 99.9% min. (anhydrous)) was chosen for this purpose, it having the appropriate buffering for the experimentally interesting p_aH range of $7 < p_aH < 9.5$. The Δp_aH for the experiments reported was less than 0.2 p_aH units over the time of the reaction.

Two preparations of MnO_2 were used in the dissolution studies of MnO_2. One was the synthetic MnO_2 described in the LCV section above and called the Lloyd preparation in further references; the other was purchased from Aldrich and used as received and called the Aldrich preparation in further references.

6.6.1 Lamp Studies for Photochemical Experiments

The redox cycling of manganese occurs in the photic zone of surface waters, and photochemical reactions are implicated in the enrichment of aqueous concentrations of

Mn (Johnson et al., 1992). Siderophores are expected to be produced in this environment

(Butler, 1998). Therefore, it is of interest to examine the stability of the Mn(III) – DFA

complex in the presence of light.

To perform these experiments a flow-through setup was used. A 365 ml jacketed vessel

having a quartz window was connected to a flow-through quartz 1 cm cell for UV-visible

detection (HP8452) via Teflon tubing and a peristaltic pump. The solution was stirred

with a magnetic stirrer. The solution was purged with O_2 or N_2 for 1 h prior to

illumination. The volume of the tubing plus the cuvet was 10 ml, and the rate of flow

was 0.9 ml s^{-1}, generating a residence time in the dead volume of ~11 s. The lamp light

was filtered with a water filled quartz windowed container acting as a UV cut-off.

6.7 Results

6.7.1 Dissolution of Manganite

Figure 7 shows the results of the LCV test for the dissolution of manganite at $p_aH_0 = 7$ in

the unbuffered system. The data show no monotonic change in the concentration of

oxidant in the system, with the average value being $3.15 \times 10^{-5} \pm 3.56 \times 10^{-6}$ equivalents

kg^{-1}. $[DFA]_0 = 1.0 \times 10^{-3}$ m. This result suggests that the DFA does not significantly

alter the net oxidation state of the γ-MnOOH over the course of the dissolution reaction.

Figure 8 shows the dissolution reaction of the unbuffered system with the initial p_aH set

at 7. The absorbance at 312 is monitored to generated the concentration of Mn(III) –

DFA. Note that the reaction seems to go to completion by approximately 24 h, in the
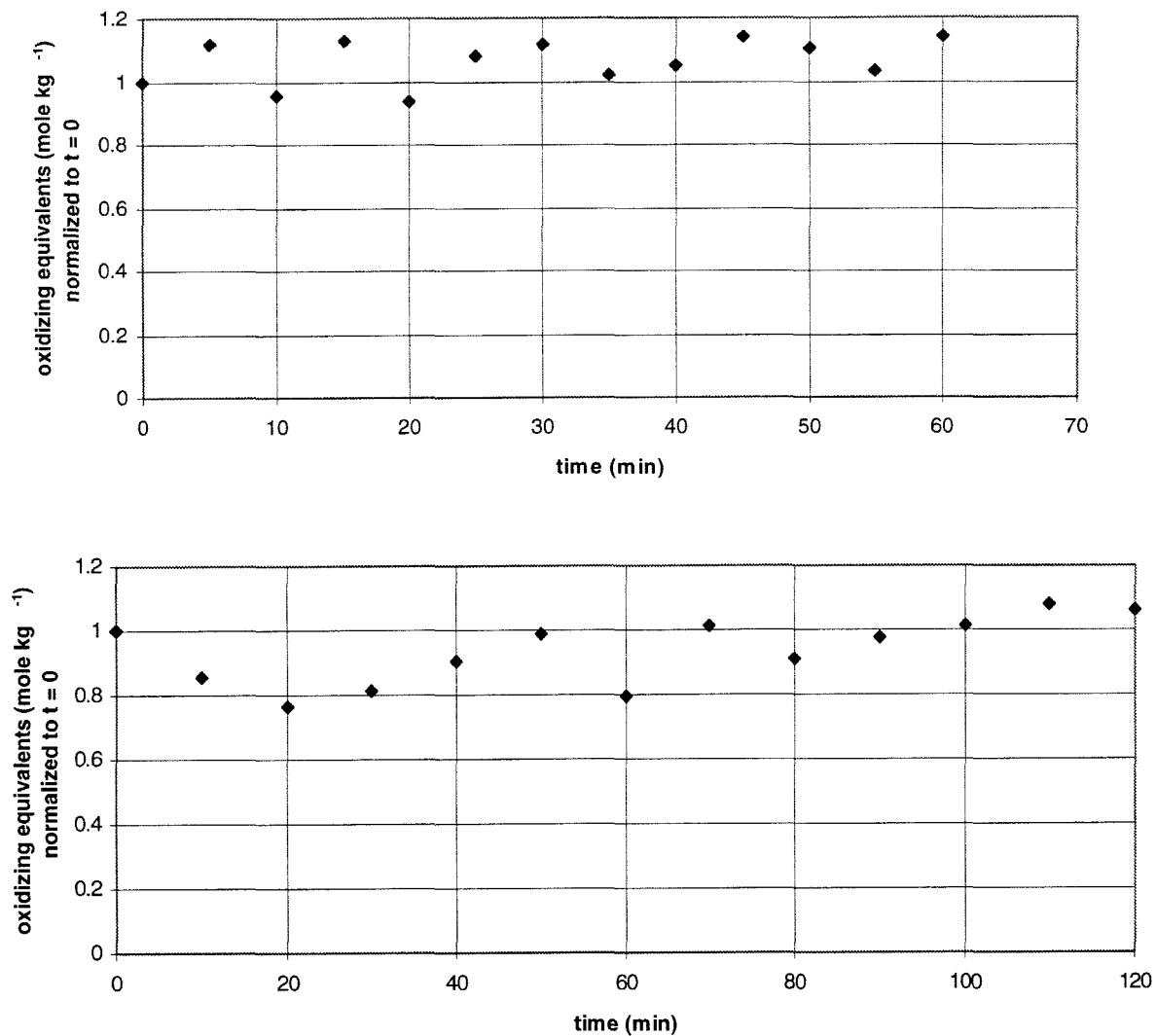
Figure 7

LCV data for two separate dissolution experiments. Solution was unbuffered, pH ~ 7.

sense that all the available DFA has formed Mn(III) – DFA by 24 h. It appears that ~0.001 *m* of DFA has degraded over the course of the reaction.

To explore the p_aH dependence of the dissolution reaction of DFA with manganite, the region chosen was between $p_aH = 7$ and $p_aH = 9.5$, the region in which the solid phase is very stable, and which is of interest with respect to sea water and other natural waters.
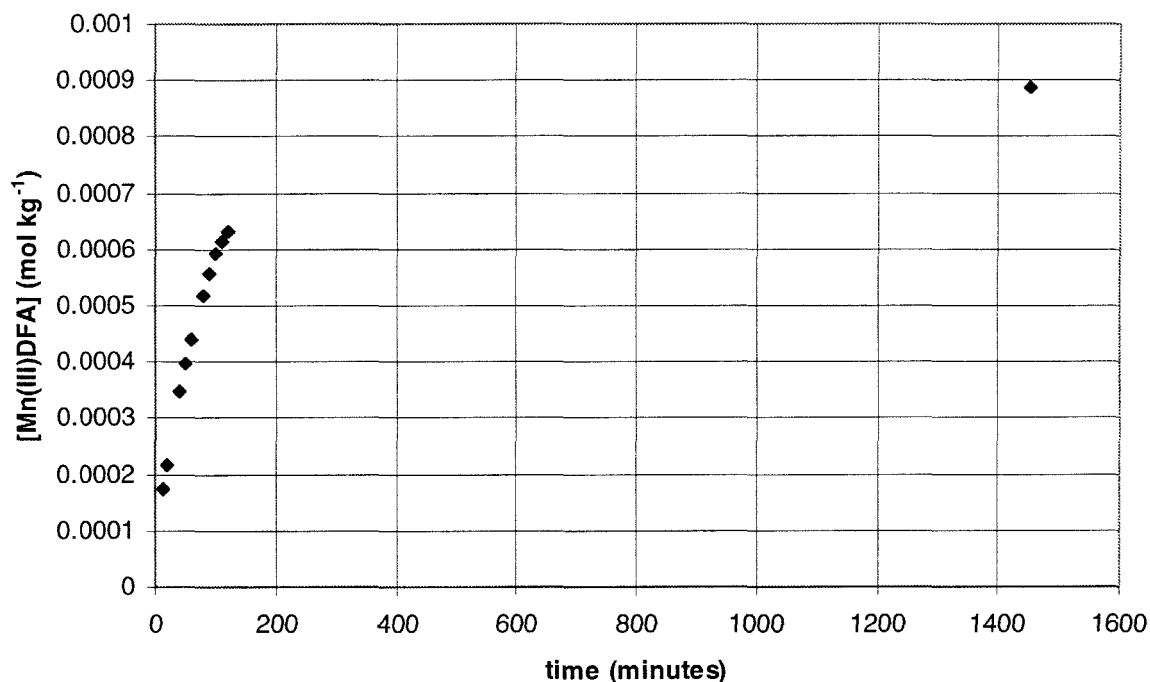
Figure 8

Dissolution of manganite in the presence of DFA; $[DFA]_0 = 1 \times 10^{-3} \, m$. System is unbuffered, $pH_0 = 7$.

Figure 9 shows the results of a set of experiments wherein $[DFA]_0 = 1 \times 10^{-3} \, m$, [$\gamma$-MnOOH] $1.00 \, g \, kg^{-1}$, and the system is buffered with $0.100 \, m$ TRIS. Figure 9 (a.) depicts the dissolution data, while figure 9 (b.) graphs the slope of the line, reporting this number as the pseudo-zero[th] order rate constant for the reaction. It is observed that the rate remains relatively constant over the whole range of p_aH's examined. The final time

datum for the $p_aH = 7$ reaction shows a concentration of Mn_{tot} that is greater than $[DFA]_0$. The error bars contain the Mn_{tot} value of 0.001 m. Thus, the reported value is not statistically different from the expected value. However, if the value is to be trusted as greater than the initial [DFA], then it may be attributed to the breakdown of DFA in solution to dissolution-active fragments that continue to dissolve the manganite.

Figure 10 shows the data for the dissolution of manganite at $p_aH = 7$ with varying $[DFA]_0$. It is clear from these data that there is an initial rapid dissolution of labile Mn(III) from the solid. In the case of $[DFA]_0 = 10^{-5}$ m the reaction goes to completion in the first five minutes of dissolution. For $[DFA]_0 = 10^{-4}$ m the reaction is ~60% complete after five minutes, and gradually reaches completion (in the sense that all the available DFA has reacted) with a constant rate of 6.3×10^{-6} mole kg^{-1} h^{-1} at 5.5 h. These results suggest that there is a highly labile pool of Mn(III) in the suspension that is weakly bound to the solid matrix. The t = 0 reading indicates that the Mn in the system is not in the aqueous form initially. Because the ligand is not in excess over the course of the reaction, it is inappropriate to model this reaction as a pseudo-zero[th] order reaction. Thus, a rate law as a function of $[DFA]_0$ cannot be ascribed to the system. To do this a flow-through reactor would have to be employed to generate steady state rates at a constant [DFA].

(a.)
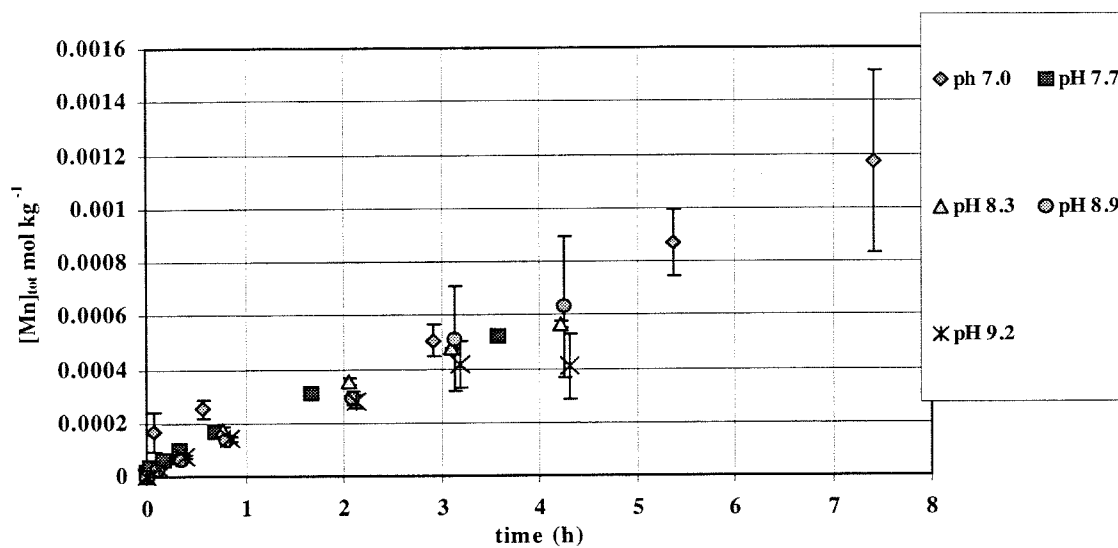
(b.)
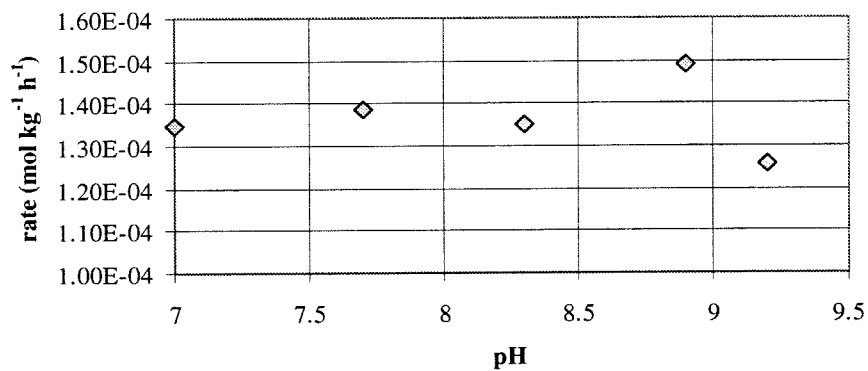
Figure 9

Dissolution of manganite. $[DFA]_0 = 1 \times 10^{-3}\ m$; $[\gamma\text{-MnOOH}] = 1.00\ g\ kg^{-1}$.

(a.) Dissolution curves as a function of pH. (b.) Pseudo-zero[th] order rate constants as a function of pH.
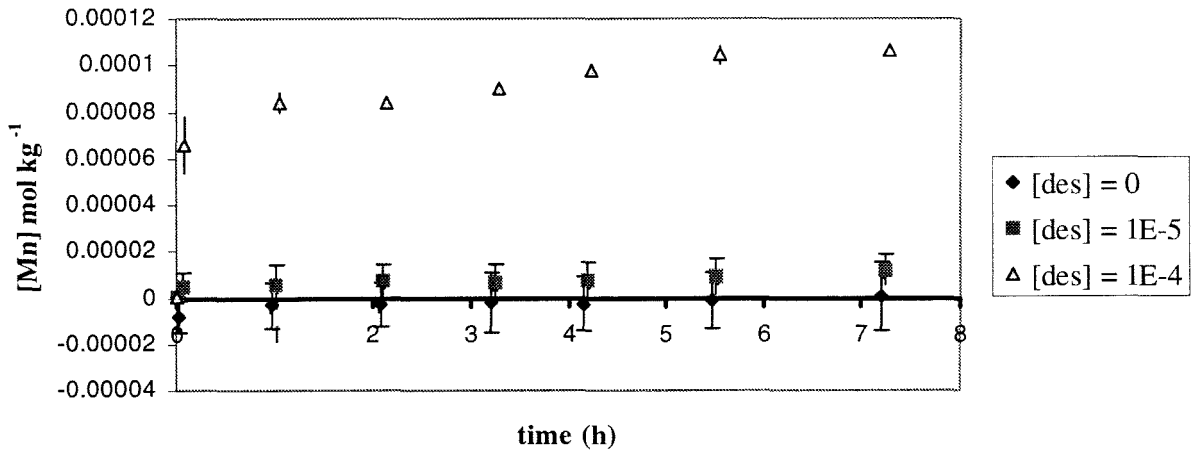
Figure 10

Manganite dissolution at pH = 7, varying $[DFA]_0$.

It is of interest to compare the results of the DFA mediated dissolution of manganite with the dissolution mediated by other ligands. Work by Xyla et al. (1992) examines the oxalate mediated dissolution of manganite. The manganite of this work was prepared in the same manner, and the characteristics of the particles are comparable. They use a [oxalate] of 0.003 $mole_{oxalate}$ $g^{-1}_{manganite}$. They propose a reductive dissolution mechanism that results in the mineralization of oxalate and the release of Mn(II) from the surface. They examined the dissolution in the p_aH region between 4 and 6, and the rates of

dissolution that they observed were highly p_aH dependent, varying by a factor of ~15

between p_aH 4 and p_aH 6, with the rate at p_aH 4 being the greatest. Although the p_aH

range in this work doesn't overlap, it is instructive to compare the nonreductive DFA

mediated rate with the reductive oxalate rates. The rate of DFA mediated dissolution at

p_aH 7 is 1.35 x 10^{-4} mol kg^{-1} h^{-1}, compared to the oxalate rate at p_aH = 6 of ~1 x 10^{-4} mol

kg^{-1} h^{-1}.

Figure 11 shows the results for two preliminary experiments that examined the effect of

DFA on the dissolution of two preparations of MnO_2, the Aldrich preparation and the

Lloyd preparation. It was hypothesized that, in contrast to the manganite experiments

wherein no reductive dissolution was observed, the Mn(IV) solid might induce a

reductive dissolution. Interestingly enough, the two MnO_2 preaparations appear to

exhibit completely different dissolution behaviors.

From figure 11 it is seen that the dissolution of the Aldrich MnO_2 differs from the

dissolution of the Lloyd MnO_2. The Mn(III) – DFA tracks the Mn_{tot} in the Aldrich

preparation initially, but then diverges, with Mn_{tot} > Mn(III) – DFA. However, the Lloyd

preparation exhibits a significant difference over the whole time regime between Mn_{tot}

and Mn(III) – DFA; with no significant appearance of Mn(III) – DFA observed at all.

Figure 12 focuses on the early time region of the Aldrich MnO_2 dissolution. Here it can

be seen that the observed [Mn] can be completely accounted for by [Mn(III) – DFA].

After this point, however, the Mn(III) – DFA reaches a plateau and further dissolution

continues, most likely via the reductive dissolution by DFA degradation products resulting from the further reaction of the DFA$^{\bullet}$ radical.

In the near time regime, where t < 5 h, it appears that the dissolution is reductive, with the $[Mn(III) - DFA] = [Mn_{tot}]$. This observation suggests a one-electron transfer mechanism that can be described as follows:

$$\equiv Mn(IV)O^{-} + H_3DFA \quad \leftrightarrow \quad \equiv Mn(IV)DFA^{2-} + H_2O + H^{+} \qquad (1)$$

$$\equiv Mn(IV)DFA^{2-} \quad \leftrightarrow \quad \equiv Mn(III)DFA^{2-} \qquad (2)$$

$$\equiv Mn(III)DFA^{2-} \quad \rightarrow \quad \equiv Mn(III) + DFA^{\bullet 2-} \qquad (3)$$

$$\equiv Mn(III) + H_3DFA^{2-} \quad \leftrightarrow \quad \equiv Mn(III)DFA + 3H^{+} \qquad (4)$$

$$\equiv Mn(III)DFA \quad \rightarrow \quad Mn(III)DFA(aq) \qquad (5)$$
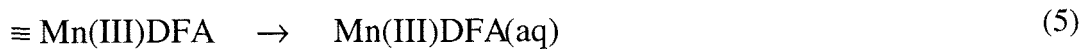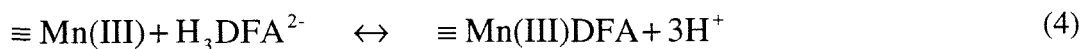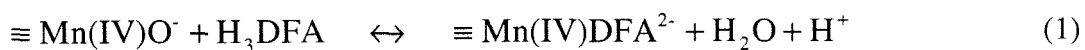
In this mechanism, it is postulated that DFA adsorbs to the surface, transfers an electron to a surface Mn(IV), at which point the DFA radical leaves the surface, probably decomposing, as evidenced by the appearance of a higher energy shoulder in the long-time spectra at 275 nm (figure 12.) The surface Mn(III) is then susceptible to a nonreductive dissolution event akin to the manganite mechanism.
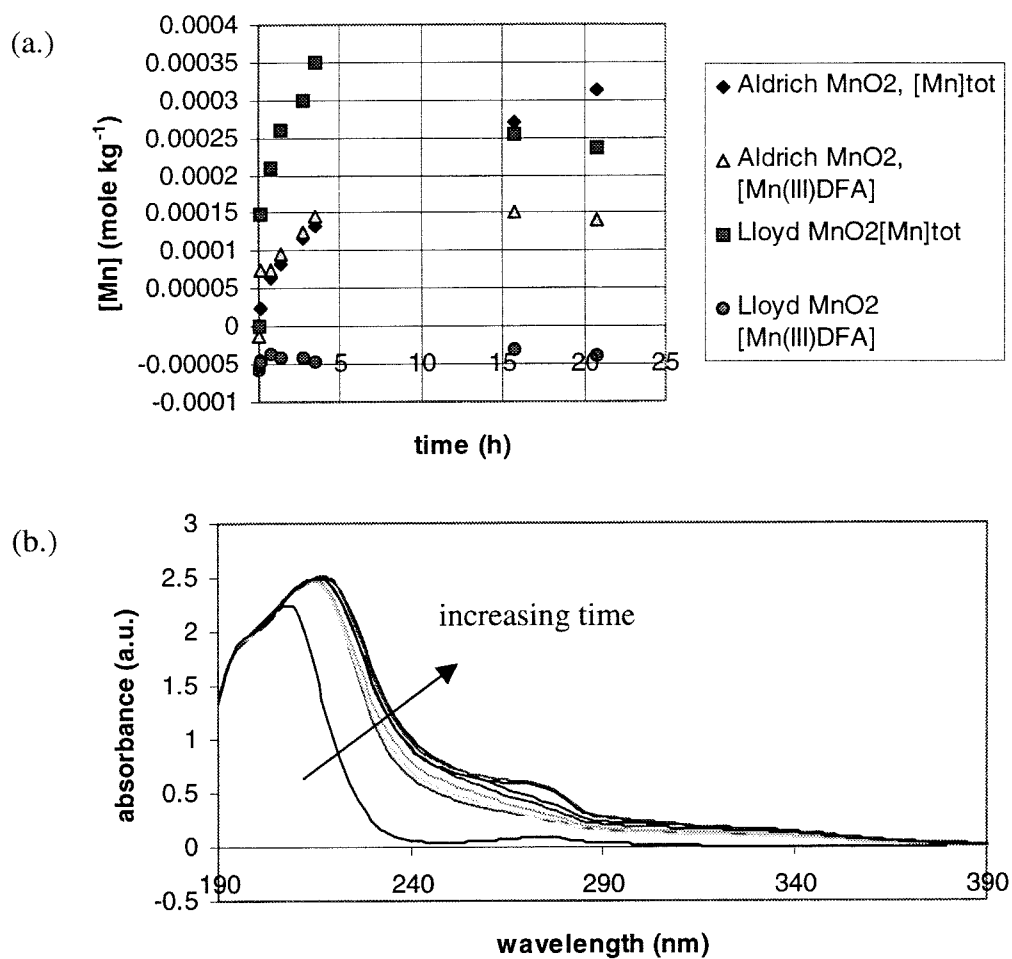
Figure 11

Dissolution of MnO_2 with DFA, pH = 7. (a.) Dissolution as a function of time; $[DFA]_0 = 10^{-3}$ m. Graph shows $[Mn]_{tot}$ and $[Mn(III)DFA]$. (b.) UV – visible spectra of the filtrate from the Aldrich MnO_2 dissolution as a function of time. Note the appearance of the shoulder at 275 nm for late time.

$y = 2.5152E-05x + 4.7209E-05$
$R^2 = 9.9567E-01$

$y = 2.4677E-05x + 5.9651E-05$
$R^2 = 9.9106E-01$
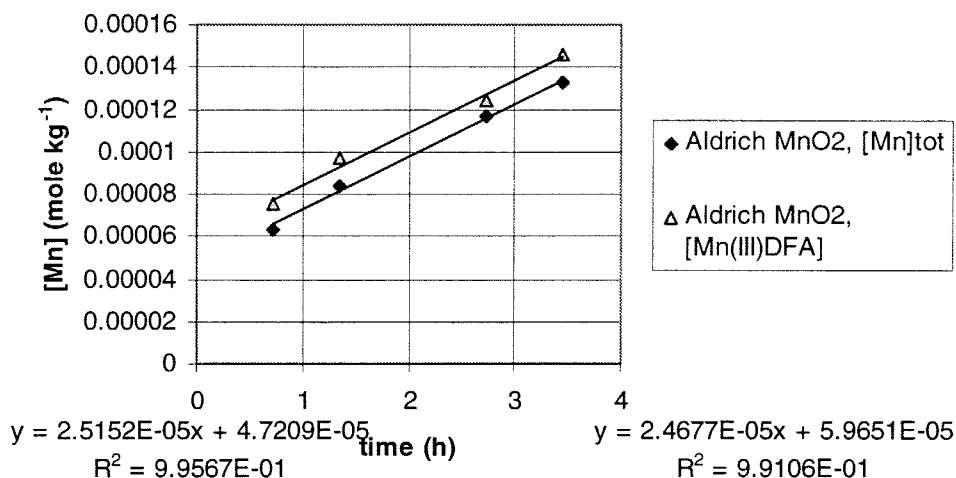
Figure 12

MnO_2 dissolution (Aldrich) in the time region of 0.7 h < t < 3.5 h. The rates match and all the Mn formed can be accounted for by Mn(III)-DFA.

At 15 h, the $[Mn_{tot}]$ diverges from [Mn(III) – DFA]. It is assumed that the remaining Mn in solution is in the form of Mn(II), since no precipitation is observed in the filtrate. However, it is not clear whether the formation of Mn(II) is the result of a two electron transfer at the surface, or whether Mn(III) is formed at the surface by ligand mediated reduction, followed by removal from the surface and consequent homogeneous reduction in solution. A more detailed analysis of the solution species is required to deconvolute these data. However, the following reaction scheme can be proposed to account for the formation of Mn(II) at late times:

$$\equiv Mn(IV) + DFA^{\bullet 2-} \quad \leftrightarrow \quad \equiv Mn(III) + \textit{degradation} \quad \textit{products} \qquad (6)$$

$$\equiv Mn(III) + DFA^{\bullet 2-} \quad \leftrightarrow \quad Mn(II) + \textit{degradation} \quad \textit{products} \qquad (7)$$

$$\equiv Mn(IV)O^{-} + Mn(II) \quad \leftrightarrow \quad \equiv Mn(III)O^{-} + Mn(III) \qquad (8)$$

$$\equiv Mn(III)O^{-} + Mn(II) \quad \leftrightarrow \quad Mn(II) + Mn(III) \qquad (9)$$
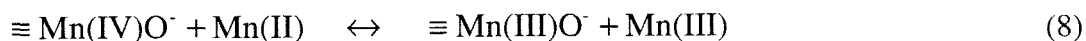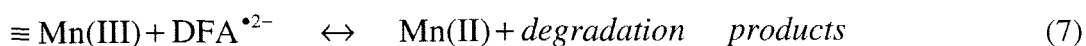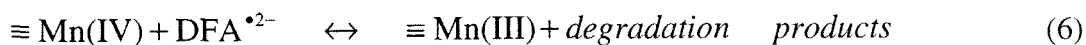
Equation 6 shows the reaction of the $\equiv Mn(IV)$ with the proposed DFA radical, leading most likely to degradation products that will react further with the surface, reducing the $Mn(IV)$ ultimately to the highly soluble $Mn(II)$. Equation 7 shows the analogous reaction with the $\equiv Mn(III)$ species. At this point the $Mn(II)$ in solution can also participate in dissolution, further accelerating the reaction, as shown in equations 8 and 9.

Figure 13 shows a detail from the spectra for the Lloyd preparation of MnO_2. By merely focusing on the absorbance at 312 nm as in figure 11, it would seem that there is no generation of $Mn(III) - DFA$. However, examining figure 13 it can be seen that there exists a definite shoulder at 312 nm, indicating the formation of the $Mn(III) - DFA$ complex. Although, given the extent of dissolution compared to the appearance of the complex, it appears as if the ratio of $[Mn(III) - DFA]$ to $[Mn]_{tot}$ is significantly less for this particle preaparation than for the Aldrich preparation.

As a result of these observations it seems that the reaction scheme laid out in equations 1 $- 9$ would have to be somewhat altered to generate the following proposed mechanism:

$$\equiv Mn(IV)O^- + H_3DFA \quad \leftrightarrow \quad \equiv Mn(IV)DFA^{2-} + H_2O + H^+ \tag{10}$$

$$\equiv Mn(IV)DFA^{2-} \quad \leftrightarrow \quad \equiv Mn(III)DFA^{2-} \tag{11}$$

$$\equiv Mn(III)DFA^{2-} \quad \rightarrow \quad \equiv Mn(III) + DFA^{\bullet 2-} \tag{12}$$

$$\equiv Mn(IV)O^- + X^- + H^+ \quad \rightarrow \quad \equiv Mn(IV)X + OH^- \tag{13}$$

$$\equiv Mn(IV)X \quad \rightarrow \quad \equiv Mn(III)X \tag{14}$$

$$\equiv Mn(III)X \quad \rightarrow \quad Mn(III)X(aq) \tag{15}$$

$$Mn(III)X(aq) \quad \rightarrow \quad Mn(II)(aq) + X^\bullet(aq) \tag{16}$$

$$\equiv Mn(III) + H_3DFA^{2-} \quad \leftrightarrow \quad \equiv Mn(III)DFA + 3H^+ \tag{17}$$

$$\equiv Mn(III)DFA \quad \rightarrow \quad Mn(III)DFA(aq) \tag{18}$$
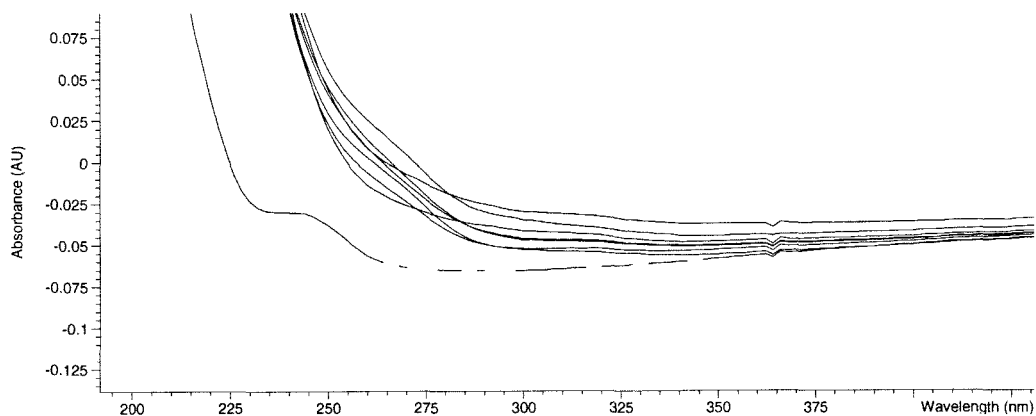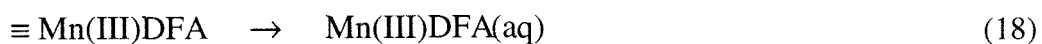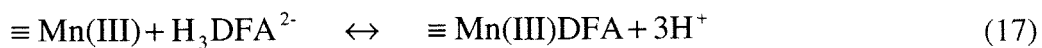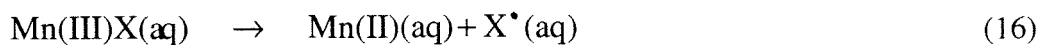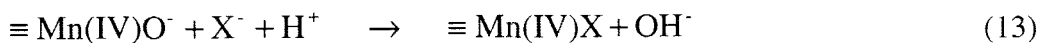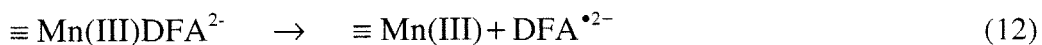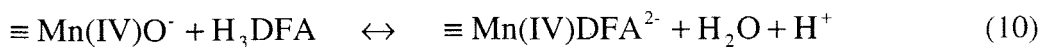
Figure 13

Spectra filtrates from the dissolution of MnO_2, Lloyd preparation, pH = 7. Note that although focusing on 312 nm gives erratic data as a function of time, there exists a peak at 312 nm.

where X^- represents the set of unknown degradation products of DFA. Other scenarios can be envisioned where the sequence of reduction of Mn(IV, III) is altered with respect to the ligands and to heterogeneous versus homogeneous electron transfer.

6.7.2 Photochemical Experiments

There has been some general interest in the activity of Mn and Mn complexes in superoxide dismutase activity (e.g., (Liu et al., 1994), (Faulkner et al., 1994), (Gray and Carmichael, 1992).) Superoxide dismutase is an antioxidant enzyme that has evolved to detoxify the strong oxidants that accumulate during aerobic respiration (Liu et al., 1994). The general reactions catalyzed by this class of enzymes are

$$Mn^{n+} \cdot SOD + O_2^- \rightleftharpoons Mn^{(n-1)+} \cdot SOD + O_2$$

$$Mn^{n+} \cdot SOD + O_2^- + 2H^+ \rightleftharpoons Mn^{(n-1)+} \cdot SOD + H_2O_2 \tag{19}$$
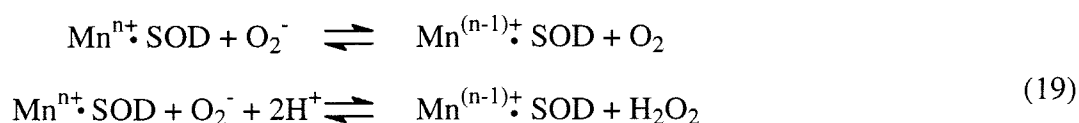
where SOD is the superoxide dismutase. Faulkner et al. (1994) observe a significant SOD activity by the Mn(III) − DFA complex and attribute its activity to electrostatic facilitation by the positively charged terminal amine and the ease of ligand displacement by the O_2^-.

These results suggested that it might be of interest to explore the effect of light on the Mn(III) − DFA complex. Manganite or some other mixed oxidation state solid such as birnessite may form in surface waters and the effect of light on the interaction of biogenic compounds such as siderophores should be explored.

Manganite is a strong oxidant:

$$MnOOH(s) + 3H^+ + e^- \leftrightarrow Mn^{2+}(aq) + 2H_2O$$
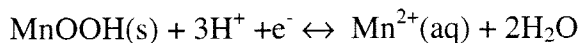
$$E\,^\circ_H = 1.50\ V \qquad (Xyla\ et\ al.,\ 1992) \qquad (20)$$

and it might be expected that manganite surface would be able to oxidize the DFA

molecule, generating a surface Mn(II). For example, the reaction sequence

$$\equiv Mn(III)O^- + H_3DFA \quad \leftrightarrow \quad \equiv Mn(III)DFA^{2-} + H_2O + H^+ \qquad (21)$$

$$\equiv Mn(III)DFA^{2-} \quad \leftrightarrow \quad \equiv Mn(II)DFA^{2-} \qquad (22)$$

$$\equiv Mn(II)DFA^{2-} \quad \rightarrow \quad \equiv Mn(II) + DFA^{\bullet 2-} \qquad (23)$$

$$\equiv Mn(II) \quad \rightarrow \quad Mn(II)(aq) \qquad (24)$$
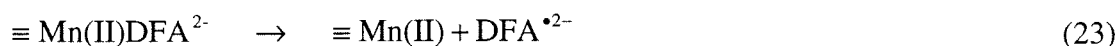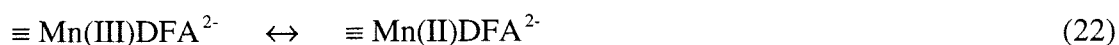
might be expected to occur with the steps in equations 18 and 19 combining to represent

the rate limiting step. It might also be expected with analogy to the oxalate – manganite

system (Xyla et al., 1992) that the introduction of light would stimulate the inner-sphere

electron transfer from DFA to the Mn(III), in both heterogeneous and homogeneous

systems. Thus, to examine the hypothesis that light might influence the chemistry of the

system, the homogeneous DFA – Mn(III) system was studied in the presence and absence

of O_2.

The effect of light on the homogeneous system was examined from $p_aH = 5$ to $p_aH = 9.5$.

No significant reaction was observed over the time scale of 12 hours for the whole p_aH

range examined. Figure 14 shows the data set for $p_aH = 8$, O_2 present. These data are

completely representative of all the experiments performed with and without O_2: no significant change in the spectra were recorded as a function of time and illumination. These results are consistent with the observations of Faulkner et al. (1994) of the shift in redox potential of the Mn(III) – DFA complex.

On the basis of these results no heterogeneous reactions were examined in the presence of light. However, to completely rule out a mechanistic change as a function of illumination, these experiments should be explored further. In particular, it would be of interest to increase the energy of the illumination to include the transition that is centered at 312 nm.

(a.)
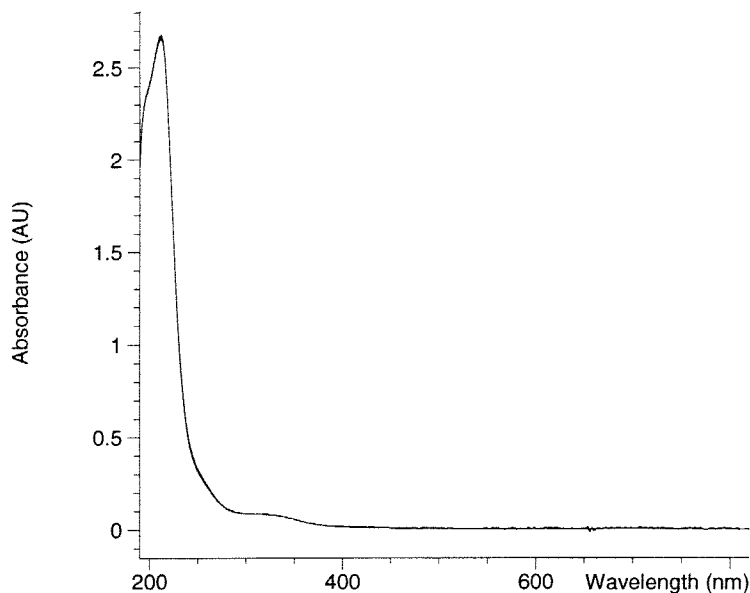
(b.)
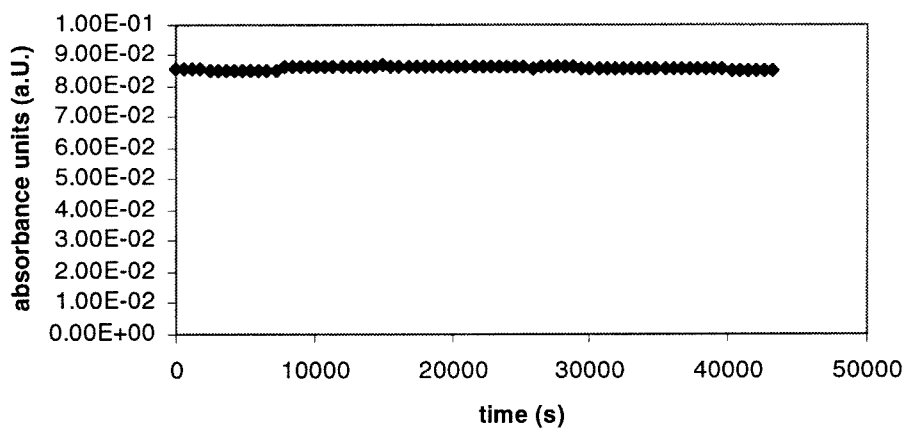
Figure 14

Illumination experiment at pH = 8, O_2 present. (a.) All spectra from t = 0 to t = 43,200 s, Δt = 600 s are pictured. Note that there is no discernible change in the spectra. (b.) Time trace of 312 nm, also showing no significant change over the course of the experiment.

One experiment was performed in which an excess of H_2O_2 was added to a Mn(III) –

DFA solution. Figure 15 shows the results of this experiment with comparisons to other

Mn(III) – DFA spectra. There exists a definite blue-shift in the absorbance band at 312, indicating either that the H_2O_2 has reduced the Mn(III) to Mn(II) or that the H_2O_2 has degraded the DFA through the formation of OH·.
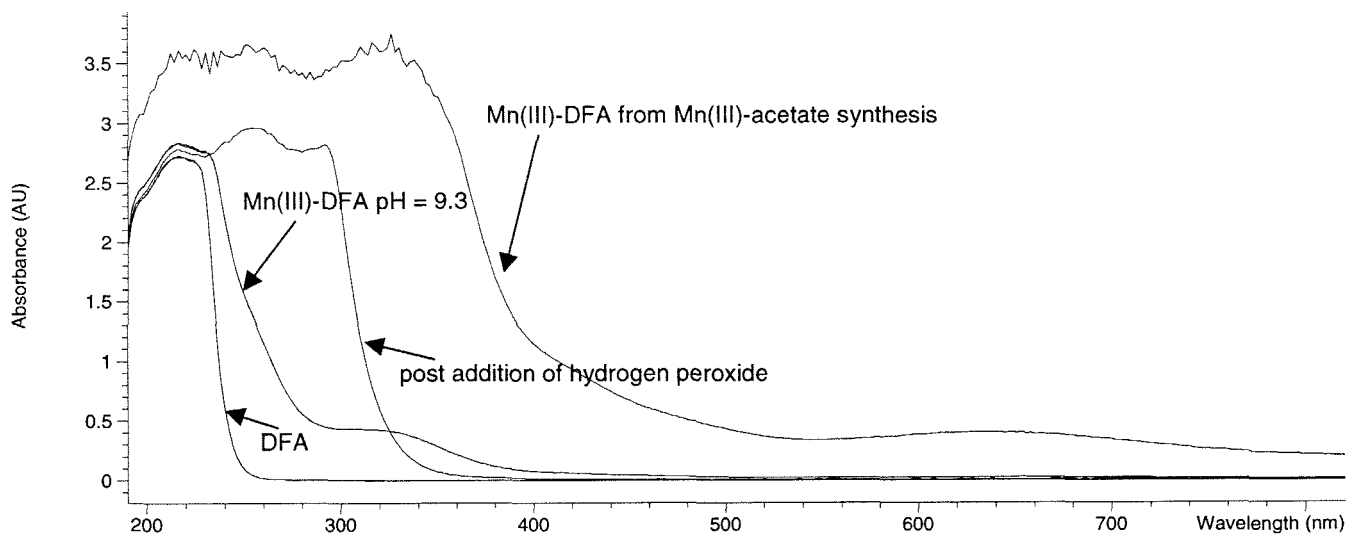
Figure 15

Spectra of various preparations of Mn(III) – DFA, comparing the spectrum of the solution after the addition of H_2O_2 in the presence of O_2.

6.8 Conclusion

The work presented in this chapter indicates that there is the potential for interesting chemistry to occur as a result of the interactions between biogenic hydroxamic acid siderophores and naturally occurring manganese species. Although the stability of the Mn(III) – DFA complex is much less than the analogous Fe(III) – DFA complex (Faulkner et al., 1994), observations of the stability of deferrioxamine E, a macrocyclic trihydroxamic acid siderophore (Faulkner et al., 1994), show that it is equivalent to the Fe(III) – DFA complex. Figure 16 shows a ligand exchange experiment where Fe^{3+} is added to a solution of Mn(III) – DFA and the rate of appearance of FA is tracked as a function of time. The results indicate that the time scale for exchange is on the order of seconds. Thus, in the presence of Fe(III), the Mn(III) – DFA species is transitory.
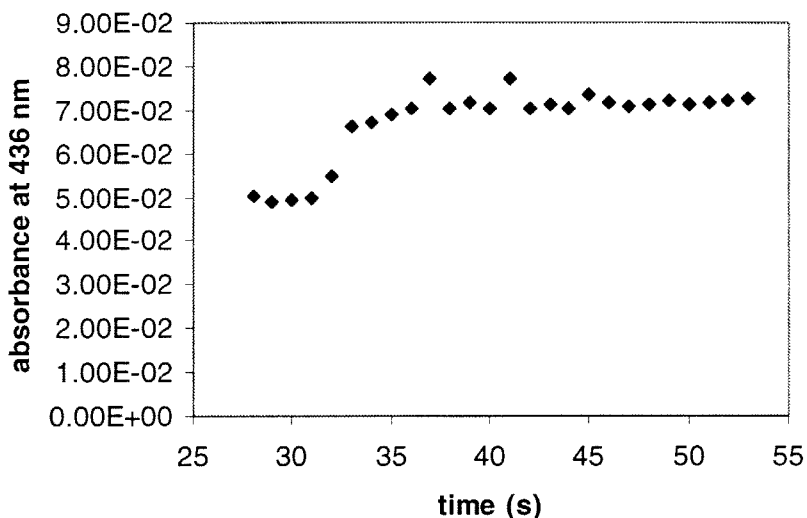
Figure 16

Exchange of Fe(III) for Mn(III) in the DFA complex. Addition of Fe(III)

was at 31 s.

The rates of DFA mediated dissolution of manganite are approximately three orders of

magnitude greater than the corresponding dissolution of hematite, perhaps generating

kinetic competition for the solid bound metals in natural waters.

Table 1 shows a comparison of the pseudo zero[th] order rates for MnOOH dissolution

reported in the literature. Although the numbers cannot be compared directly because of

the varying experimental conditions, the rate for DFA mediated dissolution is consistent

with the other reported results. Given the efficacy of catechol induced dissolution, it

would be of interest to explore the catechol siderophore mediated dissolution of

Mn(III,IV) (hydr)oxides.

Table 1

Comparison of pseudo-zeroth order rate constants for dissolution of MnOOH in the presence of ligands

ligand	[ligand]	[MnOOH] g l^{-1}	p_aH	pseudo-zeroth order rate M h^{-1}	reference
oxalate	0.001 M	0.33	4	1.5×10^{-3}	Xyla et al.
pyrophosphate β-MnOOH	0.05 M	0.22	7	2.1×10^{-4}	(Klewicki and Morgan, 1998)
EDTA	0.001 M	0.044	7.2	5.76×10^{-5}	McArdell et al.
HEEDTA	0.001 M	0.044	7.2	3.96×10^{-5}	(Stone and Morgan, 1984b)
NTA	0.001 M	0.044	7.2	1.33×10^{-5}	(Stone and Morgan, 1984b)
IDA	0.001 M	0.044	7.2	1.66×10^{-7}	(Stone and Morgan, 1984b)
catechol	1.77×10^{-5} M	0.00312	7.2	6×10^{-5}	(Stone and Morgan, 1984b)
hydroquinone	0.000429 M	0.044	7.7	1.4×10^{-4}	(Stone and Morgan, 1984a)
DFA	0.001 m	1.00	7	1.4×10^{-4}	this work

Chapter 7

Dissolution of Goethite and Lepidocrosite and a Comparison of Rates

7.1 Introduction

In this chapter data will be presented that shows the dissolution of two Fe(III) hydroxide phases: goethite (α-FeOOH) and lepidocrosite (γ-FeOOH). The work presented for goethite shows the rate of dissolution as a function of $[DFA]_0$ and pH, while the lepidocrosite data are for only one value of $[DFA]_0$ and pH.

The results presented in this chapter are concise; they are to be compared in a general sense with the hematite results in chapters 3 and 4. Goethite and lepidocrosite are also important naturally occurring Fe(III) hydroxides, and found as weathering products in soil pedogenesis, so their response to DFA is of interest in the characterization of naturally occurring oxides to the biogenic DFA.

The experiments related in this chapter were performed using exactly the same methods as presented for the sg2g hematite.

7.2 Fe(III) hydroxide Synthesis

7.2.1 Goethite

Goethite was synthesized with the method according to Schwertmann and Cornell (Schwertmann and Cornell, 1991). 100.0 g of 1 m Fe(NO$_3$)$_3$ were added to a 2 L HDPE flask to which was added 180.0 g of 5 m KOH under vigorous stirring. A brownish precipitate was observed. The suspension was diluted to 2.000 kg with MQW, capped and placed in a 70°C oven for ~60 h.

7.2.2 Lepidocrosite

Lepidocrosite was prepared using the method described by Schwertmann and Cornell (Schwertmann and Cornell, 1991). A 600 ml glass beaker was used as the reaction vessel. The vessel was equipped with a magnetic stirrer, a NaOH-containing pH stat, and a glass frit gas delivery system through which medical-grade air flowed. 11.93 g of fresh FeCl$_2$•4H$_2$O were added to 300.0 g of MQW under vigorous stirring. The pH of the solution was adjusted to pH 6.7-6.9. The air flow was initiated at 220 ml min^{-1}. The reaction was continued, maintaining the pH through additions of NaOH, until the pH became constant. The suspension was cleaned as described for sg2g hematite.

7.3 Particle Characterization

The goethite particles were characterized using XRD and TEM (methods described in chapter 3.) Whereas, the lepidocrosite particles were only characterized using XRD.

7.3.1 TEM and XRD Measurements

Figure 1 depicts the TEM micrographs of the goethite preparation. The dimensions of the particles from the TEM micrographs are 2500-3000 nm x 200 nm x 100 nm, generating a specific surface area of ~7 m^2 g^{-1}. The goethite particles are fine fibrous needles. The TEM diffraction pattern indicated that the needles were monocrystalline.
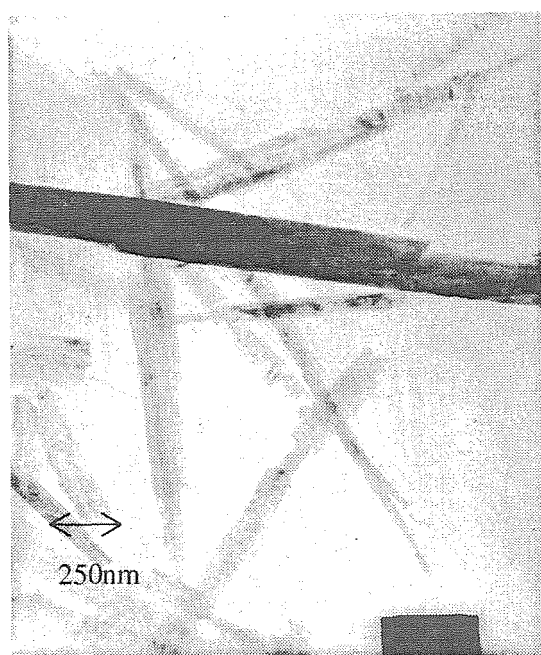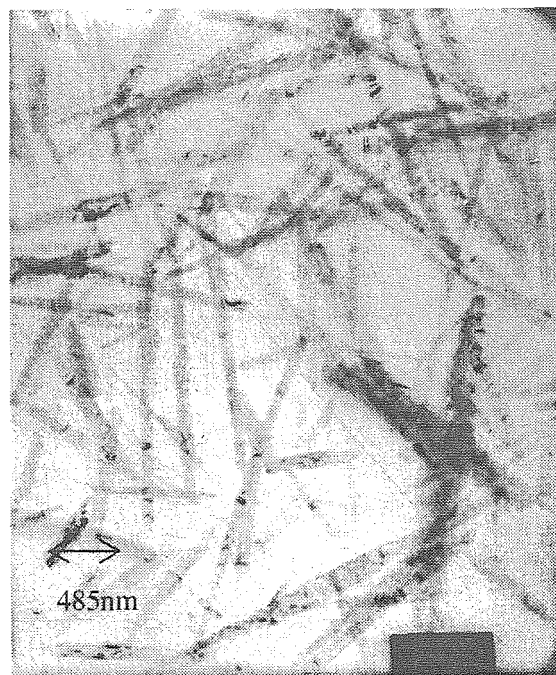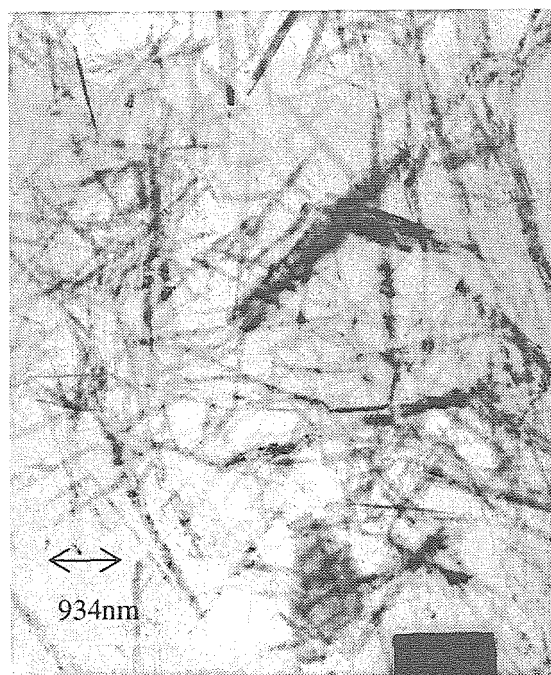
Figure 1

TEM micrographs of goethite.

Powder X-ray diffraction (XRD) (Inel with Co-radiation) generates the pattern exhibited in figure 2. As can be seen by comparing the observed spectrum with the expected diffraction lines, the product is a crystalline preparation of α-FeOOH, as expected. Note that the radiation source for the expected lines is Cu; therefore, there is an expected offset that is observed.

Figure 3 shows the results for the XRD measurements of the lepidocrosite preparation (Inel with Co-radiation). As can be seen by comparison of the expected lines and intensities with the observed lines, it appears that even with compensation for the different radiation source, the crystal phase is not pure lepidocrosite. The phase does appear to be crystalline, however. It is not clear what the impurity is.
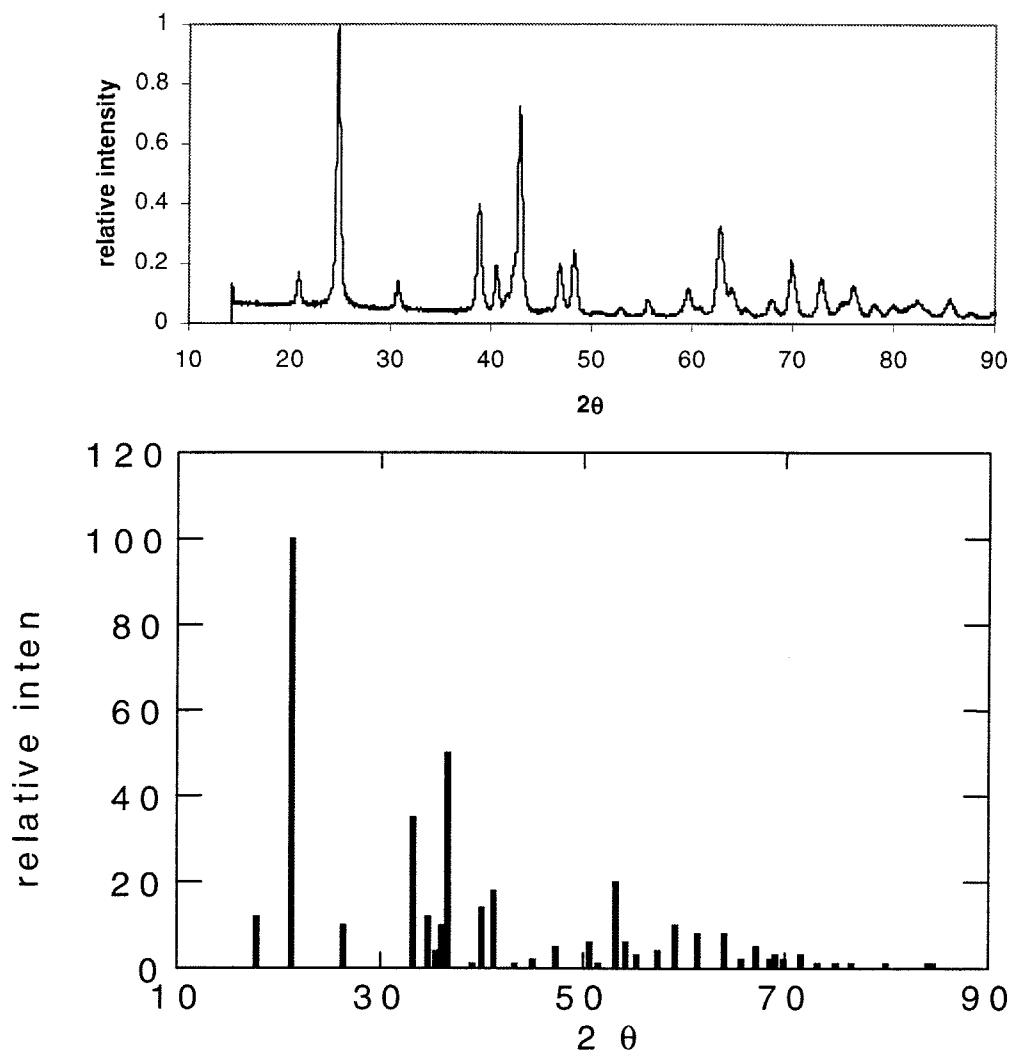
Figure 2

XRD spectrum of goethite compared to expected lines and intensities.
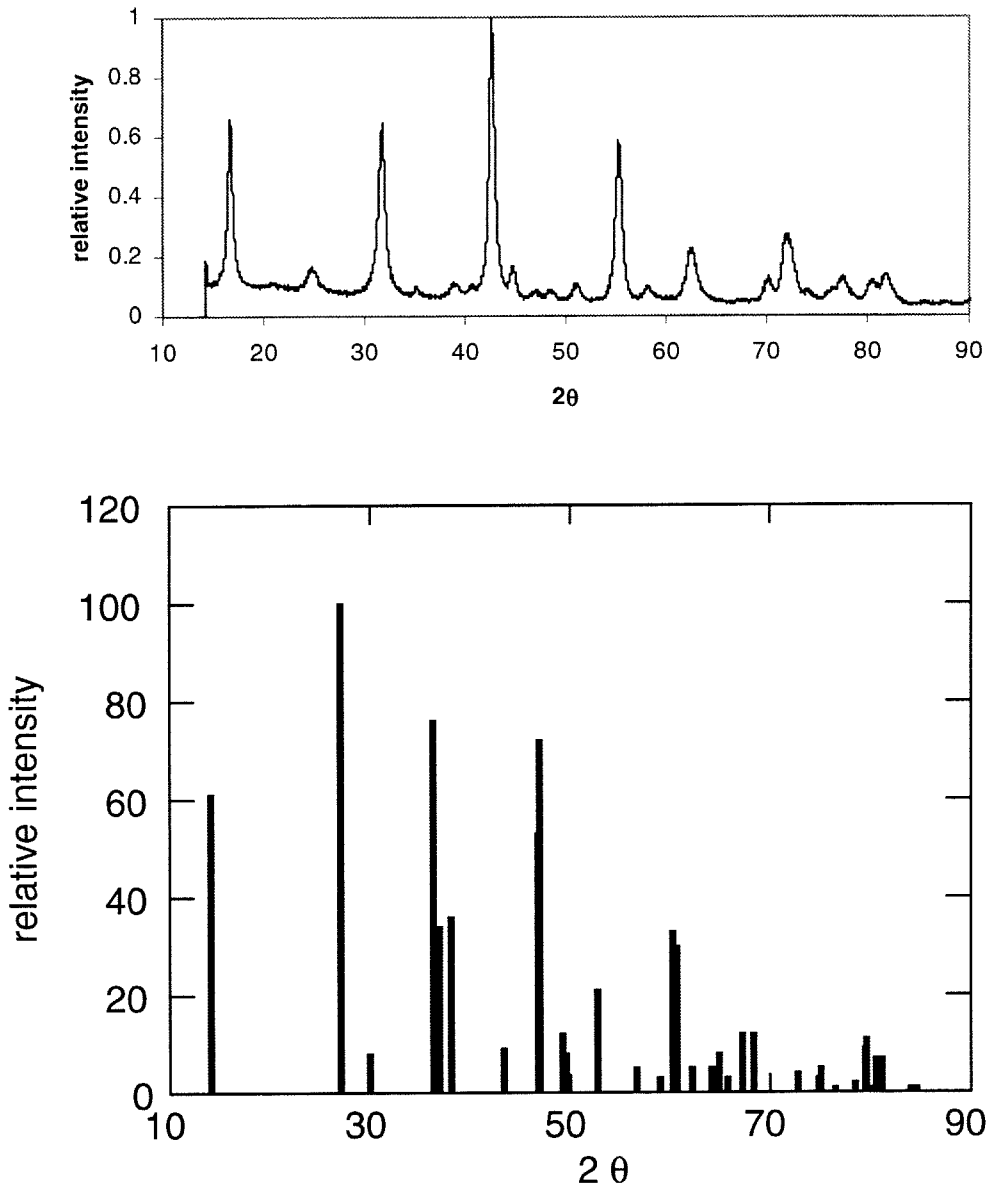
Figure 3

XRD spectrum of lepidocrosite compared to expected lines and intensities.

7.4 Results

7.4.1 Goethite Dissolution

Figure 4 shows the results of the set of dissolution experiments performed with goethite. The $[DFA]_0$ was set at 10^{-4} m for all the experiments, and the rate was observed as a function of pH.
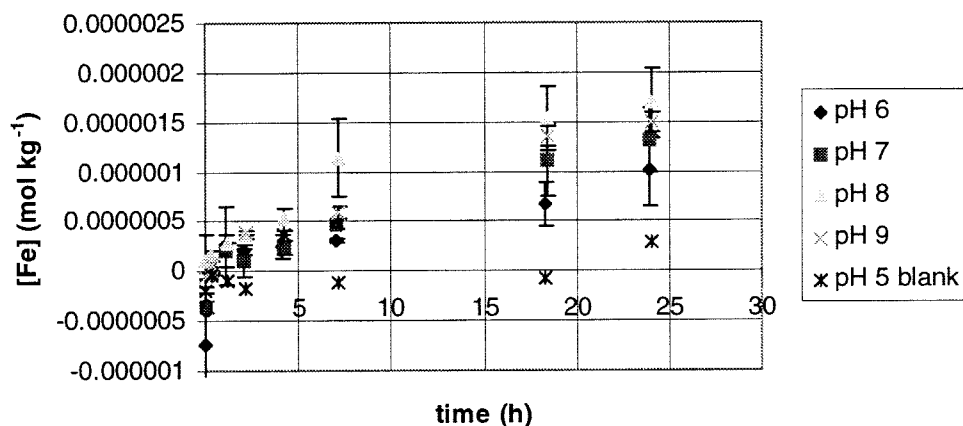
Figure 4

Dissolution of goethite by DFA. $[DFA]_0 = 10^{-4}$ m. pH varies from 5 to 9.

Figure 5 shows the pseudo-zero[th] order rate constants as a function of pH. The rates vary little as a function of pH, analogously to the hematite data. On a per gram basis, the rates are less than the hematite rates under similar conditions, however, given that the particle size of the goethite is larger than the SC hematite particles, an area-based comparison is warranted. Since the specific surface area of the SC hematite is twice that of the goethite
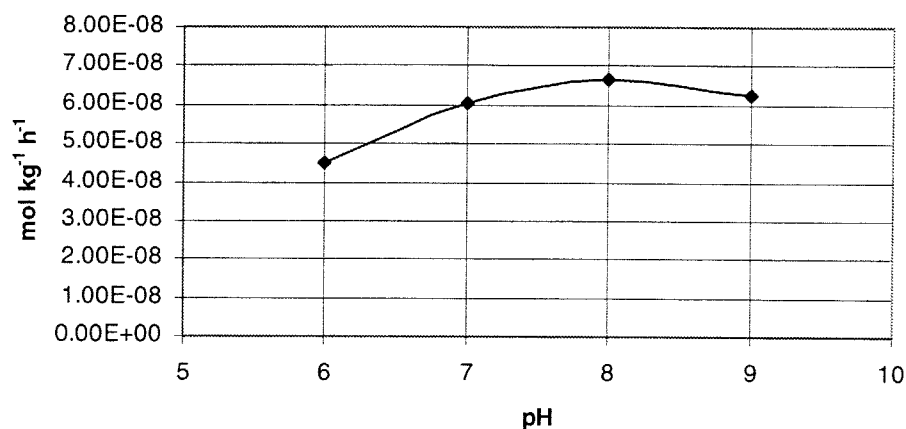
Figure 5

Pseudo-zeroth order rate constants for the dissolution of goethite in the presence of DFA. $[DFA]_0 = 10^{-4} \, m$.

preparation, the per gram-based goethite dissolution rates should be multiplied by two, generating rates that are comparable to the SC hematite rates.

Table 1 shows a comparison of the pseudo-zero[th] order rate constants for the dissolution of sg2g hematite, SC hematite, and goethite. Figure 6 graphs these same data, for visual comparison. The rates are very similar, with the largest difference being between the SC hematite and the sg2g hematite at pH 5. The trends are the same for all samples for all the observed pH's. This result suggests that there is a similar mechanism and pH dependence for the dissolution reaction.

Table 1

A comparison of pseudo-zero[th] order rates of Fe(III)-(hydr)oxide dissolution with DFA; $[DFA]_0 = 10^{-4}$ m for all data.

pH	rate (M s^{-1} g$_{hematite}$)			area -based rate (M s^{-1} m^{-2})		
	sg2g	SC	goethite	sg2g	SC	goethite
5	2.00×10^{-7}	2.99×10^{-7}		8.70×10^{-9}	2.21×10^{-8}	
6	1.30×10^{-7}	5.32×10^{-8}	4.48×10^{-8}	5.64×10^{-9}	3.94×10^{-9}	6.41×10^{-9}
7	2.11×10^{-7}	1.37×10^{-7}	6.03×10^{-8}	9.19×10^{-9}	1.01×10^{-8}	8.61×10^{-9}
8	1.70×10^{-7}	7.05×10^{-8}	6.67×10^{-8}	7.39×10^{-9}	5.22×10^{-9}	9.54×10^{-9}
9	1.70×10^{-7}	4.89×10^{-8}	6.26×10^{-8}	7.39×10^{-9}	3.62×10^{-9}	8.94×10^{-9}

Figure 6

A comparison of pseudo-zero[th] order rates of dissolution for the three Fe(III)-(hydr)oxide preparations examined in this work. $[DFA]_0 = 10^{-4}$ m for all data.

7.4.2 Lepidocrosite Dissolution

Figure 7 shows the results of the single dissolution experiment of lepidocrosite by DFA. The pH was set at 7 and $[DFA]_0 = 10^{-4}$ m. The dissolution is very rapid compared to the dissolution of hematite and goethite, with time scales on the order of the dissolution of the manganite system. Not surprisingly, these data suggest that more labile forms of oxyhydroxides are more susceptible to degradation by ligands such as DFA. Further work needs to be done to completely characterize this system along with other representative oxide systems.
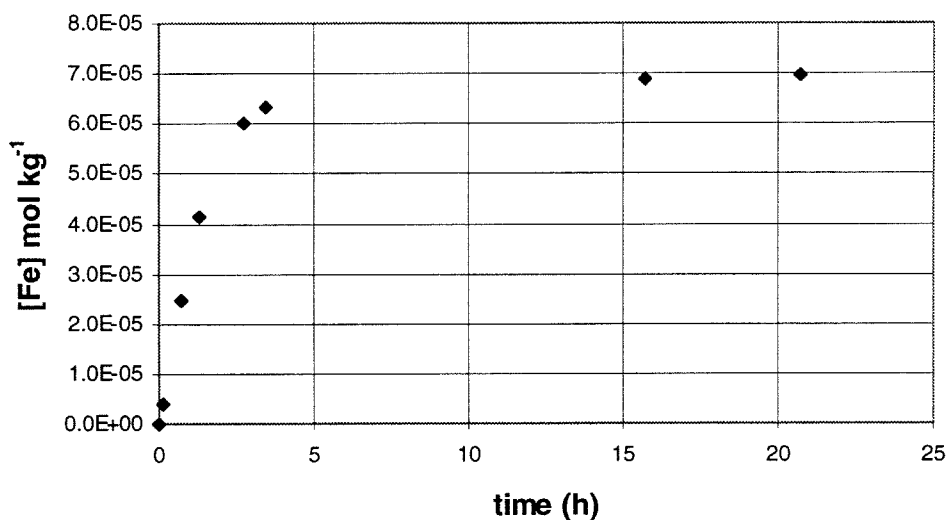
Figure 7

Dissolution of lepidocrosite by DFA; pH = 7, $[DFA]_0 = 10^{-4} m$.

7.5 Conclusion

The brief presentation in this chapter is meant primarily for the purpose of comparison, and to stimulate the need for further work. DFA is an effective agent for the dissolution of Fe and Mn oxyhydroxides, and it is reasonable to hypothesize that it can react effectively with other naturally occurring oxide phases. Siderophores are naturally produced ligands and their ubiquity in aerobic aqueous environments implies that they are important mediators in the cycling of transition metals between the solid and aqueous phases. The activity of the siderophore pool will be correlated directly with the activity of the aqueous Fe species, since a positive feedback exists between this activity and the biological production of siderophore. This correlation introduces an interesting feedback loop into the element fluxes.

Chapter 8

Conclusion

8.1 Acceleration of dissolution

The work presented in this thesis generates insight into the interaction of a model siderophore, deferrioxamine B, with a set of Fe(III)- and Mn(III, IV)- (hydr)oxides. The first and most significant question asked is, "Does DFA accelerated the rates of dissolution of these solids over their basal rates?" The answer is clearly positive.

In all cases examined herein, the rates of dissolution of the solid phases are significantly greater in the presence of DFA than in the absence. In fact, the reaction appears to be very efficient in the sense that, even at the low DFA concentrations, the reaction goes to completion and only about 10% of the FA is bound to the surface of hematite. Essentially, a switch is observed: DFA binds to the surface via covalent interactions, most likely a bidentate mononuclear interaction, while FA binds to the surface through noncovalent interactions. The switch in the nature of the chemical bond significantly changes the stability of the adsorption interaction. Upon dissolution, the strong covalent bond of the DFA-bound adsorbate converts to the weaker electrostatic and van der Waals interactions of FA with the surface. The FA is then able to diffuse from the surface to the bulk solution. This result implies that the iron uptake mechanism mediated by DFA and similar hydroxamate type siderophores are an effective strategy for microorganisms.

8.1.1 Hematite dissolution

Hematite is the solid phase examined in the greatest detail in this work. Given that the rate of dissolution is accelerated above the basal rate, the next question asked is, "What is the effect of pH and [DFA] on the rates of dissolution?" The experiments presented in this work were designed to examine a pH range and [DFA] that are representative of a large number of natural waters, from soil waters to ocean waters. As the thermodynamic stability of the oxyhydroxides increase in general with increasing pH, and the solution and surface speciation changes with pH, it might be expected that the rates of dissolution would be affected by changes in pH. Interestingly, the data indicate a weak dependence of rate on pH. This important result suggests that the siderophore release strategy by microorganisms remains efficient over a large range of proton activity.

A standard method for the examination of dissolution data involves focussing on the linear region of the dissolution curve, modeled as a pseudo-zeroth order process (Furrer and Stumm, 1983). In this approach for analyzing the data, it is postulated that the rate limiting step is the breaking of the metal – oxo bonds that bind the surface metal – ligand complex to the bulk solid. Thus, the rate of dissolution is proportional to the surface-bound ligand concentration. That the process can be modeled as a pseudo-zeroth order process depends on the concentration of the surface-bound ligand remaining constant over the course of the reaction. In the case of the DFA experiments presented in this work, this assumption is only truly valid for solution concentrations of DFA that are greater than or equal to 10^{-4} m. For experiments for which the concentrations are less than this, the pseudo-zeroth order approach is invalid, and an approach that doesn't rely

on the constant surface concentration assumption is required. However, it is clear from the data that the rate of dissolution increases monotonically with increases in the concentration of adsorbed ligand.

All the hematite dissolution curves exhibit the convex morphology that implies the existence of a pool of energetically labile iron. This pool of iron may exist as a function of the method of solid sample preparation, but may also be representative of newly formed oxides in natural waters. DFA is extremely effective in mining this pool of iron, as exhibited in the data presented in chapters 4 and 5. The order of magnitude increase in rate of dissolution of lepidochrosite over hematite indicates that the solid morphology strongly affects the efficacy of DFA in solid dissolution.

The third question asked was, "What are the effects of ionic strength and temperature on the rates of dissolution?" The range of ionic strength examined was 0.001 to 1.0 m, encompassing the ionic strengths of environmentally interesting waters. Again, it is of interest to ask whether the siderophore-mediated dissolution process will be affected negatively in any of the environments in which organisms confront iron limiting conditions. In the case examined herein, the dissolution of the sol gel prepared hematite, the rate of dissolution increases monotonically with an increase in ionic strength. Thus, it is expected that the dissolution reaction becomes would be more efficient in an oceanic or a soil system relative to a fresh-water system. The rate of dissolution also increases when the temperature is increased from 25 °C to 35 °C.

8.1.2 Dissolution of goethite and lepidochrosite

Although hematite is the thermodynamically most stable phase in an oxic environment, other oxyhydroxides are found to be metastable in natural waters. Thus, it was of interest to examine the effect of DFA on the dissolution of some other representative solid phases. For example, goethite is a ubiquitous form of Fe(III)-hydroxide in highly weathered soils. The rates of dissolution of goethite were similar to that of hematite. However, the lepidochrosite phase dissolved at a significantly greater rate than the other Fe(III)-(hydr)oxide phases examined. Lepidochrosite has the same stoichiometry as goethite, and differs only in its crystal morphology. If the lepidochrosite phase synthesized is a pure lepidochrosite preparation, then it is very interesting to note that the stability of the oxide phase with respect to DFA-mediated dissolution is such a strong function of the crystal morphology. Again, in the goethite case, there exists a weak dependence of rate on pH and a monotonic increase of rate with increasing [DFA].

8.1.3 Dissolution of manganite and pyrolusite

The microbial siderophore pathway has evolved for the uptake of Fe(III) in oxic environments. However, the DFA molecule also interacts with other transition metals, forming particularly stable aqueous complexes with the trivalent transition. In general, the stability of these complexes is fifteen to twenty orders of magnitude less than that of the comparable Fe(III) complex. Because of their significance in natural waters, however, it is of interest to explore the effect of siderophores on the stability of the oxyhydroxides of manganese. Manganese (hydr)oxides are highly reactive, mediating a large number of oxidative and reductive reactions at their surfaces. Because of their

reactivity, their chemical significance is disproportionate to their abundance. Manganese is also integral to microbially mediated redox cycling in natural waters, acting as both electron donor and acceptor.

Mn(III) is an important form of manganese in natural waters, forming metastable hydroxides at circumneutral and basic pH's. The first question asked was, "Does DFA form a stable aqueous complex with Mn(III)?" This complex had been identified by mass spectroscopy in previous work (Faulkner et al., 1994), and the work in this thesis confirmed its existence and stability. In fact, one of the methods utilized for synthesizing this complex was addition of DFA to a suspension of Mn(III)-oxide.

Since Mn(III) solids are known to oxidize organic molecules in surface mediated reactions (Stone and Morgan, 1984), it was of interest to ask whether the dissolution of manganite was reductive. Under the conditions reported in this work, the dissolution of manganite by DFA is mainly non-reductive, and appears to be completely analogous to the Fe(III) – (hydr)oxide dissolution. The Mn(III) – DFA complex formed as a result of the dissolution process is highly stable with respect to hydrolysis and light-induced degradation. The Mn(III) – DFA complex is labile with respect to metal substitution by Fe(III), with the time scale of the substitution reaction being on the order of seconds. The rates of dissolution are relatively constant in the pH range of $7 \leq pH \leq 9.3$. On a per gram basis, the pseudo-zero[th] order rates of dissolution are approximately two orders of magnitude greater than the equivalent rates for hematite and goethite. Direct comparisons of these rates are complicated by the lack of adsorption data for DFA on

manganite, but it is unlikely that the adsorption of DFA on manganite is greater than that on hematite.

Dissolution of MnO_2 appears to proceed by a more complicated mechanism than dissolution of manganite. Depending on the preparation of the solid, there appeared to be a more or less significant contribution of Mn(III) – DFA to the end products of the dissolution process. Mn(II) appeared in solution, and may be implicit in further reaction with the solid surface. Further work is necessary to elucidate the dissolution mechanism in detail.

8.2 Chemistry of DFA – Surface

It was hypothesized that DFA would have significant interactions with the solid surface and that these interactions would be significant in the mediation of solid dissolution. The evidence is very strong that this is the case. The FTIR data and the low [hematite] experiment confirm this hypothesis. One simple experiment could be performed to further test this hypothesis: separation of the solid phase from the DFA (aq) by a permeable membrane that has a size cut-off well below that of DFA.

Another set of experiments would be very valuable in increasing the understanding of the nature of the surface interactions. This set of experiments would involve the direct monitoring of the DFA at the surface using FTIR or other surface active spectroscopies. In the case of FTIR, attenuated total reflectance FTIR (ATR-FTIR) could be utilized to directly observe the surface species as the system evolves in time. It would also be

possible to utilize an aluminum oxide phase as an analog to the iron oxide and apply magnetic resonance techniques to observe the DFA and its interactions with the surface. The experimental results from PCS, diffuse reflectance FTIR, varying of ionic strength, varying [hematite], and molecular modeling all point to the dissolution being a surface mediated reaction.

8.3 Significance to siderophore-producing organisms

The concentration of the Fe-bound form of the siderophore in solution is the parameter that determines the level at which an organism will synthesize siderophore. The organisms expend a great deal of metabolic energy synthesizing siderophore, only to release the compound outside the cell, relinquishing their control over the fate of their metabolic investment. The results of Hersman (personal communication) that indicate an increased rate of siderophore production in the presence of a solid Fe(III) phase over the rate of production in an iron-free medium suggest that there exists a positive feedback between the success of dissolution-generated Fe(III) – siderophore uptake and siderophore synthesis and release. Thus, the efficiency of the dissolution reaction is very important with respect to the metabolic regulation of iron uptake by the microorganism.

The concentration of organisms vary greatly as a function of environment, with soils having the greatest density and oligotrophic surface waters having the lowest. The population densities and diversities are a strong function of the nutrient profile of a given environment, with soils in general having a large concentration of potential nutrients bound up ion the solid phase. Access to these nutrients will in part determine the success

of a given organism in competing for their ecological niche. Organisms are often found associated with solid surfaces, either intercalating into a porous structure or bound within a mass of extracellular polysaccharide material. With respect to siderophore-mediated dissolution, this type of association has a potential advantage. If the organism releases a siderophore molecule while floating freely in solution, the siderophore will diffuse away from the organism. The optimization of the process would involve maximizing the siderophore released to maximize the potential of encountering an Fe(III) – siderophore that has reacted with a surface. On the other hand, by associating with a surface, the organism increases the flux of siderophore to the surface of the particle, and increases the probability of encountering the Fe(III) – siderophore upon release from the surface. The observations of the dissolution reaction from this work would support this scenario: efficient release of Fe(III) – siderophore from the surface, even at low solution concentrations of siderophore positively affects the potential for efficient uptake of iron in the presence of Fe(III)-(hydr)oxides.

8.4 Geochemsitry or Biochemistry?

One must ask the question, "What is the significance of siderophores in natural waters?" Do siderophores mediate a significant proportion of the flux of iron and other slightly soluble metals in natural waters? Or, is the main significance of siderophores found in their ability to allow organisms to continue to live and evolve in environments in which soluble iron is in limiting supply?

Although this work does not directly address these questions, it is clear that the significance of siderophores for geochemical processes is a strong function of concentration, and therefore microbial population density. For example, in oligotrophic ocean waters, the density of organisms is very low; and, commensurately, the production of siderophore will be proportionately low. The flux of iron derived from atmospheric deposition will be minimally affected by interaction with siderophore. However, from the perspective of the organism, the ability to access this pool of iron is crucial for its reproductive success and therefore its fitness. In this case the low – [DFA] data best reflects the scenario. Even at low [DFA], the dissolution reaction is very efficient, and approximately 90% of the released FA is accessible to the organism as soluble FA.

Soils reside at the other end of the scale, wherein great potential exists for regions of high population density. Close association with particles will optimize the efficiency of the Fe(III)-bound siderophore uptake process, as mentioned above. It has been suggested that concentrations of siderophores may reach as high as 1 mM in soils (Hersman et al., 1995). This high concentration is conceivable in regions local to particle surfaces that have been colonized by microorganisms. In this case, the steady-state dissolution captured by the pseudo-zero[th] order region of the dissolution curve may indeed be applicable, and the siderophore mediated dissolution process may account for a significant fraction of the flux of iron from solid phases. Further work needs to be performed to determine the efficacy of siderophores in scavenging iron from more complicated mineral phases such as iron-substituted clay minerals.

8.5 Further work

The results of these studies indicate a rich area of further study. DFA is only one example of a diverse set of compounds that make up the pool of siderophores. It would be of great interest to examine the effect of catechol-type siderophores on the dissolution process. The challenge would be the generation of enough siderophore material to complete a comprehensive study. In the work presented here, the total amount of DFA used was on the order of ten grams for all the reported experiments.

It would be of interest to examine the low concentration regimes in greater detail. Further investigation of this type would require clean lab techniques and the development of a particle pre-treatment protocol that would ensure a reproducible surface for the solid. These experiments would also involve increasing the sensitivity of the analytical methods.

The interpretation of dissolution mechanism depends on a detailed understanding of the surface chemistry of DFA. Direct observation of surface species, as mentioned above, would be necessary to perform these studies.

This work just begins to examine the effect of siderophores on the environmentally significant iron and manganese containing minerals. Extending the range of minerals examined would greatly improve our understanding of the significance of siderophores in biogeochemical cycling of transition metals.

Appendix

The Quantification of Nanomolar Concentrations of Fe(II) Using Electrospray Mass Spectrometry

Samuel Webb and Thomas Lloyd

Introduction

Iron is one of the most abundant elements in the Earth's crust and is present as both Fe(II) and Fe(III) in a variety of rock and soil minerals (1). Iron(II) is thermodynamically unstable in oxygenated waters and is rapidly oxidized to Fe(III) under circum-neutral and alkaline conditions. Nonetheless, significant steady-state concentrations of Fe(II) have been measured in coastal oceanic waters (2) and cloudwaters (3). The biogeochemical cycles of iron and its speciation have been the focus of much attention in the past. It has been suggested that in regions where sources of N and P are abundant iron may be a limiting trace nutrient for phytoplankton primary productivity (4-8). The oxidation state is an important factor for the bioavailibility and rate of uptake of Fe by phytoplankton. Additionally, Fe(III)/Fe(II) redox couples are important mediators of charge-transfer reactions in natural waters (9). Fe(III)-carboxylate complexes have been shown to undergo photo-assisted redox reactions where Fe(III) is reduced to Fe(II) and the complexed organic anion is oxidized (10-13). Moreover, Pehkonen *et. al.*, 1993, have shown that this photochemical pathway in cloudwaters can be a significant degradation pathway for carboxylic acids in the atmosphere. The importance of iron speciation has also been stressed as a major factor in controlling the reactivity of Fe(III) as a catalyst and as a photolytic source of OH radical (14-16).

The determination of the oxidation state of iron in natural water samples has traditionally been achieved by complexation with specific, chromophoric chelating agents followed by spectrophotometric measurement. Common chelators for Fe(II) are 1,10-phenanthroline (Phen) (17-19) and ferrozine (Fz) (3-(2-pyridyl)-5,6-diphenyl-1,2,4-triazine-p,p'-disulfonic acid) (20, 21). Ferrozine has become the most prevalent spectrophotometric chelating reagent for the determination of Fe(II) in blood serum and water samples because of its high aqueous solubility and its large molar extinction coefficient (ε_{Phen} = 11,100 M^{-1} cm^{-1}; ε_{Fz} = 27,900 M^{-1} cm^{-1}) (22). Without sample pretreatment, the sensitivity of spectrophotometric methods is limited to the range of concentration • the 100 nM concentration using a 1 cm optical path length. However, analytical methods that use extraction and preconcentration of the Fe(II)–ferrozine complex on a C_{18} Sep-Pak cartridge (23) or a high performance liquid chromatographic column have resulted in improved detection limits for Fe(II) down to the nanomolar level (24, 25). Such methods require relatively large sample volumes (10 - 400 mL), limiting their applicability to systems where sample size is not restricted. Analytical procedures to determine the amount of photochemically available iron in ambient aerosols, for example, require small sample sizes (< 1 mL) and low detection limits (26).

Electrospray (ES) provides a potential solution to the problem of analyzing aqueous samples by mass spectrometry (MS). The electrospray process provides a mechanism of "soft" ionization of aqueous analytes from solution to the gas phase. Soft ionization of the analyte can eliminate the fragmentation of the analyte, allowing for the direct detection of intact molecular ions by the mass spectrometer. Within a concentration range that depends on the analyte and solvent conditions, the electrosprayed ion intensity

measured in the gas phase is directly proportional to the ion concentration in the aqueous sample (27-31). This allows the straightforward quantification of analyte ions in solution by ES-MS. The oxidation state of many compounds can also be determined through the m/z (mass to charge) ratio and the aquo complexes of transition metals have been directly observed. However, sensitivity of divalent cations in ES-MS is less than that of monovalent cations. Detection limits for most free divalent metal ions or solvated divalent metal ion clusters is around 10^{-6} M (29, 32). Thus, a different approach must be utilized to determine concentrations of the divalent oxidation state of transition metals below this level.

A method has been developed that takes advantage of the redox-selective binding of 1,10-phenanthroline and the stability of the Fe(II)-Phen complex in the electrospray source. Fe(II) selective ligands form strong complexes (log $\beta_{3,Phen}$ = 21.5) (33) that can be directly determined by ES-MS. In addition to Fe(II), 1,10-phenanthroline binds strongly with other divalent transition metals, such as Cu(II), Ni(II), Zn(II) and Co(II). These metals may interfere with spectrophotometric approaches, but can be resolved individually by ES-MS.

In this study, the use of ES-MS is explored as an analytical tool to determine the [Fe(II)(aq)] in solution by measuring the signal generated by $Fe(II)Fz_3$ or $Fe(II)Phen_3$ complexes. The dependence of the analyte signal on pH, concentration and type of background electrolyte, and various electrospray source parameters has been determined. Using the phenanthroline method under optimum conditions, a detection limit of 5 x 10^{-13}

moles of Fe(II) has been achieved, realizing a increase of sensitivity of nearly two orders of magnitude in one tenth of the sample volume over the spectrophotometric techniques.

A.2 Experimental Methods

A.2.1 Materials

All reagents and standards were prepared by dissolving high purity salts obtained from Aldrich in 18.2 MΩ Milli-Q ® water. Anhydrous 1,10-phenanthroline (Phen) (27.0 mg) and the monosodium salt of ferrozine (Fz) (73.9 mg) reagents were dissolved in 25 g Milli-Q to generate 6.00×10^{-3} molal (m) solutions; a single drop of concentrated Seastar ultra-high purity HNO_3 was added to facilitate dissolution. Ferrous iron standards were produced by dilution from a stock ferrous ammonium sulfate solution. The stock solution was stored at pH 4 and prepared freshly at regular intervals to avoid the oxidation of ferrous to ferric iron. Samples for analysis were prepared by adding 0.1 mL of 0.01 M high purity ammonium acetate buffer (Baker) and 0.01 mL of the 1,10-phenanthroline or ferrozine reagent to 1 mL of sample or standard. Ammonium salts for the buffer were chosen over sodium salts because sodium forms more persistent adducts with analyte ions than ammonium in electrosprayed solutions (34, 35). The solution was then diluted with 1.00 g of Omnisolv HPLC-grade methanol (Baker) to enhance evaporation through the reduction of the surface tension of the droplets in the electrospray process. All samples were prepared in acid-cleaned polypropylene to minimize metal contamination. Ionic strength was varied by the changing the buffer concentration or by the addition of NaCl.

The pH conditions were varied by changing the composition of the ammonium acetate buffer.

A.2.2 Analytical ES-MS Procedure

The mass spectrometric analysis was performed on a Hewlett Packard 5989B quadrupole mass spectrometer equiped with a 59987A electrospray ionization interface. The interface (Figure 1) consists of a spray capillary surrounded by a cylindrical electrode, 2 skimmers, and a system of electrostatic lenses that focus the ion beam. The desolvation of the droplets was performed using N_2 as a drying gas at 225 °C in a counter-current flow with respect to the spray chamber between the needle and the capillary entrance. Table 1 shows the optimized voltages for the electrodes, skimmers, and lenses. Pressures within the system are differentially controlled by two mechanical pumps and two turbo-pumps to maintain the pressure at approximately 0.2 torr in the ion focusing region and at 10^{-5} torr in the quadrupole region during operation. Collisionally induced dissociation (CID) was carried out in the intermediate pressure region (approximately 3 torr) by varying the kinetic energy of the ions. Adjustments to the kinetic energy are accomplished by altering the differential voltage between the capillary exit and the first skimmer from 80-300 V.
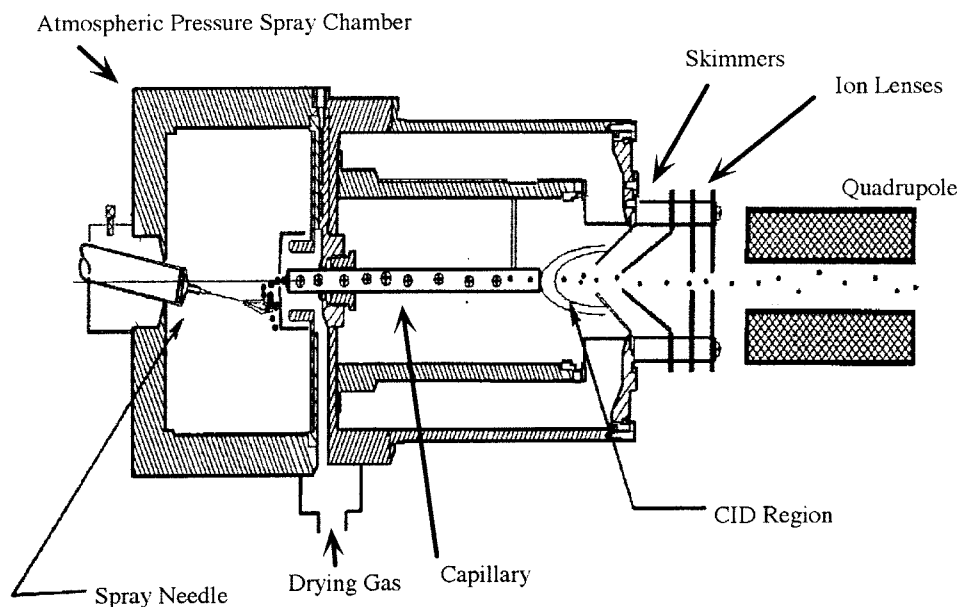
Figure 1

Overview of the HP 59987A electrospray source.

The standard ES-MS Rheodyne injection port was removed and replaced with a Western Analytical all-PEEK (Poly ether ether ketone) injection valve to reduce potential contamination of the sample with metal surfaces. To further reduce Fe contamination, samples were introduced into a 200 µL PEEK injection loop by a Hamilton Gastight syringe with a Teflon plunger, and a PEEK needle. The sample loop was rinsed with methanol between samples, and with excess sample before each injection to minimize the cross contamination of samples.

Table 1

Optimized electrospray parameters for the FePhen$_3$ system.

Capillary Voltage	-4000	V
End Plate Voltage	-3500	V
Cylinder Voltage	-6000	V
Capillary Exit Voltage	variable	V
Skimmer 1	22.0	V
Lens 1	21.2	V
Skimmer 2	6.2	V
Lens 2	8.2	V
Lens 3	-42.0	V

A Hewlett Packard 1090 LC pump delivered the flow injection solvent (50 wt %

methanol/water) to introduce the sample at a flow rate of 50 μL per minute. All

connections between instruments and valves consisted of 0.010 inch inner diameter

PEEK tubing. Two different capillary needles were used in the spray chamber, the

standard 30 gauge stainless steel needle provided by Hewlett Packard and a custom built

aluminum coated fused silica capillary (200 μm O.D., 100 μm I.D.) manufactured by

Polymicro Technologies, Phoenix, AZ. The fused silica capillary was used to minimize

the amount of iron the sample comes in direct contact with in the high electric field region of the ES-MS interface.

A.3 Results and Discussion:

The electrospray mass spectrum of the $FeFz_3$ complex solution was examined in both positive ion and negative ion mode (Figure 2). In negative ion mode, where the capillary has a positive potential relative to the spray needle, the spectrum shows peaks due to Fz^{2-} at m/z 234, HFz^- at m/z 469 and $NaFz^-$ at m/z 492. The spectrum in positive ion mode is complicated by the dimerization of ferrozine, sodium exchange for protons, and the loss of structural functionalities such as the $-SO_3$ groups (the structure of the Fz ligand is given in Figure 3). Three distinct adduct clusters can be identified, with each adjacent peak representing the exchange of H^+ for Na^+ as noted by the peak spacings of 22 amu. In addition, the Fz_2^+ and Fz_4^{2+} clusters nearly overlap resulting in doublet peaks in the mass spectra. We expect to see a peak at m/z 365 for $FeFz_3^{4-}$ in negative ion mode and peaks at m/z 733 and 1465 for the doubly and singly charged octahedral complexes of FeFz in positive ion mode. Neither of these peaks were observed. Because of these complications none of the peaks of the $FeFz_3$ solution can be unambiguously assigned as an Fe containing ion, making ferrozine a poor choice of complexing ligands for the quantification of Fe(II) by ES-MS.
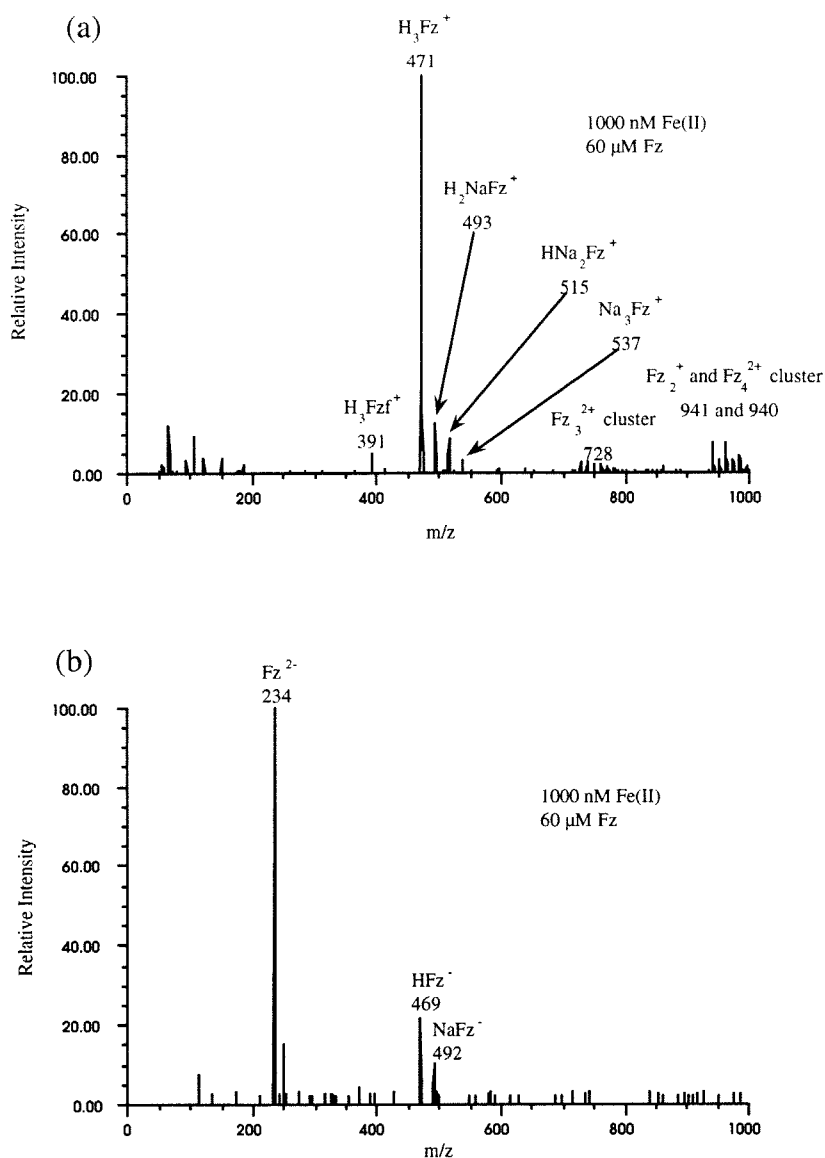
Figure 2

Mass spectra of the $FeFz_3^{2+}$ complex in (a) positive ion mode and (b) negative ion mode. The ferrozine ligand with the fragmentation loss of one sulfonate group is denoted by Fzf.

The clusters in positive ion mode refer to the exchange of H^+ for Na^+ on the sulfonate groups of Fz which leads to the adduct peak distribution of the various species.
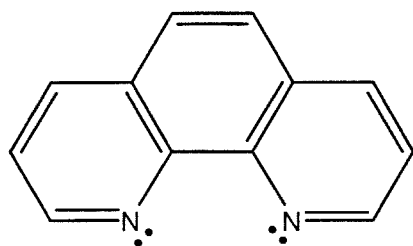
1,10 Phenanthroline
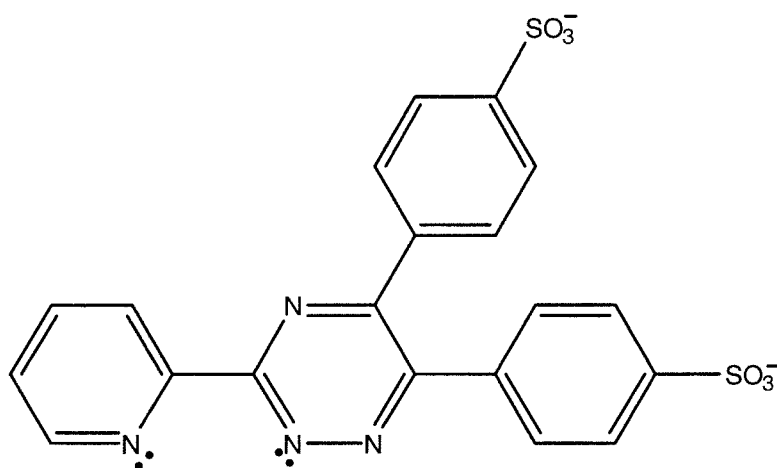
Ferrozine

Figure 3

Chemical structures of ferrozine and 1,10-phenanthroline. Lone pair of electrons on the N atoms denote the metal binding sites of the ligands.

1,10-phenanthroline was chosen as an alternative Fe(II)-specific complexing ligand. The positive ion and negative ion mass spectra were examined for the Fe-Phen solution. No peaks that were significantly above the noise level were observed in the negative ion mode. A sample of the positive ion mode spectrum is shown in Figure 4. This spectrum shows the HPhen$^+$ peak at m/z 181, the Na adduct at m/z 203, the Na bridged dimer at m/z 383, and the Fe containing species FePhen$_3$$^{2+}$ and FePhen$_2$$^{2+}$ at m/z 298 and m/z 208.

The absolute ion intensities of spectra taken on different sample runs were observed to change slightly, and calibrations were performed for each sample run. Ion intensities of samples taken during the same day were highly reproducible.
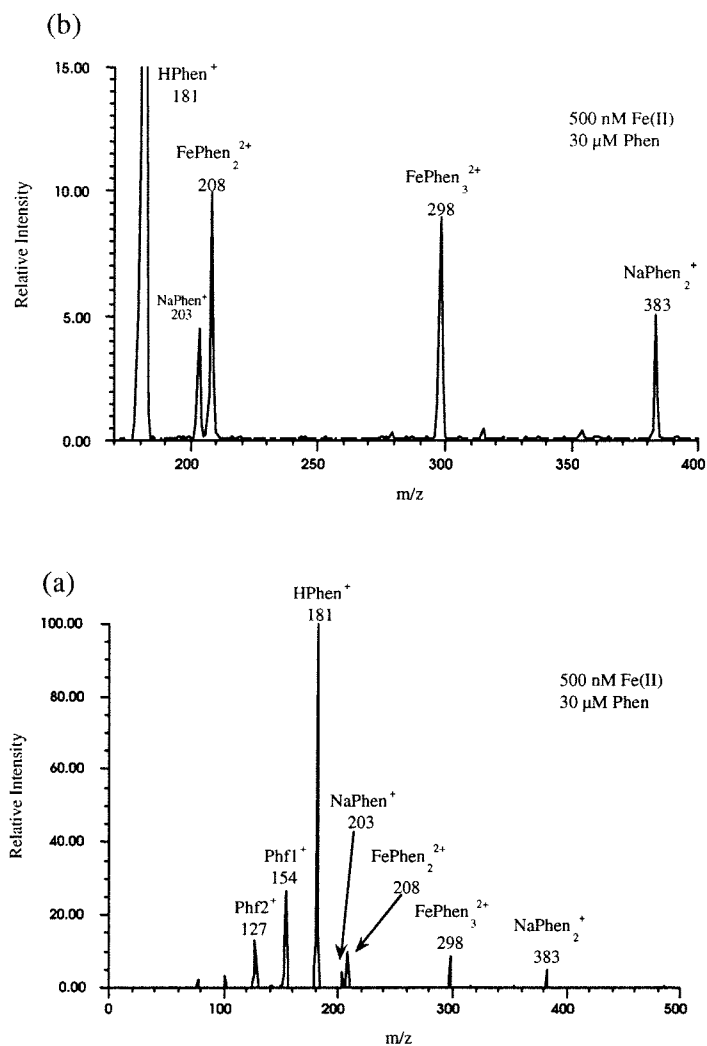
Figure 4

Positive ion mode ES mass spectrum of the FePhen$_3{}^{2+}$ complex. Shown are (a) full scan and (b) close up of the analytical peaks of interest. The phenanthroline ligand undergoes two fragmentation events, labeled Phf1 and Phf2.

Phenanthroline is also a strong ligand for several other divalent transition metals. Although in conventional UV-vis spectrometry the non-selectivity of phenanthroline is often a problem, in ES-MS these metals do not significantly interfere, as they have different mass assignments. For example, the $NiPhen_3^{2+}$ and $CuPhen_3^{2+}$ ions have m/z assignments of 299 and 301.5, respectively. These ions can easily be distinguished from the $FePhen_3^{2+}$ ion peak at m/z 298. Figure 5 displays the experimental mass spectra of several of the transition metal phenanthroline complexes that may be examined through ES-MS.
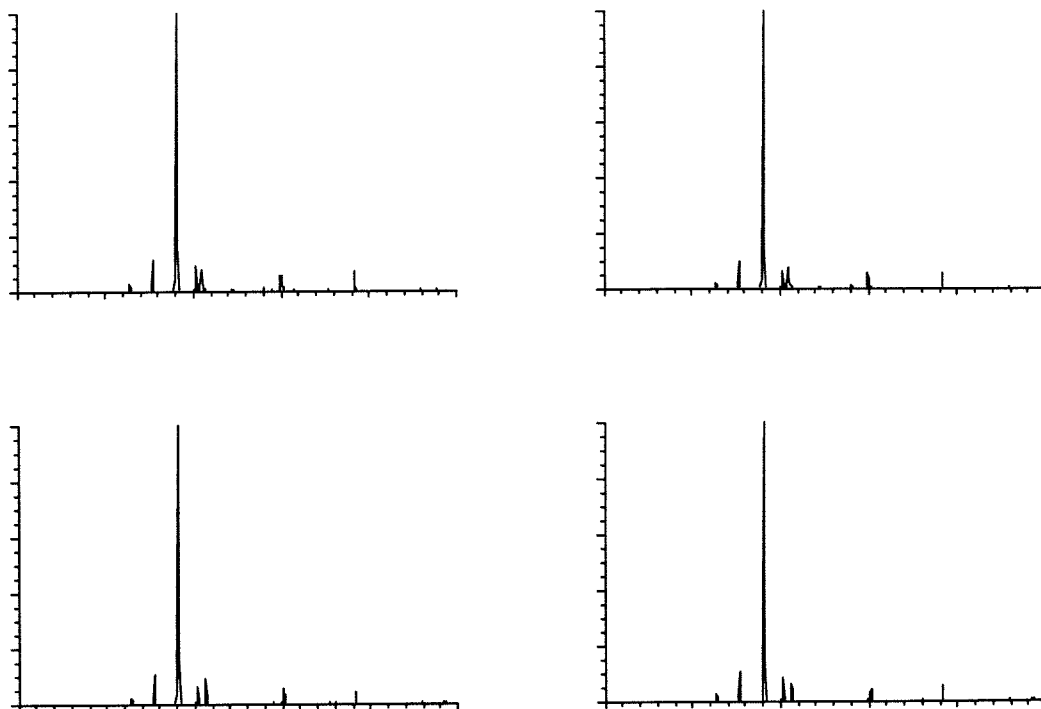
Figure 5

Positive ion mode ES mass spectra of 1,10-phenanthroline complexes of (a) Co(II), (b) Ni(II), (c) Cu(II), and (d) Zn(II).

Phenanthroline forms a stable complex with Fe(III), having a log β_3 of 13.8 (33). It has also been shown that phenanthroline may reduce Fe(III) to Fe(II) at a non-negligible rate in aqueous solution (36). It is therefore conceivable that large excesses of Fe(III) in the system may interfere with the measurement of the Fe(II)-Phen complex. This potential interference was investigated (data not shown) revealing that high concentrations of Fe(III) did not produce any detectable Fe(III) or Fe(II) complexes over several hours of

incubation, nor did excess Fe(III) added to the Fe(II)-Phen system adversely affect the signal of FePhen$_3^{2+}$ at m/z 298.

A.3.1 Solution Parameters

pH is defined throughout this discussion as the activity of the proton in the methanol/water mixture of the sample. The pH of the mixed solvent samples was determined from a calibration to oxalate, acetate, and phosphate buffers in 50% methanol solutions. The standard pH for these buffers are 2.47, 5.64, and 8.21, respectively (37). An Orion combination glass electrode (model #39532) was used for pH measurements. The importance of pH is twofold. First, the activity of the proton in solution affects the speciation of the Fe(II)-phenanthroline system, by competing as a Lewis acid with Fe(II) for the aromatic N in the phenanthroline heterocycle. Second, the formation of droplets within the ES interface is influenced by the charge state of the introduced solution, and has an effect on the efficiency of the droplet and ion formation process in the ES chamber (38). Figure 6 shows that the relative signal intensity of the m/z 298 peak for the FePhen$_3^{2+}$ complex varies as a complicated function of pH. The ionic strength of the samples are approximately constant for pH > 2.7. The optimal pH was determined to be between 4 and 5.
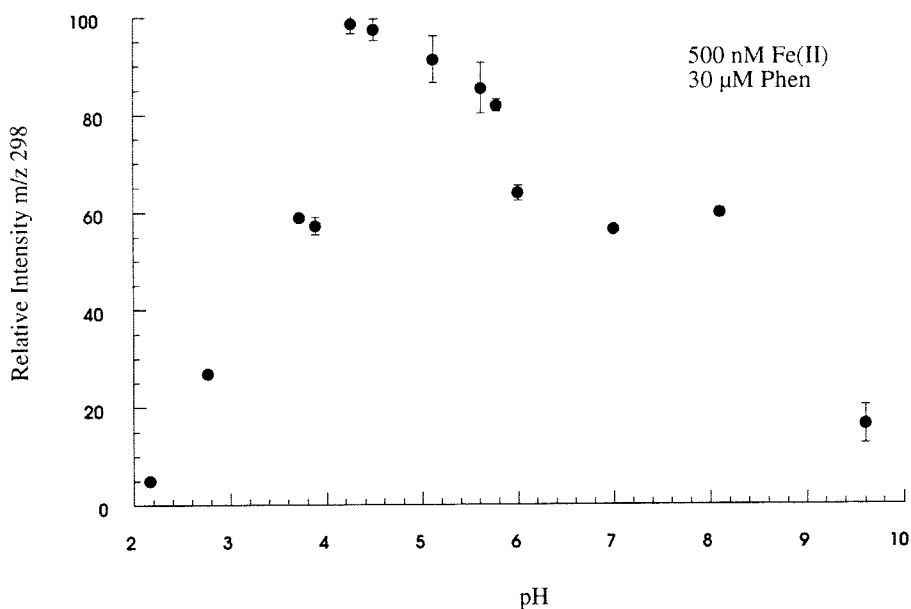
Figure 6

Dependence of the signal intensity of the $FePhen_3^{2+}$ peak at m/z 298 on pH.

The concentrations and type of external electrolytes in the sample are also important to consider. The presence of external "spectator" electrolyte ions has been studied extensively by Kebarle and coworkers (27, 39-41). They have proposed the following equation to model the mass spectrometrically detected ion abundance, (39)

$$I_{A+,ms} = \frac{pf[A^+]}{k_{A+}[A^+] + k_{E+}[E^+]} I$$

where $I_{A+,ms}$ is the detected ion current of analyte A^+, I is the total current, p is a constant expressing the efficiency of the spectrometer for detecting gas-phase ions, f is the fraction of droplet charge converted into gas-phase ions, $[A^+]$ and $[E^+]$ are respectively the analyte and external electrolyte solution concentrations, and k_A and k_E are rate constants that

express the rate of transfer of ions from the droplets to the gas-phase. This has been shown to correlate well with experimental results for singly charged ions (27). A slightly modified version of this equation also agrees for data from ions that exhibit variously charged states (42).

The ion intensity of the m/z 298 peak of $FePhen_3^{2+}$ was monitored over several orders of magnitude of ionic strength by varying the concentrations of buffer electrolyte and NaCl (Figure 7). Maximum intensity occurred for $I < 2 \times 10^{-3}$ M. At higher concentrations of NaCl and buffer, the signal rapidly decreased to 35% of maximum at 10^{-2} M. The suppression of the analyte signal intensity can be qualitatively accounted for by the expression given above. NaCl additions in general had a greater effect on the supression of signal than the buffer additions. This is due to the fact that the k_E for Na^+ is greater than the k_E for NH_4^+ (39). Note that effect of ionic strength has some minor implications for the pH experiments above, since the contribution of the proton activity of low is no longer negligible for pH < 2.7.
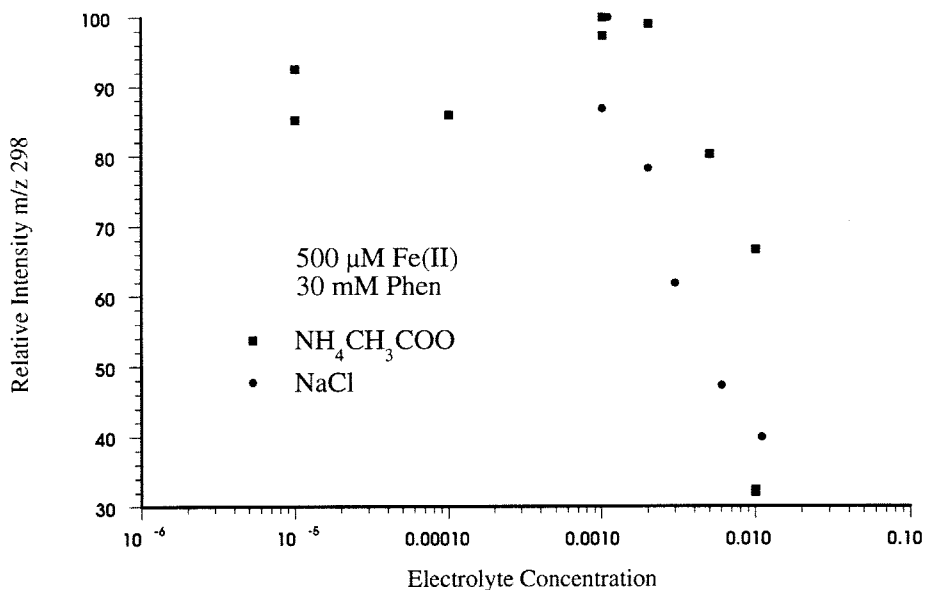
Figure 7

Dependence of the signal intensity of the FePhen$_3^{2+}$ peak at m/z 298 on the background

electrolyte concentration. Points represented by the squares are adjusted with ammonium

acetate buffer and circles are adjusted with NaCl.

A.3.2 Collisionally Induced Dissociation

The capillary exit voltage (CapEx) was also optimized. Analyte ions can undergo various

degrees of collisonally induced dissociation (CID) in the region between the capillary exit

and the first ion skimmer. In our system, the voltage of the first ion skimmer is kept

constant relative to ground, and the CapEx is varied. By varying the CapEx one varies

the collisional cross-section of the analyte and carrier gas in this region. During data

acquisition for calibrations and sample quantification, the CapEx was ramped

dynamically over the m/z axis such that the observed signal intensity at each m/z of

interest was maximized, and the CapEx for intermediate m/z's was interpolated linearly between optimized values. In the Fe-Phen system both the $FePhen_3^{2+}$ and $FePhen_2^{2+}$ ions were observed and maximized at their respective CapEx voltages. The $FePhen_2^{2+}$ ion was produced as a result of the CID of the $FePhen_3^{2+}$ ion. The phenanthroline ion may also undergo various degrees of fragmentation, producing the expected fragments Phf1 at m/z 154 and Phf2 at m/z 127. These fragments occur at higher voltages than the CID of $FePhen_3^{2+}$ since it involves the fragmentation of covalent aromatic bonds rather than the coordination complex metal-ligand bond. Figure 8 shows the successive fragmentation of Phen and the $FePhen_3^{2+}$ complex at various CapEx voltages.
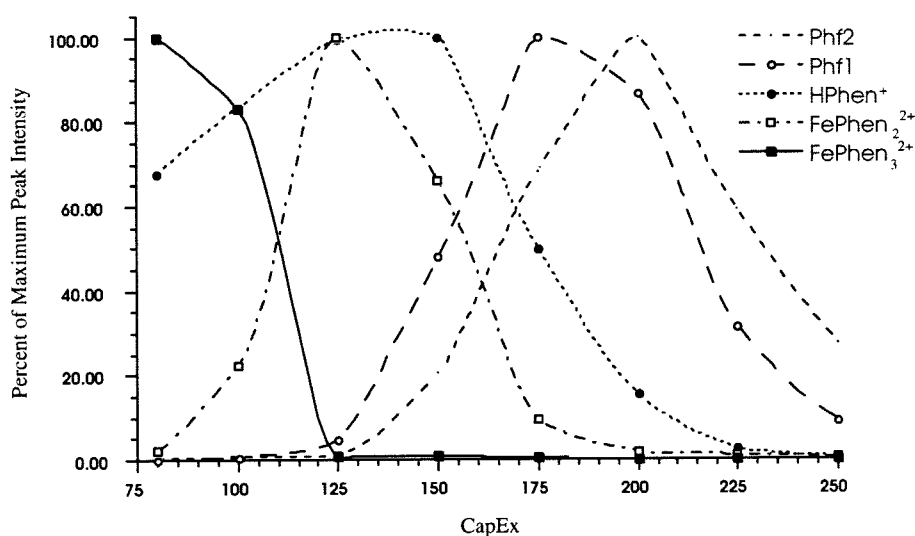

Figure 8

Fragment production of 500 nM Fe(II), 60 μM Phen system with respect to an increase in CapEx. Intensities are relative to the species maximum intensity. Note that the $FePhen_3^{2+}$ and $FePhen_2^{2+}$ are complimentary, and also produces an increase in the $HPhen^+$ intensity. At higher CapEx voltages, all of the species continue to fragment to smaller species.

It might be expected that a positive correlation should exist between the stepwise formation constant (K_3) of $MPhen_3{}^{2+}$, where M is a divalent first row transitional metal, and the applied CapEx voltage, given that each parameter is related to ligand-metal bond strength. However, K_3 is an equilibrium measure of free energy in aqueous solution, and includes entropy and the effects of solvent, while CapEx is a non-normalized voltage that has a complicated relation to the collisional cross-section. In addition, the region in which collisions occur is far from equilibrium, with large gradients of pressure, temperature and voltage. The $MPhen_3{}^{2+}$ molecule has numerous degrees of freedom and can be expected to exhibit complicated distributed behavior with respect to the energetics of bond breaking in the region prior to the detector. To relate CapEx to K_3, we define

$$E_{ce} \equiv \frac{m_{cg}M}{m_{cg}+M}\left(\text{CapEx}-V_{\text{skim1}}\right)$$

where m_{cg} = mass of the carrier gas (N_2), M = mass of the colliding molecule ($Mphen_3{}^{2+}$), and V_{skim1} is the voltage of the first skimmer lens with respect to ground. The effect of CID was examined for several other transition metals that have large stability constants with 1,10-phenanthroline, and the resulting relationship between E_{ce} and measured stability constants (33) is shown in Figure 9.
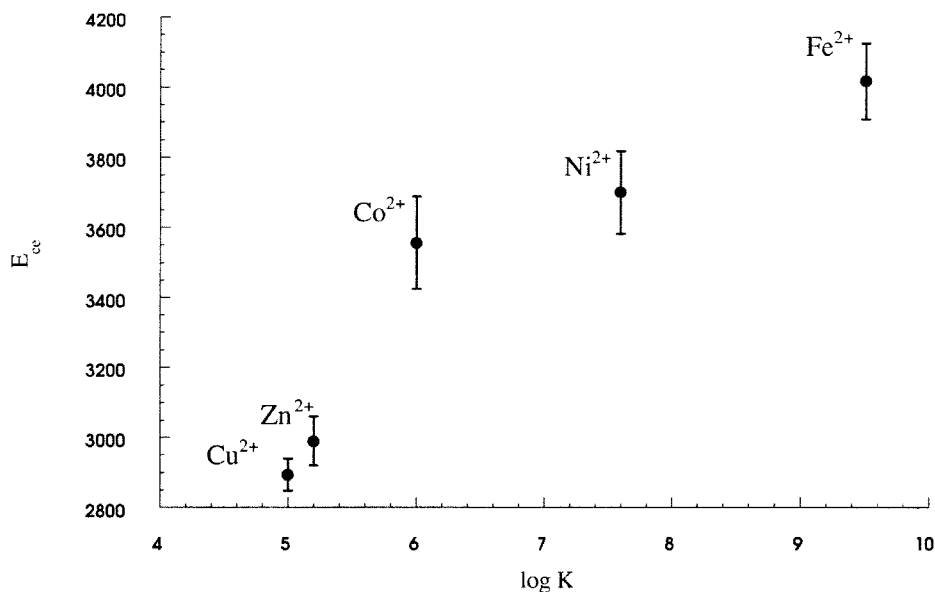
Figure 9

Variation of E_{ce} with the stepwise formation constant, K.

A.3.3 Contamination Minimization

Under certain conditions the electrospray ion source can act as an electrolytic cell (32, 43-47). Blades and coworkers (32) have shown that electrospray processes can cause the oxidation of the stainless steel capillary by the reaction $Fe_{(s)} = Fe^{2+} + 2e^-$. If the standard stainless steel capillary is used, then there is the potential to release significant concentrations of Fe^{2+} ions into the sample flow if proper electrolysis conditions exist. Experiments to determine the effective contamination introduced by this process were performed by comparing the signal obtained from an aluminum coated fused silica needle with the standard stainless steel needle. It was determined by the method of standard additions that the blank background contribution from the oxidation of the stainless

needle was approximately 20 to 30 nM Fe(II) as detected by the $FePhen_3^{2+}$ complex under optimum operating conditions. When the stainless steel needle was replaced with the fused silica needle, the background concentration of Fe(II) was reduced by nearly an order of magnitude to 3 nM. Figure 10 shows the effect of the stainless steel needle oxidation on the signal. This resultant contamination is probably due to impurities in reagents and solvents and is unavoidable without extensive reagent purification.
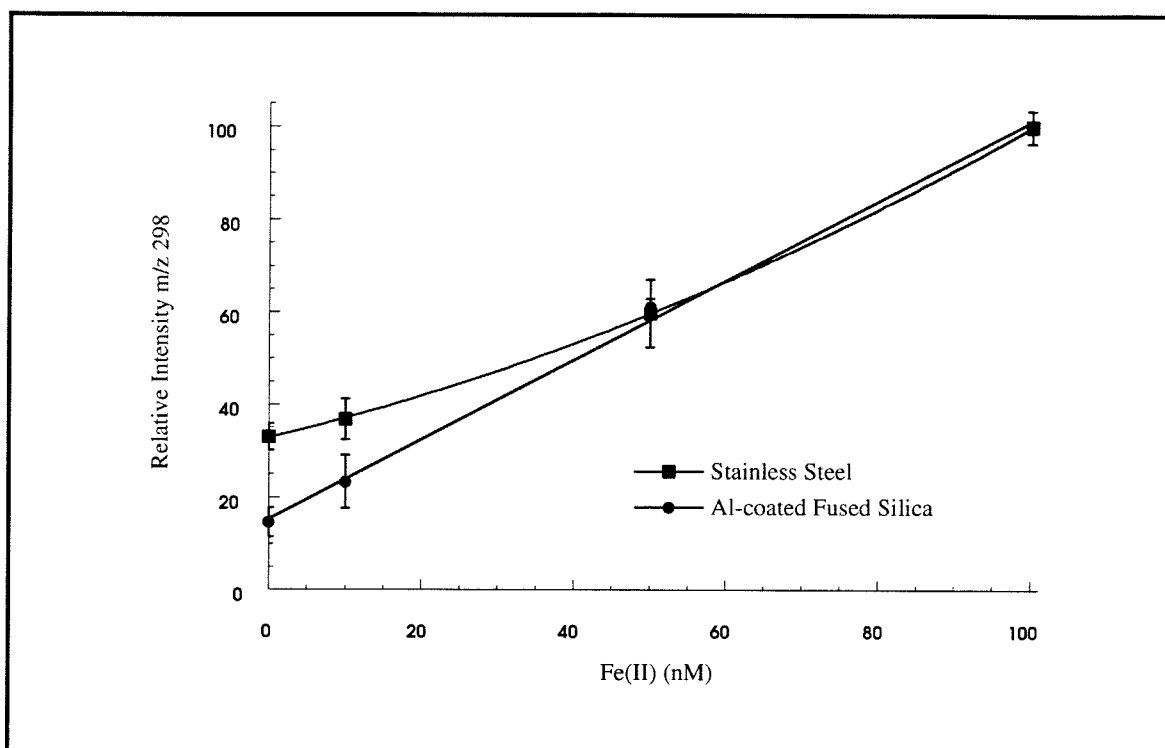
Figure 10

The effect of the oxidation of the stainless steel needle on the signal of the Fe(II)-Phen complex at m/z 298.

Low concentration calibrations were performed from 0-500 nM Fe(II) using the fuesd

silica needle. The calibrations showed a good linear correlation between the Fe(II)

concentration in the analyzed solution and the ion current for the m/z 298 and m/z 208

peaks over the entire concentration range. The experimental data fit and 95% confidence

intervals are shown in Figure 11. If careful precautions are taken to eliminate potential

contamination, detection limits of approximately 5 nM can be obtained. Additional

experiments have shown that the linear response region can be extended to over 10 μM

Fe(II) at the expense of low concentration sensitivity if higher concentrations of

phenanthroline are used.
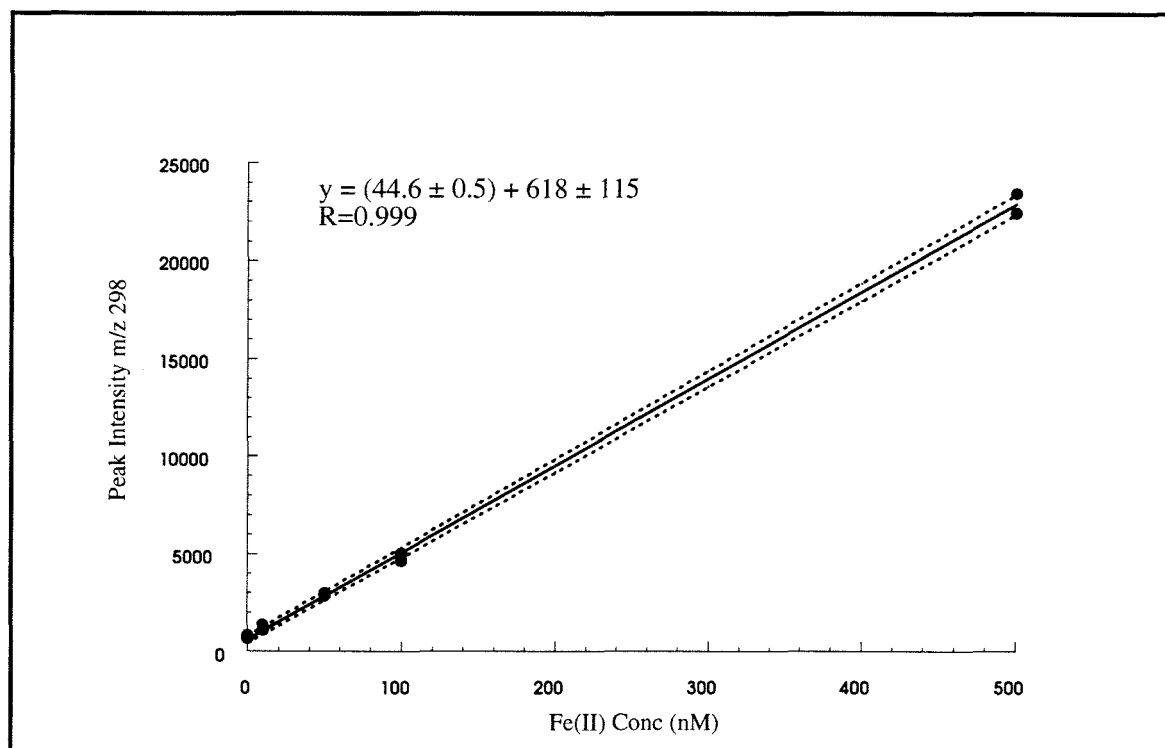
Figure 11

Calibration plot of the Fe(II)-Phen complex as deteected at m/z 298. The dashed

envelope lines represent the 95% confidence limits.

A.4 Conclusions

The results in this work demonstrate the usefulness of electrospray mass spectrometry in the detection and quantification of metal-ligand analytes. The procedure has been used to quantify concentrations of Fe(II) as the iron-phenanthroline complex. It features low detection limits from small volumes making it an ideal technique where preconcentration is not practical. The major drawbacks found in this study for the application of this method to the analysis of Fe(II) in natural water samples are the potential interferences of high levels of electrolyte and the complicated dependence of signal on pH. The equipment is also not suitable for direct use in the field. Further work is in progress to establish simultaneous detection and quantification of other divalent transition metal complexes as well as Fe(III) through ES-MS methods.

Acknowledgment for Appendix

References for Appendix

(1)   Taylor, S. R.; McLennan, S. M. *The Continental Crust: Its Composition and Evolution*, 2nd ed.; Blackwell Scientific Publications: Cambridge, MA, 1985.

(2)   Hong, H.; Kester, D. R. *Limnol. Oceanogr.* **1986,** *31*, 512-524.

(3)   Munger, J. W.; Waldman, J. M.; Jacob, D. J.; Hoffmann, M. R. *J. Geophys. Res.* **1983,** *88*, 5109-5132.

(4)   Martin, J. H.; Fitzwater, S. E.; Gordon, R. M. *Nature* **1988,** *331*, 341-343.

(5)   Martin, J. H.; Gordon, R. M. *Deep Sea Res.* **1988,** *35*, 177-196.

(6)   Martin, J. H.; Gordon, R. M.; Fitzwater, S. E. *Nature* **1990,** *345*, 156-158.

(7)   Kolber, Z. S.; Barber, R. T.; Coale, K. H.; Fitzwater, R. M.; Greene, R. M.; Johnson, K. S.; Lindley, S.; Falkowski, S. E. *Nature* **1994,** *371*, 145-149.

(8)   Price, N. M.; Ahner, B. A.; Morel, F. M. M. *Limnol. Oceanogr.* **1994,** *39*, 520-534.

(9)   Schwarzenbach, R. P.; Gschwend, P. M.; Imboden, D. M. *Environmental Organic Chemistry*; John Wiley: New York, 1993.

(10)   Pehkonen, S. O.; Siefert, R. L.; Hoffmann, M. R. *Environ. Sci. Technol.* **1995,** *29*, 1215-1222.

(11)   Pehkonen, S. O.; Siefert, R. L.; Erel, Y.; Webb, S. M.; Hoffmann, M. R. *Environ. Sci. Technol.* **1993,** *27*, 2056-2062.

(12)   Faust, B. C.; Zepp, R. G. *Environ. Sci. Technol.* **1993,** *27*, 2517-2522.

(13)   Zuo, Y.; Hoigne, J. *Environ. Sci. Technol.* **1992,** *26*, 1014-1022.

(14)   Graedel, T. E.; Mandich, M. L.; Weschler, C. J. *J. Geophys. Res.* **1986,** *91*, 5205-5221.

(15)   Faust, B. C.; Hoigne, J. *Atmos. Environ.* **1990,** *24,* 79-89.

(16)   Weschler, C. J.; Mandich, M. L.; Graedel, T. E. *J. Geophys. Res. A.* **1986,** *91,* 5189-5204.

(17)   Caldwell, D. H.; Adams, R. B. *J. Amer. Water Works Assoc.* **1946,** *38,* 727-730.

(18)   In *Standard Methods for the Examination of Water and Wastewater*; Greenberg, A. E., Clesceri, L. S., Eaton, A. D., Eds.; American Public Health Association: Washington D.C., 1992, pp 3.65-3.68.

(19)   Schilt, A. A. *Analytical Applications of 1,10-Phenanthroline and Related Compounds*; Pergamon Press: New York, 1969.

(20)   Stookey, L. L. *Anal. Chem.* **1970,** *42,* 119-781.

(21)   Carter, P. *Anal. Biochem.* **1971,** *40,* 450-458.

(22)   Thompsen, J. C.; Mottola, H. A. *Anal. Chem.* **1984,** *56,* 755-757.

(23)   King, D. W.; Lin, J.; Kester, D. R. *Anal. Chim. Acta.* **1991,** *247,* 125-132.

(24)   Blain, S.; Treguer, P. *Anal. Chim. Acta* **1995,** *308,* 425-432.

(25)   Yi, Z.; Zhuang, G. S.; Brown, P. R.; Duce, R. A. *Anal. Chem.* **1992,** *64,* 2826-2830.

(26)   Siefert, R. L.; Webb, S. M.; Hoffmann, M. R. *J. Geophys. Res.* **1996,** *101,* 14441-14449.

(27)   Tang, L.; Kebarle, P. *Anal. Chem.* **1993,** *65,* 3654-3668.

(28)   Cheng, Z. L.; Siu, K. W. M.; Guevremont, R.; Berman, S. S. *J. Am. Soc. Mass Spectrom.* **1992,** *3,* 281-288.

(29)   Agnes, G. R.; Horlick, G. *App. Spec.* **1994,** *48,* 649-654.

(30)   Agnes, G. R.; Stewart, I. I.; Horlick, G. *App. Spec.* **1994,** *48,* 1347-1359.

(31)   Agnes, G. R.; Horlick, G. *App. Spec.* **1994,** *48,* 655-661.

(32)   Blades, A. T.; Ikonomou, M. G.; Kebarle, P. *Anal. Chem.* **1991,** *63,* 2109-2114.

(33)   Smith, R. M.; Martell, A. E. *Critical Stability Constants*; Plenum Press: New York, 1976.

(34)   Kilby, G. W.; Sheil, M. M. *Org. Mass Spectrm.* **1993,** *28,* 1417-1423.

(35)   Duffin, K. L.; Henion, J. D.; Shieh, J. J. *Anal. Chem.* **1991,** *63,* 1781-1788.

(36)   Schmid, R.; Han, L. *Inorg. Chim. Acta* **1983,** *69,* 127-134.

(37)   Bates, R. G. *Determination of pH,* 2nd ed.; John Wiley: New York, 1973.

(38)   Wang, G. D.; Cole, R. B. *Organic Mass Spectrometry* **1994,** *29,* 419-427.

(39)   Tang, L.; Kebarle, P. *Anal. Chem.* **1991,** *63,* 2709-2715.

(40)   Ikonomou, M. G.; Blades, A. T.; Kebarle, P. *Anal. Chem.* **1990,** *62,* 957-967.

(41)   Ikonomou, M. G.; Blades, A. T.; Kebarle, P. *Anal. Chem.* **1991,** *63,* 1989-1998.

(42)   Wang, G.; Cole, R. B. *Anal. Chem.* **1994,** *66,* 3702-3708.

(43)   Zhou, F.; Berkel, G. J. V. *Anal. Chem.* **1995,** *67,* 3643-3649.

(44)   Van Berkel, G. J.; Zhou, F. *Anal. Chem.* **1995,** *67,* 2916-2923.

(45)   Van Berkel, G. J.; Zhou, F. *Anal. Chem.* **1995,** *67,* 3958-3964.

(46)   Van Berkel, G. J.; Zhou, F. *J. Am. Soc. Mass Spectrom* **1996,** *7,* 157-162.

(47)   Xu, X.; Nolan, S. P.; Cole, R. B. *Anal. Chem.* **1994,** *66,* 119-125.

References

Albrecht-Gary A., Blanc S., Rochel N., Ocaktan A. Z., and Abdallah M. A. (1994) Bacterial iron transport: Coordination properties of pyoverdin PaA, a peptidic siderophore of Pseudomonas aeruginosa. *Inorg. Chem.* **33**, 6391-6402.

Albrecht-Gary A., Palanche-Passerson T., Rochel N., Hennard C., and Abdallah M. A. (1995) Bacterial siderophores: iron exchange mechanism with ethylenediamineteraactic acid. *New J. Che.* **19**, 105-113.

Banwart S., Davies S., and Stumm W. (1989) The role of oxalate in accelerating the reductive dissolution of hematite (α-Fe$_2$O$_3$) by ascorbate. *Colloids and Surfaces* **39**, 303-309.

Berthelin J. (1988) Microbial weathering processes in natural environments. In *Physical and Chemical Weathering in Geochemical Cycles*, Vol. 251 (ed. A. Lerman and M. Meybeck), pp. 33-59. Kluwer Academic Publishers.

Bickel H., Keberle H., and Vischer E. (1963) *Helv. Chim. Acta* **46**, 1387.

Bolt G. H. and Bruggenwert M. G. M. (1976) Composition of the soil. In *Soil Chemistry A. Basic Elements* (ed. G. H. Bolt and M. G. M. Bruggenwert), pp. 281. Elsevier Scientific Publishing Co.

Brock T. D., Madigan M. T., Martinko J. M., and Parker J. (1994) *Biology of Microorganisms*. Prentice-Hall, Inc.

Butler A. (1998) Acquisition and utilization of transition-metal ions by marine organisms. *Science* **281**, 207-210.

Cornell R. M. (1985) Effects of simple sugars on the alkaline transformation of ferrihydrite into goethite and hematite. *Clays Clay Min.* **33**, 219-227.

Cornell R. M. and Giovanoli R. (1985) Effects of solution conditions on the proportion and morphology of goethite formed from ferrihydrite. *Clays Clay Min.* **33**(424-432).

Cornell R. M. and Schindler P. W. (1987) Photochemical dissolution of goethite in acid/oxalate solution. *Clays and Clay Minerals* **35**(5), 347-352.

Cornell R. M. and Schwertmann U. (1979) Influence of organic anions on the crystallization of ferrihydrite. *Clays Clay Min.* **27**, 402-410.

Demange P., Bateman A., Macleod J. K., Dell A., and Abdallah M. A. (1990a) Bacterial siderophores: unusual 3,4,5,6-tetrahydropyrimidine-based amino acids in pyoverdins from Pseudomonas fluorescens. *Tetrahedron Letters* **31**(52), 7611.

Demange P., Wendebaum S., Linget C., Mertz C., Cung M. T., Dell A., and Abdallah M. A. (1990b) Bacterial siderophores: structure and NMR assignment of pyoverdins Pa, siderophores of Pseudomonas aeruginosa ATCC 15692. *Biol. Metals* **3**, 155-170.

DiChristina T. J. (1994) Bioextraction (reductive dissolution) of iron from low-grade iron-ores - fundamental and applied studies. *Annals of the New York Academy of Sciences* **721**, 440-449.

Eggleston C. M. and Hochella M. F. (1992) The structure of hematite {001} surfaces by scanning tunneling microscopy: Image interpretation, surface relaxation, and step structure. *American Mineralogist* **77**, 911-922.

Ehrenreich A. and Widdel F. (1994) Anaerobic oxidation of ferrous iron by purple bacteria, a new type of phototrophic metabolism. *Applied and Environmental Microbiology* **60**(12), 4517-4526.

Ehrlich H. L. (1996) *Geomicrobiology*. Marcel Dekker.

Eisenlauer J. and Matijevic E. (1980) Interactions of metal hydrous oxides with chelating agents II. α-Fe_2O_3 - low molecular and polymeric hydroxamic acid species. *J. Colloid and Interface Science* **75**(1), 199-211.

Emerson D. and Revsbech N. P. (1994) Investigation of iron-oxidizing microbial mat community located near Aarhus, Denmark - Laboratory studies. *Applied and Environmental Microbiology* **60**(11), 4032-4038.

Faulkner K. M., Stevens R. D., and Fridovich I. (1994) Characterization of Mn(III) complexes of linear and cyclic desferrioxamines as mimics of superoxide dismutase activity. *Archives of Biochemistry and Biophysics* **310**(2), 341-346.

Fox T. R. and Comerford N. B. (1992) Influence of oxalate loading on phosphorous and aluminum solubility in spodosols. *Soil Sci. Soc. Am. J.* **56**, 290-294.

Furrer G. and Stumm W. (1983) The role of surface coordination in the dissolution of δ-Al_2O_3 in dilute acids. *Chimia* **9**, 338-341.

Gillam A. H. (1981) Quantitative determination of hydroxamic acids. *Anal. Chem.* **53**(6), 841-844.

Gray B. and Carmichael A. J. (1992) Kinetics of superoxide scavenging dismutase enzymes and manganese mimics determined by electron spin resonance. *Biochem. J.* **281**, 795-802.

Hersman L., Lloyd T., and Sposito G. (1995) Siderophore promoted dissolution of hematite. *Geochimica et Cosmochimica Acta* **59**(16), 3327.

Holmén B. A. and Casey W. H. (1996) Hydroxamate ligands, surface chemistry and the mechanism of ligand-promoted dissolution of goethite [a-FeOOH(s)]. *Geochim. Cosmochim. Acta (in press)*.

Johnson K. S., Berelson W. M., Coale K. H., Coley T. L., Elrod V. A., Faitey W. R., Iams H. D., Kilgore T. E., and Nowicki J. L. (1992) Manganese flux from continental margin sediments in transect through the oxygen minimum. *Science* **257**, 1242-1245.

Kessick M. A., Vuceta J., and Morgan J. J. (1972) Spectrophotometric determination of oxidized manganese with leuco crystal violet. *Environ. Sci. and Technol.* **6**, 642 - 644.

Klewicki J. K. and Morgan J. J. (1998) Rates of dissolution of MnOOH by ligands: pyrophosphate, ethylenediaminetetraacetate, and citrate. *Abstract from Symposium on "Speciation and Processes at the Minreral-Fluid Interface," Eighth Annual V.M. Goldschmidt Conference, Toulouse, France*.

Kosmulskim M., Matysiak J., and Szczypa J. (1993) Standard enthalpies of proton adsorption on hematite in various solvent systems. *Bulletin of the Polish Academy of Sciences-Chemistry* **41**(4), 333-337.

Kostka J. E. and Nealson K. H. (1995) Dissolution and reduction of magnetite by bacteria. *Environ. Sci. Technol* **29**, 2535-2540.

Kraemer S. M. (1997) Ligand Controlled Weathering Kinetics of Aluminum Oxide and Goethite. PhD, Technische Universität Darmstadt.

Lasaga A. C. (1995) Fundamental approaches in describing mineral dissolution and precipitation rates. In *Chemical weathering rates of silicate minerals*, Vol. 31 (ed. A. F. White, Brantley, S. L.), pp. 583. Mineralogical Society of America.

Lee Y. and Tebo B. M. (1994) Cobalt(II) oxidation by the marine manganese(II)-oxidizing Bacillus sp strain SG-1. *Applied and Environmental Microbiology* **60**(6), 2949-2957.

Liu Z., Robinson G. B., and Gregory E. M. (1994) Preparation and characterization of Mn-Salophen complex with superoxide scavenging activity. *Archives of Biochemistry and Biophysics* **315**(1), 74-81.

Lonergan D. J., Jenter H. L., Coates J. D., Phillips E. J. P., Schmidt T. M., and Lovley D. R. (1996) Phylogenetic analysis of dissimilatory Fe(III)-reducing bacteria. *J. of Bacteriology* **178**(8), 2402-2408.

Ludwig C., Casey W. H., and Rock P. A. (1995) Prediction of ligand-promoted dissolution rates from the reactivities of aqueous complexes. *Nature* **375**(4), 44-47.

Mau R. E. (1992) Particle transport through porous media: Advection, longitudinal dispersion, and filtration, California Institute of Technology.

Maurice P. A., Hochella J., M. F., Parks G. A., Sposito G., and Schwertmann U. (1995) Evolution of hematite surface microtopography upon dissolution by simple organic acids. *Clays and Clay Minerals* **43**(1), 29-38.

Mayo S. L., Olafson B. D., and Goddard W. A. (1990) Dreiding -a generic force-field for molecular simulations. *J. Phys. Chem.* **94**(26), 8897-8909.

Moffett J. W. (1994) A radiotracer study of cerium and manganese uptake onto suspended particles in Chesapeake Bay. *Geochimica et Cosmochimica Acta* **58**(2), 695-703.

Nealson K. H. and Little B. (1997) Breathing manganese and iron - Solid-state respiration. *Adv-ApplL-Mi* **45**, 213-239.

Nealson K. H. and Myers C. R. (1992) Microbial reduction of manganese and iron: New approaches to carbon cycling. *Appl. Environ. Microbio.* **58**, 439-443.

Nealson K. H. and Saffarini D. (1994) Iron and manganese in anaerobic respiration - Environmental significance, physiology, and regulation. *Annual Review of Microbiology* **48**, 311-343.

Neilands J. B. (1981) Microbial iron compounds. *Ann. Rev. Biochem.* **50**, 715-731.

Neilands J. B. (1982) Microbial envelope proteins related to iron. *Ann. Rev. Microbiol.* **36**(285-309).

Neilands J. B. (1983) Isolation and assay of 2,3-dihydroxybenzoyl derivatives of polyamines: The siderophores agrobactin and parabactin from Agrobacterium tumefaciens and Paracoccus denitrificans. *Methods in Enzymology* **94**, 437-441.

Neilands J. B. (1984) Methodology of siderophores. *Structure and Bonding* **58**, 1-24.

Nose S. (1991) Constant temperature molecular-dynamics methods. *Progress of Theoretical Physics Supplement* **103**, 1-46.

Page W. J. (1995) The effects of manganese oxides and manganese ion on growth and siderophore production by Azobacter vinelandii. *BioMetals* **8**, 30-36.

Page W. J. and Huyer M. (1984) Derepression of the Azobacter vinelandii siderophore system, using iron-containing minerals to limit iron repletion. *J. of Bacteriology* **158**(2), 496-502.

Pekhonen S. O., Siefert R., Erel Y., Webb S., and Hoffmann R. (1993) Photoreduction of iron oxyhydroxides in the presence of important atmospheric organic compounds. *Env. Sci. and Technol.* **27**(10), 2056-2062.

Petrie L. M. (1995) Molecular interpretation for SO_2 dissolution kinetics of pyrolusite, manganite and hematite. *Applied Geochemistry* **10**, 253-267.

Rappe A. K. and Goddard W. A. (1991) Charge equilibration for molecular-dynamics simulations. *JOURNAL OF PHYSICAL CHEMISTRY* **95**(8), 3358-3363.

Robinson G. D. (1993) Major-element chemistry and micromorphology of Mn-oxide coatings on stream alluvium. *Applied Geochemistry* **8**(6), 633-642.

Roden E. E. and Zachara J. M. (1996) Microbial reduction of crystalline iron(III) oxides - Influence of oxide surface=area and potential for cell-growth. *Env. Sci. & Technol.* **30**(5), 1618-1628.

Rogers S. J., Lee C. W., Chiu Y. N., and Raymond K. N. (1987) Ferric ion sequestering agents. 15. Synthesis, solution chemistry, and electrochemistry of a new cationic analogue of enterobactin. *Inorg. Chem.* **26**, 1622-1625.

Schwarzenbach G. and Schwarzenbach K. (1963) Hydroxamatkomplexe I. Die Stabilität der Eisen(III)-Komplexe einfacher Hydroxamsäuren und Ferrioxamins B. *Helv. Chim. Acta* **154**, 1391-1400.

Schwertmann U. and Cornell R. M. (1991) *Iron Oxides in the Laboratory.* VCH Verlagsgesellschaft mbH.

Schwertmann U. and Taylor R. M. (1977) Iron Oxides. In *Minerals in Soil Environments* (ed. R. C. Dinauer), pp. 145-180. Soil Science Society of America.

Siffert C. and Sulzberger B. (1991) Light-induced dissolution of hematite in the presence of oxalate: a case study. *Langmuir* **7**, 1627-1634.

Stone A. T. and J.J. Morgan. (1984a) Reduction and dissolution of manganese(III) and manganese(IV) oxides by organics: 1. Reaction with hydroquinone. *Environ. Sci. Technol.* **18**(6), 450-456.

Stone A. T. and J.J. Morgan. (1984b) Reduction and dissolution of manganese(III) and manganese(IV) oxides by organics: 2. Survey of the reactivity of organics. *Environ. Sci. Technol.* **18**(8), 617-624.

Stumm W., Furrer G., Wieland E., and Zinder B. (1984) The Effects of complex-forming ligands on the dissolution of oxides and aluminosilicates. *The Chemistry of Weathering, NATO advanced Research Workshop.*

Stumm W. and Morgan J. J. (1996) *Aquatic Chemistry.* Wiley Interscience.

Stumm W. and Sulzberger B. (1992) The cycling of iron in natural environments: Considerations based on laboratory studies of heterogeneous redox processes. *Geochimica et Cosmochimica Acta* **56**, 3233-3257.

Stumm W. and Wollast R. (1990) Coordination chemistry of weathering - Kinetics of the surface-controlled dissolution of oxide minerals. *Reviews of Geophysics* **28**(1), 53-69.

Sugimoto T. and Sakata K. (1992) Preparation of monodisperse pseudocubic a-Fe_2O_3 particles from condensed ferric hydroxide gel. *J. Colloid and Interface Science* **152**(2), 587-590.

Sulzberger B., Suter D., Siffert C., Banwart S., and Stumm W. (1989) Kinetics of dissolution of Fe(III)(hydr)oxides in natural waters; control by surface coordination. *Marine Chemistry* **28**, 127-144.

Wawrousek E. F. and McArdle J. V. (1982) *J. Inorg. Biochem.* **17**, 169-183.

Wendenbaum S., Demange P., Dell A., Meyer J. M., and Abdallah M. A. (1983) The structure of pyoverdine Pa, the siderophore of Pseudomonas aeruginosa. *Tetrahedron Letters* **24**(44), 4877-4880.

Xyla A. G., Sulzberger B., Luther G. W., Hering J. G., Van Cappellen P., and Stumm W. (1992) Reductive dissolution of manganese (III,IV) (hydr)oxides by oxalate: the effect of pH and light. *Langmuir* **8**, 95-103.

Zinder B., Furrer G., and Stumm W. (1986) The coordination chemistry of weathering: II. Dissolution of Fe(III) oxides. *Geochimica et Cosmochimica Acta* **50**, 1861-1869.